

THEORETICAL AND EXPERIMENTAL INVESTIGATIONS OF
ANION- π INTERACTIONS IN INORGANIC AND BIOLOGICAL
SUPRAMOLECULAR ARCHITECTURES

A Dissertation

by

JILL FRANK ELLENBARGER

Submitted to the Office of Graduate and Professional Studies of
Texas A&M University
in partial fulfillment of the requirements for the degree of

DOCTOR OF PHILOSOPHY

Chair of Committee,	Kim R. Dunbar
Committee Members,	Steven E. Wheeler
	Timothy R. Hughbanks
	James C. Sacchetti
Head of Department,	Simon W. North

August 2016

Major Subject: Chemistry

Copyright 2016 Jill Frank Ellenbarger

ABSTRACT

Supramolecular chemistry encompasses the interdisciplinary study of weak intermolecular forces which allows for access to sophisticated architectures and functionalities. One newly recognized supramolecular force that is becoming increasingly prevalent in theoretical, organic, inorganic and biological chemistry is the attractive interaction between an anion and an aromatic system, the anion- π interaction. By integrating theoretical and experimental methods, the nature and implications of anion- π interactions have been studied in inorganic and biological systems.

In order to expand the library of anion-templated, supramolecular metallacyclic architectures previously reported by the Dunbar group, a semi-empirical model has been developed that accurately reproduces the reported metallacyclic frameworks and predicts metallacycles available from 18 templating anions, 15 transition metals, and 2 bridging ligands. By considering the degree of overlap between the anion and the π -system, the most ideal metallacyclic candidates have been identified for future experimental studies.

A second computational study has employed DFT methods to explore the hierarchy of factors that direct to the supramolecular formation of Ag^{I} coordination complexes, polymers and extended networks. These causative factors include the transition metal, bridging ligand, anion and solvent.

Anion-templated metallacyclic architectures were further considered as building blocks for the elaboration of extended superstructures. Complexation of the pentagonal building blocks with organic bridging ligands has led to symmetrical, ambiguous

structures and reaction with a cyano-metallate bridging moiety has facilitated supramolecular transformation into the first acetonitrile-templated metallacyclic architecture containing reduced bridging ligands.

Finally, the impact of the anion- π interaction on inhibition of malate synthase, an important protein in *Mycobacterium tuberculosis*, has been probed through DFT methods. An appropriate model active site from one inhibitor-bound protein crystal structure was employed as a structural template such that the binding interactions and orientation were reproduced with a high degree of accuracy. By screening potential molecules according to the propensity of each to participate in anion- π interactions, the pre-screened predictive method efficiently incorporates the anion- π interaction into a methodology for future drug design.

This interdisciplinary exploration of the anion- π interaction has combined theoretical and experimental research to help unravel the complexities of supramolecular inorganic and biological systems, providing direction for future experimental efforts.

DEDICATION

To my family, for their abundant love, support and encouragement. To my parents, Tim and Fran; my sister, Sara; my grandmother, Sara; and my extended Frank, Herald and now Ellenbarger families.

To my husband, Michael, whom I respect and love more every day. Thank you for how you actively love and support me.

To my Lord and Savior, Jesus Christ. For the opportunity to delve into the intricacies of His creation and be constantly awed by His creativity, omniscience and faithfulness.

ACKNOWLEDGEMENTS

What a wonderful journey this has been! I am so very thankful for many individuals who have poured into my life, both academically and personally throughout the years. First and foremost, I would like to thank my advisor, Prof. Kim Dunbar. Thank you for all of your support, encouragement and guidance through the years. Your mentorship has truly prepared me to step into this next phase of life, and I greatly appreciate all that you have done for me. I would also like to thank Prof. Steven Wheeler, who has also served as a mentor throughout the course of this project. I really appreciate all of the guidance, education, patience and encouragement you have provided. I would like to extend my gratitude to Prof. James Sacchettini, for the insightful discussions and direction he has provided, and to Prof. Timothy Hughbanks, whose high standard of excellence has motivated me since my very first semester of graduate school.

I would like to thank my undergraduate mentors from Union University, Profs. Johnston, Baldwin and Salazar, for fostering my fascination with chemistry and encouraging me in this pursuit. In addition, I would like to extend my appreciation to Dr. Gaede for her guidance and mentorship in honing my teaching skills and philosophy.

I have had the pleasure of working with superb collaborators over the years on several of the projects within this dissertation. I would like to specifically acknowledge the guidance of Prof. Ioerger; Dr. Kreiger and Dr. Huang in Prof. Sacchettini's group; Dr. Ewers and Ms. Pawlicki in Prof. James Batteas' group; and Dr. Perez, director of the Laboratory of Molecular Simulation.

I have also had the joy of working alongside many wonderful members of the Dunbar group. I would like to thank my mentor, Dr. Ian Giles, for fostering my creativity in the realm of Supramolecular Chemistry. I would also like to thank Dr. Silvia Gómez-Coca for all of her expertise, guidance, and friendship. I have really enjoyed collaborating with Toby Woods, Carolyn Gunthardt, Francisco Birk, David Kempe, Haomiao Xie, Dr. Andrew Brown, Dr. Brian Dolinar, Dr. Hanhua Zhao, and Dr. Helen Chifotides; thank you all for your help, insight, friendship and encouragement! In addition to these, there are so many other members of the group who have provided encouragement and comradery throughout this fascinating graduate school adventure, specifically Dr. Amanda David, Dr. Heather Southerland-Smallwood, Dr. Xuan Zhang, Dr. Zhanyoung Li, Dr. Mohamed Saber, Dr. Bruno Peña, Dr. Maria Ballesteros Rivas, Dr. Dawid Pinkowicz, Codi Sanders, Kelsey Schulte, Ryan Coll, Agustin Millet, and Sayan Saha.

I have been so encouraged by many friends who have poured into my life these past years as well. Thank you to my high school and college girls for banding together with me through the beginning stages of this process and continuing to encourage me. Thank you to my first-year crew for all of the support and adventures amidst the insanity of graduate school. Thank you especially to my sweet friends, Jessica, Becca, Brittany, Mandy, Kay, Katelyn, Kaitlyn, Misti, Kalen, Katherine, Sonia, among others! You all have encouraged me so much and I am so thankful for each one of you!

My family has been such a source of life and support over these years, I cannot begin to fully express my gratitude. I would like to acknowledge the incredible support of my wonderful parents. You have loved me so well, cared about my “pie” research and

been amazing role models. Thank you to my sister Sara for sharing life with me and helping me maintain perspective during this process. My grandmother and extended Frank, Herald and Ellenbarger families have truly encouraged me as I have pursued this degree and I greatly appreciate it. Finally, saving the very best for last, I would like to thank my husband, Michael, for loving, serving and leading me so incredibly well. I love you and am really looking forward to the rest of this life-long adventure with you!

NOMENCLATURE

Å	Angstrom
A	Amp
AFM	Atomic force microscopy
Arg	Arginine
Asp	Aspartic acid
a.u.	Atomic unit
Au(111)	Gold on mica
bmtz	3,6-bis(2'-pyrimidyl)-1,2,4,5-tetrazine
bppn	3,6-bis(2'-pyridyl)pyridazine
bptz	3,6-bis(2'-pyridyl)-1,2,4,5-tetrazine
BSSE	Basis set superposition error
[ⁿ Bu ₄ N] ⁺	Tetrabutylammonium
°C	Degrees Celsius
CSD	Cambridge Structural Database
Cys	Cysteine
d _{C-Centroid}	Distance between the carbon atom of the Asp 633 carboxylate group and the centroid of the PDKA aryl moiety
d _{Centroid}	Distance between an anion and the centroid of an aromatic group
°	Degree
Δ	Difference in or change in a specified parameter

d_{M-M}	Distance between two metal centers
d_{X-Y}	Distance between an anion and the closest atom or bond
DMF	Dimethylformamide
DMSO	Dimethyl sulfoxide
DNA	Deoxyribonucleic acid
e^-	Electron
E	Energy
ECP	Effective core potential
ESP	Electrostatic potential
FO	Fully optimized
g	Gram
G	Gibbs free energy
GGA	Generalized Gradient Approximation
Glu	Glutamic acid
H	Enthalpy
\hat{H}	Hamiltonian operator
HF	Hartree-Fock
HOPG	Highly ordered pyrolytic graphite
IC ₅₀	Concentration at which 50% of the enzyme is inhibited
IR	Infrared
ITC	Isothermal titration calorimetry
K	Kelvin

kcal	Kilocalorie
λ	Wavelength
L	Liter
Leu	Leucine
LCAO	Linear combination of atomic orbitals
LDA	Local density approximation
MO	Molecular orbital
MS	Mass spectrometry
MHz	Megahertz
mg	Milligram
mL	Milliliter
MM	Molecular mechanics
mmol	Millimole
mol	Mole
μ M	Micromolar
mM	Millimolar
MP2	Møller-Plesset 2 nd order perturbation theory
<i>Mtb</i>	<i>Mycobacterium tuberculosis</i>
v	Vibrational mode
<i>N</i>	Number of atoms in a system
nm	Nanometer
NDI	Naphthalenediimide

NMR	Nuclear magnetic resonance
PDB	RSCB Protein Data Bank
PDKA	Phenyl-diketo acid
PPN	Bis(triphenylphosphine)iminium
RHF	Restricted Hartree-Fock
Σ	Sum of the specified factor(s)
S	Entropy
SCF	Self-consistent field
STM	Scanning tunneling microscopy
θ	Angle between an anion and the plane of an aromatic group
TCA	Tricarboxylic acid cycle
TEA	Tetraethylammonium
TEM	Transmission electron microscopy
tpa	Terephthalate
tpphz	Tetrapyrido[3,2- <i>a</i> :2',3'- <i>c</i> :3'',2''- <i>h</i> :2''',3'''- <i>j</i>]phenazine
UHF	Unrestricted Hartree-Fock
UV	Ultraviolet
V	Volt
Ψ	Wavefunction
XRD	X-ray diffraction
Z	Atomic number

TABLE OF CONTENTS

	Page
ABSTRACT	II
DEDICATION	IV
ACKNOWLEDGEMENTS	V
NOMENCLATURE	VIII
TABLE OF CONTENTS	XII
LIST OF FIGURES	XV
LIST OF TABLES	XXVI
CHAPTER I INTRODUCTION	1
Supramolecular Chemistry	1
Definition	1
Brief History of the Field	2
Types of Intermolecular Interactions	5
Anion- π Interactions	9
Definition	9
Brief History of the Field	12
Theoretical Models of Chemical Systems	24
Hartree-Fock Methods	26
DFT Methods	29
Molecular Mechanics Methods	31
The Convolution of Theoretical and Experimental Efforts	32
CHAPTER II PREDICTING STABLE SUPRAMOLECULAR ANION- TEMPLATED METALLACYCLES BY COMBINING EMPIRICAL, SEMI- EMPIRICAL AND <i>AB INITIO</i> METHODS	33
Introduction	33
Experimental Methods	46
Materials	46
Characterization Methods	47
Syntheses	47
Computational Methods	48
Results and Discussion	49
Experimental Efforts	49

	Page
Semi-Empirical Modeling of the Fe ^{II} Metallacycles	58
Semi-Empirical Prediction of the Metallacycle Library	63
Predictive Semi-Empirical Method	65
Square Metallacycle Predictions	67
Pentagonal Metallacycle Predictions.....	72
Analysis of the Semi-Empirical Treatment of Transition Metal ions	77
Analysis of the Semi-Empirical Treatment of Polyatomic Anions	82
Identification of the most promising metallacyclic predictions	91
Conclusions and Future Outlook.....	93
CHAPTER III A THEORETICAL EVALUATION OF THE HIERARCHY OF FACTORS DIRECTING AG(I) COORDINATION	96
Introduction	96
Theoretical Methods.....	101
Results and Discussion.....	105
Functional and Basis Set Determination	105
Role of the Coordinating Metal.....	107
Role of the N-Heterocyclic Bridging Ligand	110
Role of the Non-Covalent Interactions.....	117
Role of the Solvent	124
Conclusions and Future Outlook.....	131
CHAPTER IV EXPLORING THE USE OF ANION-TEMPLATED METALLACYCLES AS BUILDING BLOCKS FOR LARGER SUPRAMOLECULAR ARCHITECTURES	134
Introduction	134
Experimental Methods	141
Materials	141
Characterization Methods.....	142
Syntheses	144
Computational Methods	147
Results and Discussion.....	148
Organic bridging ligands	150
Inorganic bridging complexes	170
Conclusions and Future Outlook.....	180
CHAPTER V THE ROLE OF ANION-II INTERACTIONS IN THE INHIBITION OF MALATE SYNTHASE BY PHENYL-DIKETO ACID SUBSTRATES: DEVELOPING PREDICTIVE COMPUTATIONAL METHODS TO ADVANCE DRUG DEVELOPMENT ALGORITHMS	182

	Page
Experimental Methods	192
Computational Methods	195
Results and Discussion.....	195
Influence of Substituent Effects upon PDKA-GlcB Inhibition.....	195
Development of the Model Active Site.....	204
Development of a reference model, the H-optimized model	213
Development of the Descriptive Active Site Model	214
Conceptualization of a Predictive Active Site Model	225
Evaluation of the Predictive Active Site Model	227
Development of a Pre-Screened Predictive Method	234
Conclusions and Future Outlook.....	235
 CHAPTER VI CONCLUSIONS	 240
REFERENCES.....	249

LIST OF FIGURES

	Page
Figure 1. Examples of a crown ether by Pedersen and coworkers, ⁹ a cryptate by Lehn and coworkers, ¹⁰ and a spherand by Cram and coworkers. ¹¹ Molecules visualized as neutral compounds (top) and with an encapsulated cation (bottom). Atom colors correspond to O (red), N (blue), C (grey) and H (white). Graphical display generated by the Materials Studio Visualizer. ¹⁴	4
Figure 2. Interactions involving π -systems. Graphical displays generated by the Materials Studio Visualizer. ¹⁴	8
Figure 3. The orientation of the anion and aromatic system in anion- π interactions is defined by d_{Centroid} (the distance between the anion and the centroid of the aromatic moiety), $d_{\text{X-Y}}$ (the distance between the anion and the closest atom or bond on the aromatic group), and θ (the angle between the anion, centroid and the closest atom to the anion). Graphical display generated by the Materials Studio Visualizer. ¹⁴	10
Figure 4. a) Representation of the charge-dipole method for quantifying anion- π interactions described by Houk and coworkers. ^{24a} Adapted from Houk and coworkers. ^{24a} b) Representation of the impact of the nuclear charge on the anion- π interaction described by Wheeler and coworkers. ^{24b} Adapted with permission from Wheeler and coworkers. ^{24b} Copyright 2014 Royal Society of Chemistry.	12
Figure 5. Discovery and development of the field of anion- π interactions. a) NMR analysis by Schneider and coworkers that demonstrated an attractive interaction for the complex shown. ²⁶ Adapted with permission from Schneider and coworkers. ²⁶ Copyright 1993 WILEY-VCH GmbH & Co. b) Theoretical studies by several groups, including the image above of the study of anions in complex with perfluoro-aromatics by Alkorta and coworkers. ²⁷ Adapted from Alkorta and coworkers. ²⁷ c) Analysis of interactions of halides in close contact with perfluoro-aromatic rings within the CSD by Quiñero and coworkers. ^{25a} Adapted with permission from Quiñero and coworkers. ^{25a} Copyright 2002 Elsevier Science B.V.	14
Figure 6. Additivity of anion- π interactions, as described by Deya and coworkers. ²⁹ Adapted from Deya and coworkers. ²⁹	16
Figure 7. Directionality of the anion- π and π -anion- π interactions between $[\text{BF}_4]^-$ difluorotetrazine and $[\text{PF}_6]^-$ and difluorotetrazine. ³¹ Adapted from the dissertation of Dr. Ian Giles. ³¹	18

- Figure 8. Examples of anion- π interactions with organic molecules. a) Organo-catalysis via NDI complexes by Matile and coworkers.³² Adapted with permission from Matile and coworkers.³² Copyright 2013 WILEY-VCH GmbH & Co. b) H-bonding and Meisenheimer-type sensors by Johnson and coworkers.³³ Adapted with permission from Johnson and coworkers.³³ Copyright 2009 Royal Society of Chemistry. c) The HAT(CN)₆ molecule explored by the Dunbar Group.^{23b} Adapted from Dunbar and coworkers.^{23b}20
- Figure 9. Examples of anion- π interactions in inorganic complexes. a) Cu^{II} carousel complex by Reedjik and coworkers,^{28a} Adapted with permission from Reedjik and coworkers. Copyright 2011 WILEY-VCH GmbH & Co. b) An anion-templated, self-assembled metallacycles by Dunbar and coworkers.^{36c} Adapted from Dunbar and coworkers. c) Examples of Ag^I coordination complexes and polymers.³⁷ Adapted with permission from Reedjik and coworkers. Copyright 2011 WILEY-VCH GmbH & Co.21
- Figure 10. Biological examples of anion- π interactions. a) Oligomeric NDI slides have been shown by Matile and coworkers to function as chloride channels.⁴⁰ Adapted with permission from Matile and coworkers.⁴⁰ Copyright 2008 WILEY-VCH GmbH & Co. b) An anion- π interaction has been identified within the active site of malate synthase, an important drug target of *Mycobacterium tuberculosis*.⁴¹ Crystal structure of GlcB upon inhibition by 2-F-3-Me-6-Cl-PDKA. Structure 3SB0,⁴¹ accessed from RSCB Protein Data Bank.⁴² Graphical display generated by the PyMol visualizer.⁴³23
- Figure 11. a) The first self-assembled metallacyclic framework by Fujita and coworkers.⁶⁰ Adapted from Fujita et al.⁶⁰ b) Metallacyclic frameworks explored by Stang and coworkers.⁶¹ Adapted from Stang et al.⁶¹ c) Two-dimensional “directional bonding approach” employed by Stang and coworkers.^{59a} Adapted from Stang et al.^{59a}35
- Figure 12. Supramolecular anion-templated assembly of a) pentagonal and hexagonal architectures by Lehn and coworkers^{65, 67} (Adapted with permission from Lehn and coworkers.⁶⁷ Copyright 2007 Royal Society of Chemistry.) and b) a library of metallo-cages with varying symmetries by Nitschke and coworkers.⁶⁶ (Adapted from Nitschke and coworkers.⁶⁶).....36
- Figure 13. Templatation and interconversion of Ni^{II} metallacycles by Dunbar and coworkers.^{36c} Adapted from Dunbar and coworkers.^{36c}38
- Figure 14. ¹H NMR evidence of metallacyclic interconversion.^{31b} Adapted from Dunbar et al.^{31b}41

- Figure 15. a) Electrostatic Potential (ESP) Maps of bptz and bmtz.⁶⁹ Adapted from Dunbar et al.^{23b} b) Metallacycle 2, bridged by bptz and templated by two [SbF₆]⁻ anions. c) Metallacycle 3, bridged by bmtz and templated by one [SbF₆]⁻ anion. Graphical display generated by the Materials Studio Visualizer.¹⁴43
- Figure 16. a) Thermal ellipsoid view of the asymmetric unit of 8. Crystal packing (tube view) diagrams of 8 b) along the *a*-axis and c) along the *c*-axis. π - π interactions circled in red, H-bonding interactions circled in grey, and anion- π interactions circled in blue. Select bond distances (Å): Na1-N1 2.532(11), Na1-N3 2.555(11), Na1-F1 2.332(10), C2-N3 1.318(16). Select bond angles (°): N1-Na1-N3 63.6(3), N1-Na1-F1 101.9(3), N3-Na1-F1 181.3(3), Na1-F1-P1 148.2(5). Graphical display generated by the Mercury visualizer.⁹⁰53
- Figure 17. a) Thermal ellipsoid view of the asymmetric unit of 9. Crystal packing (tube view) diagrams of 9 b) along the *b*-axis and c) along the *c*-axis. Select bond distances (Å): C1-N1 1.389(9), C1-N4 1.273(8), C2-N2 1.280(9), C2-N3 1.401(9), N1-N2 1.409(8), N3-N4 1.427(8), C7-N7 1.339(8), C7-N8 1.327(9), C3-N5 1.336(9), C3-N6 1.353(8). Select bond angles (°): C1-N1-N2 114.9(5), C2-N2-N1 112.0(5), C1-N4-N3 112.5(6), C2-N3-N4 113.8(5), C2-C7-N7 117.7(6), C2-C7-N8 119.3(6), C1-C3-N5 117.2(6), C1-C3-N6 117.2(6), N8-C7-N7 123.1(6), N6-C3-N5 125.5(6). Graphical display generated by the Mercury visualizer.⁹⁰55
- Figure 18. a) Ball-and-Stick view of 10·MeCN. Crystal packing diagrams (tube view) of 10·MeCN b) along the *a*-axis and c) along the *c*-axis. Select bond distances (Å): Re1-O1 1.76(5), Re1-N1 2.06(5), Re1-N2 1.97(6), Re1-N3 2.00(4), Re1-N4 2.20(5), Re1-N5 1.98(5), Re2-O2 1.96(5), Re2-N8 1.94(4), Re2-N9 2.18(4), Re2-N10 2.02(4), Re2-N11 2.12(7), Re2-N12 2.03(4), N4-C11 1.41(7), C11-C12 1.46(8), C12-N5 1.47(8), C12-N6 1.34(8), N5-N8 1.30(5), N6-N7 1.41(6), N13-C25 1.26(10), C25-C26 1.34(11). Select bond angles (°): Re-O1-Re2 131(30), O1-Re1-N1 92(2), O1-Re1-N2 100(2), O1-Re1-N4 161(2), O1-Re1-O5 82(2), O1-Re2-N8 83(2), O1-Re2-N9 158.9(19), O1-Re2-N10 88.6(9), O1-Re2-N11 105(2), N4-C11-C12 113(5), C11-C12-N5 115(5), N7-C13-N8 134(5), C13-C14-N9 115(5), N13-C25-C26 169(10). Graphical display generated by the Mercury visualizer.⁹⁰57
- Figure 19. Models N, A and B for 3. Graphical display generated by the Materials Studio Visualizer.¹⁴60

	Page
Figure 20. Overlay of 1 – 3 (ball and stick) with 1A – 3A (green tube) and 1B – 3B (purple tube). Graphical display generated by the Materials Studio Visualizer. ¹⁴	62
Figure 21. [BF ₄] ⁻ with tetrahedron frame outlined between F atoms and designated F-F tetrahedron edge. Graphical display generated by the Materials Studio Visualizer. ¹⁴	68
Figure 22. Evaluation method of the anion-cavity overlap for the predicted square metallacycles. Graphical display generated by the Materials Studio Visualizer. ¹⁴	69
Figure 23. Anion-cavity compatibility determined by the degree of overlap _{Square} . The ideal overlap _{Square} range is identified by the blue box.	71
Figure 24. Evaluation method of the anion-cavity overlap for the predicted pentagonal metallacycles. Graphical display generated by the Materials Studio Visualizer. ¹⁴	74
Figure 25. Anion-cavity compatibility determined by the degree of overlap _{Pentagon} . The ideal overlap _{Pentagon} range is identified by the blue box.	76
Figure 26. Comparison of the empirically derived d _{M-N} for each metal center and the predicted d _{M-N} values for a) the predicted square metallacycles and b) the predicted pentagonal metallacycles.	81
Figure 27. Comparison of the CSD Average bond distances with the semi-empirical and <i>ab initio</i> modeled bond distances for each anion.	83
Figure 28. Representative types of complexes formed between the tetrahedral anions and difluorotetrazine. Graphical display generated by the Materials Studio Visualizer. ¹⁴	86
Figure 29. Representative types of complexes formed between the octahedral anions and difluorotetrazine. Graphical display generated by the Materials Studio Visualizer. ¹⁴	90
Figure 30. Ideal anion-cavity compatibility for tetrahedral anions that participate in anion- π interactions.	92
Figure 31. Ideal anion-cavity compatibility for octahedral anions that participate in anion- π interactions.	93

- Figure 32. Supramolecular architectures reported by Lehn and coworkers. The architectures included a) a [3x3]-Ag^I₉ grid¹⁰¹ and b) a mixture of a [4x5]-Ag^I₂₀ grid and a Ag^I₁₀ quadruple helicate¹⁰² (which preclude the formation of the [5x5]-Ag^I₂₅ grid). Adapted with permission from Lehn and Coworkers.¹⁰² Adapted with permission from Lehn and coworkers.¹⁰² Copyright 2000 WILEY-VCH GmbH & Co. 97
- Figure 33. Structures of the 3,6-bis(2'-pyridyl)pyridazine (bppn), 3,6-bis(2'-pyridyl)-1,2,4,5-tetrazine (bptz) and 3,6-bis(2'-pyrimidyl)-1,2,4,5-tetrazine (bmtz) ligands. Atom colors correspond to N (blue), C (grey) and H (white). Graphical display generated by the Materials Studio Visualizer.¹⁴ 98
- Figure 34. Electrostatic potential maps of single point energy calculations of several Ag^I coordination complexes.^{37b} Each map was generated at a 0.02 a.u. isodensity value and scaled accordingly (kcal/mol): a) 126 to -96, b) 188 to -31, c) 126 to -126, d) 157 to -63. The color scale varies according to each structure label from the blue (positive) to red (negative). Adapted from Dunbar and coworkers.^{37b} 100
- Figure 35. Model anion- π complex of [BF₄]⁻-bmtz. Atomic colors correspond to F (teal), B (pink), N (blue), C (grey) and H (white). Graphical display generated by the Materials Studio Visualizer.¹⁴ 106
- Figure 36. Asymmetric units and packing diagrams of [Ag₄(μ -bmtz)₃][(PF₆)₄] _{∞} (17) and [Na₂(μ -bmtz)][(PF₆)₂] _{∞} (8). Graphical display generated by the Mercury visualizer.⁹⁰ 109
- Figure 37. ESP maps of bridging ligands bppn, bptz, and bmtz. ESP maps generated at isodensity values of 0.02 a.u. from B3LYP/6-31+g(d,p) optimized ligand geometries. Atomic colors correspond to N (blue), C (grey) and H (white). Adapted from the dissertation of Dr. Ian Giles.³¹ 111
- Figure 38. 2x2x2 packing diagrams, along the *b*-axis, for 11, 12 and 13, and the respective model structures, 11_{Model}, 12_{Model} and 13_{Model}. Graphical display generated by the Mercury⁹⁰ and Materials Studio¹⁴ visualizers. 113
- Figure 39. Variety of binding motifs available for bppn, bptz, and bmtz. Graphical display generated by the Materials Studio Visualizer.¹⁴ 116
- Figure 40. Packing diagrams for 12, 14, 15 and 16 and the respective model structures, 12_{Model}, 14_{Model}, 15_{Model} and 16_{Model}. Graphical display generated by the Mercury⁹⁰ and Materials Studio¹⁴ visualizers. 119

- Figure 41. Structural and packing diagrams of the Ag^{I} -bmtz architectures explored by the Dunbar ($13, [\text{BF}_4]^-$), Batten ($[\text{ClO}_4]^-$)^{99b} and Murugesu ($[\text{OTf}]^-$ and $[\text{PF}_6]^-$)¹⁰⁶ research groups. $[\text{ClO}_4]^-$ portion of the figure adapted with permission from Batten and coworkers.^{99b} Copyright 2012 Royal Society of Chemistry. $[\text{OTf}]^-$ and $[\text{PF}_6]^-$ portions of the figure adapted from Murugesu and coworkers.¹⁰⁶ Published by the Royal Society of Chemistry..... 124
- Figure 42. a) Packing diagrams, generated by Toby Woods, b) non-covalent interactions included in the model structure 13_{Model} and c) the model structures 13_{Model} , $13:1_{\text{Model}}$ and $13:0_{\text{Model}}$. Graphical displays in generated by the Materials Studio Visualizer.¹⁴ 127
- Figure 43. a) $2 \times 2 \times 2$ supercell of 13 . b) Overlay of a representative portion of the original $[\text{Ag}_4(\mu\text{-bmtz})_3][(\text{BF}_4)_4]_{\infty} \cdot n\text{C}_6\text{H}_6$ supercell (light grey) with the corresponding portions of the FO $[\text{Ag}_4(\mu\text{-bmtz})_3][(\text{BF}_4)_4]_{\infty}$ frameworks with benzene (dark grey), toluene (green), *ortho*-xylene (red), *meta*-xylene (yellow) and *para*-xylene (blue). Hydrogen atoms omitted for clarity. c) Overlay of one solvent molecule and one anion from the $[\text{Ag}_4(\mu\text{-bmtz})_3][(\text{BF}_4)_4]_{\infty}$ framework pore for benzene (13 light grey, FO dark grey), toluene (green), *ortho*-xylene (red), *meta*-xylene (yellow) and *para*-xylene (blue). Hydrogen atoms omitted for clarity. Graphical display generated by the Materials Studio Visualizer.¹⁴ 130
- Figure 44. The hierarchy of factors that direct supramolecular Ag^{I} coordination. 133
- Figure 45. The first supramolecular coordination-driven polyhedral architecture by Saalfrank and coworkers.¹¹⁸ Adapted and reproduced with permission from Saalfrank et al.¹¹⁸ Copyright WILEY-VCH GmbH & Co..... 135
- Figure 46. Bonding approaches for developing three-dimensional polyhedral architectures, including the a) “Directional Bonding Approach”, b) “Paneling Approach” and c) “Symmetry Interaction Approach”. Adapted from Chakravarty et al.^{59a} 136
- Figure 47. Applications of Polyhedra. a) Large polyhedra by Stang *et al.*;¹²² b) Externally and Internally functionalized bridging ligands by Fujita *et al.*;¹²³ c) Selective gas uptake by Zhou *et al.*;¹²⁴ d) Pollutant encapsulation by Nitschke *et al.*;¹²⁵ e) Protected reactivity within polyhedra by Fujita *et al.*;^{126c} f) Anti-cancer molecular capsule by Therrien *et al.*^{59b} Adapted with permission from each reference. 138
- Figure 48. Lability of acetonitrile ligands in a substitution reaction with bromide.^{36c} Adapted from Dunbar et al.^{36c} 139

Figure 49. Proposed symmetry of polyhedra developed from pentagonal building blocks.....	141
Figure 50. Metallacyclic building blocks: a) 3 with cationic framework shown for $[\text{Fe}_5^{\text{II}}(\text{bmtz})_5(\text{MeCN})_{10}\supset\text{SbF}_6]^{9+36\text{d}}$ and b) 6 with cationic framework shown for $[\text{Ni}_5^{\text{II}}(\text{bptz})_5(\text{MeCN})_{10}\supset\text{SbF}_6]^{9+}$. ^{36b} Non-templating anions removed for the sake of clarity. Graphical display generated by the Materials Studio Visualizer. ¹⁴	149
Figure 51. N-Donor ligands tppz and tpphz. Molecular structures and the optimized (μ -Bridging Ligand)(3) ₂ models for each ligand. Graphical display generated by the Materials Studio Visualizer. ¹⁴	150
Figure 52. a) Thermal ellipsoid view of 18. Crystal packing diagrams of 18 b) along the <i>a</i> -axis and c) along the <i>c</i> -axis. Graphical display generated by the Mercury ⁹⁰ and PovRay ¹³³ visualizers. Select bond distances (Å): Fe1-N1 1.862(14), Fe1-N3 1.968(13), Fe1-N4 1.947(14), N3-C1 1.36(2), N1-C6 1.37(2), Sb1-F1 1.872(14). Select bond angles (°): N1-Fe1-N3 82.0(6), N3-Fe1-N4 165.5(6), N1-Fe1-N7 178.4(6), N1-Fe1-N9 99.0(6), N3-C5-C6 114.2(14), N1-C6-C5 111.0(14), F1-Sb1-F2 90.3(6), F1-Sb1-F6 178.3(6). ...	153
Figure 53. a) Predicted structure of tpphz+3 with a diameter of 5.43 nm. Graphical display generated by the Materials Studio Visualizer. ¹⁴ b) STM image of the 25°C tpphz+3 product and the small structures have an approximate diameter of 1 nm. Image collected under an applied current of 1V and 250 pA. c) STM image of the 45°C tpphz+3 product. Image collected under an applied current of 2V and 20 pA. The circled structures have an average diameter of 4.6 nm.....	155
Figure 54. NMR of tpphz+3 reaction at several stages: a) initial, b) final product, c) decomposition product, d) overheated but residual final product.	157
Figure 55. Qualitative UV-visible spectral analysis during the course of the tpphz+3 reaction at 45°C.	160
Figure 56. O-Donor ligands tpa acid, succinic acid, glutaric acid and adipic acid. Molecular structures and the optimized (μ -Bridging Ligand)(3) ₂ models for each ligand.	161
Figure 57. AFM image of adipic acid+3 product. Image collected in non-contact mode under an applied force load of <1nN.	162

- Figure 58. a) Predicted structure of tpa+3 with a diameter of 5.02 nm. Graphical display generated by the Materials Studio Visualizer.¹⁴ b) AFM image of the tpa acid+3 product drop-cast on the HOPG surface. Image collected in contact mode with <1nN force load. c) Analysis of trace height across the product. d) STM image of the tpa acid+3 product drop-cast on gold surface. Image collected under an applied current of 1 nA at 0.5 V. e) Histogram analysis of the diameter of the identified structures. 164
- Figure 59. NMR spectra of [¹⁰Bu₄N]₂[tpa]₃. a) ¹H NMR and b) ¹H-COSY NMR..... 167
- Figure 60. AFM images of [¹⁰Bu₄N]₂[tpa]₃ product. Image collected in non-contact mode under an applied force load of <1nN. 168
- Figure 61. DFT analysis of the energetic favorability of tpa bridging, binding and bending. tpa modeled as benzoate. 170
- Figure 62. The a) top and b) profile views of the optimized (μ-Os(CN)₆)(6)₂ complex at the NDDO/PM6/UHF^{46-47, 85} level of theory in Materials Studio 7.0¹⁴. Graphical display generated by the Materials Studio Visualizer.¹⁴ 171
- Figure 63. Thermal ellipsoid view of the asymmetric unit of 19. Graphical display generated by the Mercury⁹⁰ visualizer. 174
- Figure 64. a) Thermal ellipsoid view of the profile view of 19. b) Space-filling view of the framework of 19, showing close-assembly around the encapsulated acetonitrile molecule. Crystal packing diagrams of 19 c) along the a-axis and d) along the b-axis. Graphical display generated by the Mercury⁹⁰ visualizer. 175
- Figure 65. a) Thermal ellipsoid view of the asymmetric unit of 20. b) Charge neutral portion of 20. Crystal packing diagrams of 20 c) along the *b*-axis and d) along the *c*-axis. Graphical display generated by the Mercury⁹⁰ and PovRay¹³³ visualizers. Select bond distances (Å): Ni1-C1 1.8717(19), C1-N1 1.150(2), Ni1-C2 1.8725(18), C2-N2 1.154(2), N3-C3 1.515(2), C3-C4 1.513(3). Select bond angles (°): C1-Ni1-C1^{symm. generated} 180.00(4), C1-Ni1-C2 91.16(8), C1-Ni1-C2^{symm. generated} 88.84(8), Ni1-C1-N1 177.78(16), C3-N3-C5 111.88(14), C3-N3-C7 107.34(14), N3-C3-C4 115.62(16)..... 179
- Figure 66. The role of the glyoxylate shunt within the tricarboxylic acid (TCA) cycle of *Mycobacterium tuberculosis*. Adapted and reproduced with permission from Kaufmann, et al.^{145c} 183
- Figure 67. PDKA framework with labeled phenyl positions 2 – 6. 184

- Figure 68. Crystal structure of GlcB upon inhibition by 2-F-3-Me-6-Cl-PDKA. Structure 3SB0,⁴¹ accessed from RSCB Protein Data Bank.⁴² (Inset) GlcB active site and the residues that participate in close-contacts (green framework) with the PDKA (white framework). Non-interacting residues that obstructed the inset visualization were removed for clarity. Supramolecular interactions identified by dashed lines. Graphical display generated by the PyMol visualizer.⁴³ 185
- Figure 69. Schematic representations of the a) fully optimized, model active site for 2-GlcB by Frontera et al.¹⁵⁸ and b) an overlay of this model active site with the analogous groups from the protein crystal structure.¹⁶¹ Graphical display generated by the PyMol⁴³ and PovRay¹³³ visualizers. 190
- Figure 70. Substituted-benzene analogue of 27 in complex with Cl⁻. Model was PO along the Cl⁻-centroid axis, denoted by the dashed line. Graphical display generated by the PyMol⁴³ and PovRay¹³³ visualizers. 197
- Figure 71. Comparison of the IC₅₀ values derived from each PDKA-GlcB complex and the respective interaction energies of chloride with each substituted-benzene analogue for 21 – 33, 35 – 43. IC₅₀ value for 34 not provided. 200
- Figure 72. Comparison of ITC-Derived Entropy and the Solvent-Accessible Surface Area for 21 - 24. 203
- Figure 73. Initial Model Active Sites, including a) AS-A, involving neutral PDKA and an acetate analogue of Asp 633; (b) AS-B, involving neutral PDKA and analogues of Asp 633, Arg 339, Asp 462 and Leu 461; and (c) AS-C, involving the dianionic PDKA, Mg²⁺ ion, and acetate analogue of Asp 633. Graphical displays generated by the Materials Studio Visualizer.¹⁴ 205
- Figure 74. ESP Maps of select neutral PDKAs generated at isodensity values of 0.02 a.u. from the M06-2X/6-31+g(d)^{19b, 56, 108-52} in Gaussian 09.⁸⁶ Graphical display generated by the AMPAC Graphical User Interface Visualizer.¹⁶⁷ ... 207
- Figure 75. PDKA-GlcB model active site, including four simplified residue analogues of Asp 633, Arg 339, Glu 340 and Asp 462; the catalytic Mg²⁺ ion; two water molecules and the mono-anionic PDKA inhibitor. Graphical display generated by the PyMol⁴³ and PovRay¹³³ visualizers. 211

	Page
Figure 76. Structural comparison of PDKA-bound active sites from crystal structures with 21-22, 24-25, 27-43. a) Overlay of the descriptive active site, aligned by the PDKA backbone. b) Overlay of the Asp 633 residue, aligned by the N and O atoms on the residue backbone. Graphical display generated by the Materials Studio Visualizer. ¹⁴	212
Figure 77. H-optimized Model 27 Structure with the optimized hydrogen atoms identified in purple. Graphical display generated by the Materials Studio Visualizer. ¹⁴	214
Figure 78. Descriptive Model 27 Structure with the optimized atoms identified in blue. Graphical display generated by the Materials Studio Visualizer. ¹⁴	215
Figure 79. Comparison of the $d_{C-Centroid}$ for the Descriptive and the H-optimized Models, with an average accuracy of 0.13 Å.....	216
Figure 80. Overlays of the respective H-optimized (blue) and Descriptive (green) Model Active Sites for representative structures 21, 22, 24, 27, 33 and 43. Graphical display generated by the VMD ¹⁶⁹ and PovRay ¹³³ visualizers.....	218
Figure 81. Comparison of the PDKA binding enthalpies of the ITC experiments and the H-optimized (blue) and Descriptive Models (orange) for 21 - 24, shown relative to H-optimized 21.....	219
Figure 82. Comparison of the PDKA binding enthalpies calculated for the Descriptive and H-optimized Model structures, shown relative to H-optimized 21.....	221
Figure 83. Alternative Model Active Sites, Alt A - D. Graphical display generated by the Materials Studio Visualizer. ¹⁴	224
Figure 84. Comparison of the PO Asp 633 residue for each of the Predictive Models A - D with H-Optimized for 27. Graphical display generated by the Materials Studio Visualizer. ¹⁴	227
Figure 85. Predictive Model 27 Structure with the optimized atoms identified in green. Graphical display generated by the Materials Studio Visualizer. ¹⁴	228
Figure 86. Comparison of the a) $d_{C-Centroid}$ values, plotted for the Descriptive and Predictive Models against the H-optimized model, b) groups of PDKA-GlcB structures and the average $d_{C-Centroid}$ accuracy, and the c) PDKA binding enthalpies between both the Descriptive and Predictive Model Active Sites and the H-optimized Model.....	231

	Page
Figure 87. Overlays of the respective H-optimized (blue) and Model Active Sites (green) for the Descriptive and Predictive Models of 21, 22, and 24. Graphical display generated by the VMD ¹⁶⁹ and PovRay ¹³³ visualizers.....	232
Figure 88. Comparison of the PDKA binding enthalpies of the ITC experiments and the Predictive Model, modeled binding enthalpy shown relative to H-optimized 21.	233
Figure 89. Correlation between the Cl ⁻ - π Interaction Model and the Predictive Active Site Model is exemplified by (a) Similar proportional relationships between the respective binding energies and the ITC-derived binding enthalpy, and by a (b) Proportional relationship between the Cl ⁻ - π interaction energies and the Predictive PDKA binding enthalpies (shown relative to H-optimized 21).....	236
Figure 90. Extended bridging ligand that may foster larger metallacyclic architectures.	241
Figure 91. Linear bridging ligands that may impart flexibility and stability to the bridged polygons and polyhedra.....	246

LIST OF TABLES

	Page
Table 1. Table describing the variables of the Hamiltonian operator.	25
Table 2. bptz- and 3,6-bis(2'-pyrimidyl)-1,2,4,5-tetrazine (bmtz)-bridged metallacycles characterized by x-ray diffraction, with molecular formula [M ^{II} (bptz/bmtz) _n (MeCN) _{2n} ⊃Anion _x][Anion] _{2n-x} . Preliminary NMR and MS evidence denoted.	39
Table 3. Comparison of select computational methods for modeling chemical systems based on the applicability, computational cost, scaling factors and accuracy. Adapted with permission from K. H. Houk. ⁴⁵	45
Table 4. Crystallographic refinement parameters for 8, 9 and 10·MeCN.	51
Table 5. d _{M-M} for 1 – 3 crystal structures and the N, A and B optimized models.	60
Table 6. Comparison of the average d _{M-M} for the crystal structures and optimized models A and B for each crystallized metallacycle, 1 – 7. N/A for structures that did not converge to metallacyclic structures.	65
Table 7. The d-block elements, with the specific transition metals and oxidation states explored by semi-empirical methods highlighted in blue and orange. The PM6 parameters of the transition metals highlighted in orange did not allow for appropriate octahedral coordination.	66
Table 8. The square metallacycle d _{M-N} , pentagonal metallacycle d _{M-N} , ionic radius, Σ _{M-N} ⁹³ and the Average and most prevalent d _{M-N} identified from structures in the CSD ⁹¹ for each specified transition metal and oxidation state. NR = Not reported for the specified oxidation state. ⁹⁴	78
Table 9. MP2/def2-TZVP ⁴⁴ calculated BSSE corrected complexation energy, BBSE error, interaction type, sum of the van der Waals radii for d _{X-Y} and the close-contact d _{X-Y} between each anion and difluorotetrazine. NC = No Contact.	85
Table 10. Ag ^I complexes, formulae, types of complexes and approximate models included in this study.	103
Table 11. Comparison of the interaction energy of [BF ₄] ⁻ -bmtz calculated at the MP2/def2-TZVP level of theory and using eight DFT functional/basis set combinations.	106

Table 12. Representative coordination complex ratios, interaction energies with (ΔE_{Ionic}) and without ($\Delta E_{\text{N-C}}$) the strong contributions of the Ag^{I} ion, the approximate energy per anion- π interaction in the model structure ($\Delta E_{\text{N-C/A-}\pi}$) and average anion- π interaction distances ($d_{\text{X-Y}}$) for 11 _{Model} - 13 _{Model} .	114
Table 13. Representative coordination complex ratios, interaction energies with (ΔE_{Ionic}) and without ($\Delta E_{\text{N-C}}$) the electrostatic contributions of the Ag^{I} ion and average anion- π interaction distances ($d_{\text{X-Y}}$) for 12 _{Model} , 14 _{Model} - 16 _{Model} .	120
Table 14. Crystallographic refinement parameters for 18 – 20.	152
Table 15. Assignment of ^1H -COSY Correlations for the $[\text{Bu}_4\text{N}]_2[\text{tpa}]+3$ sample.	168
Table 16. Select Ni-N and N-N bond lengths (\AA) of 19.	176
Table 17. Select N-Ni-N bond angles ($^\circ$) of 19.	177
Table 18. Comparison of the anion- π interaction energies of the partially-optimized, model active sites for the unsubstituted- and 2- <i>ortho</i> -PDKAs at the BSSE-corrected RI-MP2/def2-TZVP level of theory ¹⁵⁸ . Evaluation of the displacement of the PDKA aryl group from each respective crystal structure ⁴¹ .	191
Table 19. PDKA molecules synthesized and characterized in complex with GlcB. Each respective IC_{50} value is included.	193
Table 20. Anion- π interaction energies for each of the complexes of Cl^- and the substituted-benzene analogues of 21 – 43. Comparable calculations performed at the MP2/def2TZVP level of theory are reported in parentheses.	198
Table 21. Thermodynamic components of PDKA-GlcB binding for 21 – 24, evaluated by ITC and the respective Cl^- - π interaction energies of the analogously substituted benzene molecules.	202
Table 22. Comparison of the anion- π interaction energies of the PO model active sites for 21 – 26 previously published by Frontera and coworkers, ¹⁵⁸ as reported at the RI-MP2/def2-TZVP level of theory and upon evaluation at M06-2X/6-31+g(d) level of theory.	209

CHAPTER I

INTRODUCTION

Elegant design of chemical systems can be realized through supramolecular chemistry, and the modification of non-covalent interactions can be tailored to achieve specific physical and chemical properties. Regarding the opportunities afforded within the realm of supramolecular chemistry, Jean Marie Lehn, one of the fathers of the field, commented that “such wide horizons are a challenge and a stimulus to the creative imagination of the chemist.”¹ Inspired by such a perspective, this dissertation provides new insight into one specific non-covalent interaction, namely the anion- π interaction. This dissertation focuses on the impact of the anion- π interaction in the fields of inorganic and biological chemistry through the combined lenses of theory and experiment.

Supramolecular Chemistry

Definition

Supramolecular chemistry has been defined as “chemistry beyond the molecule”,² and this broad definition encompasses the recognition, reactivity, transport and information storage that is available through non-covalent intermolecular interactions.¹ Just as atoms are built up through covalent bonds to form molecules, molecules can be built up through non-covalent interactions to form “supermolecules”. The non-covalent interactions of supramolecular systems can be reversibly controlled with the subtle manipulation of the shape, size and electronic nature of either the “host” or “guest” building blocks.³ The umbrella of supramolecular chemistry spans the disciplines of

chemistry, biology and physics as intermolecular interactions are pervasive within nature and across physical systems of all sizes.

Brief History of the Field

The 1987 Nobel Prize in Chemistry was awarded to Pedersen, Lehn and Cram for their fundamental work in establishing the field of supramolecular chemistry,⁴ but, nearly one hundred years prior, non-covalent interactions were already actively shaping the landscape of chemistry. In 1893, Alfred Werner introduced the concept of coordination chemistry that significantly advanced the development of the field of inorganic chemistry. Coordination chemistry studies the association of metal ions and different types of organic ligands, resulting from non-covalent interactions such as ion-ion, ion-dipole and ion-induced dipole interactions, *vide infra*.^{3,5} During the following year, 1894, Emil Fischer established the biological concept of the “lock and key” with respect to proteins, enzymes and substrates.⁶ Biological host-guest concepts are propagated by many, if not all of the non-covalent interactions that comprise supramolecular chemistry, *vide infra*. These foundational concepts led to substantial growth and understanding in both the inorganic and biological areas of study and were substantiated by the receipt of Nobel Prizes by Werner and Fischer in 1913 and 1902, respectively.

Over the subsequent decades, several classes of non-covalent interactions were identified and explored, in particular the hydrogen-bonding (H-bonding) interaction. In 1931, Linus Pauling described the electrostatic nature of H-bonding that occurs between hydrogen atoms and atoms of high electron affinity.⁷ The understanding of the implications of H-bonding interactions continued to grow, and less than two decades later,

the H-bonding interaction was recognized by Watson and Crick as the major structural motif that enables association of DNA base-pairs.⁸

During the late 1960's and early 1970's, the field of Supramolecular Chemistry was officially established upon the discovery and development of several types of cation-inclusion compounds. Recognized by the 1987 Nobel Prize in Chemistry, the foundational group of supramolecular studies included crown ether compounds by Pedersen and coworkers,⁹ cryptate compounds by Lehn and coworkers,¹⁰ and spherand compounds by Cram and coworkers,¹¹ Figure 1. Several other groups made significant contributions to the establishment of supramolecular chemistry during this time, including the independent work of Vögtle, Atwood and Stoddart.¹² Furthermore, Park and Simmons were the first to employ H-bonding interactions to selectively encapsulate anionic species within the Katapinate compounds.¹³

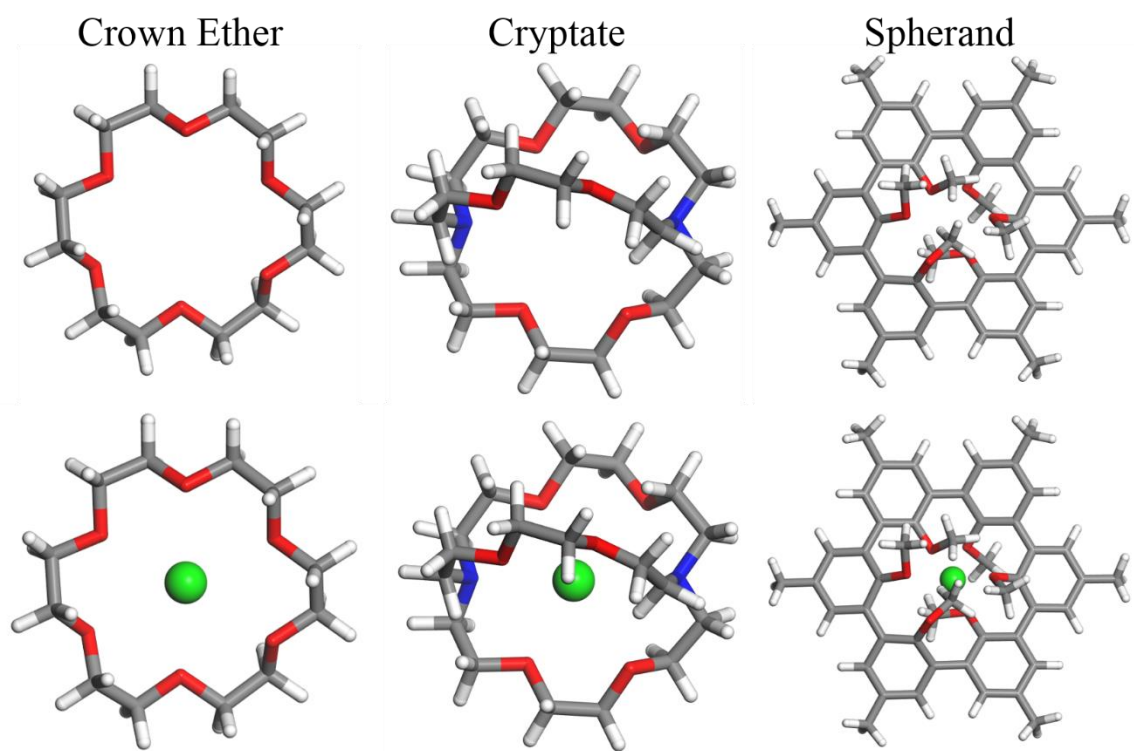


Figure 1. Examples of a crown ether by Pedersen and coworkers,⁹ a cryptate by Lehn and coworkers,¹⁰ and a spherand by Cram and coworkers.¹¹ Molecules visualized as neutral compounds (top) and with an encapsulated cation (bottom). Atom colors correspond to O (red), N (blue), C (grey) and H (white). Graphical display generated by the Materials Studio Visualizer.¹⁴

From these landmark studies, the field of supramolecular chemistry became one of the most vigorously growing areas of chemistry.³ As the understanding of intermolecular interactions continued to grow, the field began to expand to the current interdisciplinary region of study across chemistry, biology and physics. Supramolecular biochemistry was recognized in 2003 by the Nobel Prize in Chemistry for the identification and exploration of water and ion channels in biological systems.¹⁵ Due to the magnitude of the field, it is impossible to provide an exhaustive survey of the major

contributions that have followed; therefore, the next few sections of this chapter describe the major intermolecular interactions that facilitate the entire field of supramolecular science.

Types of Intermolecular Interactions

Ion-Ion Interactions

The strongest non-covalent interaction is the interaction between ionic species. Ionic bonds, such as those present in typical salts like NaCl, have lattice energies that range from several hundred to several thousand kcal/mol.¹⁶ These types of ion-ion interactions are not classified as intermolecular interactions, but supramolecular ion-ion interactions do persist between oppositely charged “host” and “guest” or donor-acceptor type species.³ These supramolecular electrostatic ion-ion interactions are pervasive across the supramolecular systems described in each of the following chapters of this dissertation.

Ion-Dipole and Ion-Induced Dipole Interactions

The electrostatic interaction between a charged ion and the complementary partially charged portion of a dipole is an important supramolecular feature, typically on the order of 10 – 30 kcal/mol.³ Furthermore, the close interaction of an ion with a non-polar molecule can induce an asymmetric orientation of the molecule’s electron density. The resulting induced dipole is therefore able to participate in an attractive electrostatic interaction with the ionic species. The magnitude of the induced dipole depends on the charge of the ion and the polarizability of the electron density of the atoms in the molecule. There are a plethora of examples of these types of interactions, including aqueous

solvation interactions, coordinative bonds and the previously described series of ion-encapsulating macrocycles developed by Pedersen, Lehn and Cram.^{3, 9-11}

Dipole-Dipole, Dipole-Induced Dipole and H-Bonding Interactions

Dipole-dipole interactions are electrostatic interactions that occur between the partially charged portions of molecular dipoles. The close interaction of a polar molecule can induce an asymmetric orientation of electron density around a non-polar molecule, and the induced dipole of the non-polar molecule can interact with the permanent dipole of the polar molecule. Dipole-dipole and dipole-induced dipole interactions typically have interaction strengths of 1 – 15 kcal/mol.³

A special case of the dipole-dipole interaction is the H-bonding interaction. As broadly defined by the International Union of Pure and Applied Chemistry (IUPAC), H-bonding occurs between a covalently bound hydrogen and an electronegative atom, typically O, N, and F,¹⁷ and the resulting intermolecular interactions have binding energies of 3 – 30 kcal/mol.^{3, 7} Dipole-dipole, dipole-induced dipole and H-bonding interactions are critical to many biological systems, as in the aforementioned DNA base-pairing interactions.⁸

van der Waals Interactions

The weakest form of intermolecular interactions, the van der Waals interaction, persists according to the spontaneous (or induced), transient asymmetry of electron density around a molecule. As molecules are brought close together, complementary momentary dipoles participate in attractive dispersion interactions, also known as London dispersion forces or induced dipole-induced dipole interactions. Attractive interaction energies are

approximately 1 – 5 kcal/mol.³ As the distance between molecules, ions or electrons decreases, the electronic exchange-repulsion between molecular orbitals increases to prevent the entities from having overlapping quantum numbers or wave-functions.¹⁸ The overall van der Waals interaction energies result from the balance between dispersion and exchange-repulsion factors.

π - π and XH- π Interactions

Attractive interactions involving aromatic π -systems result as a combination of electrostatic substituent effects that are represented by dipole-dipole, dipole-induced dipole interactions, and van der Waals interactions.¹⁹ The electronic nature of substituents on the aromatic systems have a profound effect on the resulting interactions, and these substituent effects provide a subtle method of modifying the interactions through which the π -system participates. Interactions of π -systems can be typically categorized into two groups: face-to-face and side-to-face interactions, Figure 2. Face-to-face π - π interactions typically include parallel sandwich and parallel displaced types of interactions. The parallel displaced stacked interactions have been shown to be significantly more energetically favorable, and are observed in many experimental systems.²⁰ The interaction energies between aromatic groups typically range from 0.5 – 4 kcal/mol, and primarily result from dispersion interactions and dipole-dipole interactions caused by substituent effects.^{19, 21}

Side-to-face interactions include edge-to-face and T-shaped interactions between aryl groups, Figure 2. The interactions occur between the partially positive end of the C-H dipole and the π -orbitals of the aromatic molecule and demonstrate similar interaction

energies as the face-to-face structures. Similar interactions exist between π -systems and other H-bound entities, typically identified as XH- π interactions where X is an electronegative atom, Figure 2.^{19c} Face-to-face and side-to-face interactions have been identified particularly in biological chemistry as important factors for protein and DNA recognition and stability.²⁰

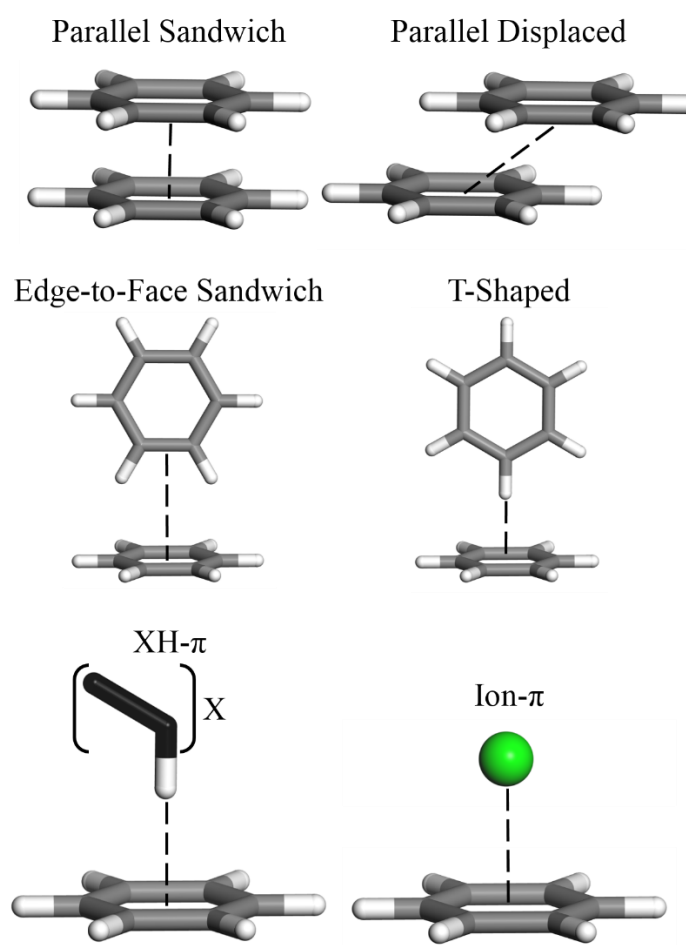


Figure 2. Interactions involving π -systems. Graphical displays generated by the Materials Studio Visualizer.¹⁴

Cation- π Interactions

The interactions of π -systems also include attractive interactions between the face of a π -system and a positively charged cation, namely the cation- π interaction, Figure 2. These attractive interactions occur between the cation and the complementary end of substituent dipoles on the aromatic ring.^{19b} The cation- π interactions typically exhibit binding energies of 10 – 40 kcal/mol. These interactions can be modified by substituent effects and have been identified as factors that facilitate recognition and catalysis in inorganic and biological chemistry.²²

Anion- π Interactions

Definition

The canonical definition of the anion- π interaction is the attractive interaction between an anion and a π -system.²³ The expected repulsion resulting from the close-contact of an anionic species and the π -orbitals of a typical ring, such as perfluorobenzene, is overcome by the combined effects of ion-dipole, van der Waals interactions and additional substituent effects.^{19b-d, 24} Attractive anion- π interactions typically have strengths of 5 – 20 kcal/mol.²³ The ideal anion- π interaction orientation, Figure 3, involves an anion that is directly above the centroid of the aromatic ring, an η^6 -type anion- π interaction where θ is approximately 90° and all values for d_{X-Y} are equal. Substituent effects and other mitigating factors can induce an asymmetry of the anion over the face of the aromatic group, resulting in non-ideal values for θ and d_{X-Y} . The most extreme examples of anion-asymmetry persist for anion-donor/ π -acceptor type complexes, which demonstrate weakly covalent close-contacts of the anion over a bond, and Meisenheimer

σ -donor type complexes that invoke weakly covalent close-contacts of the anion over an atom. Typically, anion- π interactions involve orientations with anions somewhere in between these extreme cases.

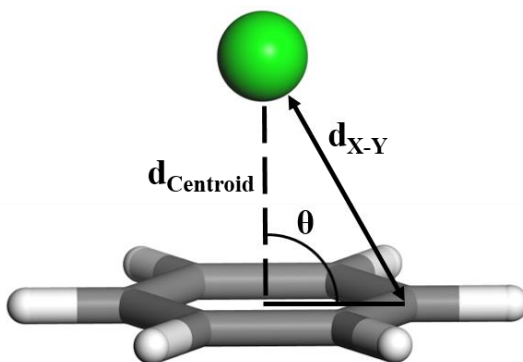


Figure 3. The orientation of the anion and aromatic system in anion- π interactions is defined by d_{Centroid} (the distance between the anion and the centroid of the aromatic moiety), d_{X-Y} (the distance between the anion and the closest atom or bond on the aromatic group), and θ (the angle between the anion, centroid and the closest atom to the anion). Graphical display generated by the Materials Studio Visualizer.¹⁴

Initially, the impetus of the attractive anion- π interaction was attributed to polarization of the aromatic π -orbitals by substituents.²⁵ According to this “ π -polarization” model, electron-withdrawing substituents and electron-donating substituents drain and impart electron density to the π -orbitals, respectively. The quadrupole moment is used as a measure of the π -acidity or π -basicity of a system, and sufficiently π -acidic or “electron-deficient” aromatic groups were expected to participate in energetically favorable anion- π interactions. While the π -polarization model is qualitatively sufficient, a more detailed

theoretical model of the electronic contributions to the anion- π interaction has been developed by Wheeler and Houk.

In this model, repulsion between the anion and π -orbitals is overcome by the ion-dipole interaction between the anion and the partially positive end of the substituent-induced dipoles on the ring. The interaction of Cl^- above the face of several substituted benzene rings was accurately modeled as the simple sum of the energy of Cl^- above a benzene molecule and the energy of the Cl^- and the partially positive end of the C-X substituent dipole, Figure 4a. This “charge-dipole” model has been successfully applied to all of the non-covalent π -system interactions.^{19, 24a} Furthermore, N-heterocyclic systems have been shown to participate in a myriad of anion- π interactions. Wheeler and coworkers have shown that this is due to the increased proximity of the nuclear charge to the center of the ring, and not due to a deficiency in the π -orbital electron density, Figure 4b.^{24b} To further elaborate, consider the iso-electronic C-H group and N atom. “Moving” the nuclear charge of the H to the C causes the nuclear charge on the ring to increase by +1 and “creating” N, but the electron density remains relatively unchanged in the sigma orbital as a lone pair of electrons. Since interaction energies are a balance of the electron-electron repulsion and the electron-nuclear attraction, increasing the nuclear charge on the ring increases the proximity of the nuclear charge to the anion and increases the interaction energy of the anion and the N-heterocyclic aromatic structure.^{24b} In light of the underlying electronic and nuclear contributions to anion- π interactions afforded by these studies, the series of anion- π interactions included in this dissertation were able to be more correctly understood and explored.^{19, 24}

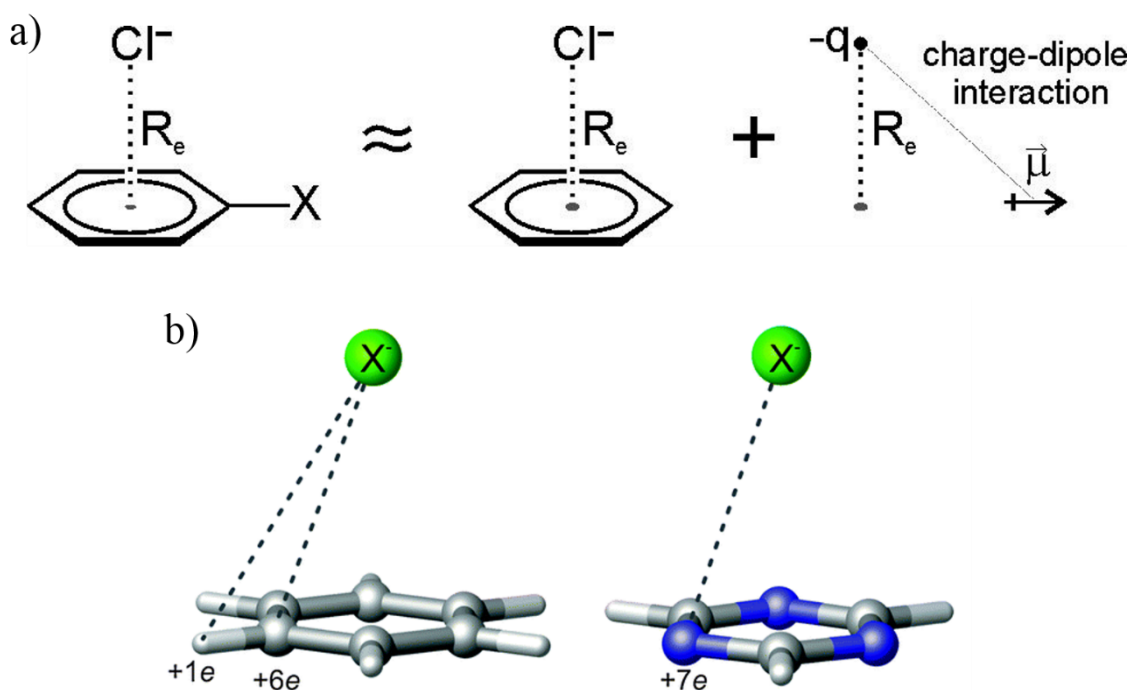


Figure 4. a) Representation of the charge-dipole method for quantifying anion- π interactions described by Houk and coworkers.^{24a} Adapted from Houk and coworkers.^{24a} b) Representation of the impact of the nuclear charge on the anion- π interaction described by Wheeler and coworkers.^{24b} Adapted with permission from Wheeler and coworkers.^{24b} Copyright 2014 Royal Society of Chemistry.

Brief History of the Field

The study of anions in supramolecular systems began during the very nascence of supramolecular chemistry. Park and Simmons developed molecular cages, dubbed “Katapinates”, that selectively bind anions through H-bonding interactions.¹³ However, owing to the higher solvation energies, electronic saturation, pH sensitivity and complex shapes and sizes of anions, as compared to cations, the study of anion presents greater challenges for chemists and progressed more slowly.³

In 1993, Schneider and coworkers identified a weakly attractive interaction of 0.5 kcal/mol between anionic calixarene hosts and neutral aromatic guest molecules using ^1H NMR solution studies, Figure 5a.²⁶ However, it was not until 2002 that three, nearly-simultaneous theoretical studies were published that identified the attractive interaction between anions and aromatic systems and outlined the initial electronic explanations for this “new” non-covalent interaction.^{25b, 25c, 27} Mascial and coworkers identified attractive interactions between 1,3,5-trinitrobenzene and several anions (F^- , Cl^- and azide).^{25c} Alkorta and coworkers evaluated the attractive interaction energies and close-contact distances between a group of anions, including F^- , Cl^- , Br^- , CN^- , etc., and a series of per-fluoro aromatic molecules, Figure 5b.²⁷ Quiñonero and coworkers identified the attractive interactions of several halides with 1,3,5-trinitrobenzene and 1,3,5-trifluorobenzene at varying close-contact distances.^{25b} Later in 2002, Quiñonero and coworkers also published a survey of the interactions of halide anions in close contact with per-fluoro aromatic systems in the Cambridge Structural Database (CSD), Figure 5c.^{25a} The supramolecular anion- π interaction was, therefore, sufficiently established through Schneider and coworker’s experimental efforts,²⁶ the series of theoretical studies of anions and per-fluoro or N-heterocyclic aromatic structures^{25, 27} and the identification of the prevalence of the anion- π interaction within the CSD.^{25a}

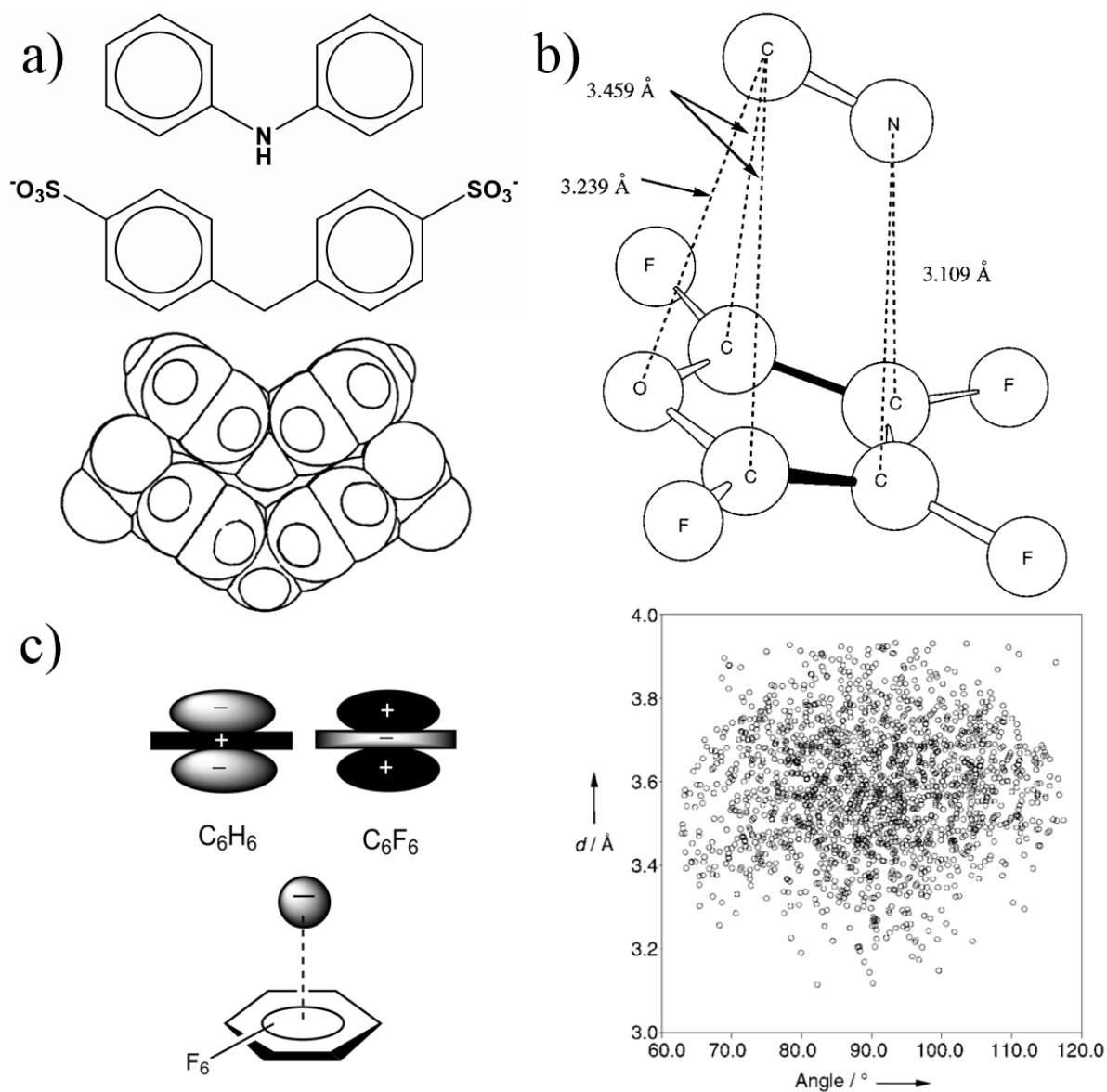


Figure 5. Discovery and development of the field of anion- π interactions. a) NMR analysis by Schneider and coworkers that demonstrated an attractive interaction for the complex shown.²⁶ Adapted with permission from Schneider and coworkers.²⁶ Copyright 1993 WILEY-VCH GmbH & Co. b) Theoretical studies by several groups, including the image above of the study of anions in complex with perfluoro-aromatics by Alkorta and coworkers.²⁷ Adapted from Alkorta and coworkers.²⁷ c) Analysis of interactions of halides in close contact with perfluoro-aromatic rings within the CSD by Quiñonero and coworkers.^{25a} Adapted with permission from Quiñonero and coworkers.^{25a} Copyright 2002 Elsevier Science B.V.

During the years following these seminal discoveries, the field of anion- π interactions has grown expansively, such that the anion- π interaction is now an important and recognized interaction within the frameworks of theoretical, organic, inorganic and biological fields of chemistry.^{23, 28} As previously discussed, the origins of the attraction between anionic and aromatic species have been debated and discussed with regards to the contrasting models involving “ π -polarization” and “charge-dipole interactions”. Amidst these discussions, Deya and coworkers identified that anion- π interactions are additive interactions. The group considered the interaction energy of the complexation of one anion and one π molecule, Figure 6, and sequentially added additional aromatic groups around the anion. The total interaction energy of the anion- π system proportionally increases in response to the added groups.²⁹ Furthermore, the cooperativity of the anion- π interaction with other non-covalent interactions has been explored, particularly in the case of anion- π - π type systems which have even been identified as factors relating to the inhibition of Flavin-dependent enzymatic activity.³⁰

Cl⁻ and trifluorotriazine Br⁻ and trifluorotriazine

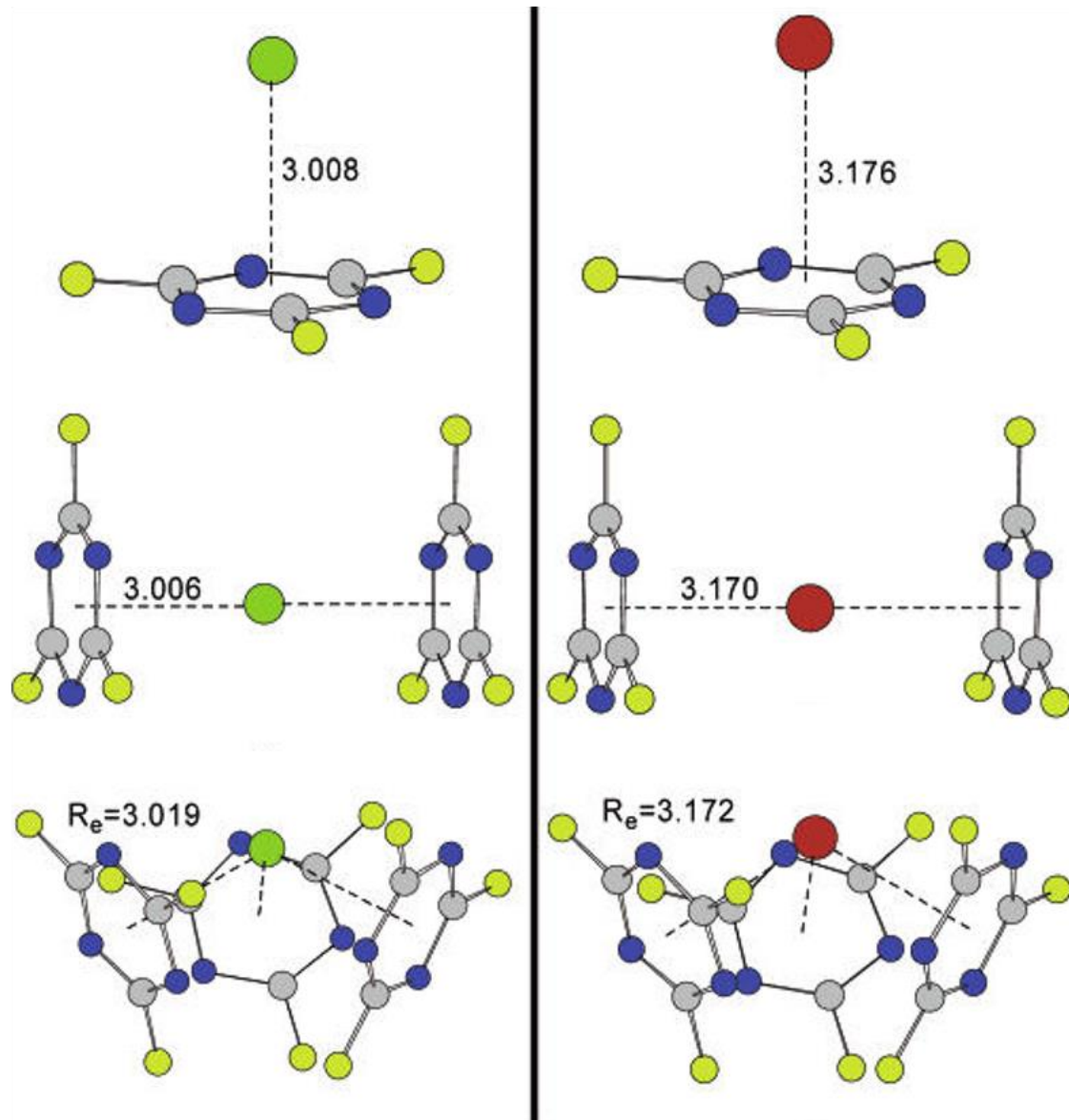


Figure 6. Additivity of anion- π interactions, as described by Deya and coworkers.²⁹ Adapted from Deya and coworkers.²⁹

Dr. Ian Giles, a previous student in the Dunbar group, demonstrated the directionality afforded by complex anions interacting with substituted-tetrazine molecules. Upon optimization of the anion- π and π -anion- π complexes, Figure 7, the pairs of fluorine atoms of the tetrahedral $[\text{BF}_4]^-$ and octahedral $[\text{PF}_6]^-$ polyatomic anions were positioned directly above the partially-positive carbon atoms of the difluorotetrazine ring. The orientation of each fluorine atom demonstrates simultaneous interaction of the fluorine atom with the partially-positive carbon atoms and a pair of nitrogen atoms on the ring. In the π -anion- π complexes, the symmetry of the anion determined the orientation of the tetrazine rings with respect to each other, either staggered or eclipsed as shown in Figure 7, and highlighted the role of anion symmetry upon the templation and interconversion of metallacyclic supramolecular architectures, as further elaborated in Chapter II.³¹

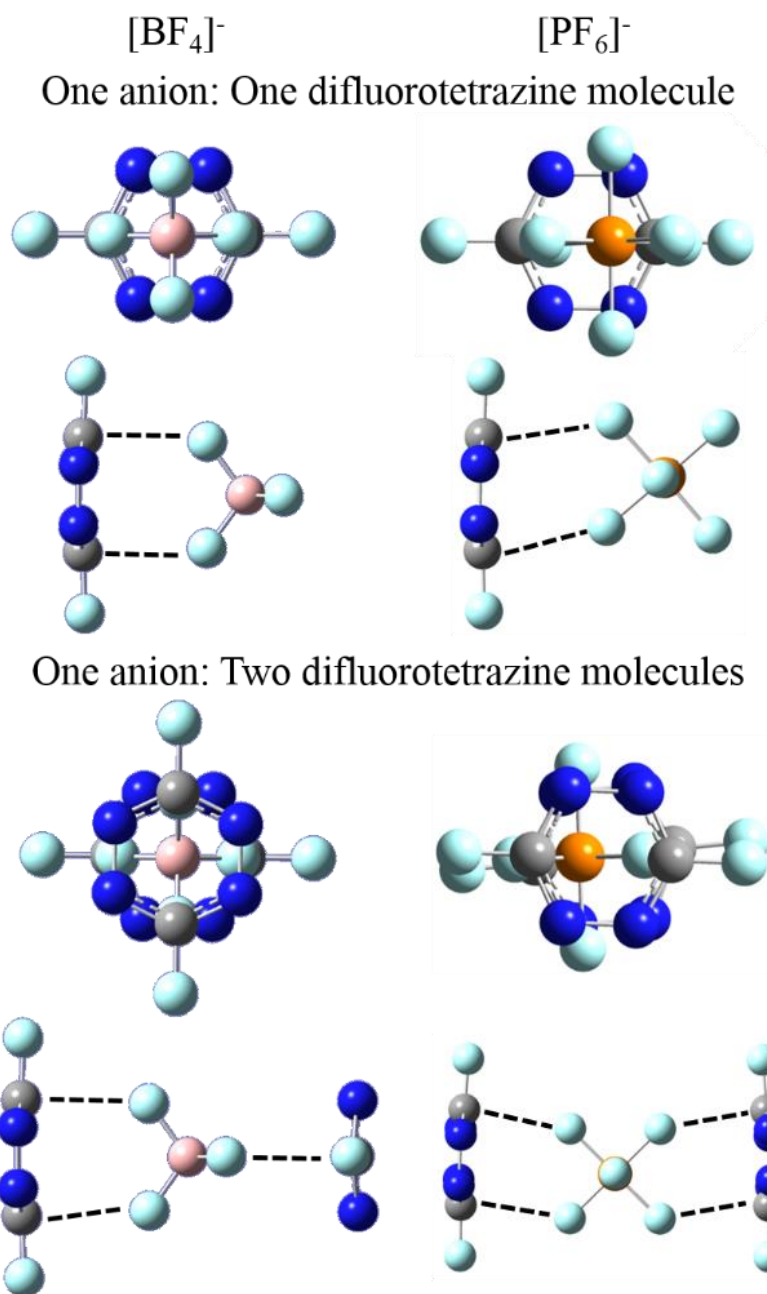


Figure 7. Directionality of the anion- π and π -anion- π interactions between $[\text{BF}_4]^-$ difluorotetrazine and $[\text{PF}_6]^-$ and difluorotetrazine.³¹ Adapted from the dissertation of Dr. Ian Giles.³¹

Experimental evidence for anion- π interactions was particularly elaborated within the area of organic chemistry. Matile and coworkers have developed a series of naphthalenediimide (NDI)-based architectures that facilitate various combinations of anion- π , ion-dipole and H-bonding interactions. One such NDI structure promotes catalysis *via* the Kemp elimination of various substrates by stabilizing the anionic transition state, Figure 8a.³² Johnson and coworkers have developed anion sensors using “ π -acidic” aromatic ligands that enable different types of non-covalent interactions based on the slight modifications to the substituents on the ligand, such as the differences in the H-bonding sensor and the Meseinheimer-type sensor in Figure 8b.³³ Finally, the 1,4,5,8,9,12-hexaazatriphenylene-hexacarbonitrile (HAT(CN)₆) molecule has held significant interest in the field due to the variety of anion- π interactions present in the structure (Figure 8c) and due to the interesting charge-transfer and electron-transfer behavior described by several researchers in both the Dunbar and Ballester groups.^{23b, 34}

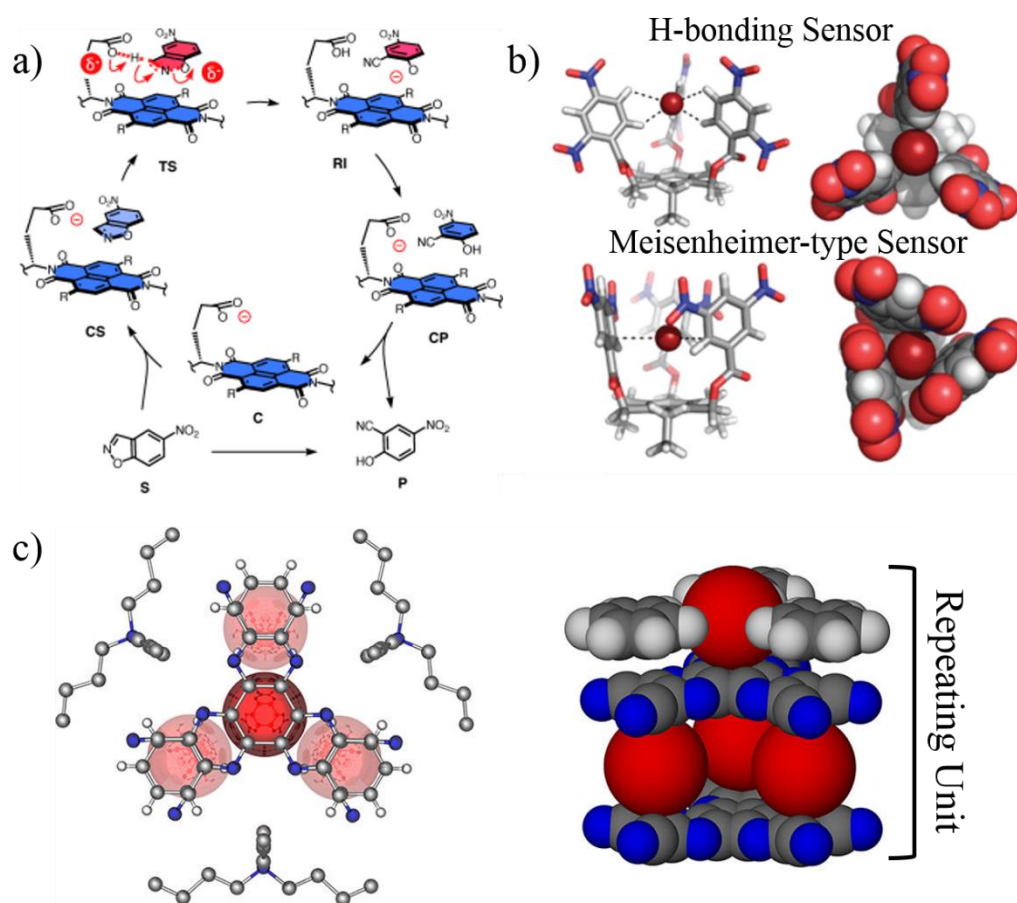


Figure 8. Examples of anion- π interactions with organic molecules. a) Organocatalysis *via* NDI complexes by Matile and coworkers.³² Adapted with permission from Matile and coworkers.³² Copyright 2013 WILEY-VCH GmbH & Co. b) H-bonding and Meisenheimer-type sensors by Johnson and coworkers.³³ Adapted with permission from Johnson and coworkers.³³ Copyright 2009 Royal Society of Chemistry. c) The HAT(CN)₆ molecule explored by the Dunbar Group.^{23b} Adapted from Dunbar and coworkers.^{23b}

Anion- π interactions have also been explored within the scope of inorganic coordination chemistry. Efforts by researchers in the Meyer and Reedjik groups have tailored architecturally beautiful, anion-sensing Cu^{II} structures that involve N-heterocyclic ligands that bind to the Cu^{II} and encapsulate different groups of anions, Figure 9a.³⁵ The

Dunbar group research was highly influential in establishing anion- π interactions within the field of inorganic chemistry, particularly through the development of anion-templated, self-assembled metallacycles (Figure 9b)^{31b, 36} and by advancing the anion-directed complexation of Ag^{I} coordination complexes and polymers (Figure 9c)³⁷. These particular topics will be further elaborated in Chapters II and III respectively.

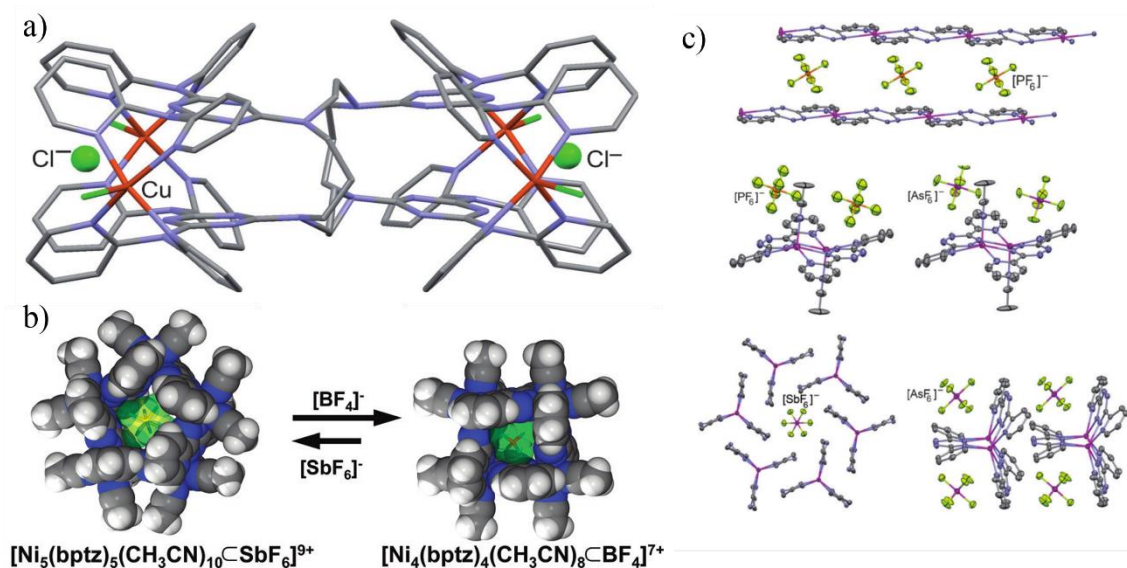


Figure 9. Examples of anion- π interactions in inorganic complexes. a) Cu^{II} carousel complex by Reedjik and coworkers,^{28a} Adapted with permission from Reedjik and coworkers. Copyright 2011 WILEY-VCH GmbH & Co. b) An anion-templated, self-assembled metallacycles by Dunbar and coworkers.^{36c} Adapted from Dunbar and coworkers. c) Examples of Ag^{I} coordination complexes and polymers.³⁷ Adapted with permission from Reedjik and coworkers. Copyright 2011 WILEY-VCH GmbH & Co.

Anion- π interactions are being identified in the field of biological chemistry in increasing numbers, particularly over the course of the last few years. Anion- π interactions

have been shown to contribute to biomolecular recognition,³⁸ protein structural stabilization,³⁹ enzyme inhibition,^{30b} and more. Of particular note is the research of Matile and coworkers who developed oligomeric NDI compounds that function as chloride channels, where the anion descends the “ π -slide” by interacting with the series of NDI groups, Figure 10a.⁴⁰ These channels have been used as anion channels in phosphatidylcholine and are being considered for application in future treatments of channelopathy diseases, such as cystic fibrosis. Sacchetti and coworkers have recently identified an anion- π interaction critical for inhibition of a target protein in *Mycobacterium tuberculosis*.⁴¹ The resulting collaboration with the Dunbar group and elucidation of the interaction is the focus of Chapter V.

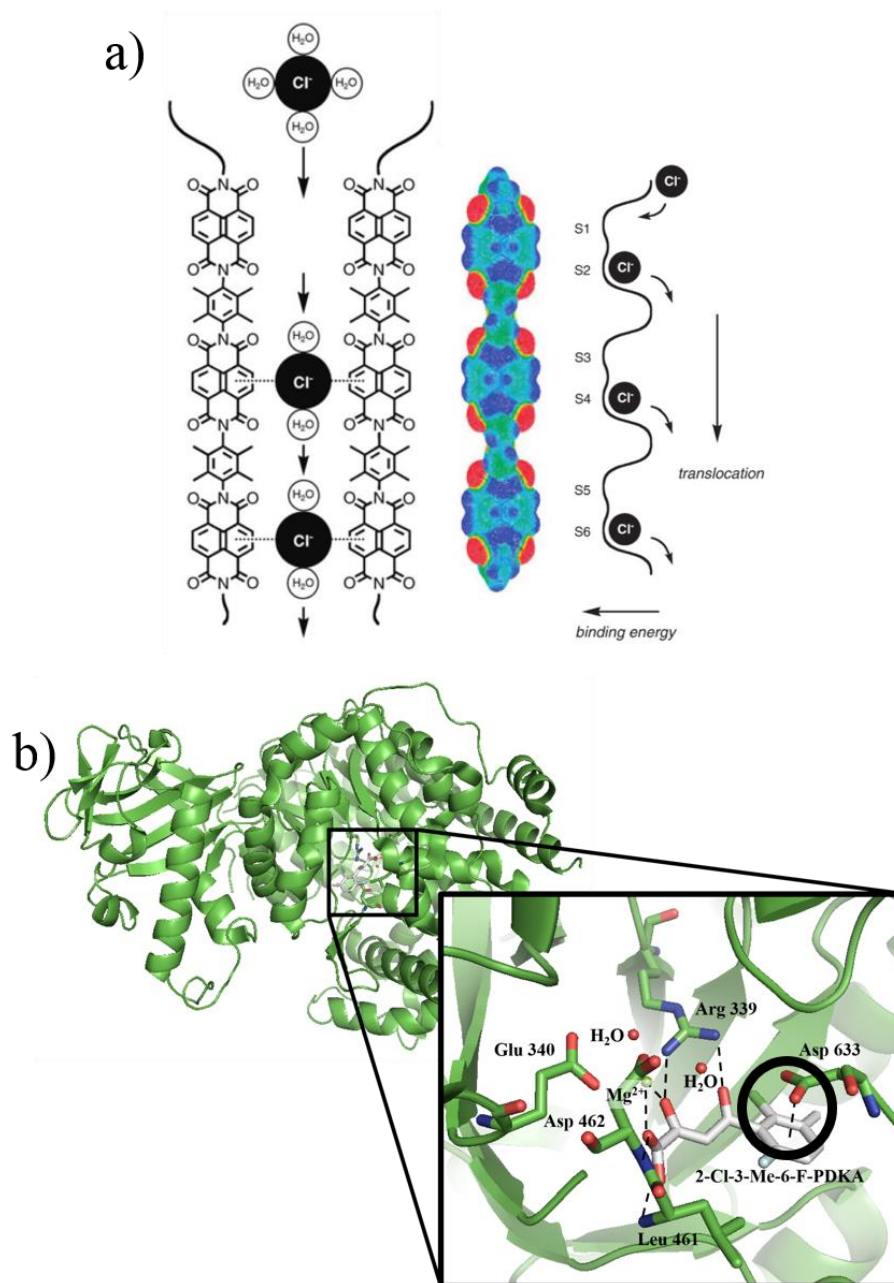


Figure 10. Biological examples of anion- π interactions. a) Oligomeric NDI slides have been shown by Matile and coworkers to function as chloride channels.⁴⁰ Adapted with permission from Matile and coworkers.⁴⁰ Copyright 2008 WILEY-VCH GmbH & Co. b) An anion- π interaction has been identified within the active site of malate synthase, an important drug target of *Mycobacterium tuberculosis*.⁴¹ Crystal structure of GlcB upon inhibition by 2-F-3-Me-6-Cl-PDKA. Structure 3SB0,⁴¹ accessed from RSCB Protein Data Bank.⁴² Graphical display generated by the PyMol visualizer.⁴³

The studies in this dissertation are aimed at further expanding the understanding of the anion- π interaction through a combination of experimental and theoretical efforts. The following section provides a brief tutorial on the various types of theoretical methods employed throughout the remainder of this dissertation.

Theoretical Models of Chemical Systems

To exactly calculate the energy of a system, the Schrödinger equation, Equation 1, must be solved such that the Hamiltonian (\hat{H}) operates on the wavefunctions of the system (Ψ), resulting in the total energy of the system (E).

$$\hat{H}\Psi = E\Psi \quad \text{Equation 1}$$

The Hamiltonian operator can be fragmented into the five major components (Equation 2 and Table 1) that consider the kinetic energy of the electrons ($-\sum_i \frac{\hbar^2}{2m_e} \nabla_i^2$) and nuclei ($-\sum_k \frac{\hbar^2}{2m_k} \nabla_k^2$), the attraction between the electrons and the nuclei ($-\sum_i \sum_k \frac{e^2 Z_k}{r_{ik}}$), the electron-electron repulsion ($\sum_{i<j} \frac{e^2}{r_{ij}}$), and the nuclear-nuclear repulsion ($\sum_{k<l} \frac{e^2 Z_k Z_l}{r_{kl}}$).¹⁸

$$\hat{H} = -\sum_i \frac{\hbar^2}{2m_e} \nabla_i^2 - \sum_k \frac{\hbar^2}{2m_k} \nabla_k^2 - \sum_i \sum_k \frac{e^2 Z_k}{r_{ik}} + \sum_{i<j} \frac{e^2}{r_{ij}} + \sum_{k<l} \frac{e^2 Z_k Z_l}{r_{kl}} \quad \text{Equation 2}$$

Table 1. Table describing the variables of the Hamiltonian operator.

Variable	Definition
i and j	Series of electrons
k and l	Series of nuclei
\hbar	Plank's constant divided by 2π
m_e	Mass of electron
m_k	Mass of nucleus k
∇^2	Laplacian operator
e	Charge on electron
Z	Atomic number
r_{ab}	Distance between particles a and b

Furthermore, upon the application of an electric or magnetic field, the presence of heavy atoms with spin-orbit coupling, or relativistic effects, the complexity of the Hamiltonian grows.¹⁸ The complete and accurate evaluation of one molecule of hydrogen is complex and only grows in complexity as more atoms are included such that accurately evaluating supramolecular systems, such as the ones in this dissertation. In order to theoretically study molecular systems, different levels of theory have been employed, which apply various approximations to solve the Schrödinger equation. The election of one level of theory over another depends on the size of each system, expected accuracy and desired types of results.

Hartree-Fock Methods

One of the major *ab initio* methods that has emerged for treating chemical systems is Hartree-Fock (HF) theory. HF theory describes the electrons of a chemical system by a series of Fock operators that is combined into and evaluated as a single Slater determinant. This level of theory applies three major approximations in order to simplify this treatment. First, HF theory uses the Born-Oppenheimer approximation to assume that the electrons of a system can be considered independently of the nuclei of that system. Molecular orbitals are also assumed to consist of linear combinations of atomic orbitals (LCAO). Furthermore, the hallmark of the HF formalism is the mean-field approximation, or Self-Consistent Field (SCF) theory, that assumes that each electron experiences the surrounding electrons as a field instead of as individual entities. Typical (restricted) HF theory automatically assumes that all electrons are spin-paired and fill each core orbital, but unpaired electrons can be accounted for with unrestricted HF methods by calculating separate energies for all of the spin up and all of the spin down electrons, allowing for a small amount of perturbation of the orbital energies. HF calculations employ a broad range of basis sets and the convergence timeframe scales according to N^{3-4} , where N is the number of atoms in the system.

There are significant limitations of the HF method however. The mathematical treatment of the electrons and the mean-field approximation exclude the possibility of evaluating electron correlation. Also, the choice of basis set is important for appropriately modeling the orbitals, but applying a larger basis set to improve accuracy magnifies the problem of a computational calculation bottleneck. The two main approaches to mitigating

the limitations of HF theory include, first, improving the theory by treating the correlation and configuration of the electrons more accurately or, second, simplifying the HF theory further by applying empirical parameters to decrease the computational cost.

Møller-Plesset Perturbation Theory

Møller-Plesset perturbation theory (MP n) attempts to incorporate dynamic electron correlation interactions to the HF formalism by calculating the correlation energy associated with exciting n electrons into higher energy molecular orbitals (MOs).¹⁸ MP2 calculations account for all single and double electron excitations, but tend to overcorrect for the correlation energy. MP3 and MP4 calculations consider more elaborate excitations but the computational cost typically exceeds the improvement of the energy approximation.¹⁸ In Chapters II, III and V, MP2 calculations are performed in combination with the def2-TZVP basis set for medium to smaller sized systems.⁴⁴ The updated (def2) triple zeta valence (TZV) basis set with polarization (P) was used in order to accurately account for the spatial orientation and polarization of the atoms being studied.^{44d, 44e} The MP2/def2-TZVP⁴⁴ level calculations included in this dissertation were performed as energetic standards with which other calculations were compared to evaluate the accuracy of the alternative methods.

MP n calculations improve on the HF formalism by incorporating electron correlation energy to the n^{th} order, however, the computational cost scales by N^{3+n} or greater. Further improvements to the HF formalism can be achieved through including full configuration interactions, but these methods were considered to be too time intensive with respect to the size of molecular systems in the studies within this dissertation.

Semi-empirical Methods

Semi-empirical methods simplify the HF formalism and incorporate empirically-derived atomic parameters to calculate the molecular system. The HF framework is simplified by neglecting the core 1s electrons and replacing the core electron integrals with an empirical or calculated parameter. Further simplifications are applied depending on the type of semi-empirical method chosen.^{18,45} The theoretical methods in Chapters II, III and IV use the semi-empirical Neglect of Diatomic Differential Overlap (NDDO) method.⁴⁶ According to the NDDO approach, all of the integrals that are centered on different atoms but which depend on the same electron(s) are set to zero. The remaining integrals are neglected as a result of the mathematical assessment of the integrals or are parameterized by empirical data.^{18, 45-46}

Furthermore, parameterization methods are used to provide additional empirical parameters for improved accuracy. The parameterization method VI (PM6)⁴⁷ includes suitable parameters for the majority of the periodic table, including all of the transition metals studied in this dissertation, so the NDDO/PM6 semi-empirical level of theory⁴⁶⁻⁴⁷ was employed within this dissertation. In general, semi-empirical methods improve upon the HF formalism by decreasing computational time and moderately improving the physical relevance of the calculations, but, semi-empirical methods are limited by the scope of the parameters included (and the experimental data used to obtain the parameters).

DFT Methods

The second major theoretical methodology used in this dissertation research is Density Functional Theory (DFT) which is founded on the Hohenberg-Kohn theorem that states that a functional exists that can determine the energy of the ground state of a molecular system from its electron density.⁴⁸ In this way, the many body problem is simplified from N electrons with $3N$ corresponding spatial coordinates to the 3 spatial coordinates that describe the electron density. However, the exact expression of that functional is unknown. Kohn and Sham were able to derive the major contributions to the theoretical functional by first assuming that the system included non-interacting electrons (which includes the kinetic energy of the system and the classically computed electrostatic potential but not include the electron-electron repulsion term) and then adding in the exchange and correlation of the electrons in the system.^{18,49} In general, DFT methods are more efficient than *ab initio* calculations, but the inability to solve for the exact functional results in many different functionals that must be tailored for the treatment of each chemical system. The tailoring of functionals to a specific system of study can occur through additional approximations, such as the local (spin) density approximation (LDA or LSDA), the generalized gradient approximation (GGA) and hybrid functionals. The GGA approximation is used in of the functionals used in this dissertation to account for the exchange and correlation energies of the electrons as a function of both the local electron density (LDA) and the change (or gradient) in the electron density.¹⁸ Hybrid functionals incorporate a mixture of HF exchange and DFT electron-correlation contributions.⁵⁰

In this dissertation, several functional and basis set combinations were explored. In Chapter III, the hybrid GGA functional ω B97X-D was used to evaluate isolated portions of Ag^I coordination polymers because it incorporates empirical dispersion and corrections for long-range exchange interactions.⁵⁰ The non-relativistic, multi-electron fit Stuttgart/Dresden effective core potentials (ECPs) were used for the heavy Ag and Sb atoms (with the DKH keyword to incorporate scalar relativistic effects),⁵¹ and the remaining atoms were described by the 6-31+g(d,p) Pople basis set⁵² and the def2-TZVP triple zeta valence basis set with polarization⁴⁴ were used for the remaining atoms to evaluate the impact of the basis set. This level of theory was able to calculate highly accurate interaction energies for components of isolated portions of the Ag^I coordination polymers upon comparison to the MP2/def2-TZVP derived interaction energies. The functional used in Chapter IV, BP86, is a combination of the Becke GGA exchange functional⁵³ (B) and the Perdew GGA correlation functional⁵⁴ (P86). In combination with the multi-electron, fully-relativistic Stuttgart/Dresden Fe ECP⁵⁵ and the 6-31+g(d)⁵² basis set, this level of theory was used to efficiently evaluate the binding energy of the transition metal complex. The biological chemistry studies in Chapter V used the meta-GGA hybrid Truhlar and Zhao M06-2X functional with the 6-31+g(d) basis set in to accurately evaluate the non-covalent interactions of the system.⁵⁶ The meta feature of the meta-GGA hybrid functional builds upon the GGA and hybrid approximations by also incorporating the second derivative of the electron density gradient.

Molecular Mechanics Methods

Molecular Mechanics (MM) is one of the most simplistic methods of evaluating chemical systems, and is particularly suited for systems with many atoms, such as proteins.¹⁸ MM theory evaluates chemical systems by simplifying the expression of the vibrational potential energy for the bonds within a system to Hooke's law for a spring, where the "force constant", k , can be quantified with various spectroscopic measurements.¹⁸ The approximate ability to transfer the "force constants", bond lengths and strain between atoms enables MM theory to predict the likely atomic and molecular orientations within a chemical system. MM methods approximate the energy of a chemical system as the sum of the bond energies involved, but is unable to account for other interaction energies involved in molecular bonding. Therefore, several potential energy functional forms are added through the use of force fields to account for bond stretching, torsion, bending, van der Waals interactions, electrostatic interactions, parameterization from empirical data, etc.¹⁸

The Universal Force Field (UFF) is used in Chapter III to evaluate the supercells of Ag^I-based coordination polymers. The supercells contain approximately 20,000 atoms and the full optimization would be nearly, if not entirely, impossible to perform at a higher level of theory within a remotely plausible timeframe. Therefore, MM methods provide an opportunity to evaluate very large and extended structures, but this is at the expense of the accuracy of the calculations.¹⁸

The Convolution of Theoretical and Experimental Efforts

The studies elaborated in this dissertation explore four supramolecular anion- π systems using a combination of experimental and theoretical approaches. In the first study, the anion-templation of metallacyclic architectures was evaluated and a predictive model was developed to identify suitable anion templates for many transition-metal based metallacycles. In the second study, the factors contributing to the formation of Ag^{I} coordination complexes and polymers have been evaluated, elucidating the subtle interplay between metal size, bridging ligand, anion and solvent choice. The third study describes the experimental and theoretical efforts that were employed to build the metallacyclic complexes into larger supramolecular complexes, and the interesting architectures that resulted. The final study used theoretical methods to determine the non-covalent contributions to protein inhibition within the malate synthase active site of *Mycobacterium tuberculosis* (*Mtb*). A predictive screening method has been developed for identifying potential targets for future *Mtb* drug development. The experimental and theoretical results described by these studies have been pursued in the spirit of promoting a greater understanding of the role of anion- π interactions in supramolecular inorganic and biological chemistry.

CHAPTER II
PREDICTING STABLE SUPRAMOLECULAR ANION-TEMPLATED
METALLACYCLES BY COMBINING EMPIRICAL, SEMI-EMPIRICAL AND *AB*
INITIO METHODS

Introduction

Supramolecular chemistry has been defined as “chemistry beyond the molecule,” involving chemical recognition, organization and self-assembly motivated by intermolecular interactions.² The design of molecular systems controlled by intermolecular interactions can be achieved by manipulating the shape, size, and electronic nature of the constituents, as observed across the fields of chemistry, biology and physics.¹
⁵⁷ Within the interdisciplinary area of supramolecular chemistry, this chapter focuses on predicting the supramolecular design⁵⁸ of metallacyclic, anion-templated architectures.⁵⁹

Fujita and coworkers were the first to explore the area of supramolecular coordination-driven self-assembly of metallacycles⁶⁰ by reacting $[\text{Pd}^{\text{II}}(\text{ethylenediamine})][\text{NO}_3]_2$ with 4,4'-bipyrimidine to form the original self-assembled square metallacycle. The quantitative reaction produced the supramolecular product under thermodynamic control⁶⁰, Figure 11a. This novel concept of supramolecular coordination-driven, self-assembly was also explored extensively by Stang and workers who probed the assembly of square metallacycles consisting of $[\text{M}^{\text{II}}(1.3\text{-bis}(\text{diphenylphosphino})\text{propane})]^{2+}$ vertices and 4,4'-bipyridine bridging ligands, for Pd^{II} and Pt^{II} as shown in Figure 11b.⁶¹ The square supramolecular metallacycles, initially

explored by Fujita and Stang, are the most amenable to templation due to the 90° angles afforded by the linear organic linkers and the square planar metal vertices. Stang and coworkers developed the “directional bonding approach” in order to identify and design suitable building blocks for the successful self-assembly of metallacycles with varied sizes and geometries,^{59a, 62} Figure 11c. Similar building block methodologies have been employed by several groups as the field has grown in recent years, resulting in high selectivity and quantitative yields of many two-dimensional^{59a, 59e, 63} and three-dimensional (See Chapter III) supramolecular structures.

External factors, such as solvent choice, reagent concentration, counter ion identity, additional templating agents, *etc.*, can be modified to promote the spontaneous self-assembly of supramolecular complexes.^{31b, 64} Templating agents have been used to promote thermodynamically stable supramolecular complexes that are unable to be synthesized as the stable or single product by the native building blocks alone.^{64a} Upon complexation, templating agents may be released or retained depending on the stability and steric restrictions of the final supramolecular complex.^{64b} The role of anions in supramolecular coordination-driven self-assembly and templation was highlighted by Lehn and coworkers in the formation of large Fe^{II} metallacycles bridged by tris-bipyridine.⁶⁵ A pentagonal structure was templated by a chloride counter ion which remained encapsulated for pentagonal stabilization. A hexagonal structure was templated by a sulfate counter ion which was not retained after assembly, Figure 12a. Nitschke and coworkers explored the role of an anion template in dictating the nuclearity of a series of

supramolecular 3d transition metal complexes,⁶⁶ Figure 12b. The shape and nuclearity of the resulting metallacyclic structures resulted from the very subtle interplay between the anion template, transition metal ionic size and the coordinative flexibility around the metal nodes to access a library of supramolecular, templated metallacyclic architectures.⁶⁶

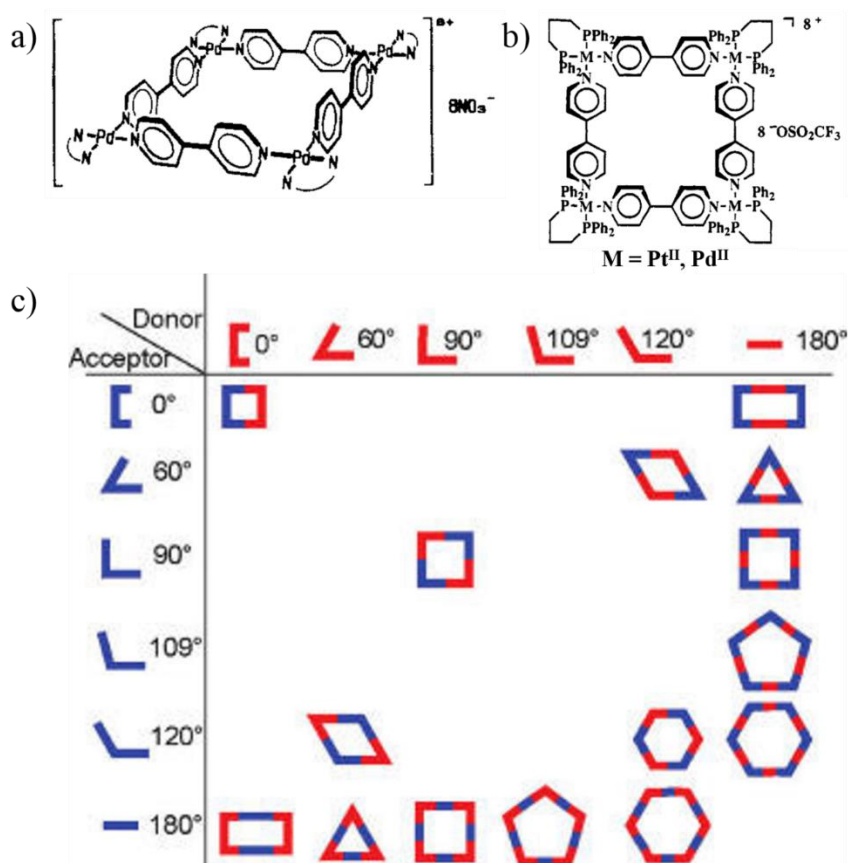


Figure 11. a) The first self-assembled metallacyclic framework by Fujita and coworkers.⁶⁰ Adapted from Fujita et al.⁶⁰ b) Metallacyclic frameworks explored by Stang and coworkers.⁶¹ Adapted from Stang et al.⁶¹ c) Two-dimensional “directional bonding approach” employed by Stang and coworkers.^{59a} Adapted from Stang et al.^{59a}

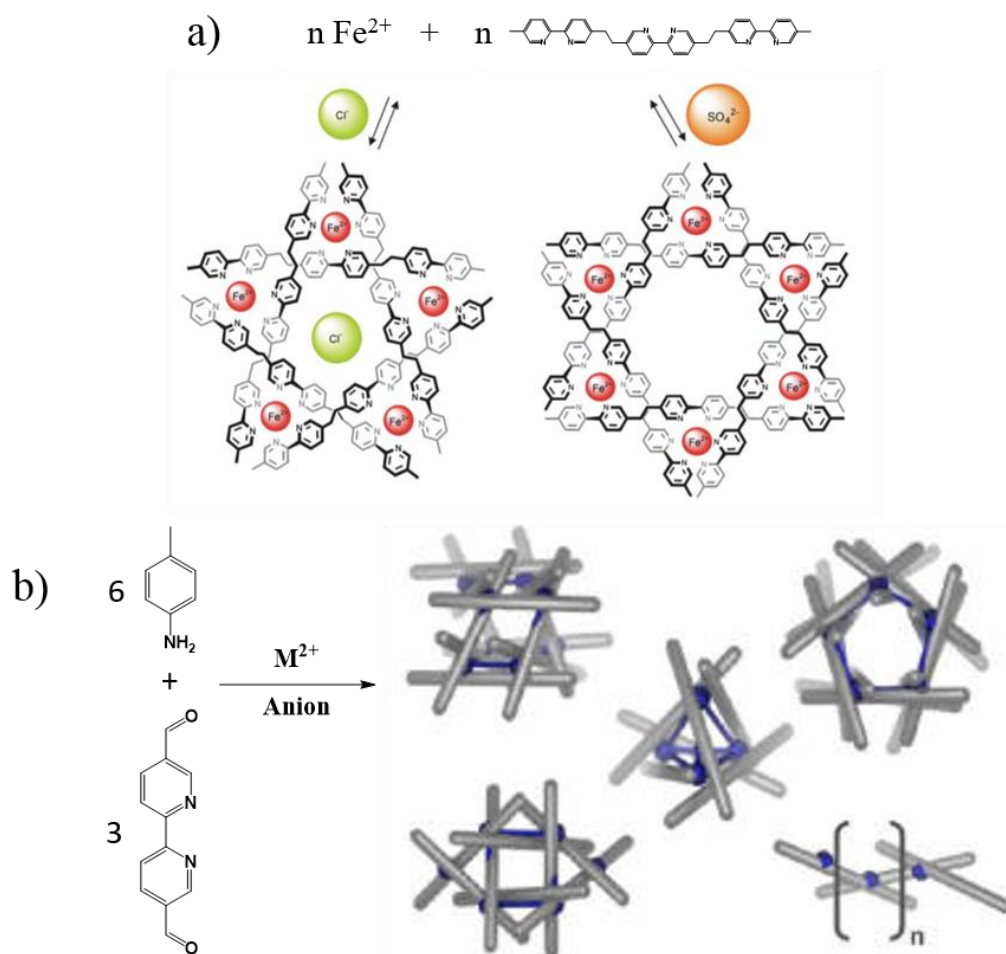


Figure 12. Supramolecular anion-templated assembly of a) pentagonal and hexagonal architectures by Lehn and coworkers^{65, 67} (Adapted with permission from Lehn and coworkers.⁶⁷ Copyright 2007 Royal Society of Chemistry.) and b) a library of metallogages with varying symmetries by Nitschke and coworkers.⁶⁶ (Adapted from Nitschke and coworkers.⁶⁶)

Initial efforts in the Dunbar group to promote complexation between $[\text{Ni}(\text{MeCN})_6][\text{BF}_4]_2$ and 3,6-bis(2'-pyridyl)-1,2,4,5-tetrazine (bptz) led to an anion-templated square metallacycle that is stabilized by anion- π interactions (See Chapter I) between an anion located in the center of the metallacyclic cavity and the organic bridging

ligands,^{36a} Figure 13. Upon reaction of $[\text{Ni}(\text{MeCN})_6][\text{SbF}_6]_2$ and bptz, a pentagonal metallacyclic product was exclusively formed around one encapsulated octahedral anion. The anion interacts closely with the tetrazine rings of the bptz ligand through anion- π interactions and is retained in the cavity for metallacyclic stability,^{36b} Figure 13. The square and pentagonal metallacycles were exclusively templated through the close anion- π interactions afforded by the symmetries of the tetrahedral and octahedral anions, respectively.

The structural dependence on anion symmetry was verified by mass spectrometry measured on solutions after interconversion between the square and pentagonal frameworks was achieved by addition of an excess of a specific templating anion as outlined in Figure 13.^{31b, 36c} Demonstrating fine supramolecular control, this early work from the Dunbar group established a new research arena at the interface of supramolecular coordination-driven self-assembly and anion- π interactions.

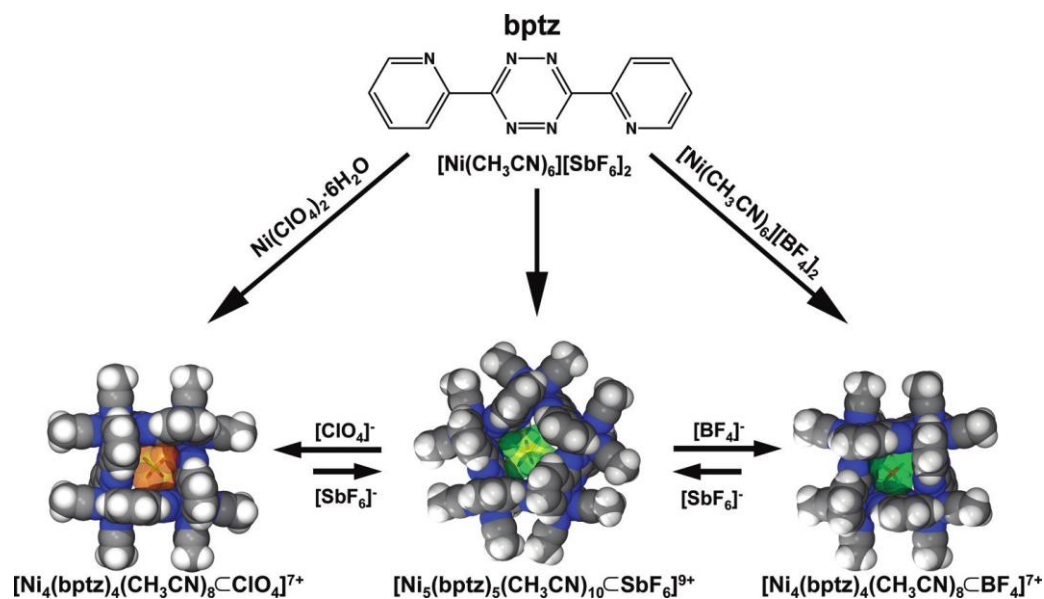


Figure 13. Templation and interconversion of Ni^{II} metallacycles by Dunbar and coworkers.^{36c} Adapted from Dunbar and coworkers.^{36c}

The Dunbar group developed a library of anion-templated metallacycles by modifying the transition metal capped vertices, templating anions and bridging ligands,^{31, 36} Table 2. The compounds span many of the first row transition metals, with crystal structures of the metallacycles having been determined with divalent Fe ,^{31b, 36d} Co ,^{31a} Ni ,^{36a, 36b} and Zn ^{36c} metal ions. The Mn^{II} and Cu^{II} structures templated by $[\text{ClO}_4]^-$ are less stable and have only been characterized by mass spectrometry.^{36c} After the initial studies from this group were published, Shionoya and coworkers reported the stability of the Zn^{II} square metallacycle by synthesizing a Zn^{II} square metallacycle, $[\text{Zn}_4^{\text{II}}(\text{bptz})_4(\text{MeCN})_3(\text{H}_2\text{O})_3][\text{ClO}_4]_8$, which is partially solvated by water and acetonitrile molecules and does not contain an encapsulated anion.⁶⁸

Table 2. bptz- and 3,6-bis(2'-pyrimidyl)-1,2,4,5-tetrazine (bmtz)-bridged metallaacycles characterized by x-ray diffraction, with molecular formula $[M^{II}(\text{bptz}/\text{bmtz})_n(\text{MeCN})_{2n} \supset \text{Anion}_x][\text{Anion}_x]_{2n-x}$. Preliminary NMR and MS evidence denoted.

	[I] ⁻	[Br ₃] ⁻	[NO ₃] ⁻	[BF ₄] ⁻	[ClO ₄] ⁻	[PF ₆] ⁻	[AsF ₆] ⁻	[SbF ₆] ⁻
Mn^{II}					MS ^{36c}			
Fe^{II}				1^{31b} : n = 4, x = 1	NMR, MS ^{31b}	NMR ^{31b}	NMR ^{31b}	2^{36d} : n = 5, x = 2 3^{36d} : μ-bmtz n = 5, x = 1
Co^{II}				4^{31a} : n = 4, x = 1				
Ni^{II}	n = 4 x = 1 ^{36c}	n = 4 x = 1 ^{36c}	MS ^{36c}	5^{36b} : n = 4, x = 1	n = 4 x = 1 ^{36c}			6^{36b} : n = 5, x = 1
Cu^{II}					MS ^{36c}			
Zn^{II}				7^{36c} : n = 4, x = 1	n = 4 x = 0 ⁶⁸			

The role of the templating anion was also probed for the diamagnetic Fe^{II} complexes which were characterized by ¹H NMR spectroscopy.^{31b} The anions [ClO₄]⁻, [BF₄]⁻, [PF₆]⁻, [AsF₆]⁻ and [SbF₆]⁻ have all been shown to template Fe^{II} pentagonal metallacycles with bptz, but [OTf]⁻ lacks the typical size and symmetry of templating anions and does not template a single preferred product, as evidenced by the multitude of peaks in the NMR spectrum, Figure 14^{31b}.

Data from ¹⁹F NMR spectroscopy studies have been used to calculate the binding energies of the internal anions in [Zn₄^{II}(bptz)₄(MeCN)₈][BF₄]₈ and [Fe₅^{II}(bptz)₅(MeCN)₁₀][PF₆]₁₀, -11.5 and -11 kcal/mol, respectively.⁶² Additional studies by the Dunbar group showed that the stability and anion interaction energies of the Fe^{II} metallacycle series increases according to [PF₆]⁻ << [SbF₆]⁻ < [AsF₆]⁻.^{31b} Therefore, the the variation in metal center and templating anion does determine the strength of the anion interactions with the metallacycle, but there is a range of anion sizes, and even shapes i.e. [I]⁻ and [Br₃]⁻,^{36c} that can lead to sufficient overlap and metallacycle complexation.

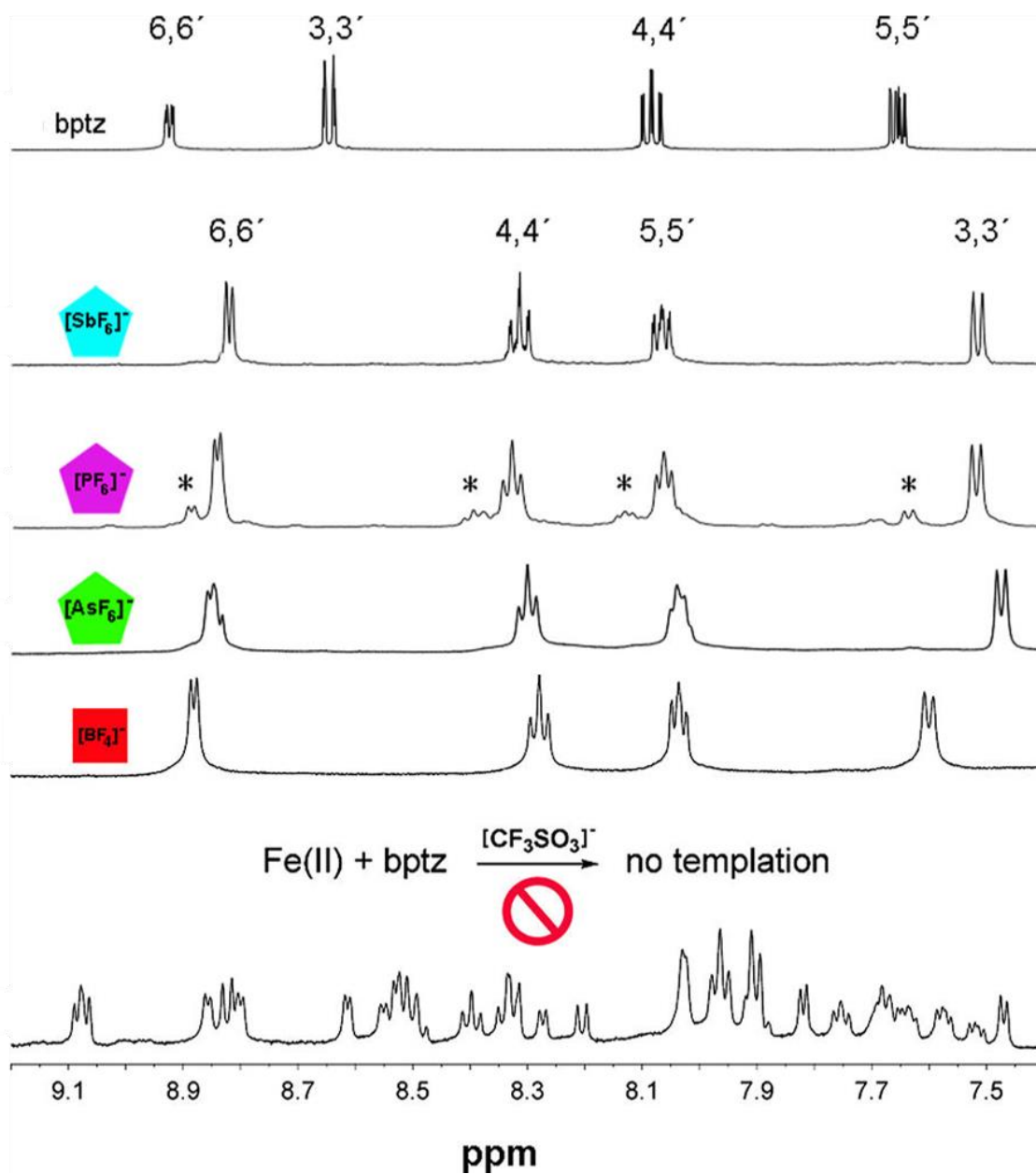


Figure 14. ^1H NMR evidence of metallacyclic interconversion.^{31b} Adapted from Dunbar et al.^{31b}

The organic bridging ligands have also been modified to investigate the impact on metallacyclic self-assembly. Electrostatic potential (ESP) maps visually represent the interaction of a positive point charge with a molecule, so the increase in the blue region of the ESP map from bptz to 3,6-bis(2'-pyrimidyl)-1,2,4,5-tetrazine (bmtz) indicates that bmtz has a greater attraction to anions, Figure 15.⁶⁹ Additionally, bmtz has a lower reduction potential than bptz.⁷⁰ According to the ESP maps and relative reduction potentials, the more “ π -acidic” bmtz ligand is expected to more readily participate in anion- π interactions. The difference in “ π -acidity” between bptz and bmtz contributes to the templating anion presence in the Fe^{II}-metallacycle cavities of **2** and **3**, Figure 15.^{36d} In complex **2**, two anions are closely positioned in the center of the metallacycle cavity and each anion participates in several anion- π interactions with the bptz ligands, Figure 15. The anion-anion repulsion within the cavity is overcome by the attractive anion- π interactions between the anions and the bptz ligands.^{36d} In complex **3**, only one anion is positioned in the cavity and participates in anion- π interactions with five all of the bmtz ligands, Figure 15.^{36d} The greater propensity for bmtz to participate in anion- π interactions is hypothesized to be attracting the central templating anion into the center of the cavity of **3** so that it can simultaneously participate in all of the possible anion- π interactions.

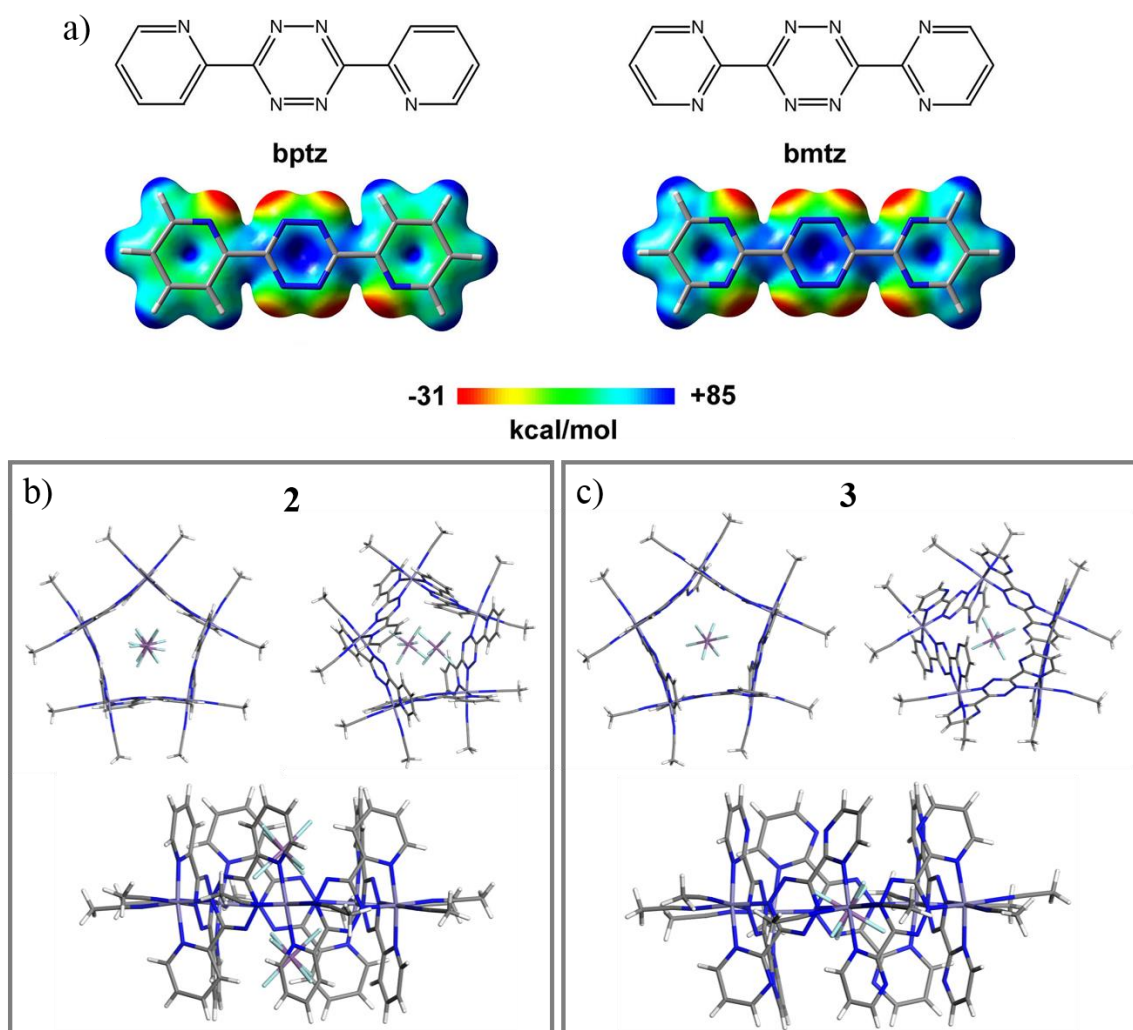


Figure 15. a) Electrostatic Potential (ESP) Maps of bptz and bmtz.⁶⁹ Adapted from Dunbar et al.^{23b} b) Metallacycle **2**, bridged by bptz and templated by two [SbF₆]⁻ anions. c) Metallacycle **3**, bridged by bmtz and templated by one [SbF₆]⁻ anion. Graphical display generated by the Materials Studio Visualizer.¹⁴

The supramolecular anion-templated metallacycle research is being aimed at the elaboration of bptz- and bmtz-bridged metallacycles with octahedral metal vertices that span the 3d, 4d and 5d transition metals. Transition metals that impart interesting photophysical, electrochemical or magnetic properties, such as Ru^{II}, Re^{II} and Cr^{III} are of particular interest. Anions with higher charges, larger sizes and additional symmetries are also proposed as possible templating agents for larger metallacycles. It was hypothesized that the vast array of metallacycle combinations resulting from the proposed bridging ligands, transition metals as well as templating anions could be pared down intuitively from the steric parameters of the building blocks. The relationships between metal ion size, templating anion size, and ligand flexibility can be very subtle, as identified by the Dunbar^{36c} and Nitschke⁶⁶ groups; therefore, a computational screening method was devised to identify the most synthetically feasible supramolecular architectures.

In order to develop an appropriate computational screening method for the supramolecular metallacycles, the continuum of computational methods available for modeling chemical systems was considered on the basis of computational cost and accuracy as outlined in Table 2 and further discussed in Chapter I. The computational cost of calculations at the Molecular Mechanics level of theory scales according to the number of atoms in the system, N, but the lack of accuracy, particularly with respect to transition metals, disqualifies these methods from screening possible metallacycle structures,¹⁸ Table 2. Higher levels of theory, exemplified by the CCSD(T)/cc-pVTZ and MP2 methods in Table 2, are able to calculate the energies of molecular systems with much higher accuracy, and, for this reason, MP2 calculations were used in this study to probe

representative anion- π interactions for each anion studied. However, CCSD(T)/cc-pVTZ and MP2 methods are incapable of accounting for the 150+ atoms present in the complete supramolecular complexes. DFT methods are capable of evaluating the entire supramolecular framework,^{31a} but the computational cost is still very expensive, especially when considering the necessary basis sets for the heavy transition metals and templating anions. With the expansive list of proposed structures, a more efficient screening method was necessary. Of the remaining Hartree-Fock and semi-empirical methods, semi-empirical methods were chosen for screening of the metallacycle frameworks because these methods combine a lower computational cost with a higher accuracy.

Table 3. Comparison of select computational methods for modeling chemical systems based on the applicability, computational cost, scaling factors and accuracy. Adapted with permission from K. H. Houk.⁴⁵

Method	N	Computational Cost	Scale	Relative Accuracy
Molecular Mechanics	100,000	¢	N^1	Low
Semi-Empirical	5,000	¢¢¢	$N^{1\sim 2}$	Medium
Hartree-Fock	500	\$	$N^{3\sim 4}$	Low
DFT	200	\$\$	$N^{3\sim 4}$	Medium-High
MP2	100	\$\$\$	N^5	Medium-High
CCSD(T)/cc-pVTZ	10	\$\$\$\$\$	N^7	High/Very High

In general, semi-empirical methods are based on the Hartree-Fock formalism¹⁸ and simplified by making specific assumptions that account for certain types of atomic orbital integrals, *i.e.* 1 e⁻ integrals involving three centers, as described further in Chapter I. The choice of the parameterization method accounts for the remaining integrals and handles electron correlation effects by applying empirical parameters. For this study, the Neglect of Diatomic Differential Overlap (NDDO)⁴⁶ was used in combination with Parameterization Method 6 (PM6),⁴⁷ to appropriately handle the d-orbitals of the transition metals and heavy main group atoms of interest. Several groups have shown the utility of the NDDO/PM6 methods for looking at small molecules,⁴⁷ supramolecular architectures,⁷¹ crystal structures⁷² and even protein structures.⁷³ In order to narrow the proposed library of supramolecular self-assembled, anion-templated metallacyclic structures to those that are the most synthetically favorable, this study combines semi-empirical calculations, empirical data and MP2 calculations to develop the first predictive method for supramolecular metallacycles.

Experimental Methods

Materials

All reactions were performed in an inert environment, using an MBraun glovebox or standard Schlenk-line techniques. Solvents were distilled prior to use. Acetonitrile was distilled over 3 Å sieves and toluene was distilled using an MBraun solvent purification system. Glassware was appropriately cleaned and oven-dried before use. [V(MeCN)₆][BPh₄]₂ and [Re₂(MeCN)₁₀][[BF₄]₄] were prepared according to reported

methods.⁷⁴ The bptz and bmtz bridging ligands were prepared and dried thoroughly under vacuum, according to literature procedures.⁷⁵

Characterization Methods

Samples for IR analysis were prepared as Nujol mulls between KBr plates and were analyzed using a Nicolet 740 FT-IR spectrometer. X-ray diffraction data for each single crystal, **8** – **10**, were collected at 110 K on an APEXII CCD detector using a MoK α source ($\lambda = 0.71073 \text{ \AA}$) and were integrated using SAINT⁷⁶ in the APEXII software suite.⁷⁷ Absorption corrections were performed using SADABS⁷⁸ or TWINABS⁷⁹ as specified, and the crystal structures were solved by direct methods using SHELXS⁸⁰ as implemented in the OLEX2 software suite.⁸¹ The final crystal structures were refined by least squares refinement with SHELXL.⁸² All non-hydrogen atoms were refined anisotropically.

Syntheses

[(μ -bmtz)Na₄(PF₆)₄]_∞ (8) and [trihydro-bmtz][PF₆] (9)

A 25 mL acetonitrile suspension of bmtz (63.5 mg, 0.267 mmol) was added to an 80 mL acetonitrile mixture of [V(MeCN)₆][BPh₄]₂ (250.8 mg, 0.262 mmol) and NaPF₆ (167.95 mg, 0.314 mmol). The mixture was stirred under N₂ at 25°C for 48 hours. Toluene was added as a precipitating solvent and the final brown solid was collected upon filtration, 97.5 mg. The solid was recrystallized with toluene, and two distinct products were characterized by single crystal x-ray diffraction: [(μ -bmtz)Na₄(PF₆)₄]_∞ (**8**) and [trihydro-bmtz][PF₆] (**9**). Although these by-products do not contain the transition metal, their structures will be described in light of the supramolecular interactions observed.



A 5 mL acetonitrile suspension of bptz (42.4 mg, 0.180 mmol) was added to a 2 mL acetonitrile solution of $[Re_2(MeCN)_{10}][[BF_4]_4]$ (100.2 mg, 0.089 mmol). The mixture was stirred in the drybox at 25°C for 24 hours. Toluene was added as a precipitating solvent and a brown solid was collected upon filtration. The product was recrystallized with toluene and characterized by single crystal x-ray diffraction: $[(\mu-O)(\mu-bptz)(Re(MeCN)_3)_2][BF_4]_2$ (**10**). Yield: 61.5 mg. IR (KBr mull), cm^{-1} : 2328, 2295, 2361(s, s, s, $\nu(C\equiv N)$), 1032, 520 (s, sh, $\nu(B-F)$).

Computational Methods

The metallacycle and anion geometries in this study were fully optimized using the semi-empirical, Neglect of Differential Diatomic Overlap approach (NDDO)⁴⁶ and the PM6 parameterization method⁴⁷ within the VAMP⁸³ module of Materials Studio 7.0,¹⁴ produced by Accelrys Software Inc. The hybridization of the main group atoms and the overall charge were assigned for each structure. The multiplicity was determined automatically by the software. The molecular orbitals were evaluated using restricted Hartree Fock (RHF)⁸⁴ and unrestricted Hartree Fock (UHF)⁸⁵ methods for closed-shell and open-shell structures, respectively. The geometry optimizations converged to a “medium” self-consistent field (SCF) with a tolerance of 1.0×10^{-5} eV and upon reaching a gradient norm of less than 0.4 kcal/mol/Å. Graphical displays of the computational results were generated by the Materials Studio Visualizer.

The abilities of many of the proposed polyatomic anions to participate in anion- π interactions with difluorotetrazine were evaluated using second order *ab initio* Mølller-

Plesset perturbation theory (MP2)^{44a-c} with the def2-TZVP^{44d, 44e} basis set in Gaussian 09, Revision E.01.⁸⁶ Anions composed of atoms beyond Kr in the periodic table ($Z > 36$) were excluded from this analysis because the atoms were not able to be fully described by the all-electron basis set def2-TZVP.^{44d, 44e} First, the geometry of difluorotetrazine and each anion was fully optimized (FO) separately. Each FO anion was placed above the face of the FO difluorotetrazine molecule such that the terminal atoms of the anion were aligned with the electropositive carbon atoms on the difluorotetrazine rings at a distance of 0.3 Å less than the sum of the vdW radii. The atomic coordinates of the difluorotetrazine molecule was restrained and the anion was optimized over the face of the ring. For each partially optimized (PO) anion- π complex, the basis set superposition error (BSSE) and the BSSE-corrected interaction energies were calculated using the counterpoise-corrected method.⁸⁷ All *ab initio* calculations were performed through Texas A&M University's High Performance Research center on a 3.088 core IBM "iDataplex" commodity cluster that includes 362 nodes of memory that are based on Intel's 64-bit Nehalem and Westmere processor.⁸⁸

Results and Discussion

Experimental Efforts

In an effort to expand the breadth of the fully-characterized metallacycle library **1–7** into the early 3d transition metals, vanadium metallacycles were pursued. V^{II} coordination was promising because many V^{II} complexes demonstrate octahedral coordination and several are being explored as therapeutics for diabetes.⁸⁹ The starting material, [V(MeCN)₆][BPh₄]₂, contains a large, diffuse tetraphenylborate anion which is

not expected to promote metallacycle templation, so sodium hexafluorophosphate was reacted with $[V(\text{MeCN})_6][\text{BPh}_4]_2$ and bptz to provide a source of templating anions. From this reaction, compounds **8** and **9** were crystallized, Table 4.

In the crystal structure of **8**, the sodium ions were coordinated to each of the four possible positions around the tetrazine ring of bmtz, Table 4 and Figure 16. While most transition metals coordinate to the bptz and bmtz ligands in a trans-fashion across the tetrazine ring, the Na^+ cations are able to access all of the positions around the tetrazine ring, similar to the Ag^+ ion's size and coordination as discussed in Chapter IV. The saturated bmtz coordination results from the coordinative flexibility of the spherical ion and the lack of steric bulk of ligands coordinated to the ion. The phosphate anion is bound to the sodium ion and participates in a series of anion- π and H-bonding interactions with the near-by bmtz bridging ligands.

Table 4. Crystallographic refinement parameters for **8**, **9** and **10**·MeCN.

Compound	8	9	10 ·MeCN
Empirical formula	C ₅ H ₃ F ₆ N ₄ NaP	C ₁₀ H ₉ F ₆ N ₃ P	C ₂₆ H ₃₂ B _{1.95} F _{7.79} N ₁₃ ORe ₂
Formula weight	287.07	386.22	1084.15
Temperature/K	110	110	110
Crystal system	triclinic	monoclinic	monoclinic
Space group	$P\bar{1}$	Pn	$P2_1/c$
a/Å	6.6541(13)	8.2089(16)	10.464(2)
b/Å	7.2488(14)	9.0982(18)	24.176(5)
c/Å	9.944(2)	9.859(2)	16.284(3)
α/°	93.36(3)	90	90
β/°	92.08(3)	93.58(3)	101.33(3)
γ/°	97.21(3)	90	90
Volume/Å³	474.59(17)	734.9(3)	4039.0(15)
Z	2	2	4
ρ_{calc}/cm³	2.009	1.745	1.783
μ/mm⁻¹	0.41	0.271	6.063
F(000)	282	388	2067
Color	Brown	Brown	Brown
Radiation	MoKα (λ = 0.71073)	MoKα (λ = 0.71073)	MoKα (λ = 0.71073)
2θ range for data collection/°	4.106 to 46.984	4.476 to 46.736	3.97 to 37.008
Index ranges	-7 ≤ h ≤ 6, -7 ≤ k ≤ 7, -10 ≤ l ≤ 11	-8 ≤ h ≤ 9, -10 ≤ k ≤ 9, -10 ≤ l ≤ 10	-9 ≤ h ≤ 9, 0 ≤ k ≤ 21, 0 ≤ l ≤ 14
Reflections collected	3309	5405	2989
Independent reflections	1279 [R _{int} = 0.0659, R _{sigma} = 0.1020]	1961 [R _{int} = 0.0439, R _{sigma} = 0.0495]	2989 [R _{int} = 0.2005, R _{sigma} = 0.1362] Derived using TWINABS
Data/restraints/parameters	1279/0/149	1961/2/235	2989/3/211
Goodness-of-fit on F²	1.843	1.106	1.576
Final R indexes [I > 2σ (I)]	R ₁ = 0.1169, wR ₂ = 0.3012	R ₁ = 0.0511, wR ₂ = 0.1293	R ₁ = 0.1732, wR ₂ = 0.4125
Final R indexes [all data]	R ₁ = 0.1575, wR ₂ = 0.3186	R ₁ = 0.0531, wR ₂ = 0.1319	R ₁ = 0.1950, wR ₂ = 0.4259
Largest diff. peak/hole / e Å⁻³	1.96/-0.78	0.46/-0.73	6.71/-3.86
Flack parameter	N/A	0.3(3)	N/A

While the bond between the Na^+ cation and the $[\text{PF}_6]^-$ anion in **8** is considerably stronger than the anion- π type interactions, the weaker anion- π interaction modifies the orientation of the anion and bmtz ligand, canting the groups from ideal 90° angles with respect to each other in order to optimize the contact between the bmtz and the phosphate anion, Figure 16b. The bmtz and anion are canted towards each other by approximately 20° , such that one F interacts closely with the tetrazine ring of one bmtz ligand, at a distance of 2.917 \AA , and the opposite F interacts closely with the pyrimidine ring of another bmtz, at a distance of 3.353 \AA and 3.433 \AA from the closest N and C atoms, respectively, circled in blue in Figure 16c. The F atoms of the $[\text{PF}_6]^-$ anions also participate in hydrogen bonding interactions with nearby hydrogen atoms of bmtz, representative contacts are 2.539 and 2.601 \AA long and are circled in grey in Figure 16b. Finally, there are π - π stacking interactions between the pyrimidine rings of neighboring columns of bmtz. The π - π stacking interactions have contact lengths of 3.570 \AA between the ring faces and are circled in red in Figure 16b. The entire group of non-covalent interactions propagates the coordination polymer observed in the crystal structure of **8**. The bmtz ligand preferentially binds to Na^+ instead of V^{2+} and the lack of directionality afforded by the Na^+ ion contributes to the polymeric structures in **8**. This structure will be further discussed in Chapter III in comparison to similar types of coordination with Ag^I .

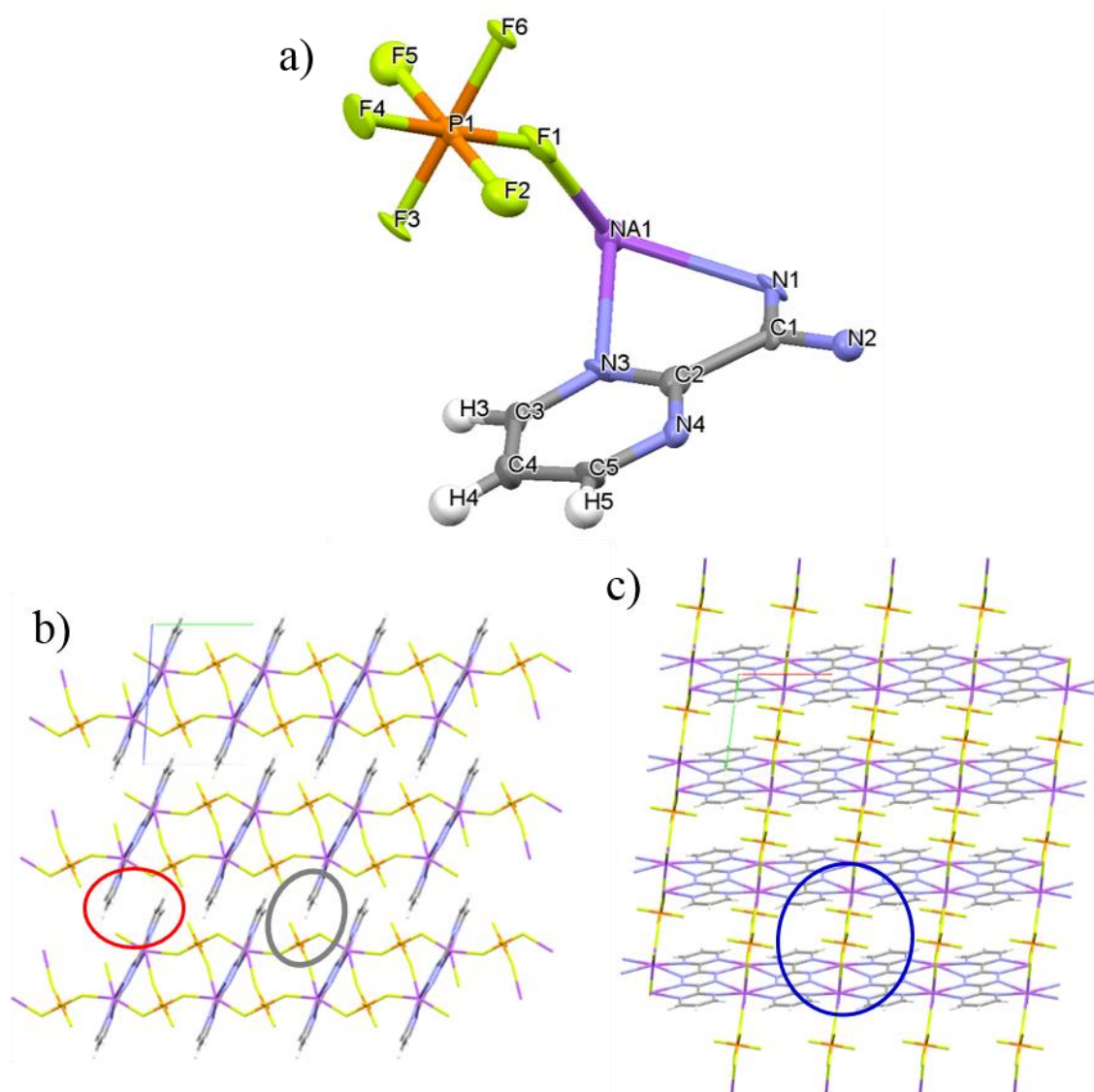


Figure 16. a) Thermal ellipsoid view of the asymmetric unit of **8**. Crystal packing (tube view) diagrams of **8** b) along the a-axis and c) along the c-axis. π - π interactions circled in red, H-bonding interactions circled in grey, and anion- π interactions circled in blue. Select bond distances (\AA): Na1-N1 2.532(11), Na1-N3 2.555(11), Na1-F1 2.332(10), C2-N3 1.318(16). Select bond angles ($^\circ$): N1-Na1-N3 63.6(3), N1-Na1-F1 101.9(3), N3-Na1-F1 181.3(3), Na1-F1-P1 148.2(5). Graphical display generated by the Mercury visualizer.⁹⁰

The second product, **9**, highlights the unpredictable chemistry of V^{II}, Table 4 and Figure 17. Complex **9** consists of one triply protonated bmtz cation and one hexafluorophosphate anion. Triple-protonation of bmtz is surprising because bmtz is synthesized upon deprotonation of the H₂-bmtz compound. The stable dihydro-bmtz compound is synthesized in acidic media but does not result in the triply protonated state. The formation of [trihydro-bmtz]⁺ and subsequent broken aromaticity was expected to be energetically unfavorable and was likely catalyzed by the V^{II} complex. The anion interacts with the cationic [trihydro-bmtz]⁺ group through electrostatic interactions, such that there are short contacts between F1-N7 of 3.055 Å and between F5-N8 and F5-C7 of 2.853 Å and 2.763 Å, respectively. The lack of V^{II} binding prompted the investigation of other transition metals, particularly larger 4d and 5d ions.

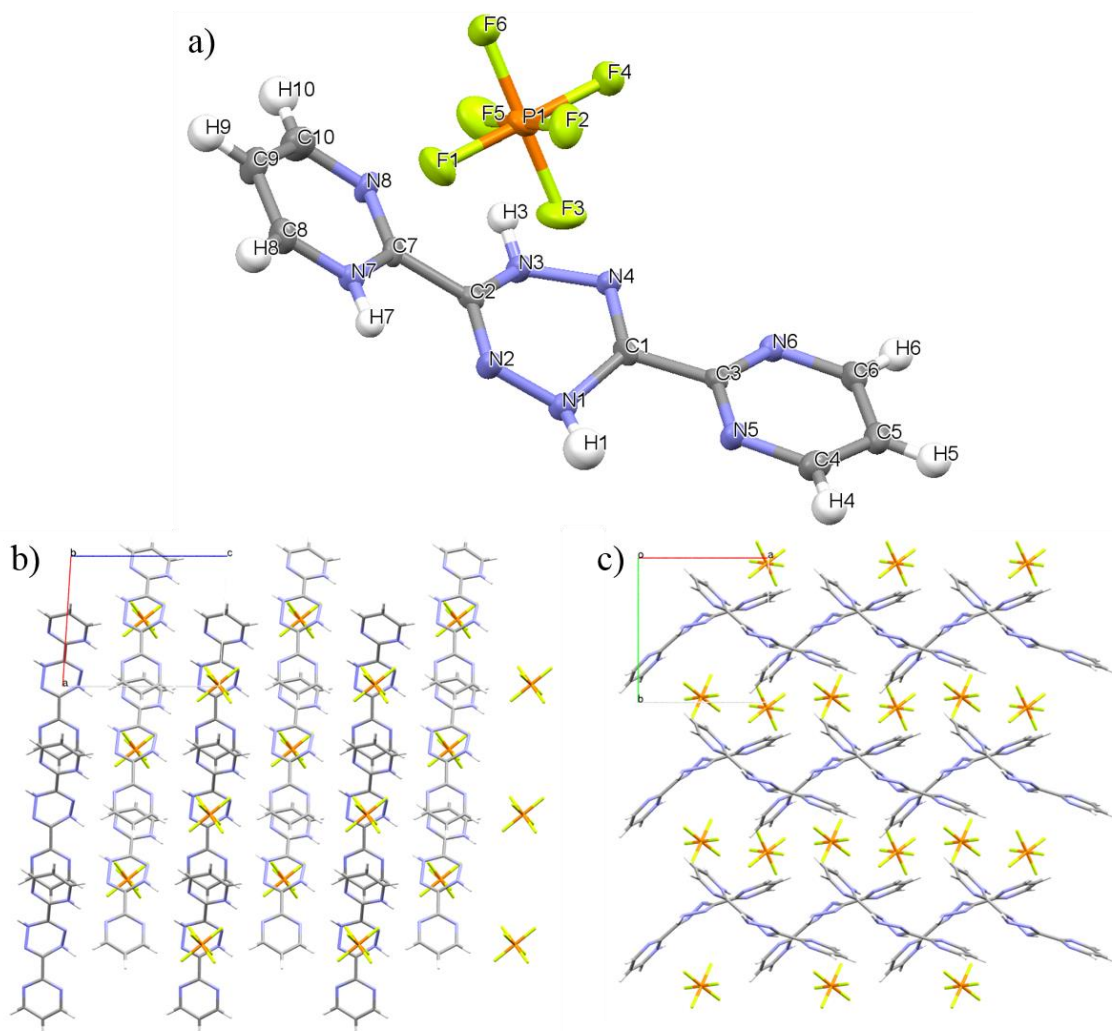


Figure 17. a) Thermal ellipsoid view of the asymmetric unit of **9**. Crystal packing (tube view) diagrams of **9** b) along the b-axis and c) along the c-axis. Select bond distances (Å): C1-N1 1.389(9), C1-N4 1.273(8), C2-N2 1.280(9), C2-N3 1.401(9), N1-N2 1.409(8), N3-N4 1.427(8), C7-N7 1.339(8), C7-N8 1.327(9), C3-N5 1.336(9), C3-N6 1.353(8). Select bond angles (°): C1-N1-N2 114.9(5), C2-N2-N1 112.0(5), C1-N4-N3 112.5(6), C2-N3-N4 113.8(5), C2-C7-N7 117.7(6), C2-C7-N8 119.3(6), C1-C3-N5 117.2(6), C1-C3-N6 117.2(6), N8-C7-N7 123.1(6), N6-C3-N5 125.5(6). Graphical display generated by the by the Mercury visualizer.⁹⁰

The reaction between $[\text{Re}_2(\text{MeCN})_{10}][\text{BF}_4]_4$ and bptz was performed in order to determine if the M-M bond would be preferentially broken to form a metallacyclic structure. Compound **10** was crystallized and the twinned crystal was characterized as an acetonitrile solvate, revealing that, while not a metallacycle, the metal-metal bond was broken, Table 4 and Figure 18. The Re ions are bound to bptz in a cis-fashion, and this unusual coordination about the tetrazine ring results from an oxo-bridge between the mixed-valent metal centers, with one typical oxo-bridging bond distance of 1.96 Å.⁹¹ Re1 is assigned as trivalent and Re2 is assigned as monovalent to accommodate the different Re-O bond distances and overall charge, but the low quality of the data prevents an accurate determination of the oxidation state of the metals. Additional efforts should be pursued to conclusively determine the oxidation states of the Re ions. There are anion- π interactions between one of the $[\text{BF}_4]^-$ anions and the bptz ligand, 2.860 Å and 2.965 Å between the F atoms and the carbon atoms of the tetrazine ring. The pyrimidyl rings of the bmtz participate in slipped π - π interactions with the pyrimidyl rings of adjacent complexes, and the close-contact is 3.401 Å between the faces. Finally, there is a series of H-bonding interactions, ranging from 2.287 Å to 3.716 Å, between the $[\text{BF}_4]^-$ anions and the methyl protons on the acetonitrile ligands. The non-covalent interactions cause the molecule to orient in the packing diagrams of Figure 18. While replete with non-covalent interactions, the complex did not involve anion templation of a Re^{II} metallacycle.

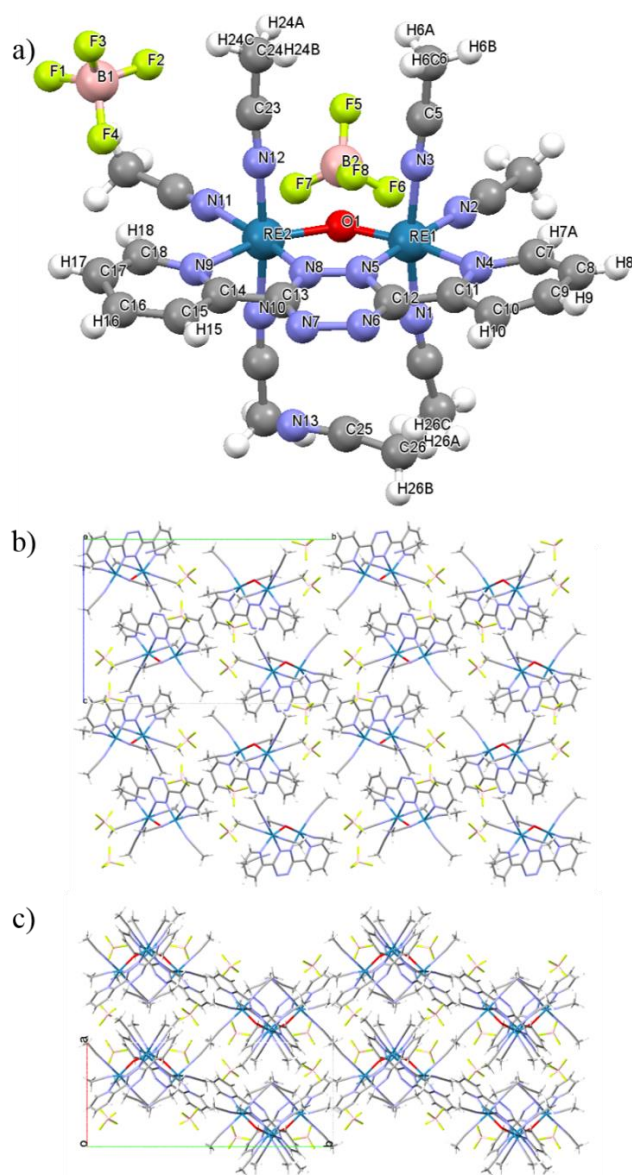


Figure 18. a) Ball-and-Stick view of **10**·MeCN. Crystal packing diagrams (tube view) of **10**·MeCN b) along the *a*-axis and c) along the *c*-axis. Select bond distances (Å): Re1-O1 1.76(5), Re1-N1 2.06(5), Re1-N2 1.97(6), Re1-N3 2.00(4), Re1-N4 2.20(5), Re1-N5 1.98(5), Re2-O2 1.96(5), Re2-N8 1.94(4), Re2-N9 2.18(4), Re2-N10 2.02(4), Re2-N11 2.12(7), Re2-N12 2.03(4), N4-C11 1.41(7), C11-C12 1.46(8), C12-N5 1.47(8), C12-N6 1.34(8), N5-N8 1.30(5), N6-N7 1.41(6), N13-C25 1.26(10), C25-C26 1.34(11). Select bond angles (°): Re-O1-Re2 131(30), O1-Re1-N1 92(2), O1-Re1-N2 100(2), O1-Re1-N4 161(2), O1-Re1-O5 82(2), O1-Re2-N8 83(2), O1-Re2-N9 158.9(19), O1-Re2-N10 88.6(9), O1-Re2-N11 105(2), N4-C11-C12 113(5), C11-C12-N5 115(5), N7-C13-N8 134(5), C13-C14-N9 115(5), N13-C25-C26 169(10). Graphical display generated by the Mercury visualizer.⁹⁰

Additional reactions were performed between both bptz and bmtz and the acetonitrile solvated transition metal complexes of Cr^{II}, Mn^{II}, Fe^{II}, Co^{II}, Ni^{II}, Mo^{II}, Ru^{II}, Rh^{III} and Cd^{II}, following similar reaction conditions for **10**. The counter anions of the fully-solvated metal salts included [BF₄]⁻, [PF₆]⁻, [AsF₆]⁻, [SbF₆]⁻, [TaF₇]²⁻, [NbF₇]²⁻, [perfluoro-BPh₄]⁻, [BPh₄]⁻ and [ClB₁₁C₁₂]⁻. The reactions of [Ru(MeCN)₆][SbF₆]₂, [Ru(MeCN)₆][BF₄]₂ and Ru(DMSO)₄(Cl)₂ with bmtz in DMSO/acetonitrile solutions were heated to reflux and irradiated with UV-light and blue light, respectively. For many of these reactions, the solutions underwent a color change, denoting a reaction taking place. NMR and IR spectra of several of the products supported the presence of the organic species and anions, but were unable to provide conclusive evidence of the reaction product frameworks. The reaction products were layered over a series of precipitating solvents, in attempts to grow single crystals, but the subsequent crystallization attempts were unsuccessful. Therefore, a computational model of possible metallacyclic structures was undertaken to identify ideal metallacyclic structures to target synthetically.

Semi-Empirical Modeling of the Fe^{II} Metallacycles

In order to develop such a predictive model for evaluating possible supramolecular structures, the crystal structures of the diamagnetic, low-spin Fe^{II} frameworks **1**,^{31b} **2**^{31b} and **3**^{36d} were explored computationally. For each structure, the metallacyclic framework and the eight to ten closest counter ions were retained for neutral model structures **1N** – **3N**, Figure 19. The geometries of **1N** – **3N** were fully optimized at the NDDO/PM6/RHF level of theory.^{46-47, 84} By selecting only the closest eight to ten anions for the neutrally charged model system **N**, several anions were eliminated from the close-packed crystal

structure that did participate in close electrostatic interactions in the solid state. There is moderate deviation of the predicted metal to metal cross-ligand distance (d_{M-M}) and the Metal-Ligand_{Centroid}-Metal angles from the parent crystal structures and this is expected due to the removal of some of those close packed anions. In each of the optimized **1N** – **3N** structures, the d_{M-M} varies by 0.1 Å and the Metal-Ligand_{Centroid}-Metal angles vary by $\sim 10^\circ$, but the crystal structures only show a variation in the d_{M-M} and Metal-Ligand_{Centroid}-Metal angles of 0.04 Å and $\sim 2^\circ$, respectively.

For this reason, the peripheral anions were removed from the Fe^{II} models and each system was simplified to the metallacycle framework and the interior anion(s), **1A** – **3A**, Figure 19. The structures were further simplified in Model B to just the metallacyclic framework, without the interior anion, **1B** – **3B** shown in Figure 19. The geometries of **1A, B** – **3A, B** were fully optimized and demonstrated significant agreement with crystal data. To quantify the agreement between the structures, the average d_{M-M} was compared for the original crystal structures **1** – **3** and optimized model structures **1N, A, B** – **3N, A, B**, Table 5.

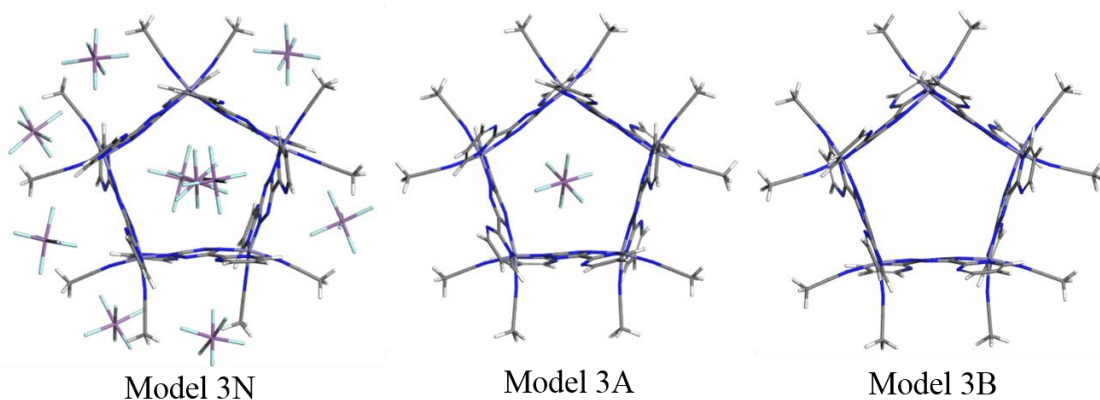


Figure 19. Models N, A and B for 3. Graphical display generated by the Materials Studio Visualizer.¹⁴

Table 5. d_{M-M} for 1 – 3 crystal structures and the N, A and B optimized models.

	Crystal Structure	Model N	Model A	Model B
	d_{M-M} (Å)	d_{M-M} (Å)	d_{M-M} (Å)	d_{M-M} (Å)
1	6.452(3)	6.494(20)	6.372(13)	6.420(2)
2	6.426(4)	6.528(39)	6.420(6)	6.465(1)
3	6.430(19)	6.339(33)	6.424(4)	6.450(1)
	Average d_{M-M} Error:	0.079(31)	0.043(8)	0.039(3)

The average Model N d_{M-M} error, 0.079 Å, and standard deviation, 0.031 Å, was greater than for Models A and B, so Model N was discarded. Models A and B are able to suitably reproduce the crystal structure data for 1 – 3; the average d_{M-M} error and standard deviations for Models A and B was 0.043(8) Å and 0.039(3) Å, respectively. In Figure 20, the crystal structures are overlaid with the Model A (green framework) and B (purple framework) structures, visually representing the ability of the simplified models to

describe the metallacyclic structures (ball and stick framework). The most significant deviation from the crystal structure frameworks is the orientation of the terminal acetonitrile ligands and the rotation of the pyridine and pyrimidine groups, but this deviation is inconsequential for the analysis of the metallacycle cavity.

The degree of overlap in Figure 20 also indicates that the NDDO/PM6/RHF level of theory^{46-47, 84} is able to appropriately accommodate the heavy atoms within the supramolecular metallacyclic architectures. The optimized octahedral Fe^{II} vertices demonstrate physically relevant Fe^{II}-N bond distances and N-Fe^{II}-N angles, and the flexibility and torsion of the octahedral coordination sphere was accurately reproduced in the **1A, B – 3A, B**. The level of theory also appropriately optimized the templating anions in Model A. The optimized B-F and Sb-F bond distances for [BF₄]⁻ and for [SbF₆]⁻ deviated from those in the crystal structure by less than 0.1 Å, and the placement of the optimized anion in the cavity was translated less than 2.5 Å from the templating anion position within the cavities of **1 – 3**. Electrostatic interactions between the cavity and the anion appear to contribute to the general placement of the anion in the cavity, this likely includes the Fe^{II} vertices and the π -acidic bridging ligands. The deviation of the modeled anion placement from that observed in the crystal structure likely occurs from an incomplete assessment of the anion- π interactions between the templating anion with the bridging ligands, by the semi-empirical methods.

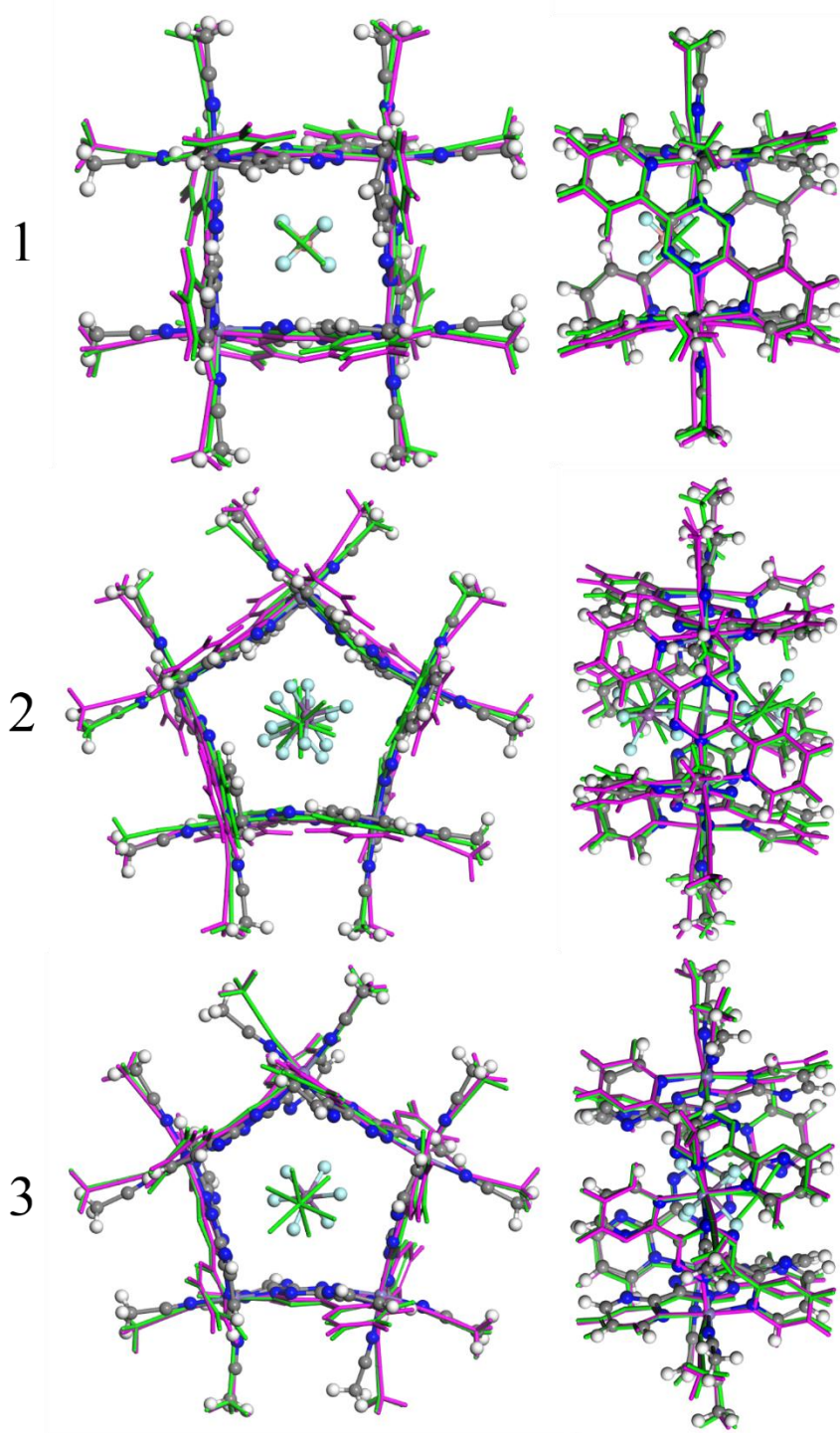


Figure 20. Overlay of **1 – 3** (ball and stick) with **1A – 3A** (green tube) and **1B – 3B** (purple tube). Graphical display generated by the Materials Studio Visualizer.¹⁴

The Dunbar group has previously shown that many of the metallacyclic structures do not persist in solution without an appropriate templating anion,^{31b, 36c} but the series of Model B structures remain stable enough to be explored computationally. In fact, the d_{M-M} error and standard deviation for **1B** – **3B** is lower than for **1A** – **3A** because the Fe^{II} vertices of the Model B frameworks are not competing for close electrostatic interactions with the anion. Therefore, Model B structures are the most symmetric depictions of the frameworks for **1** – **3**.

Semi-Empirical Prediction of the Metallacycle Library

The next step in developing a predictive model of metallacyclic frameworks was to employ the semi-empirical methods to predict the remaining supramolecular metallacycles templated by [BF₄]⁻ and [SbF₆]⁻ and crystallized by the Dunbar group.^{31, 36a-c} Due to the presence of a single anion in each of the cavities of **1** and **3**, these frameworks were used as templates for modeling the remaining divalent Fe,^{31b} Ni,^{36a, 36b} Co^{31a} and Zn^{36c} metallacycles. The atomic assignments of the metal vertices and bridging ligands of the templates **1A, B** and **3A, B** were modified, and representative architectures were developed for the square and pentagonal bptz-bridged metallacycles for **2, 4** – **7**. Fully optimized structures **1A, B** – **6A, B** show strong correlation to the crystal structure data, with an average d_{M-M} error of 0.165(36) Å and 0.166(20) Å, respectively, for **1** – **6**, Table 6.

The Fe^{II} and Ni^{II} metallacycles (**1** – **3, 5** – **6**) are reproduced particularly well by Models A and B. The average d_{M-M} error for the Model A and B structures of **1** – **3, 5** – **6** was 0.078(28) and the 0.054(16), respectively. The higher degree of accuracy for the Fe^{II}-

and Ni^{II}-based structures reflects the ability of the semi-empirical methods to appropriately handle the transition metal vertices, electrostatic interactions and bridging ligand coordination. The greater d_{M-M} deviation between the crystal structures and predicted model structures of **4** and **7** resulted from the parameters for Co^{II} and Zn^{II} within PM6. For **4**, the PM6 parameters cause the Co^{II} vertices to ascribe to a strictly octahedral coordination sphere, with insignificant deviation from ideal 90° angles between bound atoms,⁴⁷ but the bidentate binding angle for the bptz ligand ranges from 74.4° – 83.2° depending on the metal center.^{31a} In order to accommodate the PM6 parameters and binding to two bptz ligands with such non-ideal bite angles, **4A** and **4B** underwent significant torsion along each bridging bptz ligand that is not observed in the crystal structures. For **7**, the PM6 parameters for Zn^{II} require that the metal center adopt a tetrahedral coordination environment,⁴⁷ instead of the octahedral coordination necessary for the metallacycle framework.^{36c} To accommodate the coordination restrictions, the optimized structures of **7A** and **7B** decomposed into four tetrahedral [Zn^{II}(bptz)(MeCN)₂]²⁺ cations.

Therefore, the PM6 parameters⁴⁷ limit the scope metallacycles that can be accurately modeled to those metal centers allowed to have relatively flexible, octahedral coordination environments. Within the limitations of the NDDO/PM6 semi-empirical methods,⁴⁶⁻⁴⁷ highly charged, supramolecular crystal structures have been reproduced with very high accuracy.

Table 6. Comparison of the average d_{M-M} for the crystal structures and optimized models **A** and **B** for each crystallized metallacycle, **1** – **7**. N/A for structures that did not converge to metallacyclic structures.

Metallacycle	Crystal Structure d_{M-M} (Å)	Model A d_{M-M} (Å)	Model B d_{M-M} (Å)
1^{31b}	6.452(3)	6.372(13)	6.420(2)
3^{36d}	6.430(19)	6.424(4)	6.450(1)
2^{31b}	6.426(3)	6.485(76)	6.464(1)
4^{31a}	6.976(57)	6.377(76)	6.251(38)
5^{36a}	6.868(15)	6.674(20)	6.712(38)
6^{36b}	6.748(15)	6.697(26)	6.723(37)
7^{36c}	7.177(28)	N/A	N/A
	Average d_{M-M} Error:	0.165(36)	0.166(20)

Predictive Semi-Empirical Method

The semi-empirical metallacyclic model was therefore elaborated as a predictive tool to identify supramolecular synthetic targets. Due to the presence of a single anion in each of the cavities of **1** and **3** and the lower average d_{M-M} error and standard deviation for the Model B structures in Table 6, Models **1B** and **3B** were used as the square and pentagonal templates for the remainder of this study. The atomic assignments of the bridging ligand atoms of **1B** and **3B** were modified to explore bptz- and bmtz-bridged metallacycles. The atomic assignments and oxidation states of the transition metal vertices

were also modified to predict square and pentagonal structures for each of the transition metals highlighted in blue and orange in Table 7. The geometries of the predicted metallacycles were fully optimized. For the square and pentagonal architectures involving Co^{II} , Co^{III} , Zn^{II} , Mo^{IV} , Rh^{I} , Rh^{III} , Ag^{I} and Cd^{II} , the PM6 parameters did not allow for an appropriate octahedral coordination at the metal center, highlighted in orange in Table 7.⁴⁷ Instead, the optimized structures adopted distorted octahedral, tetrahedral or linear coordination geometries that have not been further analyzed.

Table 7. The d-block elements, with the specific transition metals and oxidation states explored by semi-empirical methods highlighted in blue and orange. The PM6 parameters of the transition metals highlighted in orange did not allow for appropriate octahedral coordination.

Sc	Ti	V^{II}	Cr^{II} Cr^{III}	Mn^{II} Mn^{III}	Fe^{II} Fe^{III}	Co^{II} Co^{III}	Ni^{II}	Cu^{I} Cu^{II}	Zn^{II}
Y	Zr	Nb	Mo^{II} Mo^{IV}	Tc	Ru^{II} Ru^{III}	Rh^{I} Rh^{III}	Pd	Ag^{I}	Cd^{II}
La	Hf	Ta	W	Re^{II}	Os	Ir	Pt^{II}	Au	Hg

A series of tetrahedral and octahedral anions were also fully optimized at the semi-empirical NDDO/PM6 level of theory⁴⁶⁻⁴⁷ in order to identify ideal anions for templation. The tetrahedral anions included $[\text{BF}_4]^-$, $[\text{ClO}_4]^-$, $[\text{SO}_4]^{2-}$, $[\text{BrO}_4]^-$, $[\text{PO}_4]^{3-}$, $[\text{MnO}_4]^-$,

[CrO₄]²⁻, [IO₄]⁻, [SeO₄]²⁻, [AsO₄]³⁻, [VO₄]³⁻, [TeO₄]²⁻ and [ZnCl₄]²⁻. The octahedral anions included [PF₆]⁻, [AsF₆]⁻, [SbF₆]⁻, [BiCl₆]²⁻ and [TeCl₆]²⁻.

Square Metallacycle Predictions

To evaluate anion-cavity compatibility for the square metallacycles, the length of the metallacycle cavity was compared to the size of the tetrahedral anions. The size of the square cavity was measured as the average cross-cavity distance between the centroids of opposite tetrazine rings, $d_{OppCentroids}$, because this accounts for the curvature that can occur along the bridging ligands. The van der Waals radius for carbon⁹² was deducted from this distance twice to account for the van der Waals surfaces of the tetrazine rings on either side of the cavity. The resulting cavity length, L_{Cavity} , denotes the length of available space within the square metallacycles, Equation 3.

$$L_{Cavity} = d_{OppCentroids} - 2 \text{vdW } C \quad \text{Equation 3}$$

In the square metallacycle crystal structures (**1**, **4**, **5** and **7**), the tetrahedral anion is oriented such that the pairs of the fluorine atoms on [BF₄]⁻ are in close-contact with the tetrazine carbon atoms on either side of the metallacyclic cavity. Opposite F-F edges of the tetrahedron formed by the templating anion, Figure 21, interact in an ordered fashion with opposite tetrazine rings of the framework such that the resulting anion- π interactions were optimized with opposite pairs of tetrazine rings, Figure 22.

F-F Tetrahedron Edge

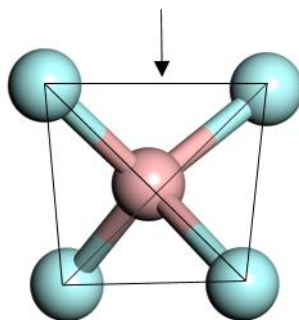


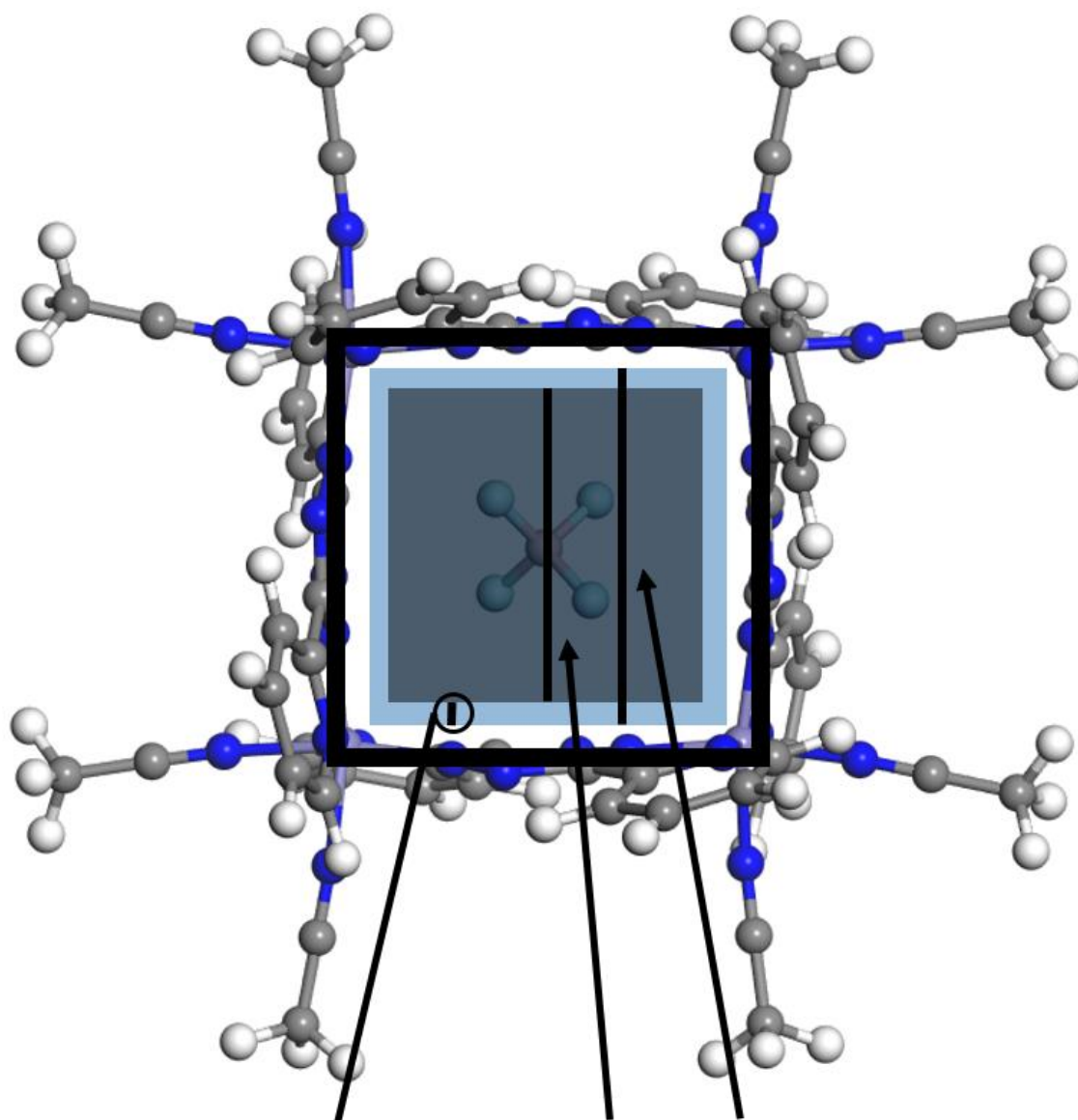
Figure 21. $[\text{BF}_4]^-$ with tetrahedron frame outlined between F atoms and designated F-F tetrahedron edge. Graphical display generated by the Materials Studio Visualizer.¹⁴

The length of the anion, L_{Anion} , within the cavity corresponds to the distance between the opposite edges of the anion tetrahedron plus twice the van der Waals radius for the atoms along the tetrahedron edges, Equation 4.

$$L_{\text{Anion}} = d_{\text{TetrahedronEdge}} + 2 \text{vdW} (F, O \text{ or } Cl) \quad \text{Equation 4}$$

The degree of overlap between the anion and the tetrazine rings on one side of the metallacyclic framework corresponds to half of the difference between L_{Cavity} and L_{Anion} , Equation 5 and Figure 22.

$$\text{Overlap}_{\text{square}} = \frac{L_{\text{Cavity}} - L_{\text{Anion}}}{2} \quad \text{Equation 5}$$



$$\text{Overlap}_{\text{Square}} = \frac{L_{\text{Cavity}} - L_{\text{Anion}}}{2}$$

Figure 22. Evaluation method of the anion-cavity overlap for the predicted square metallacycles. Graphical display generated by the Materials Studio Visualizer.¹⁴

The $\text{overlap}_{\text{square}}$ of each of the predicted structures was plotted with respect to the tetrahedral templating anion and the transition metal at each vertex, Figure 23. The $\text{overlap}_{\text{square}}$ for **1**, **4**, **5**, **7** and the respective A and B model structures ranges from -0.446 to -0.725 Å, and is considered “ideal” because this is the amount of overlap identified upon metallacycle templation. The ideal overlap spans nearly 0.3 Å because the two-dimensional $\text{overlap}_{\text{square}}$ model assumes that the anion sits in the direct center of the cavity. The anions within the frameworks of the crystal structures are not situated at the ideal center of the cavity, however, and are situated in an “off-center” position to maximize anion- π interactions and minimize steric repulsion, as can be seen by the images of the profiles of the metallacycles in Figure 20. The broad range of “ideal” overlap therefore accounts for each anion to adopt the most favorable position within the predicted three-dimensional cavities. The anion-cavity combinations that exhibit predicted overlap in the ideal range of -0.446 – -0.725 Å are expected to be synthetically favorable and are identified within the blue boxes in Figure 23. Promising anion-cavity combinations exist for each of the transition metals and many of the templating anions, and will be further evaluated in the following sections.

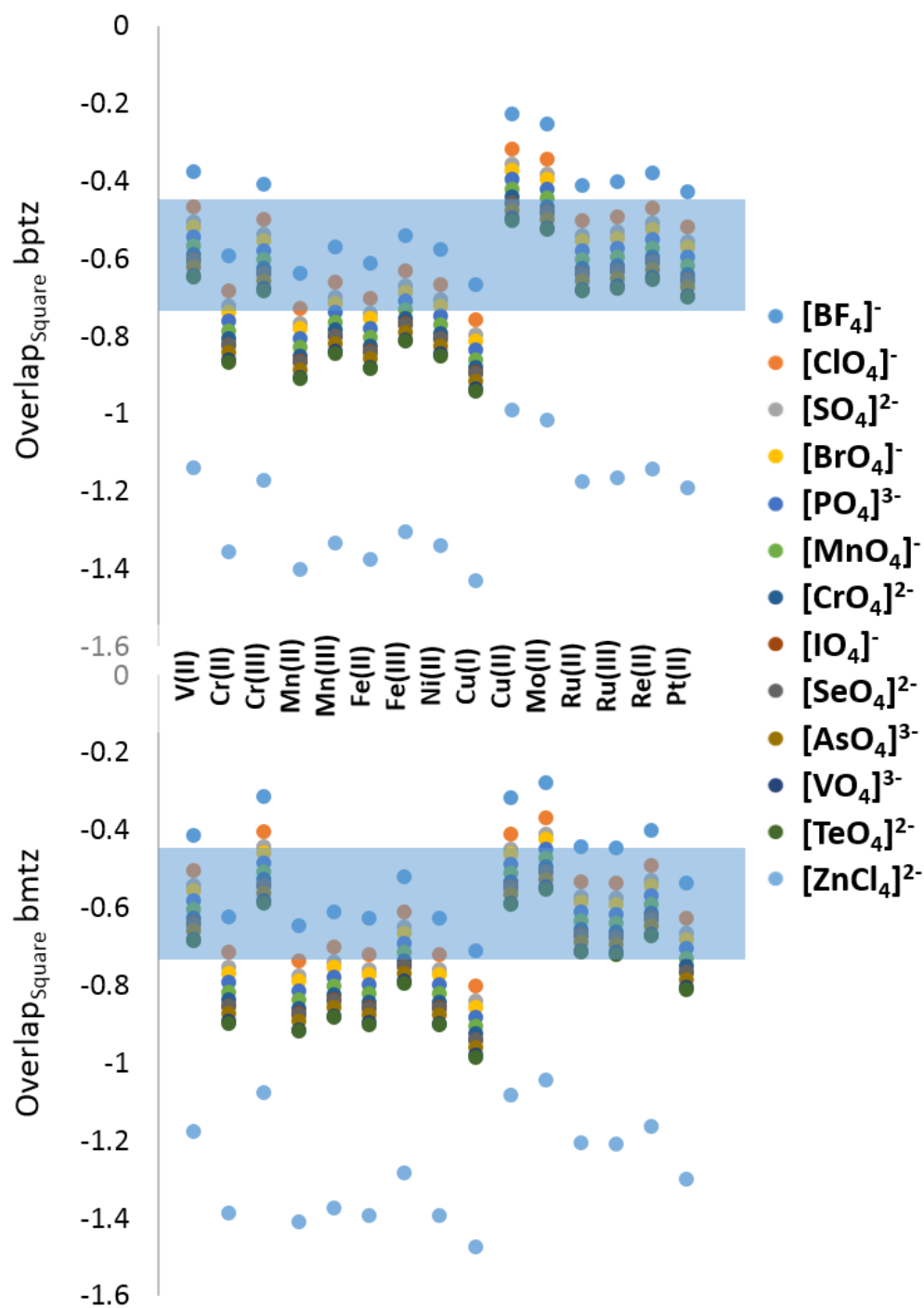


Figure 23. Anion-cavity compatibility determined by the degree of overlap_{Square}. The ideal overlap_{Square} range is identified by the blue box.

Pentagonal Metallacycle Predictions

In a similar manner, the anion-cavity compatibility for the pentagonal metallacycles was evaluated by comparing the radius of the metallacycle cavity with the radius of each optimized octahedral anion. For each of the optimized pentagonal metallacyclic structures, the average d_{M-M} was measured, and an ideal pentagon with length d_{M-M} was calculated, the outlined pentagon in Figure 24. The radius of the incircle of the ideal pentagon was calculated, where the incircle is defined as a circle that touches each side of the regular pentagon without crossing outside of the polygon, and is the outlined circle in Figure 24. The van der Waals radius of carbon was subtracted from the incircle radius to account for the protrusion of the van der Waals surface of the tetrazine ring into the incircle of the ideal pentagon. The resulting distance, R_{Cavity} , is the radius of the vacant cavity available for anion-templation, Equation 6 and the grey interior circle in Figure 24.

$$R_{Cavity} = \left(\frac{d_{M-M}}{2 \tan \frac{180}{5}} \right) - vdw C \quad \text{Equation 6}$$

In the crystal structures for **2**, **3** and **6**, the octahedral templating anion is oriented such that the anion- π interactions of the metallacycle are optimized, but the pentagonal symmetry prevents a symmetrical orientation of the terminal atoms of the octahedral anion with each tetrazine ring.^{31b, 36d} Therefore, the directionality of the templating anion was modeled as a simple circle, with radius R_{Anion} . This R_{Anion} includes the optimized X-F or

X-Cl bond length, $d_{\text{BondLength}}$, plus the appropriate van der Waal radius for the terminal atom, Equation 7 and the blue circle in Figure 24.

$$R_{\text{Anion}} = d_{\text{BondLength}} + vdw \text{ (F or Cl)} \quad \text{Equation 7}$$

The overlap of each framework and the prospective templating anions was calculated as the difference between R_{Cavity} and R_{Anion} , Equation 8 and Figure 24.

$$\text{Overlap}_{\text{Pentagon}} = R_{\text{Cavity}} - R_{\text{Anion}} \quad \text{Equation 8}$$

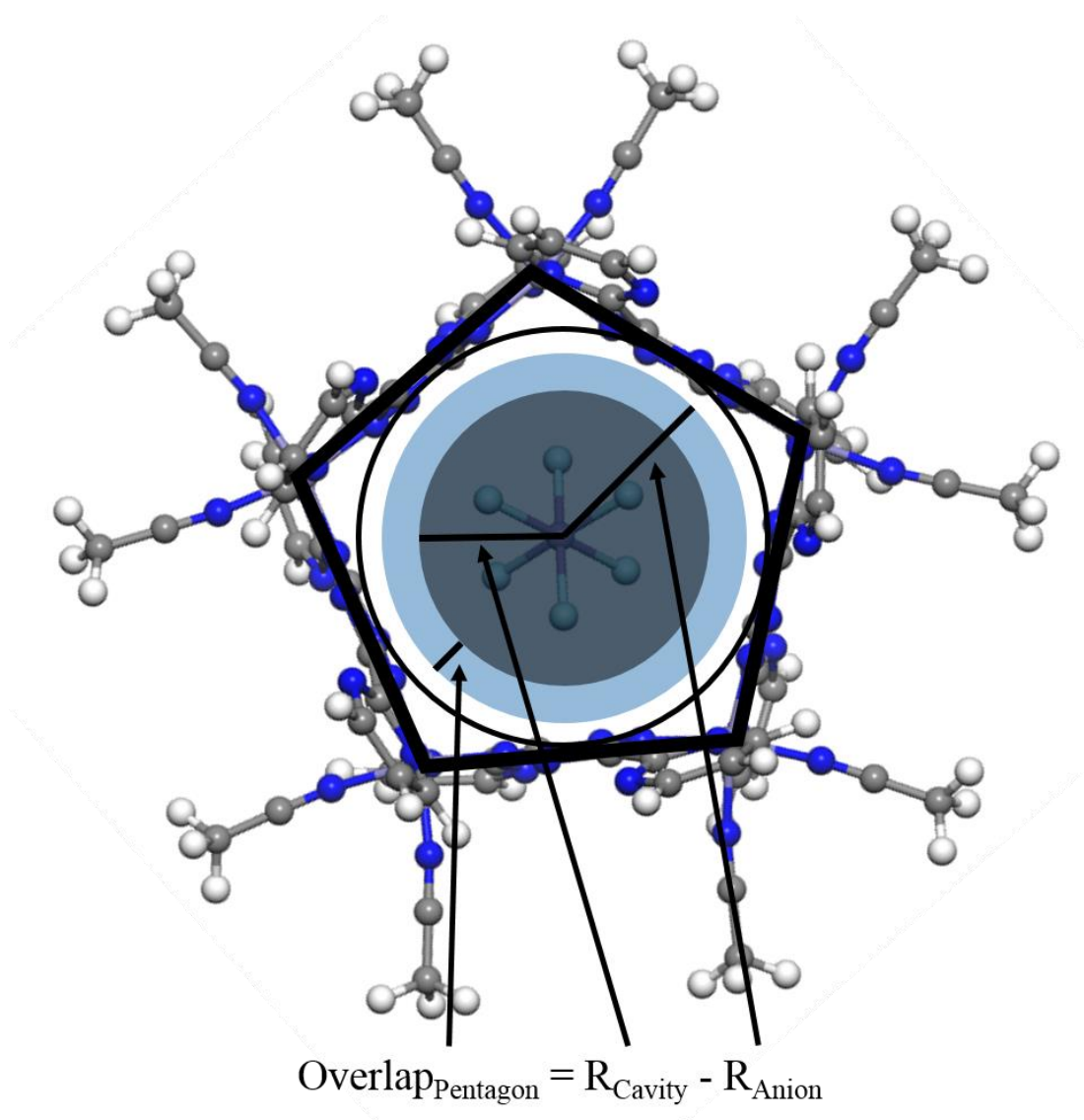


Figure 24. Evaluation method of the anion-cavity overlap for the predicted pentagonal metallacycles. Graphical display generated by the Materials Studio Visualizer.¹⁴

The $\text{overlap}_{\text{pentagon}}$ of the predicted structures with each of the templating octahedral anions was plotted with respect to the metal center vertices, Figure 25. The anion-cavity overlap calculated for the crystal structures and metallacycle models of **2**, **3**, and **6** ranges from $-0.524 - -0.746 \text{ \AA}$. Previous studies by the Dunbar group led to the conclusion that the $[\text{Fe}_5(\text{bptz})_5(\text{MeCN})_{10}][\text{AsF}_6]_{10}$ metallacycle is more stable than **2** in solution,^{31b} so the $\text{overlap}_{\text{pentagon}}$ predicted for $[\text{Fe}_5(\text{bptz})_5(\text{MeCN})_{10}][\text{AsF}_6]_{10}$ was also included in the ideal overlap range. Therefore, the final ideal range of overlap is $-0.475 - -0.746 \text{ \AA}$. As with the square structures, the $\sim 0.3 \text{ \AA}$ range of ideal overlap results from the optimized, non-central placement of the anion within the cavity, as depicted by the images of the metallacyclic profiles in Figure 20. The non-central location of the templating anions in **2**, **3** and **6** maximizes the anion- π interactions with the bridging ligands and minimizes the steric repulsions within the cavity. Pentagonal architectures predicted to be templated in such an ideal fashion are identified by the blue boxes in Figure 25. Experimentally favorable metallacycles include bptz and bmtz-bridged structures based on Cr^{II} , Mn^{II} , Fe^{II} , Fe^{III} , Ni^{II} , Cu^{I} , Cu^{II} and Ru^{II} with appropriate templating anions including $[\text{AsF}_6]^-$, $[\text{SbF}_6]^-$ and $[\text{TeCl}_6]^{2-}$. In order to refine the set of experimentally-favorable metallacycle predictions and to evaluate the accuracy of the anion-cavity compatibility model, the semi-empirical treatment of the transition metal vertices and polyatomic anions were assessed separately and are discussed in the following sections.

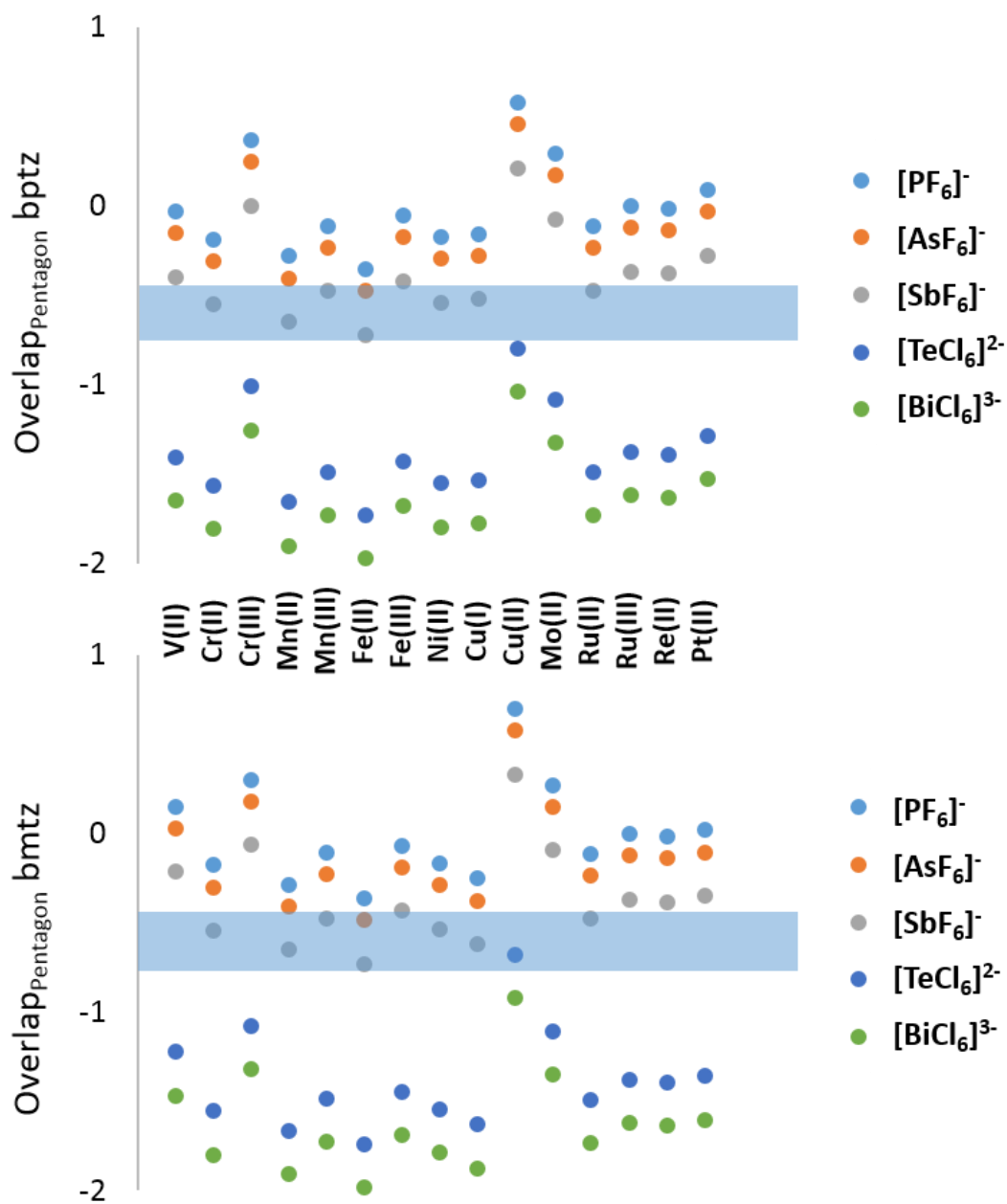


Figure 25. Anion-cavity compatibility determined by the degree of $\text{overlap}_{\text{Pentagon}}$. The ideal $\text{overlap}_{\text{Pentagon}}$ range is identified by the blue box.

Analysis of the Semi-Empirical Treatment of Transition Metal ions

The ability of the semi-empirical method to appropriately treat metal centers is paramount to the accuracy of the metallacycle predictions. The PM6 parameters⁴⁷ for each metal dictate the respective M-N distances and coordination flexibility, and these factors determine the size of the metallacycle cavity, torsion of the bridging ligands and anion(s) suitable for templation. For the semi-empirical model to be a successful predictive method, the relative octahedral coordination environment and size of each metal center must be appropriately modeled. As mentioned previously, many of the initially identified transition metals at each of the designated oxidation states were optimized as ideal metallacyclic structures. Transition metal ions that did not promote ideal optimization included Co^{II} and Co^{III}, transition metals that demonstrated too little octahedral coordination flexibility, and Zn^{II}, Mo^{IV}, Rh^I, Ag^I and Cd^{II} that resulted in non-ideal tetrahedral, square planar and linear symmetries and furthermore caused separation of the metallacyclic template frameworks.

For each of the ideally optimized metal centers, the average M-N bond distance, d_{M-N} , was measured to evaluate the semi-empirical model's treatment of the transition metal ion's size within each framework. All six d_{M-N} were measured for one representative vertex of each of the predicted bmtz-bridged metallacycles, Table 8. The d_{M-N} for analogous bptz metallacycles are very similar to the bmtz structures and were not included.

Table 8. The square metallacycle d_{M-N} , pentagonal metallacycle d_{M-N} , ionic radius, Σ_{M-N}^{93} and the Average and most prevalent d_{M-N} identified from structures in the CSD⁹¹ for each specified transition metal and oxidation state. NR = Not reported for the specified oxidation state.⁹⁴

Transition Metal	Square d_{M-N} (Å)	Pentagonal d_{M-N} (Å)	Ionic Radius ⁹⁴ (Å)	Σ_{M-N}^{93} (Å)	CSD ⁹¹ d_{M-N} Average (Å)	CSD ⁹¹ d_{M-N} Prevalent (Å)
V ^{II}	2.13	2.16	0.79	2.24	2.1	2.12
Cr ^{II}	1.99	2.00	0.73	2.1	2.04	2.02
Cr ^{III}	2.05	2.01	0.605	2.1	2.04	2.02
Mn ^{II}	1.94	1.94	0.67	2.1	1.97	1.96
Mn ^{III}	1.96	1.98	0.58	2.1	1.97	1.96
Fe ^{II}	1.95	1.94	0.61	2.03	1.98	1.98
Fe ^{III}	2.00	2.00	0.55	2.03	1.98	1.98
Ni ^{II}	1.97	1.97	0.69	1.95	2.1	2.1
Cu ^I	2.08	2.08	0.77	2.03	2.16	2.14
Cu ^{II}	2.11	2.22	0.73	2.03	2.16	2.14
Mo ^{II}	2.24	2.26	NR	2.25	2.116	2.1
Ru ^{II}	2.08	2.08	NR	2.17	2.06	2.06
Ru ^{III}	2.07	2.08	NR	2.17	2.06	2.06
Re ^{II}	2.11	2.11	NR	2.22	2.02	2.02
Pt ^{II}	2.07	2.03	0.80	2.07	2.06	2.06

Each d_{M-N} was compared with the respective ionic radii of the metal centers.⁹⁴ The nitrogen contribution to d_{M-N} was assumed to be consistent across the series of metal centers, simplifying the analysis, and the relationship between the d_{M-N} for the metallacycles and the ionic radius of each metal was expected to be proportional. Progressing across the transition metal period, the d_{M-N} values correlate to the ionic contraction of the transition metal radii, Table 8. Also, the d_{M-N} values appropriately increase upon descending the group from Ni^{II} to Pt^{II} .⁹³⁻⁹⁴ However, for each pair of M^n/M^{n+1} modeled by the semi-empirical methods which includes $Cr^{II,III}$, $Mn^{II,III}$, $Fe^{II,III}$ and $Cu^{I,II}$, the more highly oxidized metal center, M^{n+1} , has a larger d_{M-N} than the more reduced counterpart, M^n . This is in direct opposition to the trend of decreasing ionic radius upon oxidation. This oxidation state inconsistency may be a result of the PM6 parameterization of oxidation states and must be considered upon qualitative evaluation of the templating anions.

The predicted d_{M-N} values were also compared to the sum of the covalent radii (Σ_{M-N}) of each respective metal and nitrogen, Table 8 and Figure 26. The reported covalent radii were derived from the evaluation of many published crystallographic structures.⁹³ The predicted d_{M-N} values closely correspond to the Σ_{M-N} values for Fe^{III} , Ni^{II} , Mo^{II} and Pt^{II} with an average deviation of 0.02 Å. For the remainder of the structures, the difference between the d_{M-N} and Σ_{M-N} values is less than 0.2 Å and is approximately the difference expected upon changing the oxidation state or spin state of the metal center. The predicted structures likely adopt an electronic configuration or oxidation state that is not the most prevalent state for the structures from which the Σ_{M-N} values were calculated.

To further refine the evaluation of the most likely d_{M-N} values for the series of transition metals in an octahedral coordination environment, a systematic analysis of structures in the Cambridge Structural Database (CSD)⁹¹ was performed in collaboration with Dr. Silvia Gómez-Coca in the Dunbar group. The octahedral, all nitrogen-donor complexes were identified for each transition metal, and the d_{M-N} values were tabulated from each structure per transition metal. From these data, the average d_{M-N} was calculated, CSD d_{M-N} Average, and the most prevalent d_{M-N} values were identified, CSD d_{M-N} Prevalent. The CSD d_{M-N} Average and Prevalent distances were also compared to the d_{M-N} for the predicted metallacyclic structures (Table 8 and Figure 26). For all of the metal centers except the Ni^{II}, Cu^I, Cu^{II} pentagons and Re^{II}, the CSD d_{M-N} Average is reproduced by the metallacycles within 0.05 Å and the most prevalent CSD d_{M-N} is reproduced even more accurately, with an average discrepancy of 0.02 Å.

For each of the modeled metallacycles, the predicted d_{M-N} reproduces the Σ_{M-N} , CSD d_{M-N} average or CSD d_{M-N} Prevalent within 0.09 Å, with an average discrepancy of only 0.03 Å. The predicted square metallacycle d_{M-N} values demonstrate a higher degree of proportionality to the Σ_{M-N} , CSD d_{M-N} average or CSD d_{M-N} Prevalent d_{M-N} values than do the pentagonal metallacycle d_{M-N} values, Table 8 and Figure 26. These differences result from the increased steric strain associated with forming the pentagonal architectures. Using this empirical method of analysis, the predictive, semi-empirical metallacycle model accurately models the transition metal contributions to the metallacyclic frameworks.

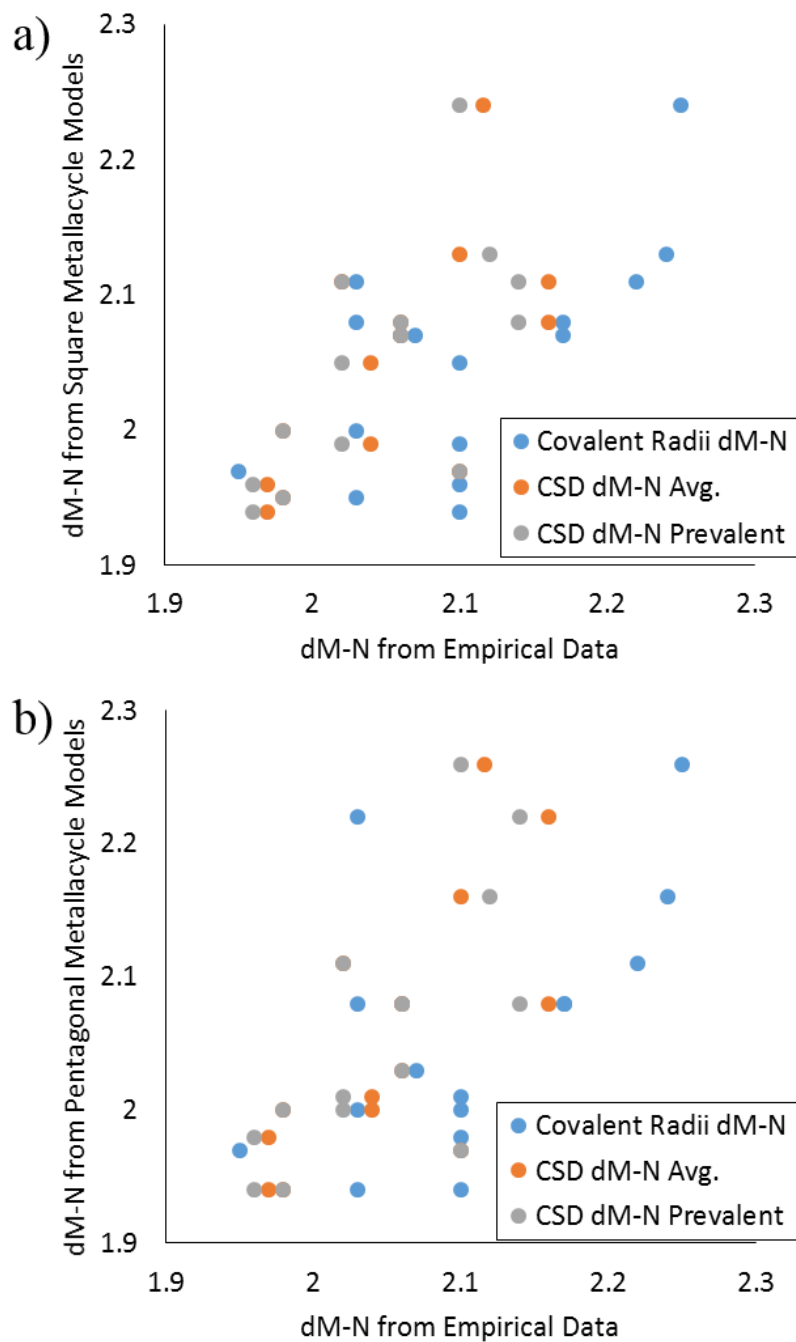


Figure 26. Comparison of the empirically derived d_{M-N} for each metal center and the predicted d_{M-N} values for a) the predicted square metallacycles and b) the predicted pentagonal metallacycles.

Analysis of the Semi-Empirical Treatment of Polyatomic Anions

The semi-empirical treatment of the proposed templating anions was also explored in order to evaluate the integrity of the predictive metallacycle model. In collaboration with Dr. Silvia Gómez-Coca, a systematic analysis of the structure of each anion in the Cambridge Structural Database (CSD)⁹¹ was performed. The tetrahedral and octahedral anions were identified, and the structures with anions coordinated to transition metals or part of a larger polynuclear structure were discounted. The average bond distance was tabulated for the remaining structures and plotted against the NDDO/PM6⁴⁶⁻⁴⁷ modeled bond distance, Figure 27. The empirical V-O bond distance for $[\text{VO}_4]^{3-}$ was not able to be reported as all of the structures were discounted as coordination compounds, polymeric or polynuclear structures. The semi-empirical treatment of the anions yielded bond distances that strongly correlate to the empirically derived bond distances, with an average $d_{\text{M-N}}$ error of 0.088 Å. The larger anions demonstrate a greater discrepancy from the CSD derived bond distances than the smaller, more prevalent anions.

Each anion was also optimized at the *ab initio* MP2/def2-TZVP level of theory⁴⁴ in Gaussian 09. Due to the atomic size restrictions of the def2-TZVP basis set, anions were restricted to those composed of atoms with atomic numbers less than Kr ($Z=36$).^{44d, 44e} The CSD average bond distance was compared to the *ab initio* optimized templating anions, Figure 27. The bond distances are strongly correlated, with an average error of 0.073 Å. As observed with the semi-empirical data, the smaller anions are very well described by the *ab initio* methods but the error increases as the bond distance increases.

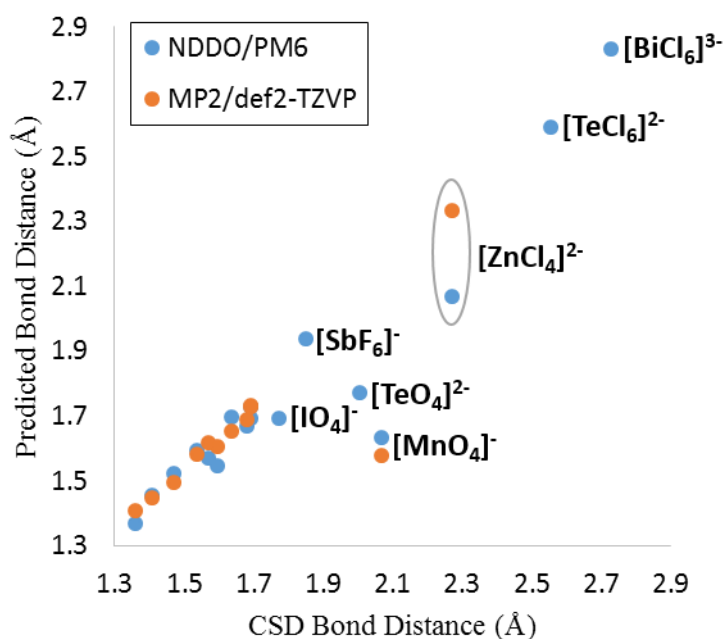


Figure 27. Comparison of the CSD Average bond distances with the semi-empirical and *ab initio* modeled bond distances for each anion.

In comparison to the CSD derived average anion bond distances, both the semi-empirical and *ab initio* methods incorrectly modeled [MnO₄]⁻, deviating from the CSD average distance by 0.434 Å and 0.487 Å, respectively. This deviation from the empirically derived bond distances must be considered when identifying ideal anion templates. Additionally, the semi-empirical methods also inaccurately modeled the [ZnCl₄]²⁻ anion bond distance by 0.201 Å. This may be a result of the parameters implied for transition metals in the semi-empirical methods. Overall, the *ab initio* and the semi-empirical methods result in accurate bond distances for most of the anions described. The

average difference between the bond distances modeled with semi-empirical and *ab initio* methods is 0.062 Å.

In addition to the anion size, the relative ability of each proposed templating anion to participate in anion- π interactions is critical for identifying stable metallacycles. Previous computational studies by the Dunbar group have focused on the favorable interactions of [BF₄]⁻ and [PF₆]⁻ with several N-heteraromatic molecules.^{31, 70, 95} The studies explored the impact of the symmetry of the substituents on the orientation of the anion above the aromatic group, and concluded that anion- π interactions are directional, additive and cooperative.^{31a, 70, 95} Such factors underscore the stabilizing role of the anion template(s) and series of anion- π interactions within each metallacycle cavity. The series of proposed FO templating anions was evaluated in complexes with difluorotetrazine, at close-contact distances, to determine the ability of each anion to participate in anion- π interactions. The FO anion was optimized over the face of the FO difluorotetrazine ring, and the BSSE corrected interaction energies were measured for each partially optimized complex, Table 9. BSSE describes the error that occurs when the basis sets of individual atoms overlap and get mixed during theoretical analyses, and this type of error is quantified and corrected by using the counterpoise method.⁸⁷ As can be seen in Table 9, the degree of BSSE scales according to the magnitude of the interaction energy between the two monomers. The optimized close-contacts of each anion- π complex were also measured between the terminal atoms of the anion and the closest atom or bond of the difluorotetrazine molecule, d_{X-Y} in Table 9.

Table 9. MP2/def2-TZVP⁴⁴ calculated BSSE corrected complexation energy, BSSE error, interaction type, sum of the van der Waals radii for d_{X-Y} and the close-contact d_{X-Y} between each anion and difluorotetrazine. NC = No Contact.

Anion	BSSE Corr. Complex. Energy (kcal/mol)	BSSE (kcal/mol)	Interaction Type(s)	Σ_{vdw} of d_{X-Y} (Å)	Close- Contact d_{X-Y} (Å)
[BrO ₄] ⁻	-13.54	2.40	Anion- π	3.27	2.72
[BF ₄] ⁻	-13.56	2.00	Anion- π	3.23	2.65
[ClO ₄] ⁻	-14.06	2.24	Anion- π	3.27	2.70
[ZnCl ₄] ²⁻	-17.45	3.19	Anion- π	3.59	3.08
[SeO ₄] ²⁻	-31.74	5.67	Anion- π	3.27	2.45
[SO ₄] ²⁻	-34.36	5.62	Anion- π	3.27	2.43
[VO ₄] ³⁻	-48.39	10.88	Anion- π	3.27	2.80
[CrO ₄] ²⁻	-51.06	7.85	Donor/Acceptor	3.27	2.12
[MnO ₄] ⁻	-54.95	5.22	Donor/Acceptor	3.27	2.13
[AsO ₄] ³⁻	-89.27	16.86	Meisenheimer	3.16	2.00
[PO ₄] ³⁻	NC	NC	NC	NC	NC
[AsF ₆] ⁻	-10.75	2.11	Anion- π	3.23	2.71
[PF ₆] ⁻	-11.2	2.01	Anion- π	3.23	2.72

The tetrahedral anions [BF₄]⁻ and [ClO₄]⁻ have been shown experimentally to be suitable templating anions for square metallacycles with divalent Fe,^{31b} Ni,^{36a} Co^{31a} and Zn^{36c} vertices, and the anion- π interaction between [BF₄]⁻ and difluorotetrazine was previously calculated to be -12.3 kcal/mol at the B3LYP/6-31+g(d) level of theory.^{31b} Accordingly, similar favorable anion- π interactions for [BF₄]⁻ and [ClO₄]⁻ with difluorotetrazine were calculated at the MP2/def2-TZVP level of theory⁴⁴ to be -13.56 and

-14.06 kcal/mol, respectively, (Table 9) and exemplified by the anion- π complex in Figure 28. As expected for anion- π complexes, the close-contact distances (d_{X-Y}) between the terminal atoms of $[\text{BF}_4]^-$ and $[\text{ClO}_4]^-$ and the carbon atoms of difluorotetrazine are well within the sum of the van der Waals radii. The d_{X-Y} between $[\text{BF}_4]^-$ and the closest carbon atom on the tetrazine ring was 2.65 Å, which is less than the Σ_{vdW} by 0.58. For $[\text{ClO}_4]^-$, the d_{X-Y} was 2.70 Å, which is 0.57 Å less than the Σ_{vdW} . In addition to those metallacycles previously characterized, the $[\text{BF}_4]^-$ anion has been predicted to template metallacycles for Cr^{II} , Pt^{II} and possibly Rh^{III} . The $[\text{ClO}_4]^-$ anion has been predicted to template metallacycles for V^{II} , Cr^{II} , Ru^{II} , Ru^{III} , Re^{II} and Pt^{II} .

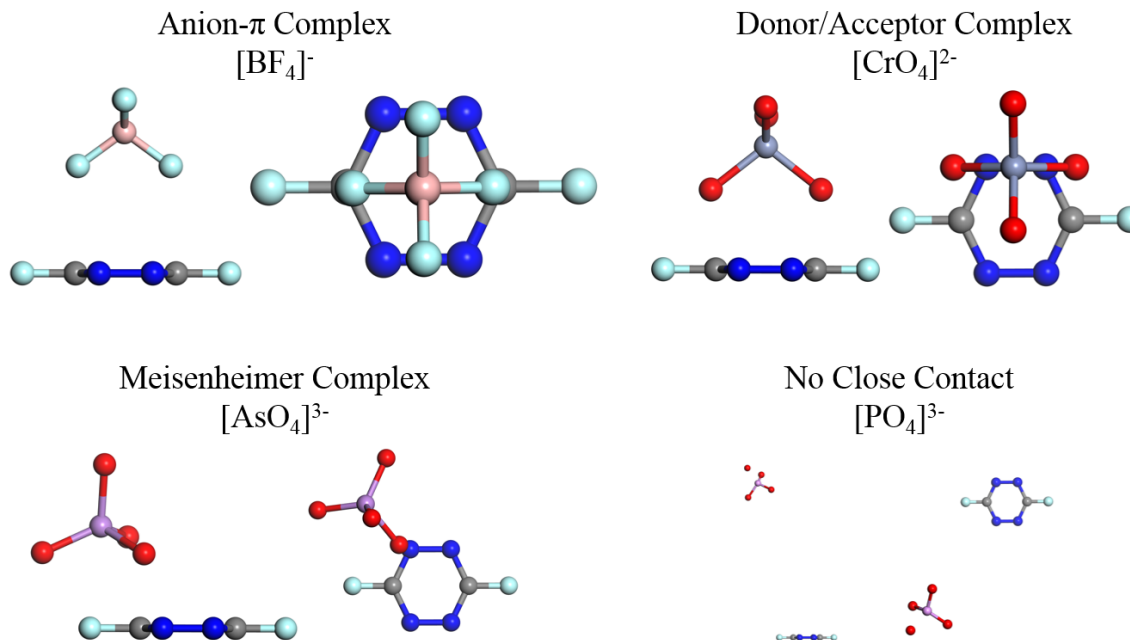


Figure 28. Representative types of complexes formed between the tetrahedral anions and difluorotetrazine. Graphical display generated by the Materials Studio Visualizer.¹⁴

The other tetrahedral anions that remain in close contact over the face of the difluorotetrazine molecule and which participate in anion- π interactions upon optimization include $[\text{BrO}_4]^-$, $[\text{ZnCl}_4]^{2-}$, $[\text{SeO}_4]^{2-}$, $[\text{SO}_4]^{2-}$ and $[\text{VO}_4]^{3-}$. The interactions of these anions over the face of difluorotetrazine are quite similar to the anion- π interaction exemplified by $[\text{BF}_4]^-$ in Figure 28. Furthermore, the ability of all of the proposed oxo-anions to coordinate to transition metals is greater than that of $[\text{BF}_4]^-$ and other fluoro-anions. Upon an in-depth evaluation of complexes within the CSD, Alvarez and coworkers identified the ability and likelihood of anions to coordinate to transition metals and to lanthanides. The ability and propensity of oxo-anions to coordinate to transition metals increases from $[\text{ClO}_4]^- < [\text{SO}_4]^{2-} < [\text{PO}_4]^{3-}$ and must remain a consideration during the remaining anion discussion.⁹⁶

The interactions of $[\text{BrO}_4]^-$ and $[\text{ZnCl}_4]^{2-}$ with difluorotetrazine are similar in magnitude to those of $[\text{BF}_4]^-$ and $[\text{ClO}_4]^-$. The close $d_{\text{X-Y}}$ for $[\text{BrO}_4]^-$ is also comparable to that of $[\text{ClO}_4]^-$, 2.72 Å, and, as seen from the plot in Figure 23, $[\text{BrO}_4]^-$ is a suitable anion for templating square metallacycles for V^{II} , Cr^{III} , Fe^{III} , Cu^{III} , Ru^{II} , Ru^{III} , Re^{II} and Pt^{II} . The $d_{\text{X-Y}}$ of $[\text{ZnCl}_4]^{2-}$, 3.08 Å, is significantly longer than those of the other tetrahedral anions due to the larger, more diffuse terminal chloride atoms. The $[\text{ZnCl}_4]^{2-}$ dianion is too large to participate in ideal contacts with the difluorotetrazine ring and the anion- π interaction is considerably weaker than the other dianion complexes, with an interaction energy of -17.45 kcal/mol and a contact distance only 0.51 less than the Σ_{vdW} , Table 9. As demonstrated by Figure 23, the $[\text{ZnCl}_4]^{2-}$ anion is too large to template square

metallacycles with any of the metal centers currently proposed, but this anion may be interesting for templating metallacycles with higher nuclearities.

The dianions $[\text{SO}_4]^{2-}$ and $[\text{SeO}_4]^{2-}$ participate in relatively strong anion- π interactions, greater than -30 kcal/mol, which is over twice as strong as the anion- π interaction energies involving $[\text{BF}_4]^-$ and $[\text{ClO}_4]^-$. This increase in strength is accompanied by a significantly shorter $d_{\text{X-Y}}$ values of 2.43 Å and 2.45 Å, less than the respective Σ_{vdw} by more than 0.82 Å, Table 9. The stronger interaction energies are likely due to the increased anionic charges and polarizability of the anions. The $[\text{SO}_4]^{2-}$ dianion is predicted to template metallacycles with vertices including V^{II} , Mn^{III} , Fe^{III} , Ru^{II} , Ru^{III} , Re^{II} and Pt^{II} . The $[\text{SeO}_4]^{2-}$ dianion is predicted to template metallacycles with vertices including V^{II} , Cr^{III} , Fe^{III} , Cu^{II} , Mo^{II} , Ru^{II} , Ru^{III} , Re^{II} and Pt^{II} .

The trianionic $[\text{VO}_4]^{3-}$ participates in the strongest interactions with difluorotetrazine of the tetrahedral anions, -48.39 kcal/mol; this value is greater than three times the strength of the interactions with $[\text{BF}_4]^-$ and $[\text{ClO}_4]^-$. It is interesting to note that the close-contact $d_{\text{X-Y}}$ for this complex is 2.80 Å, comparable to that of $[\text{ClO}_4]^-$. A search of the CSD, however, revealed that there are no complexes where $[\text{VO}_4]^{3-}$ is a discrete anion. Each instance of $[\text{VO}_4]^{3-}$ involves a coordination complex, a polynuclear structure or a polymer. While $[\text{VO}_4]^{3-}$ is predicted to demonstrate ideal overlap with several metallacycle cages, the anion is not expected to remain an innocent anion.

For the remainder of the tetrahedral anions, the increase in anionic charge was hypothesized to increase the strength of the anion- π interaction, and, while the interaction energies do increase in strength, the remaining anion-difluorotetrazine complexes

preferentially participate in anion- π interactions with more covalent character (i.e. anion-donor/ π -acceptor and σ -type Meisenheimer complexes). Several anions interact with difluorotetrazine through very strong and very short anion-donor/ π -acceptor interactions ($[\text{CrO}_4]^{2-}$, $[\text{MnO}_4]^{2-}$) and σ -type Meisenheimer complex interactions ($[\text{AsO}_4]^{3-}$), Table 9. Conversely, the $[\text{PO}_4]^{3-}$ anion was repelled by the difluorotetrazine molecule and did not participate in any close interaction with the π -system, Figure 28. While interactions of $[\text{CrO}_4]^{2-}$, $[\text{MnO}_4]^{2-}$ and $[\text{AsO}_4]^{3-}$ with bmtz or bptz may be mediated in solution to include anion- π interactions, the magnitude of the theoretical anion-donor/ π -acceptor and Meisenheimer interactions would likely preclude anion-templated metallacycle formation.

The $[\text{IO}_4]^-$ and $[\text{TeO}_4]^{2-}$ anions are composed of atoms that are too large to be evaluated by the def2-TZVP basis set,^{44d, 44e} but these large anions are expected to template metallacycles for V^{II} , Cr^{III} , Cu^{II} , Mo^{II} , Ru^{II} , Ru^{III} and Re^{II} .

The two most ideal octahedral anions evaluated by MP2/def2-TZVP methods⁴⁴ are $[\text{PF}_6]^-$ and $[\text{AsF}_6]^-$. These two anions have previously been reported previously to template Fe^{II} metallacycles in solution,^{36d} and the theoretical interaction of $[\text{PF}_6]^-$ with difluorotetrazine was reported as -9.6 kcal/mol at the B3LYP/6-31+g(d) level of theory.^{31b} Accordingly, the MP2/def2-TZVP⁴⁴ interaction energies of $[\text{PF}_6]^-$ and $[\text{AsF}_6]^-$ with difluorotetrazine were calculated to be -11.2 kcal/mol and -10.75 kcal/mol, respectively. The octahedral anions participate in ideal close anion- π contacts with difluorotetrazine, with $d_{\text{X-Y}}$ values of 2.71 Å and 2.73 Å, as described by Table 9 and exemplified in Figure 29. The interaction energies of $[\text{PF}_6]^-$ and $[\text{AsF}_6]^-$ are weaker than the interaction energy of $[\text{BF}_4]^-$ by approximately 2 - 3 kcal/mol and the $d_{\text{X-Y}}$ values for the octahedral anions are

proportionally longer than for the tetrahedral anions as well, by 0.06 – 0.07 Å, Table 9. While both octahedral anions are favorable for anion- π interactions, only $[\text{AsF}_6]^-$ is sufficiently large to template metallacycles, exclusively those with Fe^{II} and possibly Mn^{II} vertices, Figure 25.

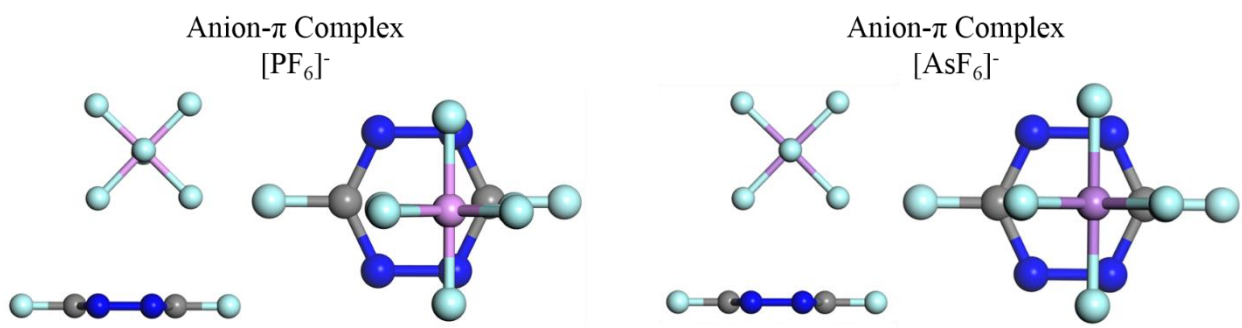


Figure 29. Representative types of complexes formed between the octahedral anions and difluorotetrazine. Graphical display generated by the Materials Studio Visualizer.¹⁴

Several octahedral anions were too large to be evaluated by the all-electron basis set, these include $[\text{SbF}_6]^-$, $[\text{BiCl}_6]^{3-}$ and $[\text{TeCl}_6]^{2-}$. Of the nine pentagonal metallacycles predicted to have ideal overlap, seven are templated by $[\text{SbF}_6]^-$. $[\text{SbF}_6]^-$ has been shown to be an ideal templation anion for Fe^{II} and Ni^{II} metallacycles, and NMR suggests that $[\text{SbF}_6]^-$ is bound in the pentagonal cavity slightly more weakly than $[\text{AsF}_6]^-$. Additionally, the facile dimerization of the $[\text{BiCl}_6]^{3-}$ anion and the prevalent coordination chemistry and redox activity of the $[\text{TeCl}_6]^{2-}$ anion would likely impede the templation of discrete pentagonal or hexagonal structures with larger metal vertices.⁹⁷

Identification of the most promising metallacyclic predictions

Upon careful consideration of the semi-empirical treatment of the metal centers and the propensities of each anion to participate in anion- π interactions, the predicted series of metallacycles with ideal anion-cavity compatibility was further clarified. Anions that do not participate in the more ideal, approximately η^6 anion- π interactions were removed for the sake of clarity and the ability of oxo-anions to bind to transition metals has also been highlighted.⁹⁶ Many stable square metallacyclic structures are predicted, spanning all of the proposed transition metal centers and include the anions $[\text{BF}_4]^-$, $[\text{ClO}_4]^-$, $[\text{SO}_4]^{2-}$, $[\text{BrO}_4]^-$, $[\text{IO}_4]^-$, $[\text{SeO}_4]^{2-}$ and $[\text{TeO}_4]^{2-}$, Figure 30.

From the possible pentagonal metallacycles, there were only eight metallacycles that demonstrate ideal overlap with each bridging ligand. The possible structures involve Cr^{II} , Mn^{II} , Mn^{III} , Fe^{II} , Ni^{II} , Cu^{I} and Ru^{II} vertices and $[\text{AsF}_6]^-$ and $[\text{SbF}_6]^-$, Figure 31.

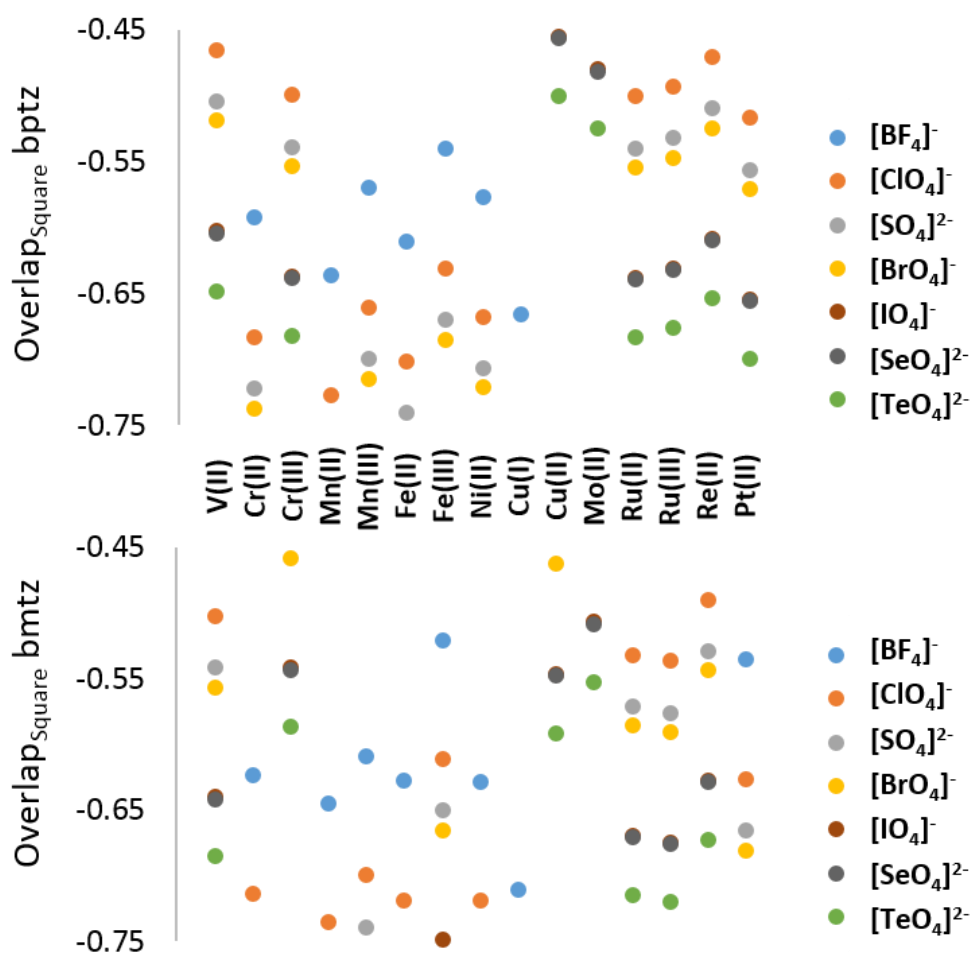


Figure 30. Ideal anion-cavity compatibility for tetrahedral anions that participate in anion- π interactions.

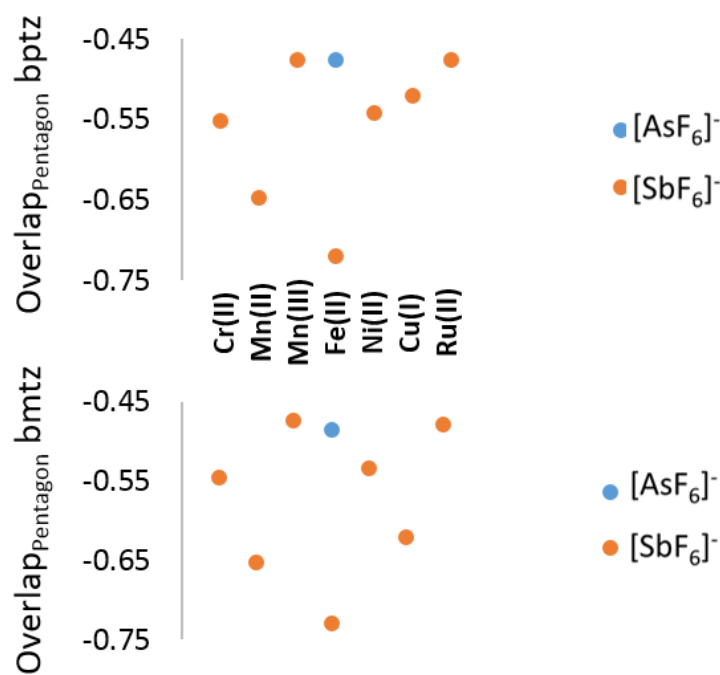


Figure 31. Ideal anion-cavity compatibility for octahedral anions that participate in anion- π interactions.

Conclusions and Future Outlook

In the field of supramolecular coordination-driven self-assembly, the Dunbar group has characterized a library of anion-templated metallacycles with transition metal vertices spanning several of the first row transition metals.^{31, 36} The anion templates stabilize the supramolecular architectures through anion- π interactions with the bptz or bmtz bridging ligands. Synthetic efforts described in this chapter were aimed at developing various bptz- and bmtz-bridged metallacycles with different templating anions and transition metal vertices. The unsuccessful synthetic efforts, many of which are not described herein, motivated me to develop a predictive, semi-empirical approach for

identifying supramolecular metallacycles with ideal anion- π overlap for further experimental study.

The semi-empirical NDDO/PM6 level of theory⁴⁶⁻⁴⁷ was used within the VAMP⁸³ module of Materials Studio 7.0¹⁴ to reproduce the Fe^{II}-metallacycles, **1** – **3**, with very high accuracy. Models **1A, B** and **3A, B** were used as templates to reproduce **2, 4 – 7**, and the resulting model structures with Fe^{II} and Ni^{II} vertices demonstrated very high accuracy, with average d_{M-M} errors of 0.078 Å and 0.054 Å for Model A and B structures respectively. The improper semi-empirical parameters for Co^{II} and Zn^{II} prevented accurate optimizations of the metallacycles. Model structures **1B** and **3B** were adapted as bptz- and bmtz-bridged templates to predict the square and pentagonal metallacyclic structures for fifteen transition metals. Thirteen tetrahedral and five octahedral anions were also optimized. Geometrical analyses of the resulting templating anions and metallacyclic cavities were performed, and compatibility of the anion-metallacycles combinations was evaluated against the ideal anion-cavity overlap of **1-7**.

The semi-empirical treatment of the metal centers and anions were further evaluated. The representative d_{M-N} distance for the predicted structures for each transition metal was compared to the ionic radius and a series of empirically-derived d_{M-N} values for each metal center. The d_{M-N} for each transition metal successfully reproduced one of the empirically-derived d_{M-N} values to within 0.03 Å on average. Future computational efforts may further narrow the field of ideal transition metal candidates by evaluating the flexibility of coordination available for transition metal.

The bond distances of the NDDO/PM6⁴⁶⁻⁴⁷ optimized anions were compared to the MP2/def2-TZVP⁴⁴ optimized anion and the respective empirically-derived average bond lengths. The anions optimized at the semi-empirical and *ab initio* levels of theory were highly similar, average discrepancy of 0.062 Å, and accurately reproduced the empirical data, with average bond length errors of 0.088 Å and 0.072 Å, respectively. The propensity of each anion to participate in anion- π interactions was also evaluated in complexes with difluorotetrazine. The tetrahedral anions that participate in ideal anion- π interactions include [BF₄]⁻, [ClO₄]⁻, [SO₄]²⁻, [BrO₄]⁻, [IO₄]⁻, [SeO₄]²⁻, [VO₄]³⁻ and [TeO₄]²⁻. The octahedral anions [PF₆]⁻ and [AsF₆]⁻ also participate in ideal anion- π interactions with difluorotetrazine. The anions with heavy atoms, including [IO₄]⁻, [TeO₄]²⁻, [SbF₆]⁻, [BiCl₆]³⁻ and [TeCl₆]²⁻, were not able to be evaluated at the MP2/def2-TZVP level of theory,⁴⁴ but future studies may be able to determine the relative strength of these anions in complexes by modifying the basis set or utilizing the appropriate effective core potentials for the heavy atoms.

By combining empirical data and the *ab initio* analyses with the predictive semi-empirical model, the library of ideal, proposed metallacycles was narrowed down considerably, and the most sterically and energetically favorable metallacycles were identified (Figure 30 and Figure 31). Future experimental efforts will benefit from focusing on metallacycles with ideal anion-cavity compatibility identified by this predictive model.

CHAPTER III
A THEORETICAL EVALUATION OF THE HIERARCHY OF FACTORS
DIRECTING AG(I) COORDINATION

Introduction

The diversity of structural motifs afforded by Ag^I coordination has been an active area of study for several decades.⁹⁸ A wealth of studies has established a wide library of architectures available between the soft Lewis acid, Ag^I, and the relatively soft Lewis bases, especially N-donor ligands.⁹⁹ The geometries of the resulting structures range from 2- to 6-coordinate and encompass many of the possible geometries for each mode of coordination.¹⁰⁰

Beginning in 1994, Lehn and coworkers explored the supramolecular coordination of Ag^I ions with a tris-bidentate oligopyridazine, leading to the self-assembly of a [3x3]-Ag^I₉ grid, Figure 32a.¹⁰¹ The bridging ligand was extended by two additional pyridazine moieties, and complexation of the oligopyridazine with Ag^I was expected to lead to a [5x5]-Ag^I₂₅ grid, Figure 32b.¹⁰² This reaction, however, resulted in two distinct alternative structures, a [4x5]-Ag^I₂₀ grid and a Ag^I₁₀ quadruple helicate that preferentially assemble at different temperatures, Figure 32.¹⁰² Lehn and coworkers therefore identified that there exists a delicate balance between the effects of non-covalent interactions, solvation and structural strain, among other energetic factors that can lead to unexpected architectures.¹⁰²

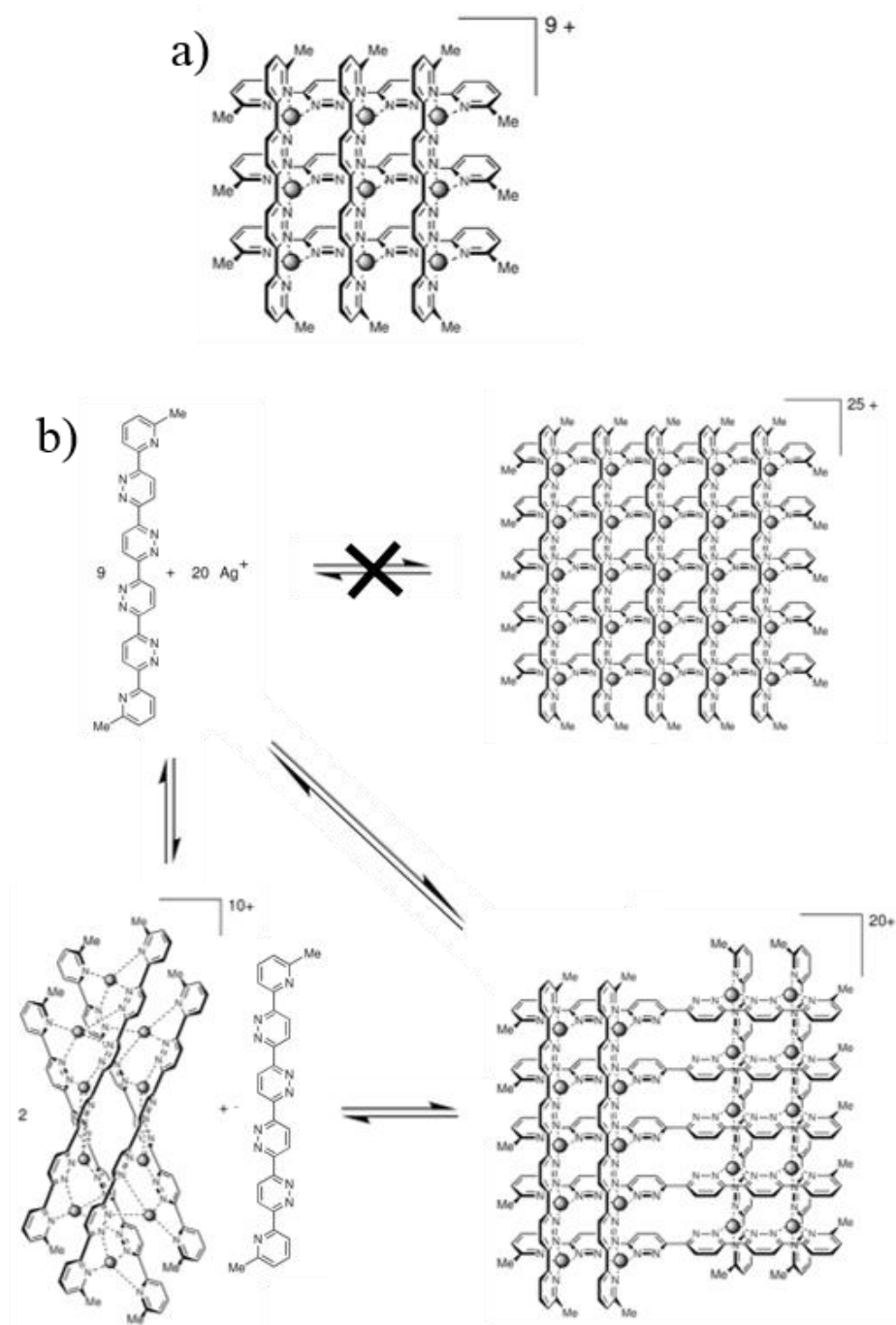


Figure 32. Supramolecular architectures reported by Lehn and coworkers. The architectures included a) a [3x3]-Ag^I₉ grid¹⁰¹ and b) a mixture of a [4x5]-Ag^I₂₀ grid and a Ag^I₁₀ quadruple helicate¹⁰² (which preclude the formation of the [5x5]-Ag^I₂₅ grid). Adapted with permission from Lehn and Coworkers.¹⁰² Adapted with permission from Lehn and coworkers.¹⁰² Copyright 2000 WILEY-VCH GmbH & Co.

The goal of the research described in this chapter is to further develop the assessment made by Lehn and coworkers by disentangling the factors that govern supramolecular assembly reactions between Ag^{I} and the 3,6-bis(2'-pyridyl)pyridazine (bppn), 3,6-bis(2'-pyridyl)-1,2,4,5-tetrazine (bptz) and 3,6-bis(2'-pyrimidyl)-1,2,4,5-tetrazine (bmtz) ligands.^{75, 103} The ligands bppn, bptz and bmtz promote the assembly of several types of complexes according to the specific *syn*- and/or *anti*-conformations of each of the molecules.

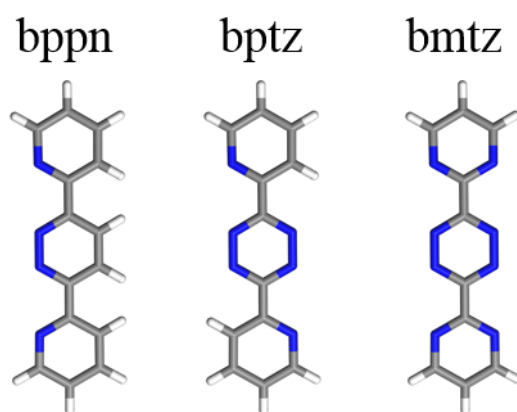


Figure 33. Structures of the 3,6-bis(2'-pyridyl)pyridazine (bppn), 3,6-bis(2'-pyridyl)-1,2,4,5-tetrazine (bptz) and 3,6-bis(2'-pyrimidyl)-1,2,4,5-tetrazine (bmtz) ligands. Atom colors correspond to N (blue), C (grey) and H (white). Graphical display generated by the Materials Studio Visualizer.¹⁴

Constable and coworkers first explored the supramolecular architectures available through Ag^{I} -bptz coordination.¹⁰⁴ These researchers characterized the nearly planar cation in $[\text{Ag}_2(\mu\text{-bptz})_2][\text{OTf}]_2$ and the polymeric structure $[\text{Ag}^{\text{I}}(\mu\text{-bptz})(\text{bptz})][\text{BF}_4]_{\infty}$, and concluded that the counter anion of the Ag^{I} salt contributes to the overall geometry of the

bptz coordination complex.¹⁰⁴⁻¹⁰⁵ A propeller-type Ag^I-bptz coordination complex was also characterized with the [OTf]⁻ anion upon modification of the reaction concentration.¹⁰⁵ This study led to the vague conclusion that the subtle factors governing the Ag^I coordination complexes must include more than just the choice in counter anion.

As a natural extension of the Dunbar group's research regarding anion-templation of metallacyclic structures, *vide supra* Chapter II, researchers in the group began to investigate the coordination chemistry of Ag^I with bppn and bptz ligands, with a specific focus on the symmetric polyatomic anions, including [BF₄]⁻, [PF₆]⁻, [AsF₆]⁻ and [SbF₆]⁻.^{37, 95} The resulting coordination geometries varied according to the identity of the anion as well as concentration of the reaction solution, corroborating the studies by Constable and coworkers. Electrostatic potential (ESP) maps were generated for each structure, and the presence, orientation and relative interaction of each anion and corresponding anion- π interactions were qualitatively evaluated, Figure 34. An increase in the π -acidity of the bridging ligands was identified according to the increased blue coloring of the ESP map, and the convolution of the blue coloration and orientation of the anion was associated with stronger anion- π interactions. Also, higher reaction concentrations favored the larger nuclearity structures, whereas more dilute reaction conditions produced the dinuclear complex [Ag₂(bptz)₂(MeCN)₂][PF₆]₂.

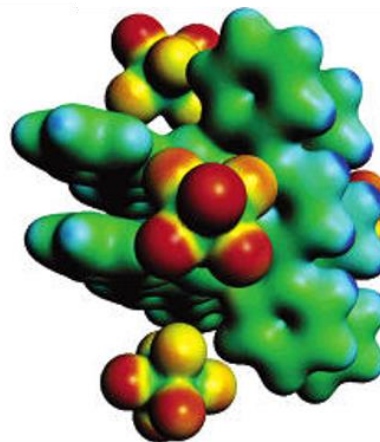
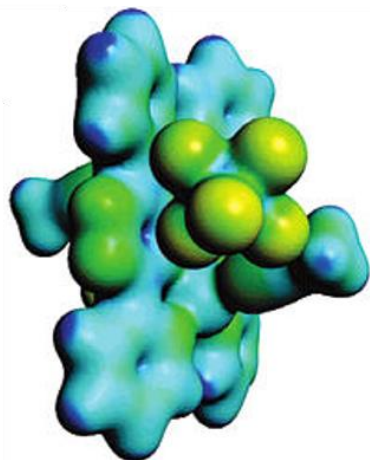
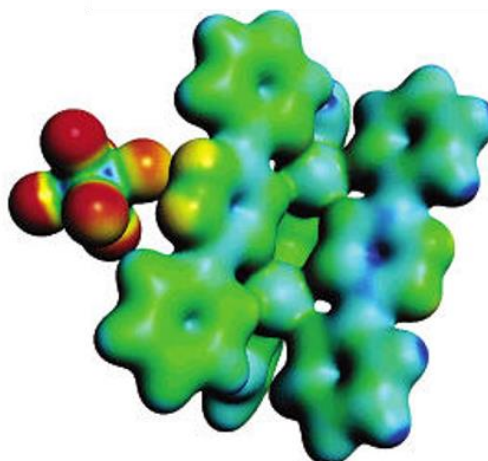
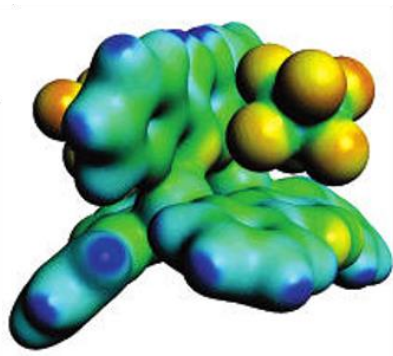
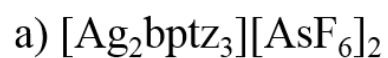


Figure 34. Electrostatic potential maps of single point energy calculations of several Ag^{I} coordination complexes.^{37b} Each map was generated at a 0.02 a.u. isodensity value and scaled accordingly (kcal/mol): a) 126 to -96, b) 188 to -31, c) 126 to -126, d) 157 to -63. The color scale varies according to each structure label from the blue (positive) to red (negative). Adapted from Dunbar and coworkers.^{37b}

Preliminary studies by Toby Woods, a current member of the Dunbar group, have resulted in the characterization of the $[\text{Ag}_4(\mu\text{-bmtz})_3][(\text{BF}_4)_4]_\infty \cdot n\text{C}_6\text{H}_6$ extended coordination network. The Ag^{I} -bmtz coordination network is stabilized by several factors, including two anions and two benzene molecules that participate in anion- π and π - π interactions, respectively, in each pore and a layer of anions positioned between the planes of the extended network that participate in H-bonding interactions with the bmtz ligands. The complex only forms upon precipitation with benzene and, upon dissolution in acetonitrile, the supramolecular system disassembles into the Ag^{I} salt and free bmtz, as observed by preliminary ^1H NMR spectroscopy, mass spectrometry and electronic spectroscopy.

In recent years, work by researchers in the Batten^{99b} and Murugesu¹⁰⁶ groups have developed additional one-dimensional and two-dimensional polymeric Ag^{I} -bptz and Ag^{I} -bmtz architectures that differ significantly depending on the choice of bridging ligand and anion. The library of structures identified by the Constable, Dunbar, Batten and Murugesu groups underscore the fact that anions as well as the reaction conditions play an important role in determining the Ag^{I} -bptz architectures.^{37, 95} Therefore, armed with a series of Ag^{I} structures involving bppn, bptz and bmtz, the following study was undertaken to evaluate the hierarchy of factors that direct the supramolecular assembly of these compounds, including the metal ion, bridging ligand, anion, and solvent choice.

Theoretical Methods

Second order Mølller-Plesset perturbation theory (MP2)^{44a-c} calculations were first performed with the def2-TZVP^{44d, 44e} basis set in Gaussian 09, Revision E.01,⁸⁶ in order

to determine the interaction energies of two small model systems. The small model structure $[\text{BF}_4]^-$ with bmtz was isolated from the $[\text{Ag}_4(\mu\text{-bmtz})_3][(\text{BF}_4)_4] \cdot n\text{C}_6\text{H}_6$ crystal structure and was partially optimized (PO) by restraining the atomic coordinates of the non-hydrogen atoms and optimizing the atomic coordinates of the hydrogen atoms.

Single point (SP) energies of $[\text{BF}_4]^-$, bmtz, and the PO small model complex were calculated at the MP2/def2-TZVP level of theory⁴⁴. SP energies of $[\text{BF}_4]^-$, bmtz, and the PO small model complex were also calculated with each combination of the functionals, B3LYP,^{53, 107} BP86-D3,⁵³⁻⁵⁴ M06-2X,^{19b, 56, 108} and ω B97X-D,⁵⁰ and basis sets, 6-31+g(d,p)⁵² and def2-TZVP.^{44d, 44e} Interaction energies were obtained as a difference in energy between the final complex and the sum of the model active site parts, $\Delta E_{\text{F-I}}$. Additionally, the basis set superposition error (BSSE)-corrected interaction energies, ΔE_{BSSE} , were calculated using the counterpoise-corrected method.⁸⁷ By comparing the interaction energies obtained by the *ab initio* and DFT methods, the ω B97X-D/def2-TZVP^{44d, 44e, 50} level of theory was identified to best describe the Ag^{I} coordination system.

Each structure **12** – **17**, Table 10, was simplified to the corresponding model structures **12**_{Model} – **17**_{Model}, *vide infra*. Each model structure was PO using the ω B97X-D functional,⁵⁰ the def2-TZVP^{44d, 44e} basis set for the main group atoms and the Stuttgart/Dresden multi-electron non-relativistic effective core potentials (SDD^{MHF})^{51a} for Ag^{I} and Sb in Gaussian 09.⁸⁶ The PO calculations were performed by restraining the atomic coordinates of the non-hydrogen atoms and optimizing the atomic coordinates of the hydrogen atoms. SP energies of the PO model structures were calculated using the ω B97X-D/def2-TZVP/SDD^{HF} level of theory and adding the Douglas-Kroll-Hess second

order scalar relativistic term (DKH)^{51b} to account for the relativistic effects of the heavy atoms. SP energies of each component of the PO model structures were also calculated using the ω B97X-D/def2-TZVP/SDD^{HF}/DKH level of theory, including the π -system with Ag^I ions, the π -system without Ag^I ions, the anion(s) and the solvent molecule(s), as appropriate.

Table 10. Ag^I complexes, formulae, types of complexes and approximate models included in this study.

Complex	Structural Formula	Type	Model Formula
11^{37b}	[Ag ^I ₄ (μ -bppn) ₄][BF ₄] ₄ •3MeCN•1C ₆ H ₆	Discrete	[Ag ^I ₄ (μ -bptz) ₄][BF ₄] ₄ •3MeCN•1C ₆ H ₆
12¹⁰⁵	[Ag ^I (μ -bptz)(bptz)][BF ₄] _{∞}	1-D	[Ag ^I ₂ (μ -bptz) ₂ (bptz)][BF ₄] ₂
13	[Ag ₄ (μ -bmtz) ₃][(BF ₄) ₄] _{∞} • <i>n</i> C ₆ H ₆	2-D	[Ag ₂ (μ -bmtz) ₃][(BF ₄) ₂] •2C ₆ H ₆
14^{37b}	[Ag ^I (μ -bptz)][PF ₆] _{∞}	1-D	[Ag ^I ₂ (bptz) ₂ (pyridine) ₂][PF ₆] ₂
15^{37a}	[Ag ^I ₂ (μ -bptz) ₃][AsF ₆] ₂ •2MeCN	Discrete	[Ag ^I ₂ (μ -bptz) ₃][AsF ₆] ₂
16^{37b}	[Ag ^I ₂ (μ -bptz) ₃][SbF ₆] ₂	Discrete	[Ag ^I ₂ (μ -bptz) ₃][SbF ₆] ₂

From the SP energy calculations, interaction energies were obtained as a difference in energy between the final complex and the sum of the model active site parts. The interaction energy of the total complex including the ion-ion and ion-dipole contributions of the Ag^I ion, ΔE_{Ionic} , was calculated as Equation 9.

$$\Delta E_{Ionic} = E_{Final\ Complex\ w/Ag^I} - (E_{\pi\ w/Ag^I} + E_{Anion} + E_{Solvent}) \quad \text{Equation 9}$$

The interaction energy of the non-covalent interactions of the complex excluding the contributions of the Ag^I ion, ΔE_{N-C} , was calculated for the negatively charged complex according to Equation 10.

$$\Delta E_{N-C} = E_{Final\ Complex\ w/\emptyset\ Ag^I} - (E_{\pi\ w/\emptyset\ Ag^I} + E_{Anion} + E_{Solvent}) \quad \text{Equation 10}$$

All *ab initio* and DFT calculations were performed through Texas A&M University's High Performance Research center on a 3.088 core IBM "iDataplex" commodity cluster that includes 362 nodes of memory based on Intel's 64-bit Nehalem and Westmere processor.⁸⁸

Each crystal structure was imported into Materials Studio 7.0 suite, produced by Accelrys.¹⁴ The extra atoms generated by symmetry were removed, the hybridization of the N and C atoms was assigned as appropriate, and each unit cell was tiled to create a supercell with dimensions of between [2x2x2] and [6x6x6], depending on the size of the unit cell. For structure **13**, the benzene solvent molecules were modified to explore the role of the solvent molecules. Modified supercells of **13** were generated for toluene, nitrobenzene, *ortho*-xylene, *meta*-xylene and *para*-xylene. The superstructures were fully optimized (FO) using Molecular Mechanics Methods by applying the Universal Force Field (UFF)¹⁰⁹ within the Forcite module of Materials Studio 7.0.¹⁴ Graphical displays of the computational results were generated by the Materials Studio Visualizer.

Results and Discussion

Functional and Basis Set Determination

The interaction energy of the model complex $[\text{BF}_4]^-$ -bmtz (Figure 35) was evaluated at the *ab initio* MP2/def2-TZVP level of theory and compared to a series of DFT functionals, with either the def2-TZVP or 6-31+g(d,p) basis sets, to determine the appropriate DFT method to use for examining the non-covalent interactions present in the series of Ag^{I} complexes. The $\Delta E_{\text{F-I}}$ and the ΔE_{BSSE} interaction energies of the model complex were determined at each level of theory as identified in Table 11. There is considerable BSSE associated with the MP2/def2-TZVP interaction energy of the model complex, but the $\omega\text{B97X-D}$ functional reproduces the BSSE-corrected MP2/def2-TZVP interaction energy, with and without correcting for BSSE.

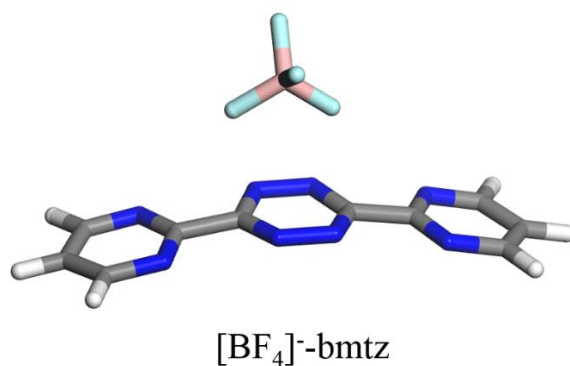


Figure 35. Model anion- π complex of [BF₄]⁻-bmtz. Atomic colors correspond to F (teal), B (pink), N (blue), C (grey) and H (white). Graphical display generated by the Materials Studio Visualizer.¹⁴

Table 11. Comparison of the interaction energy of [BF₄]⁻-bmtz calculated at the MP2/def2-TZVP level of theory and using eight DFT functional/basis set combinations.

Functional/Basis Set	ΔE_{F-I}	ΔE_{BSSE}
	[BF ₄] ⁻ -bmtz (kcal/mol)	[BF ₄] ⁻ -bmtz (kcal/mol)
MP2/def2-TZVP	2.69	-2.41
B3LYP/def2-TZVP	0.19	1.32
B3LYP/6-31+g(d,p)	0.65	1.6
BP86-D3/def2-TZVP	9.47	-2.95
BP86-D3/6-31+g(d,p)	-3.4	-2.47
M06-2X/def2-TZVP	-3.45	-2.69
M06-2X/6-31+g(d,p)	-3.75	-2.73
ω B97X-D/def2-TZVP	-3.17	-2.27
ω B97X-D /6-31+g(d,p)	-2.99	-2.03

The hybrid GGA functional ω B97X-D incorporates empirical dispersion and long-range exchange interaction corrections, critical for the extended systems, non-covalent interactions and long-range electrostatic interactions encompassed within the architectures of this study.⁵⁰ The triple zeta valence basis set with polarization (def2-TZVP) and the non-relativistic, multi-electron fit Stuttgart/Dresden effective core potentials (SDD^{MHF}) with the DKH keyword were used to describe the main group and heavy atoms, respectively, in the Ag^I systems. Using the ω B97X-D/def2-TZVP/SDD^{MHF}/DKH level of theory, several simplified Ag^I complex models were evaluated in order to determine the hierarchy of factors that direct the formation and symmetry of the architectures.

Role of the Coordinating Metal

The most important factor that promotes the variety of architectures in this study is the Ag^I ion. The d¹⁰ Ag^I configuration affords significant coordinative flexibility, such that structures characterized by the Dunbar group alone include tetrahedral, square planar, square pyramidal, octahedral, and trigonal prismatic coordination symmetries.^{37, 95} Furthermore, the softness and relatively large ionic radius of the Ag^I Lewis acid is suitable for coordination to soft Lewis base ligands, and the soft Lewis base ligands demonstrate a propensity for propagating extended structures through weak, non-covalent interactions.^{99c}

Consider the two polymers: [Ag₄(μ -bmtz)₃][(PF₆)₄]_∞ (**17**, characterized by Murgesu and coworkers¹⁰⁶) and [Na₂(μ -bmtz)][(PF₆)₂]_∞ (**8**, *vide supra* Chapter II), Figure 36. The structural formulas of **17** and **8** both contain bmtz bridging ligands and [PF₆]⁻ counter anions; however, the coordinating metal ion varies from Ag⁺ to Na⁺ and results in

significant differences in the symmetry and packing of the complex. The ionic radius of Ag^+ is approximately 13 pm larger than that of Na^+ ,⁹⁴ however, the average metal-nitrogen bond distance ($d_{\text{M-N}}$) for **17** is 2.513 Å and the $d_{\text{M-N}}$ for **8** is 2.541 Å, opposite to the trend of the ionic radii. Furthermore, the role of the $[\text{PF}_6]^-$ anion differs between **17** and **8**. In **17**, $[\text{PF}_6]^-$ non-covalently interacts with the tetrazine ring of the bmtz through anion- π interactions, but, in **8**, the $[\text{PF}_6]^-$ anion is ionically bound to the Na^+ ion. The difference in preferential binding of the anion results from the relative hardness and softness of the Lewis acids and the Lewis bases. In **17**, the softer Lewis acid, Ag^{I} , preferentially coordinates to the softer Lewis base, bmtz. In **8**, the harder Lewis acid, Na^+ , binds more closely to the harder Lewis base, $[\text{PF}_6]^-$ than to the softer Lewis base, bmtz, Figure 36. The binding differences between the Ag^{I} and Na^+ Lewis acids result in significant modifications to the overall architectures and orientations of non-covalent interactions.

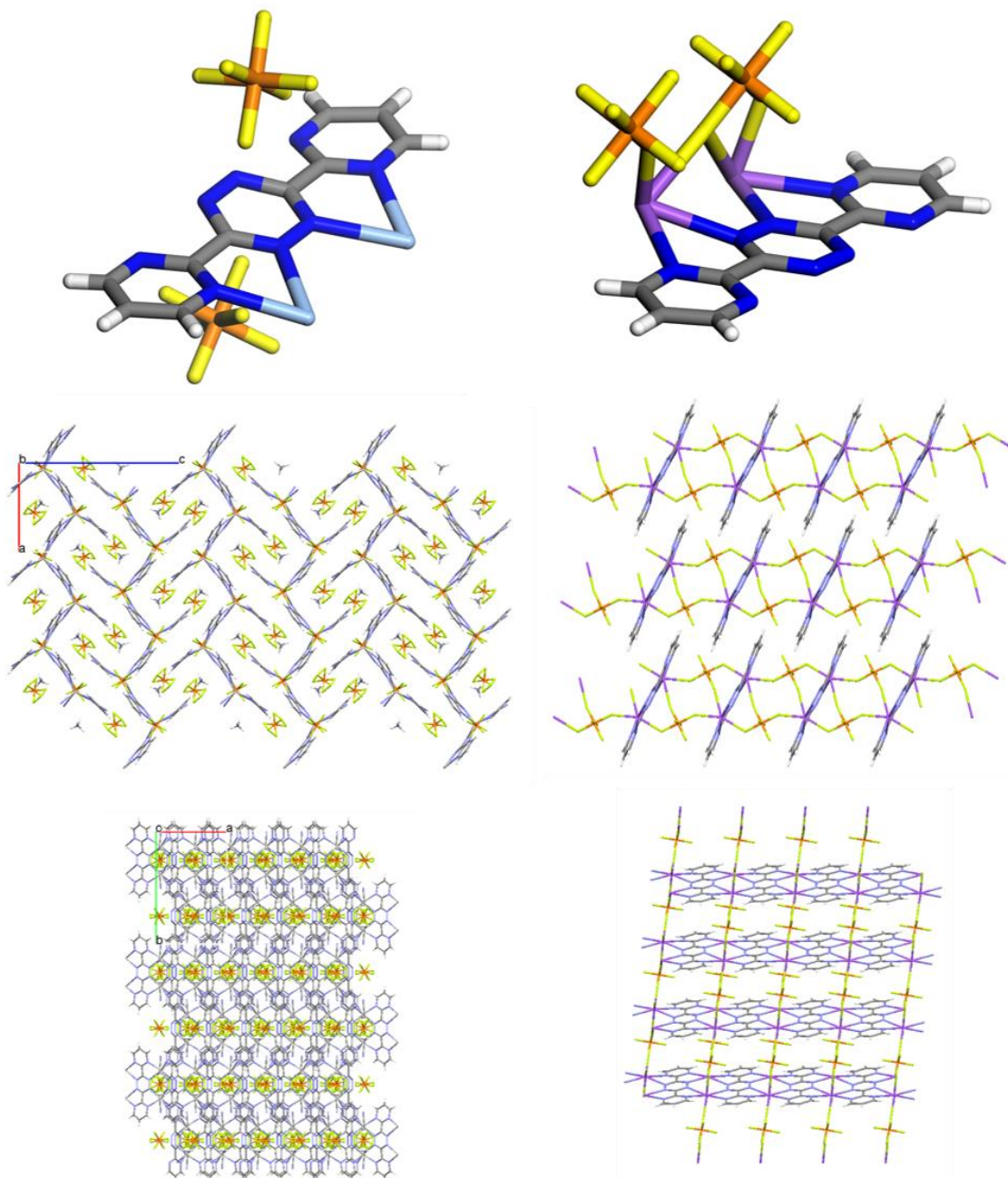
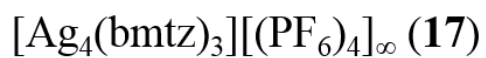


Figure 36. Asymmetric units and packing diagrams of $[\text{Ag}_4(\mu\text{-bmtz})_3][(\text{PF}_6)_4]_\infty$ (17) and $[\text{Na}_2(\mu\text{-bmtz})][(\text{PF}_6)_2]_\infty$ (8). Graphical display generated by the Mercury visualizer.⁹⁰

Role of the N-Heterocyclic Bridging Ligand

Energetic Contributions

Previous work by Dr. Brandi Schottel and Dr. Ian Giles, former members of the Dunbar group, led to qualitative evaluations of the π -acidity of a series of N-heterocyclic bridging ligands, Figure 37. These ESP maps visually depict the interaction that a positive point charge experiences at a specified distance from a molecule, and the interactions are a result of the balance between electron-electron and electron-nuclear interactions. As the number of N-heteroatoms on the rings increases, the “ π -acidity” proportionally increases and is represented by the increasing blue region of the ESP maps. The concept of “ π -acidity”, as used in this dissertation, does not refer to “electropositive” or “electron-deficient” π -orbitals but rather it is used to describe the propensity of a molecule to participate in anion- π interactions. These interactions occurs through charge-dipole electrostatic effects and the proximity of the N nuclear charges on N-heterocyclic structures, as described in detail in Chapter I.²⁴ The more π -acidic ligands are hypothesized to participate in stronger anion- π interactions, and, upon Ag^{I} complexation of N-heterocyclic bridging ligands in Figure 37, the ESP maps of the coordination complexes qualitatively demonstrate an increase in the anion- π interaction according to the π -acidity of the bridging ligands, Figure 34.

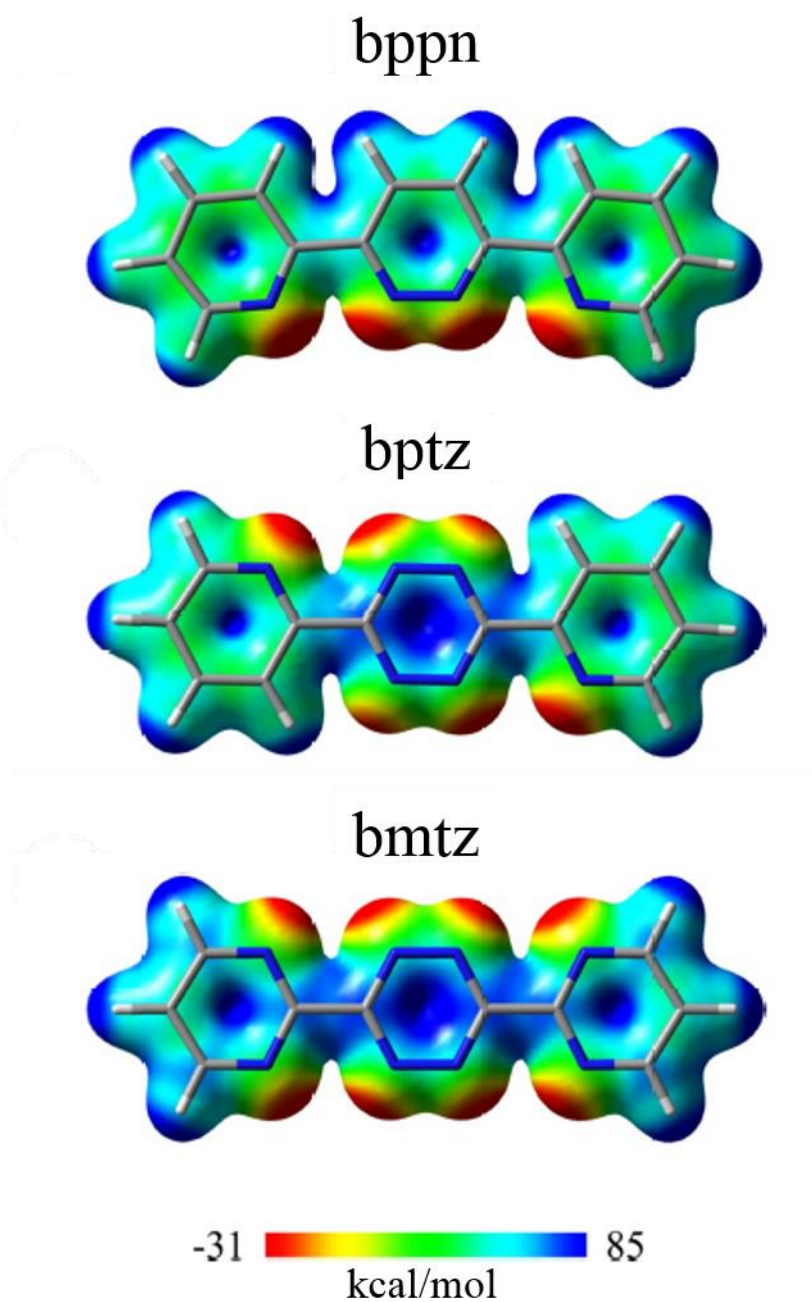


Figure 37. ESP maps of bridging ligands bppn, bptz, and bmtz. ESP maps generated at isodensity values of 0.02 a.u. from B3LYP/6-31+g(d,p) optimized ligand geometries. Atomic colors correspond to N (blue), C (grey) and H (white). Adapted from the dissertation of Dr. Ian Giles.³¹

In order to more quantitatively evaluate the relationship between π -acidity and the integration of the anion, the Ag^{I} complexes of bppn, bptz and bmtz with $[\text{BF}_4]^-$ anions were considered, Figure 38. The crystal structures were pared down to include the simplest coordinated portion of the structure that includes representative interactions of the anion and solvent with the framework, including anion- π and H-bonding interactions, Figure 38. The entire grid complex and solvent molecules in the unit cell of **11** were included in the model structure **11_{Model}**. The polymer in **12** was simplified to include three bptz ligands, two Ag^{I} ions and two $[\text{BF}_4]^-$ anions in the model structure **12_{Model}**. The simplified model did not include the close π - π interactions between intercalated bptz ligands but retained two anion- π interactions along one of the polymer backbones. The extended polymeric network characterized by the crystal structure of **13** was simplified to the propeller-like structure in **13_{Model}**, which includes representative anion- π and H-bonding interactions but does not include the additive, cross-cavity π -anion- π and π - π - π interactions, Figure 38.

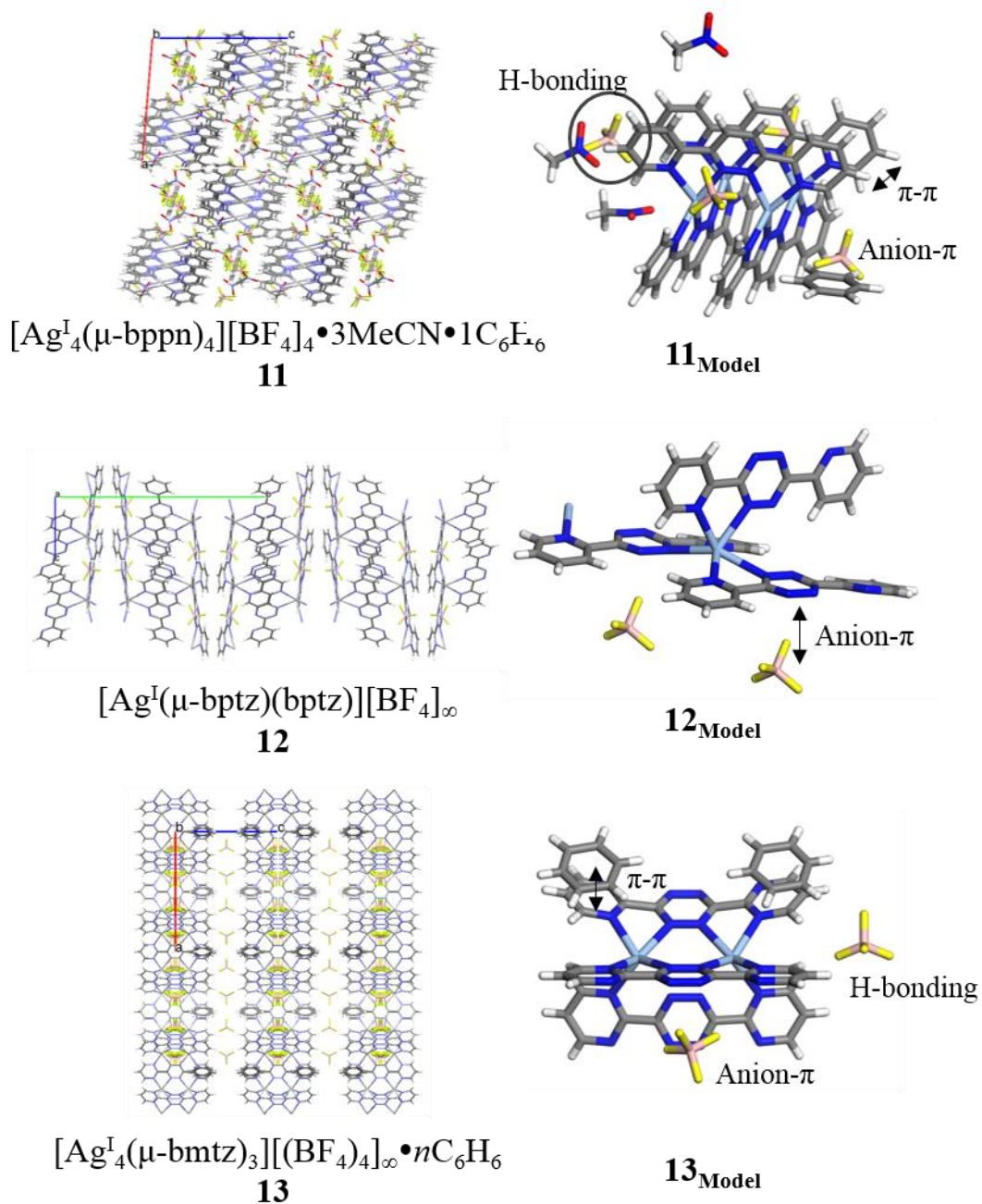


Figure 38. 2x2x2 packing diagrams, along the *b*-axis, for **11**, **12** and **13**, and the respective model structures, **11_{Model}**, **12_{Model}** and **13_{Model}**. Graphical display generated by the by the Mercury⁹⁰ and Materials Studio¹⁴ visualizers.

The interaction energies of each of the model complexes, **11**_{Model} – **13**_{Model}, were calculated with (ΔE_{Ionic}) and without ($\Delta E_{\text{N-C}}$) the strong ion-ion and ion-dipole contributions of the Ag^{I} ion, Table 12. The significant energy difference between the ΔE_{Ionic} and $\Delta E_{\text{N-C}}$ demonstrates that the electrostatic interactions of the Ag^{I} ion are significantly stronger than the non-covalent interactions in the system, as expected. By removing the Ag^{I} ions from the model complexes, the remaining $\Delta E_{\text{N-C}}$ encompasses the anion- π , H-bonding, dipole-dipole and van der Waals interactions involved in the complexes. The $\text{Ag:L:}[\text{BF}_4]^-$ ratios for complexes **11**_{Model} – **13**_{Model} are slightly different, so the $\Delta E_{\text{N-C}}$ was divided by the number of anion- π interactions in the complex for a more approximate comparison, $\Delta E_{\text{N-C}}/\text{A-}\pi$. The $\Delta E_{\text{N-C}}/\text{A-}\pi$ for **11**_{Model} and **13**_{Model} also includes contributions from the H-bonding interactions of the anions in the system. In fact, the $\Delta E_{\text{N-C}}/\text{A-}\pi$ for **13**_{Model} is calculated from the two anion- π interactions through a single anion, but due to the additivity of anion- π interactions, this is approximately representative.²⁹

Table 12. Representative coordination complex ratios, interaction energies with (ΔE_{Ionic}) and without ($\Delta E_{\text{N-C}}$) the strong contributions of the Ag^{I} ion, the approximate energy per anion- π interaction in the model structure ($\Delta E_{\text{N-C}}/\text{A-}\pi$) and average anion- π interaction distances ($d_{\text{X-Y}}$) for **11**_{Model} - **13**_{Model}.

Complex	L	Ag:L:[BF ₄] ⁻	ΔE_{Ionic} (kcal/mol)	$\Delta E_{\text{N-C}}$ (kcal/mol)	$\Delta E_{\text{N-C}}/\text{A-}\pi$ (kcal/mol)	$d_{\text{X-Y}}$ (Å)
11 _{Model}	bppn	4:4:4	-828.78	-20.75	-5.19	3.112
12 _{Model}	bptz	2:3:2	-203.18	-15.33	-7.67	2.991
13 _{Model}	bmtz	2:3:2	-274.07	-49.21	-24.61	2.633

In Table 12, the $\Delta E_{N-C/A-\pi}$ interaction energies of the model complexes increase in strength as the π -acidity of the bridging ligand increases, $\mathbf{11}_{\text{Model}} < \mathbf{12}_{\text{Model}} < \mathbf{13}_{\text{Model}}$. The anion- π interaction is particularly sensitive to the change in π -acidity of the ligand, and the average distance of the close-contact between each anion and aromatic ring, d_{X-Y} , also decreases according to the change in π -acidity, $\mathbf{11} < \mathbf{12} < \mathbf{13}$. Therefore, the corroborating changes in the $\Delta E_{N-C/A-\pi}$ interaction energies and the d_{X-Y} further support that the increase in π -acidity of the bridging ligand leads to stronger anion- π interactions.

Structural Contributions

Additionally, the binding motifs of each of the tetrazine-based bridging ligands determines the symmetries available for the respective Ag^{I} coordination complexes, polymers or extended networks, Figure 39. The bppn ligand enforces a *syn*-conformation of binding, Figure 39. The discrete grid structures, such as **11**, are the only coordination complexes characterized for this ligand and are stabilized through ion-dipole, π - π , anion- π , H-bonding and dipole-dipole interactions. The magnitude of stabilization, with an overall ΔE_{Ionic} of -828.78 kcal/mol for **11**_{Model}, is significantly higher per metal center than the other model complexes and precludes supramolecular rearrangement to an extended or distorted structure, Table 12.

The bptz ligand has been shown to energetically favor the *anti*-conformation, as exemplified in **12**.⁹⁵ However, the energetic barrier to *syn*-type orientation about the central tetrazine ring is relatively small and can be surmounted upon adequate stabilization of the resulting complexes, Figure 39. Also, although the bptz can bind in the *syn*-conformation, grid-like structures, akin to that of **11**, do not form. Instead, propeller

structures have been characterized that facilitate closer anion- π and intermolecular π - π interactions. The bptz ligand demonstrates the greatest variety of binding motifs, as highlighted by the various discrete (propeller-type) and one-dimensional polymers of **12**, **14** – **16**, *vide infra*.

Finally, the bmtz ligand promotes stability of the binding motifs through either *syn*-, *anti*-,¹¹⁰ or saturated-conformations, Figure 39, depending on the steric constraints, anion identity and precipitating solvent, *vide infra*. In the Ag^I architectures included in this study, the bmtz ligands propagate as one-dimensional or two-dimensional polymeric structures through saturated-conformations with the terminal bmtz molecules adopting a *syn*-conformation.

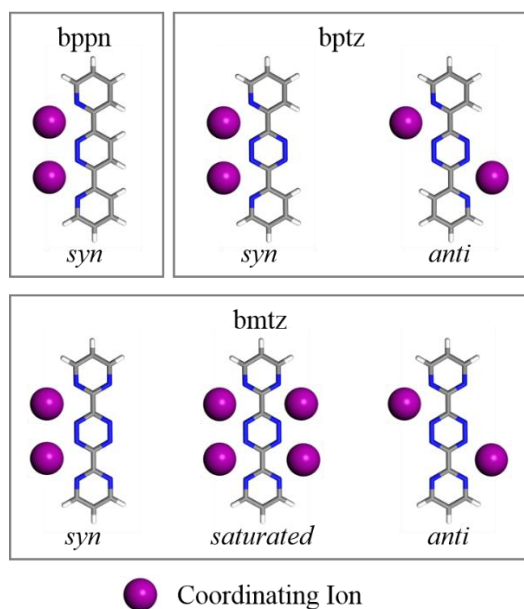


Figure 39. Variety of binding motifs available for bppn, bptz, and bmtz. Graphical display generated by the Materials Studio Visualizer.¹⁴

Role of the Non-Covalent Interactions

The directing nature of the anion has been lauded in several supramolecular systems because variations in the symmetry and size of the anion have been shown to selectively stabilize different geometries of transition metal architectures.^{23, 31b, 36-37} Ag^I-bptz coordination complexes have been previously characterized with the series of symmetrical, non-covalently bound [BF₄]⁻, [PF₆]⁻, [AsF₆]⁻ and [SbF₆]⁻ anions, providing a suitable series for computational evaluation.^{37b, 105}

In a similar manner to the bridging ligand model structures **11**_{Model} – **13**_{Model}, the crystal structures of **12** and **14** – **16** were pared down to include the simplest unit of the structure that includes representative interactions of the anion in the framework, Figure 40. The non-covalent interactions included in the model structures span anion- π , H-bonding and π - π interactions. The Ag^I-bptz complexes with [OTf]⁻ and [NO₃]⁻ structures were not included in this analysis due to the asymmetry of the [OTf]⁻ anion and the coordination between Ag^I and the softer [NO₃]⁻ anion.

As previously discussed, **12**_{Model} includes three bptz ligands, two Ag^I cations and two [BF₄]⁻ anions. The **12**_{Model} encompasses anion- π and H-bonding interactions from one polymeric portion of the crystal structure of the polymer but does not include interactions of the anion and π -system with additional, close-contacting polymers, Figure 40. The polymeric structure of **14** was simplified to two bptz ligands, two “cleaved” bptz (pyridine molecules), two Ag^I cations and two [PF₆]⁻ anions. Two bptz ligands were cleaved to pyridine molecules in an attempt to approximately retain the Ag^I coordination environment and to include the π - π interactions between the layers of bptz, Figure 40. The

π - π stacked networks of **15** and **16** were each simplified to include one of the respective propeller structures, **15_{Model}** and **16_{Model}**, Figure 40. The propeller structures of **15_{Model}** and **16_{Model}** include representative anion- π and H-bonding interactions but do not include the intermolecular π - π interactions of close-contacting propeller molecules. The anion-complex interaction energies were calculated for each of the model structures with (ΔE_{Ionic}) and without ($\Delta E_{\text{N-C}}$) the strong electrostatic interactions of the Ag^{I} ion, Table 13.

Due to the delicate balance of non-covalent interactions within supramolecular systems, the role of the anion must be considered in light of the non-covalent contributing factors. However, it has been impossible to precisely deconvolute individual intermolecular interactions and retain completely representative model structures. In order to evaluate the ΔE_{Ionic} and $\Delta E_{\text{N-C}}$ values for this series, each complex will be discussed in light of the contributing interactions and limitations of the model complex.

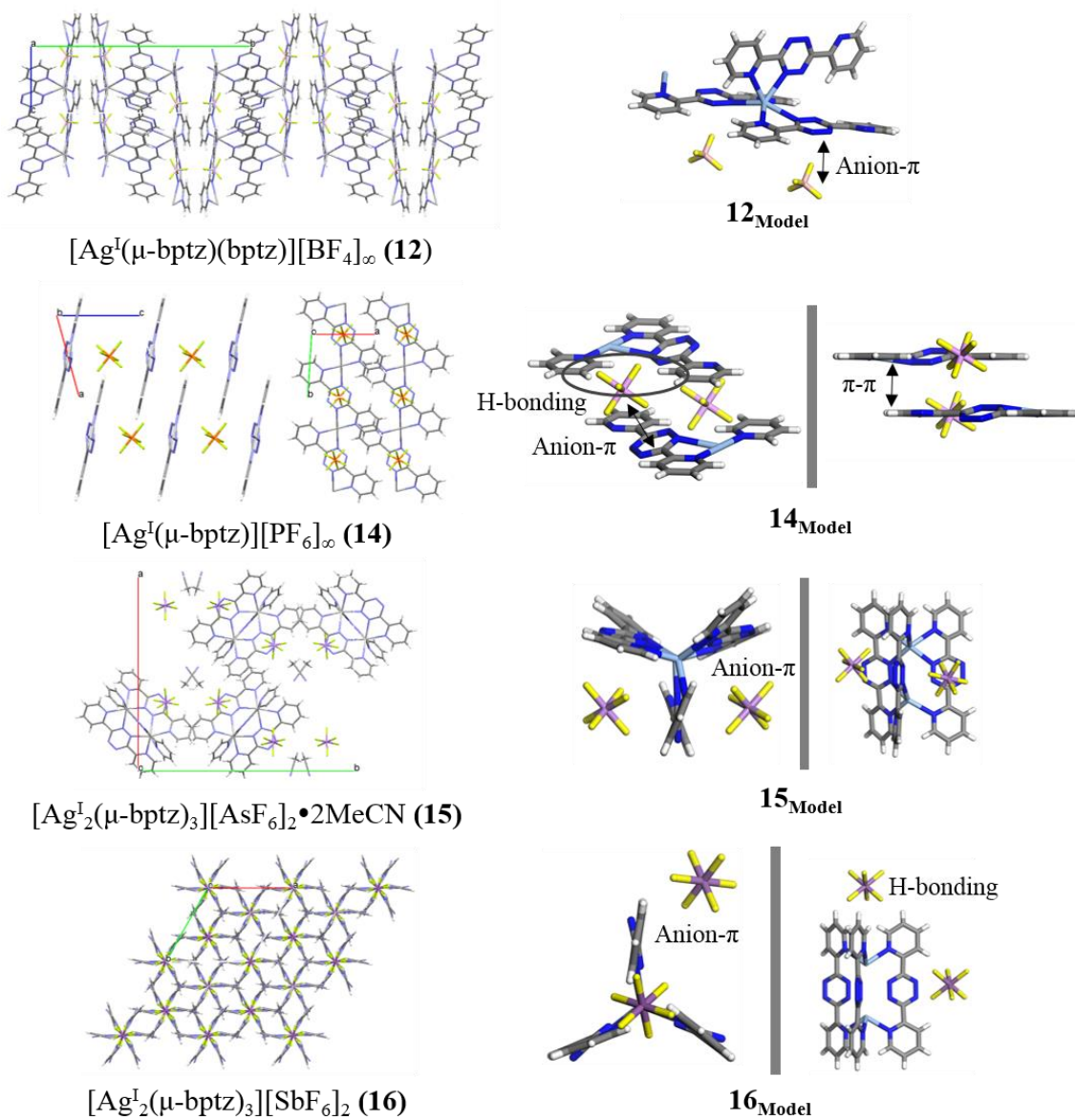


Figure 40. Packing diagrams for **12**, **14**, **15** and **16** and the respective model structures, **12_{Model}**, **14_{Model}**, **15_{Model}** and **16_{Model}**. Graphical display generated by the by the Mercury⁹⁰ and Materials Studio¹⁴ visualizers.

Table 13. Representative coordination complex ratios, interaction energies with (ΔE_{Ionic}) and without ($\Delta E_{\text{N-C}}$) the electrostatic contributions of the Ag^{I} ion and average anion- π interaction distances ($d_{\text{X-Y}}$) for **12**_{Model}, **14**_{Model} - **16**_{Model}.

Complex	Anion	Ag:bptz:Anion	ΔE_{Ionic} (kcal/mol)	$\Delta E_{\text{N-C}}$ (kcal/mol)	$d_{\text{X-Y}}$ (Å)
12 _{Model}	$[\text{BF}_4]^-$	2:3:2	-203.18	-15.33	2.991
14 _{Model}	$[\text{PF}_6]^-$	2:3*:2	-251.96	-21.68	2.839
15 _{Model}	$[\text{AsF}_6]^-$	2:3:2	-245.06	-11.96	2.986
16 _{Model}	$[\text{SbF}_6]^-$	2:3:2	-203.14	-21.77	2.893

The “zipper”-like polymeric structure of **12** is formed by two polymeric strands, propagated down the zipper bptz ligands in the anti-conformation. The “tines” of the “zipper” polymer are formed by the two polymeric strands of bptz ligands bound to Ag^{I} in the *syn*-conformation that intercalate with one another and form the π - π stacked “zipper” polymer. The $[\text{BF}_4]^-$ anion spans the layers of polymeric “zippers” by interacting with one set of polymers through several H-bonding interactions and interacting with another polymeric “zipper” through an anion- π interaction, with a moderate $d_{\text{X-Y}}$ of 2.991 Å. The anion- π contact distance is longer than the rest of the bptz model complexes because the anion preferentially forms shorter contacts through the series of H-bonding interactions than the anion- π interaction. The **12**_{Model} structure only modeled a portion of one side of the polymeric “zipper” and cannot properly account for the stability gained from the π - π stacking of the N-heterocyclic ligands. The $\Delta E_{\text{N-C}}$ of **12**_{Model} does account for the two long anion- π interactions in the complex, however, and demonstrates a moderate interaction energy of -15.33 kcal/mol.

The $[\text{PF}_6]^-$ anion is the smallest octahedral anion in the Ag^{I} -bptz series and favors the formation of a polymer that propagates through the *anti*-conformation of bptz, structure **14**. The octahedral anion intercalates between the layers of the close-contacting bptz polymer and maximizes interactions with four separate polymeric groups, two polymers that encircle the anion and two polymers that are oriented above and below the anion. Each of the fluorine atoms interacts with the two polymeric groups that surround the anion through H-bonding interactions. Furthermore, two of the fluorine atoms also interact with the tetrazine rings of the polymeric groups above and below the anion through η^6 -type anion- π interactions. The Ag^{I} -bptz polymers are further stabilized by π - π stacking interactions between the polymeric groups, with π - π contact distances of 3.561 Å. The **14**_{Model} structure contains several of the π - π stacking, H-bonding and anion- π interactions of the crystal structure. The ΔE_{Ionic} and $\Delta E_{\text{N-C}}$ are both quite energetically favorable with respect to this series of structures, and the strong interaction energies contribute to the shortest $d_{\text{X-Y}}$, in the Ag^{I} -bptz series, 2.839 Å.

The difference in directionality between the tetrahedral and octahedral anions optimizes the non-covalent interactions available for each anion. The symmetry of the $[\text{BF}_4]^-$ anion promotes H-bonding interactions with three of the fluorine atoms and an anion- π interaction with the fourth fluorine. The symmetry of the $[\text{PF}_6]^-$ anion promotes H-bonding interactions in the plane around the anion and anion- π interactions above and below the anion.

Increasing the octahedral anion size to $[\text{AsF}_6]^-$ favors the formation of propeller structures that orient in the crystal structure in order to facilitate π - π interactions between

neighboring propellers. As included in **15**_{Model}, the two anions participate in μ^6 -type anion- π interactions with all of the tetrazine rings of the Ag^{I} -bptz propeller. The $\Delta E_{\text{N-C}}$ is the least energetically favorable of the series, -11.96 kcal/mol, and the $d_{\text{X-Y}}$ is rather long at 2.986 Å. However, the *syn*-conformation of bptz in the propeller structure is stabilized by the stronger interactions of Ag^{I} with the $[\text{AsF}_6]^-$ anions and complex, demonstrated by the higher ΔE_{Ionic} of **15**_{Model}.

Reactions with the largest octahedral anion in the series, $[\text{SbF}_6]^-$, resulted in two co-crystallized propeller-type structures that exhibit different packing orientations. The first $[\text{SbF}_6]^-$ propeller structure is isostructural with **15** and is stabilized by anion- π , ion-ion and π - π interactions. In the second structure, **16**, one of the $[\text{SbF}_6]^-$ anions interacts with all of the bptz ligands at one end of the propeller through H-bonding interactions. The other $[\text{SbF}_6]^-$ anion participates in anion- π interactions with each of the six close bptz ligands. The fluorine atom is closest to one of the nitrogen atoms on each of the tetrazine rings, indicative of σ -complex character. The propellers orient in order to maximize the σ -complex/anion- π interactions and facilitate π - π interactions between the bptz ligands of adjacent molecules. While **16**_{Model} could not include all of the symmetry afforded by the packing of the propeller structures, the model propeller structure includes the σ -complex/anion- π interaction and the H-bonding interaction. The $\Delta E_{\text{N-C}}$ of **16**_{Model} is the strongest of the Ag^{I} -bptz model series at -21.77 kcal/mol, and the $d_{\text{X-Y}}$ is suitably short at 2.893 Å.

Therefore, the size of the anion, which decreases as $[\text{PF}_6]^- < [\text{AsF}_6]^- < [\text{SbF}_6]^-$, has a significant impact on the molecular structure and packing interactions of the complex.

Only the smaller $[\text{PF}_6]^-$ anion is able to intercalate between the layers of the Ag^{I} -bptz polymers and promote π - π , anion- π and H-bonding, but only the largest $[\text{SbF}_6]^-$ anion is able to span the σ -complex/anion- π interactions of six propeller structures.

Structural dependence on the size of the anion is also observed for the Ag^{I} -bmtz structures. For the smaller $[\text{BF}_4]^-$ and $[\text{OTf}]^-$ anions, the fully-coordinated two-dimensional network is formed. As the anion size increases to $[\text{ClO}_4]^-$ and $[\text{PF}_6]^-$, the pore is too small to contain the anions and corrugated polymers are formed. The polymers are further stabilized by π - π interactions between the pyrimidine rings of the bmtz ligands of the stacked polymers, Figure 41. Therefore, the tertiary factor related to directing the coordination of Ag^{I} complexes is the body of non-covalent interactions, with the size and symmetry of the anionic species being particularly critical.

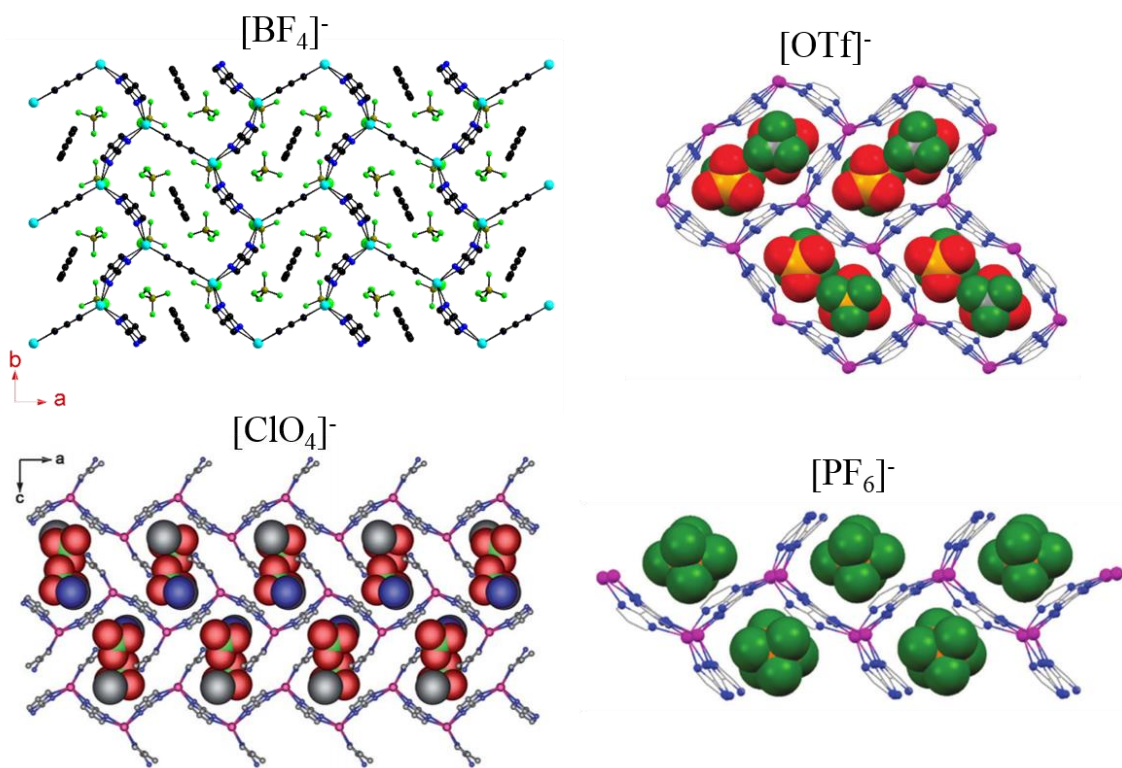


Figure 41. Structural and packing diagrams of the Ag^{I} -bmtz architectures explored by the Dunbar (**13**, $[\text{BF}_4]^-$), Batten ($[\text{ClO}_4]^-$)^{99b} and Murugesu ($[\text{OTf}]^-$ and $[\text{PF}_6]^-$)¹⁰⁶ research groups. $[\text{ClO}_4]^-$ portion of the figure adapted with permission from Batten and coworkers.^{99b} Copyright 2012 Royal Society of Chemistry. $[\text{OTf}]^-$ and $[\text{PF}_6]^-$ portions of the figure adapted from Murugesu and coworkers.¹⁰⁶ Published by the Royal Society of Chemistry.

Role of the Solvent

The final factor that contributes to Ag^{I} -coordination is the choice of solvent. The concentration at which supramolecular self-assembly and coordination reactions are performed has been shown in the literature to be particularly important, such that discrete complexes are entropically favored over larger supramolecular assemblies in dilute solutions.¹¹¹ This relationship is exemplified by the Ag^{I} -bptz complexes of $[\text{OTf}]^-$, $[\text{PF}_6]^-$

and $[\text{AsF}_6]^-$. At higher reaction concentrations, the polymeric and propeller-type supramolecular structures are formed, but at lower concentrations, dinuclear complexes are formed that are bound to two coordinating molecules of acetonitrile. The concentration dependence of these systems demonstrates one contribution of solvent to structural formation and highlights the importance of proper reaction conditions for facilitating supramolecular chemistry under kinetic versus thermal control.

Solvent molecules can also impact the supramolecular structures through non-covalent interactions. The most prevalent non-covalent interaction between solvent molecules and the Ag^{I} coordination complexes is through H-bonding interactions. The directing nature of these interactions have not been established, but the short contacts are expected to lend energetic stability to the architecture.

Furthermore, benzene has been shown to play a significant role in complex formation and stability. Many of the Ag^{I} -bptz and Ag^{I} -bppn crystal structures were grown upon slow diffusion of benzene, and a molecule of benzene is present in the $[\text{Ag}_4(\mu\text{-bmtz})_3][(\text{BF}_4)_4] \cdot n\text{C}_6\text{H}_6$ (**13**) unit cell. The molecule closely interacts with one of the bppn pyridine rings in an edge-to-face manner.

Recent work in the Dunbar laboratories by Toby Woods has identified that the formation of **13** is entirely dependent on benzene. Upon the stoichiometric reaction of four equivalents of AgBF_4 and three equivalents of bmtz in acetonitrile, there is no apparent color change or evidence of complexation. Slow diffusion of benzene into the solution leads to green crystals of **13** which crystallizes as a porous extended network consisting of alternating layers of the complex network and counter anions, Figure 42a. The structure

is stabilized by two anions in each pore that participate in anion- π interactions with the surrounding bmtz ligands, Figure 42b. The remaining void space in each pore is filled by two benzene molecules that stabilize the architecture by participating in π - π interactions with the pyrimidine rings of the bmtz ligands, Figure 42b. $[\text{BF}_4]^-$ anions are also between the layers of the coordination network and interact with the pyrimidine rings of the bmtz ligands through H-bonding interactions, Figure 42b. Despite the series of non-covalent interactions stabilizing this architecture, the complexation of **13** is fully reversible and complete disassociation of the complex occurs upon dissolution in acetonitrile, as determined by Toby Woods through preliminary ^1H NMR spectroscopy, mass spectrometry and electronic spectroscopy.

In order to computationally evaluate the energetic contributions of the benzene molecules, the crystal structure of the complex was pared down to include only one of the propeller units, two $[\text{BF}_4]^-$ anions and two benzene molecules, **13**_{Model}, Figure 42c. The structure was sequentially simplified by removing one of the benzene molecules, **13:1**_{Model}, and by removing both benzene molecules, **13:0**_{Model}, Figure 42c. The interaction energies were calculated for each of the model structures with (ΔE_{Ionic}) and without ($\Delta E_{\text{N-}}$) the strong electrostatic interactions of the Ag^{I} ion.

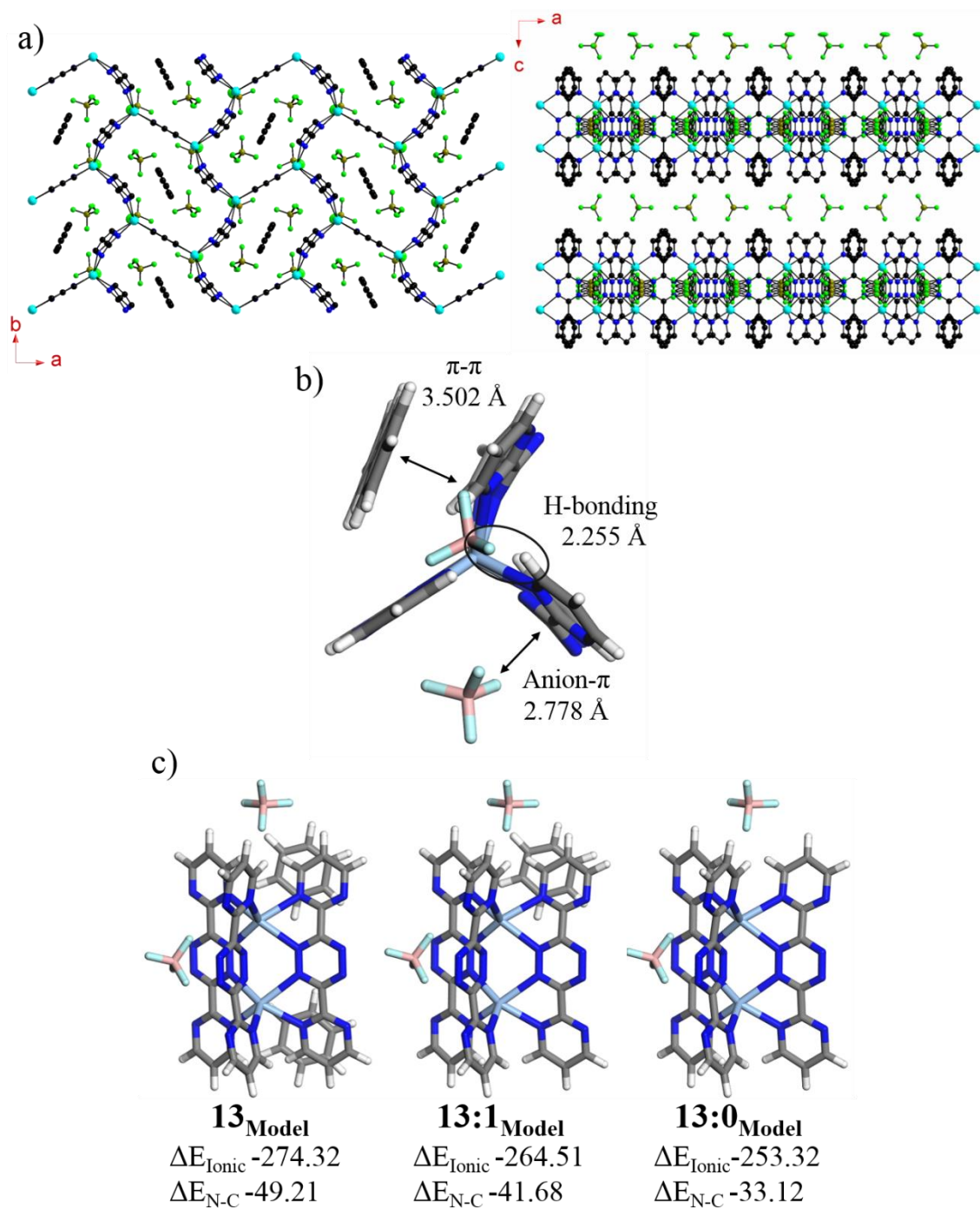


Figure 42. a) Packing diagrams, generated by Toby Woods, b) non-covalent interactions included in the model structure **13_{Model}** and c) the model structures **13_{Model}**, **13:1_{Model}** and **13:0_{Model}**. Graphical displays in generated by the Materials Studio Visualizer.¹⁴

Sequentially removing the benzene molecules from the model structures resulted in changes in the ΔE_{Ionic} and $\Delta E_{\text{N-C}}$ values of approximately 8-10 kcal/mol for each molecule, Figure 42. The difference in $\Delta E_{\text{N-C}}$ between **13**_{Model} and **13:0**_{Model} is 16.09 kcal/mol and accounts for 33% of the total non-covalent interaction energy of the model system. These data provide theoretical support for the necessity of the benzene for complexation because these calculations identify that the interactions of the benzene molecules with the framework provides significant stabilization to the structural motif.

Due to the capacity of the pores and the flexibility afforded by the layer of anions between the layers, substituted-benzene solvents were also considered for integration into the $[\text{Ag}_4(\mu\text{-bmtz})_3][(\text{BF}_4)_4]_\infty \cdot n\text{C}_6\text{H}_6$ crystal structure, including toluene, nitrobenzene and mixtures of xylenes. The various substituents were hypothesized to promote additional non-covalent interactions and stabilize or modify the supramolecular architecture. To this end, the crystal structure was imported into Materials Studio 7.0, and the unit cell was tiled to form a [2x2x2] supercell, Figure 43a. For each of the proposed solvents, the benzene solvent molecules were modified and the superstructures were fully optimized (FO) using the Universal Force Field (UFF)¹⁰⁹ within the Forcite module of Materials Studio 7.0.¹⁴ The UFF FO calculations cleaved the nitrobenzene molecules and the results were discarded. The FO supercells for toluene, *ortho*-xylene, *meta*-xylene and *para*-xylenes were overlaid with the original supercell for **13**. As can be seen in Figure 43b, the UFF force field appropriately treats the **13** framework, resulting in only slight deviations in the FO supercells. Likewise, the FO supercells of toluene and each xylene resulted in ideally optimized Ag^{I} -bmtz frameworks and in optimized solvent molecule orientation

within the pores, Figure 43c. These results suggest that toluene and xylenes could be used as precipitating solvents in order to derive similar structures. In fact, preliminary crystallographic results suggest that similar architectures are being formed upon precipitation with toluene. The initial structure is currently being refined and will be pursued in the future. Further UFF FO were performed on supercells of all of the remaining Ag^I complexes with bppn, bptz and bmtz. In nearly all of the structures, the supercells accurately reproduce the molecular framework. Anion and solvent orientation is only moderately modified, as shown in Figure 43. On the basis of this theoretical treatment, future solvation studies can be performed on a larger scale to elaborate the balancing point of solvent interactions. In light of the solvation studies presented herein, the solvent in such supramolecular systems acts as a switch between smaller, discrete coordination complexes and larger supramolecular formations. A mix of reaction conditions and the identity of the solvent molecules contribute to the final factors governing the formation of supramolecular Ag^I coordination complexes, polymers and networks.

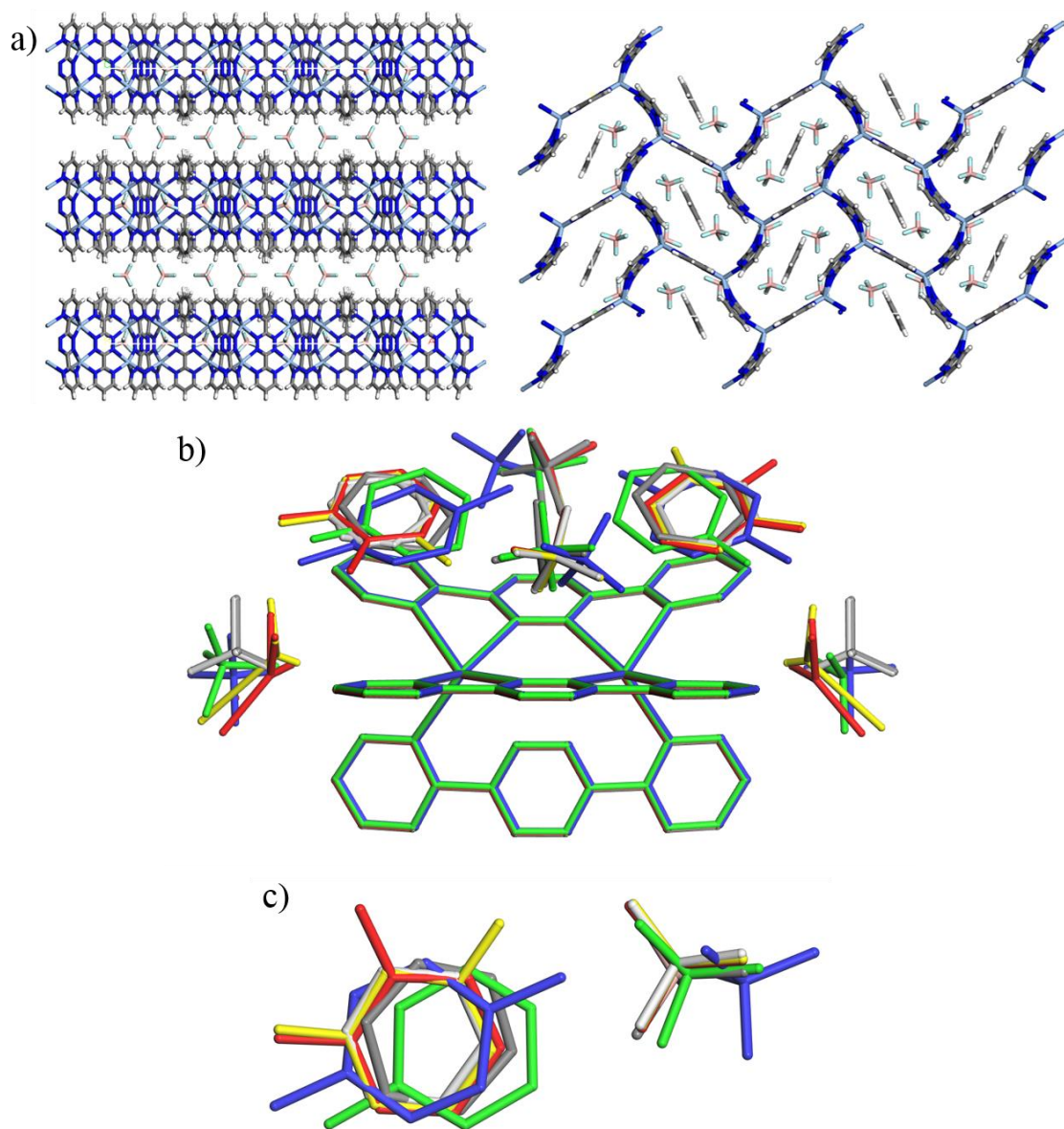


Figure 43. a) 2x2x2 supercell of **13**. b) Overlay of a representative portion of the original $[\text{Ag}_4(\mu\text{-bmtz})_3][(\text{BF}_4)_4]_\infty \cdot n\text{C}_6\text{H}_6$ supercell (light grey) with the corresponding portions of the FO $[\text{Ag}_4(\mu\text{-bmtz})_3][(\text{BF}_4)_4]_\infty$ frameworks with benzene (dark grey), toluene (green), *ortho*-xylene (red), *meta*-xylene (yellow) and *para*-xylene (blue). Hydrogen atoms omitted for clarity. c) Overlay of one solvent molecule and one anion from the $[\text{Ag}_4(\mu\text{-bmtz})_3][(\text{BF}_4)_4]_\infty$ framework pore for benzene (**13** light grey, FO dark grey), toluene (green), *ortho*-xylene (red), *meta*-xylene (yellow) and *para*-xylene (blue). Hydrogen atoms omitted for clarity. Graphical display generated by the Materials Studio Visualizer.¹⁴

Conclusions and Future Outlook

A hierarchy of factors that direct Ag^{I} assembly has been established, Figure 44, for a library of supramolecular, Ag^{I} coordination complexes, polymers and extended networks. The primary factor that facilitates such a wide variety of architectures is the Ag^{I} ion itself. The metal ion has a d^{10} electronic configuration that allows for significant coordination flexibility, and the softness of the Ag^{I} Lewis acid promotes coordination to N-heterocyclic ligands. Further investigations into the different modes of N-heterocyclic coordination of Na^+ and Ag^+ may lend further insight into the role of Lewis acidity and ion size.

A secondary factor that directs Ag^{I} coordination is the nature of the N-heterocyclic bridging ligands, both the structural and energetic contributions. The binding motif of each bridging ligand restricts the possible types of coordination, and the variability of the binding motif enables increased dimensionality of the resulting structures, i.e. discrete coordination complexes in **11**, one-dimensional polymers in **12**, and two-dimensional networks in **13**. The π -acidity of the bridging ligand also contributes to the differences in architectures. As the π -acidity of the ligands increases from *bppn*, *bptz* to *bmtz*, the $\Delta E_{\text{N-C}}$ and average $d_{\text{X-Y}}$ demonstrated stronger non-covalent interactions of the complexes. Further theoretical studies are necessary for probing the energetic impact of modifying the identity of the ligand in each type of architecture, as possible, with respect to the coordination motif of each complex.

The tertiary factor that directs the supramolecular assembly of the Ag^{I} architectures is the series of non-covalent interactions within the system, particularly the

interactions involving the anions. As evaluated by **12**_{Model}, **14**_{Model} – **16**_{Model}, the differences in anion symmetry and size were optimized within each structure to stabilize the architecture through long-range ion-ion interactions (**15**_{Model}) or anion- π , H-bonding and π - π interactions (**12**_{Model}, **14**_{Model} and **16**_{Model}). The dependence on anion size was also highlighted as the determining factor for the dimensionality of the Ag^I-bmtz structures, either one-dimensional polymers or two-dimensional coordination networks.

The major limitation identified by the bridging ligand and anion studies was the inability to adequately represent the coordination and non-covalent interactions of each crystal structure. In order to improve on these efforts, future studies will benefit from expanding the model structures to encompass more of the non-covalent interactions integral to the architectures. The ω B97X-D/6-31+g(d,p) level of theory yielded suitable results upon analysis of the model complex, Table 11, and would likely be able to calculate a larger system without loss of computational integrity when evaluating the non-covalent interactions.

The fourth and final factor that impacts the assembly of Ag^I architectures is the solvent. Supramolecular structures are typically influenced by concentrated reaction conditions and solvent molecules can provide crucial stability by interacting with the main structure through non-covalent interactions. Benzene was shown to be a supramolecular “switch” to enable the formation of **13** due to the significant energetic stabilization afforded by the π - π interactions with the bmtz ligands, accounting for 33% of the overall non-covalent interaction energy of the model compound **13**_{Model}. This architecture was further explored using Molecular Mechanics methods, and it was shown that other

substituted-benzene type solvents should be capable of stabilizing **13**, or a similar form of the structure. Future studies will benefit from a combined theoretical and experimental approach to further elucidate the role of solvent in these supramolecular architectures.

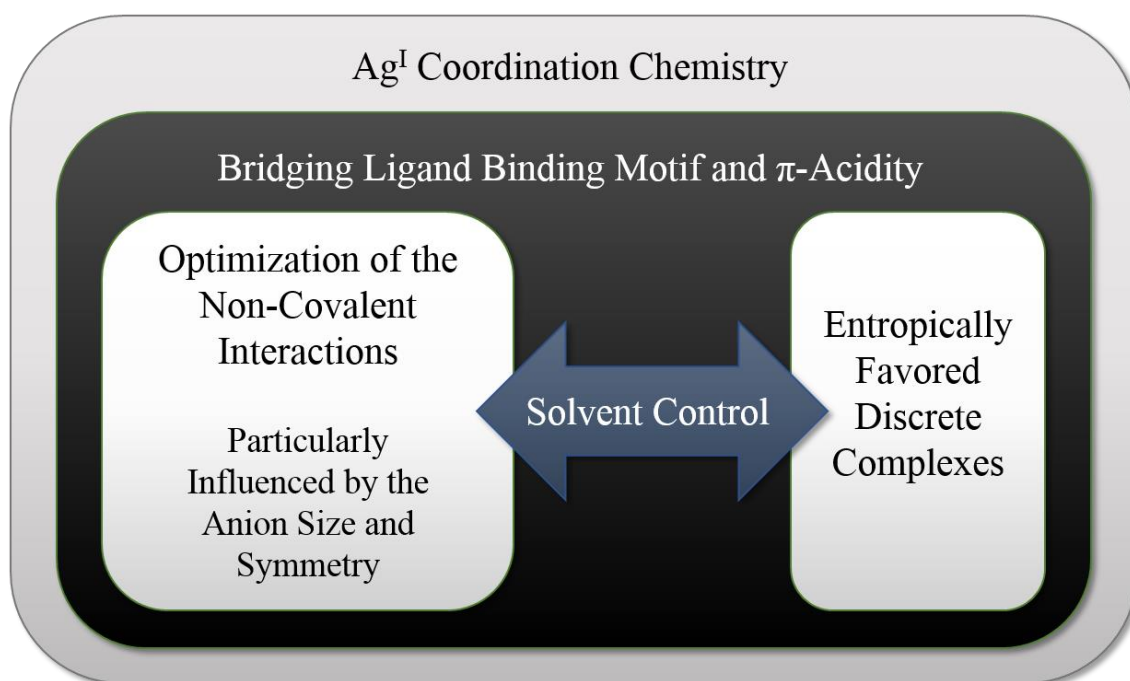


Figure 44. The hierarchy of factors that direct supramolecular Ag^I coordination.

CHAPTER IV

EXPLORING THE USE OF ANION-TEMPLATED METALLACYCLES AS BUILDING BLOCKS FOR LARGER SUPRAMOLECULAR ARCHITECTURES

Introduction

Supramolecular chemistry elegantly directs molecular interactions such that the same principles that contribute to discrete molecular recognition can motivate the assembly of very large, complex architectures.^{23a, 59a, 112} The foundational supramolecular driving forces of coordination chemistry and self-assembly of building blocks, as discussed in Chapter II, have been successfully applied by many groups to elaborate architectures with increased dimensionality and complexity.^{59d} Through simple modification of the building blocks, many classes of extended architectures can be realized, including coordination polymers,¹¹³ metal-organic frameworks¹¹⁴ and metal-organic polyhedra,^{59a, 59e, 115} among others.¹¹⁶ Within the broad array of extended supramolecular structures, the scope of this chapter focuses on the extension of supramolecular metallacyclic building blocks into discrete polyhedral architectures.

The 1987 Nobel Prize in Chemistry, awarded to Pedersen, Lehn and Cram for their decades of fundamental work on supramolecular chemistry,⁴ involved the study of two-dimensional and three-dimensional organic structures, including crown-ethers,^{9, 117} cryptates¹⁰ and sphereands¹¹ It was not until 1988, however, that the first supramolecular, self-assembled coordination-driven polyhedral structure was developed by Saalfrank and coworkers,¹¹⁸ Figure 45. Research involving the design of three-dimensional cage-like

structures that directly followed this discovery, by groups such as Saalfrank, Raymond, Ward, Nitschke, Fujita and Stang, among others, quickly expanded into a thriving area of research.^{59a, 59c-e, 115}

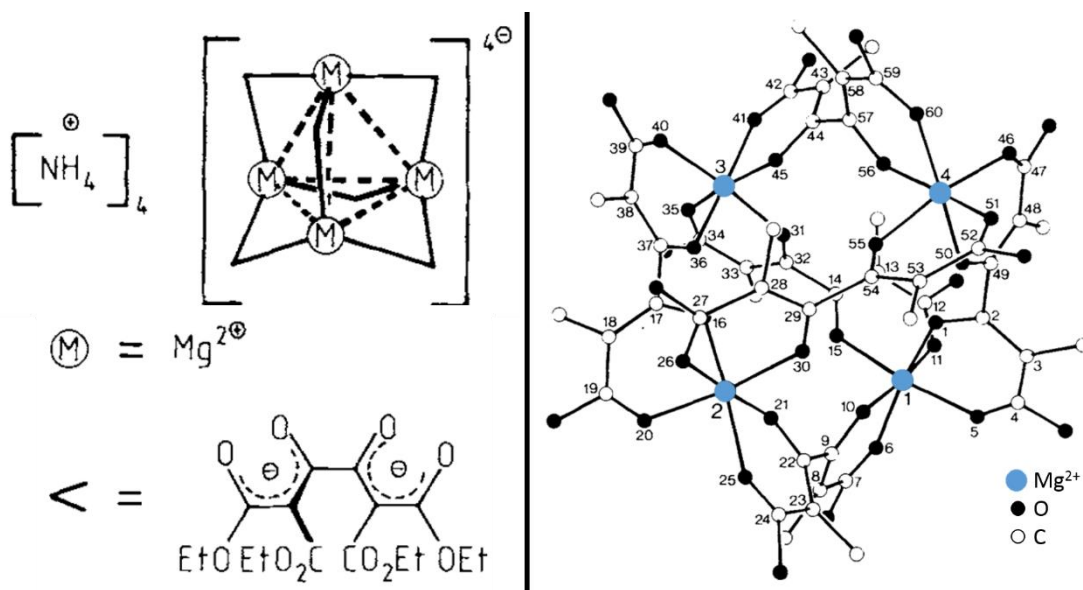


Figure 45. The first supramolecular coordination-driven polyhedral architecture by Saalfrank and coworkers.¹¹⁸ Adapted and reproduced with permission from Saalfrank et al.¹¹⁸ Copyright WILEY-VCH GmbH & Co.

Three-dimensional polyhedral architectures with Archimedean and Platonic symmetries have been developed according to a series of logical supramolecular approaches, employed by several groups.^{59a} The “Directional Bonding Approach” employed by Stang and coworkers,¹¹⁹ Figure 46a, utilizes judiciously chosen ditopic and tritopic building units to access polyhedra with varied Archimedean and Platonic

symmetries. The “Paneling Approach” has been used by Fujita and coworkers,¹²⁰ Figure 46b, to coordinate organic ligand “panels” at transition metal nodes to facilitate the development of regular platonic solids. The “Symmetry Interaction Approach” has been used by Raymond and coworkers,¹²¹ Figure 46c, to coordinate bis-bidentate or tris-bidentate ligands to directional metal centers, resulting in symmetric polyhedra. As more research groups have explored the topic of three-dimensional polyhedral structures, the compendium of building approaches proportionally expands, but the logical consideration of steric favorability remains constant.

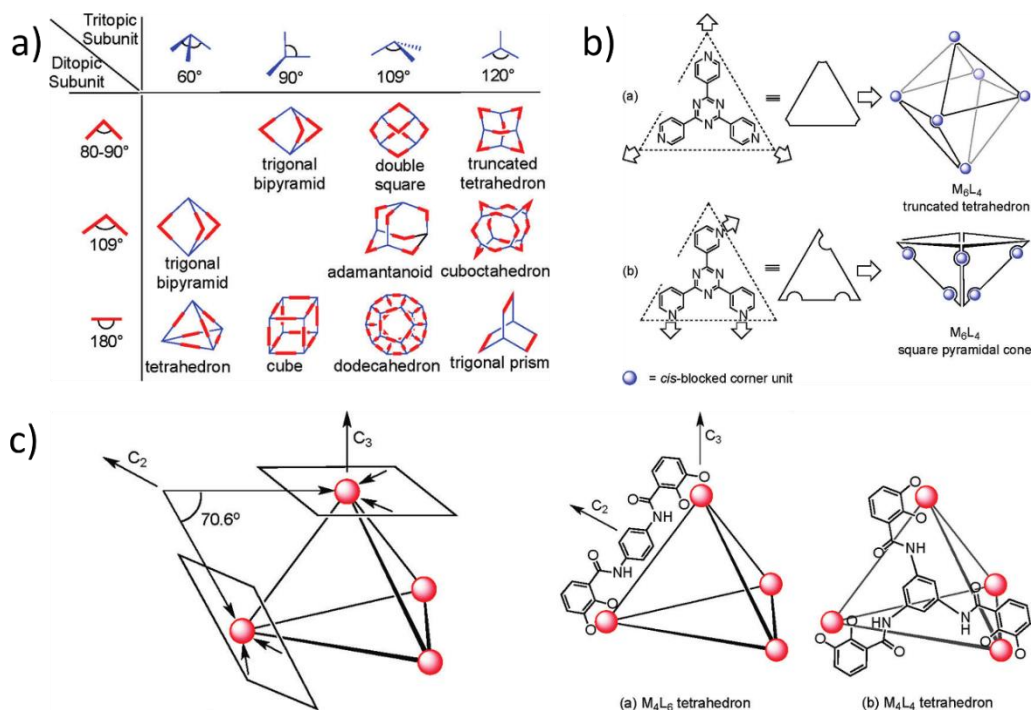


Figure 46. Bonding approaches for developing three-dimensional polyhedral architectures, including the a) “Directional Bonding Approach”, b) “Paneling Approach” and c) “Symmetry Interaction Approach”. Adapted from Chakravarty et al.^{59a}

Several synthetic studies that focused on architectural design have led to the isolation of larger and more complex polyhedral architectures, such as the highly charged dodecahedron synthesized by Stang and coworkers that has a diameter of approximately 7.5 nm,¹²² Figure 47. Other studies have taken an application-driven approach by designing ligands with specific utilities. Fujita and coworkers were able to functionalize the convex- and concave-edges of bridging ligands within the M_nL_{2n} family of polyhedra to increase solubility and incorporate recognition properties,¹²³ Figure 47b. Intermolecular interactions afforded by the transition metals and organic ligands can also selectively tune the encapsulation and release of gas molecules, pollutants, etc., Figure 47c and d. Selective uptake and release of various molecular entities have been developed by researchers under the leadership of Zhou¹²⁴ and Nitschke.¹²⁵ In addition to encapsulation, several groups have explored the use of the polyhedral architectures as molecular vessels. Fujita and coworkers have accessed sensitive and unique compounds by synthesizing them inside of the sterically constrained, protected environment of the polyhedra,¹²⁶ Figure 47e. In addition, applications of polyhedra are now growing to encompass drug uptake, transport and programmed release, as exemplified by the work of Therrien and coworkers,¹²⁷ Figure 47f. Not only is the metal-organic cage able to selectively encapsulate and release drugs under programmed conditions, the polyhedral cage itself has activity as an anti-cancer agent.¹²⁷ While the scope of this introduction is unable to provide an exhaustive review of the field, these foundational studies provide the architectural and functional inspiration for this work.

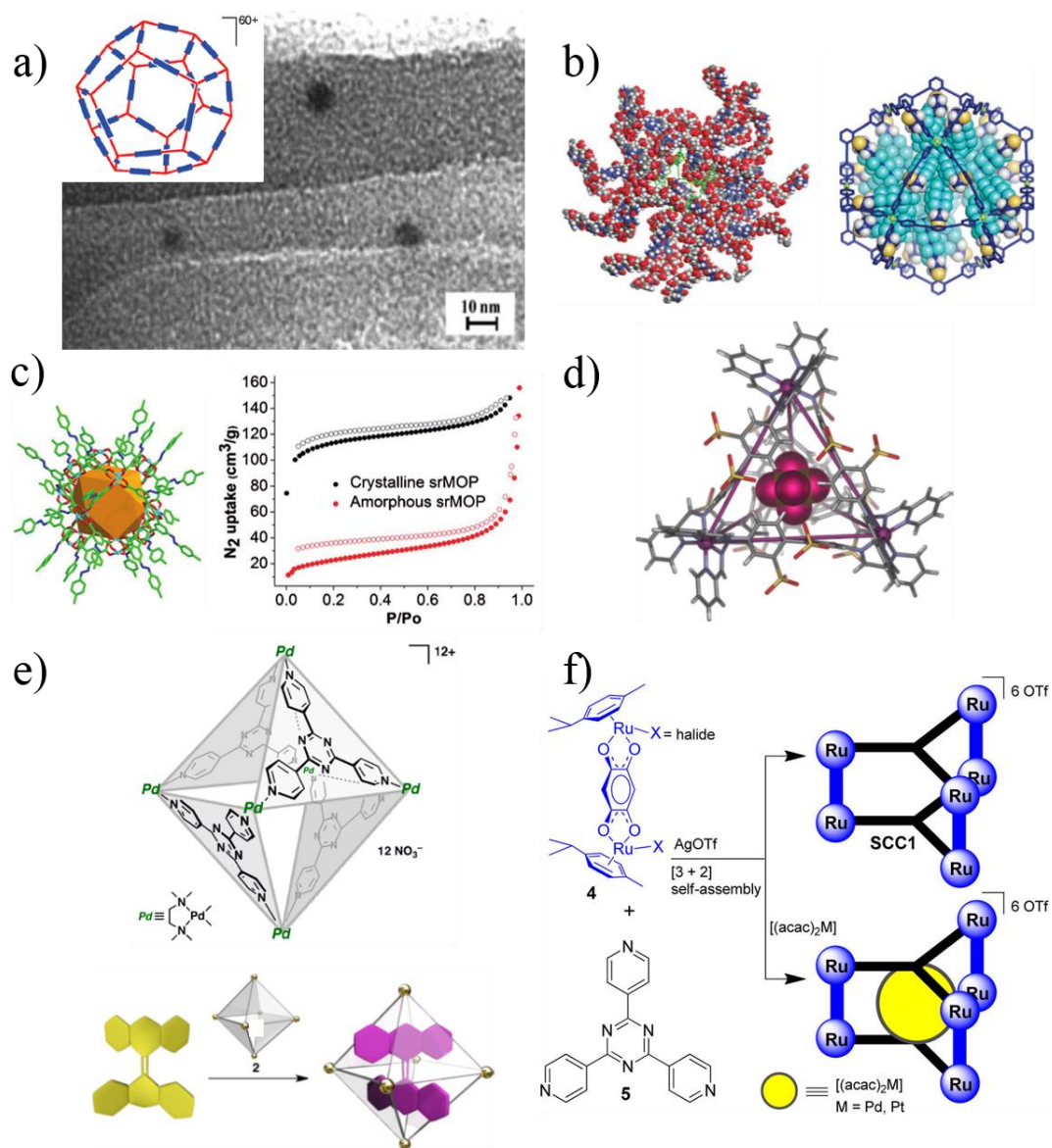


Figure 47. Applications of Polyhedra. a) Large polyhedra by Stang *et al.*;¹²² b) Externally and Internally functionalized bridging ligands by Fujita *et al.*;¹²³ c) Selective gas uptake by Zhou *et al.*;¹²⁴ d) Pollutant encapsulation by Nitschke *et al.*;¹²⁵ e) Protected reactivity within polyhedra by Fujita *et al.*;^{126c} f) Anti-cancer molecular capsule by Therrien *et al.*^{59b} Adapted with permission from each reference.

As described in Chapter II, the Dunbar group has developed a library of anion-templated, self-assembled supramolecular square and pentagonal metallacycles.^{31, 36} The metallacyclic self-assembly was achieved by combining transition metal vertices, bis-bidentate bridging ligands and appropriate templating anions.^{23, 37b} At each metallacycle vertex, the transition metal is coordinated to two bis-bidentate bridging ligands (bmtz or bptz) and two acetonitrile ligands. The acetonitrile ligands have been shown to be labile when in the presence of the more energetically favorable, anionic bromide ligand,^{36c} Figure 48.

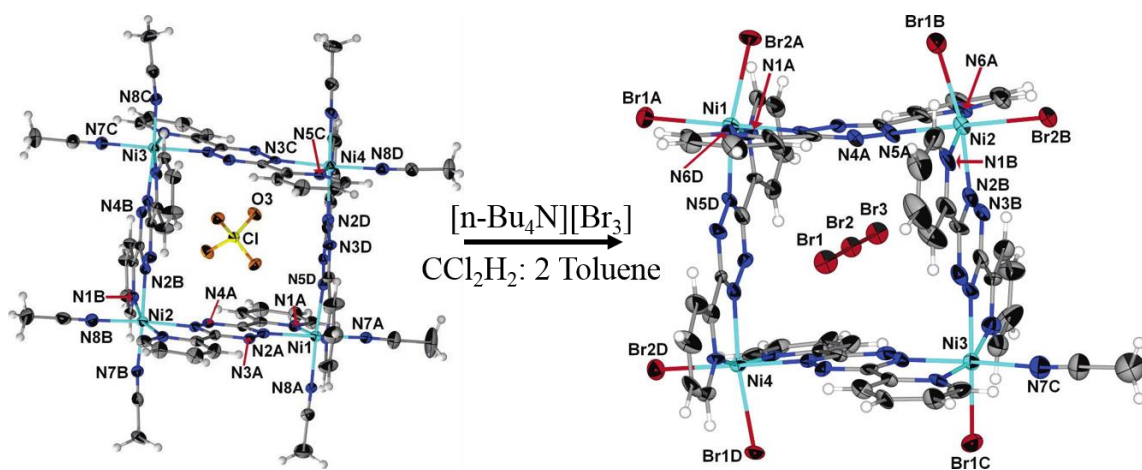


Figure 48. Lability of acetonitrile ligands in a substitution reaction with bromide.^{36c} Adapted from Dunbar et al.^{36c}

Historically, pentagonal supramolecular assemblies, such as those by Nitschke and Lehn, have been rare and coordinately saturated,⁶⁵⁻⁶⁶ but this is not the case for the

pentagonal metallacycles characterized by the Dunbar group.^{31b, 36b, 36d} The substitutional lability of the pendant acetonitrile ligands at each vertex, Figure 48, renders the pentagonal metallacycles to be pursued as unique supramolecular building blocks. The pentagonal structures exhibit a symmetry that has not been accessed previously and would facilitate the development of new symmetries of polyhedral architectures.

Therefore, upon the substitution of the labile acetonitrile ligands for bis-bidentate or tris-bidentate chelating ligands, a net of coordinated pentagons is predicted to form, Figure 49. The combination of thermodynamic control and kinetic healing, as identified within other polyhedral systems,^{59a} is hypothesized to lead to discrete polyhedral architectures with truncated icosahedral and rhombicosidodecahedral symmetries, Figure 49. With the wealth of bridging ligands available, this chapter describes efforts to develop truncated icosahedral architectures for two classes of bridging groups: organic bis-bidentate bridging ligands (including N-donor and O-donor ligands) and inorganic bridging complexes (including cyano-metallate complexes of several 4d and 5d transition metals).

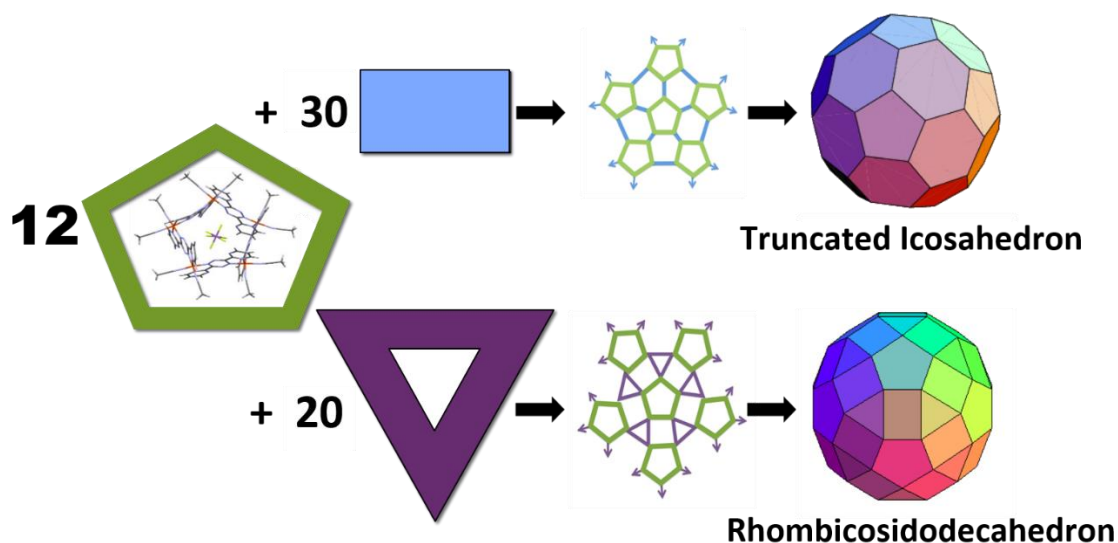


Figure 49. Proposed symmetry of polyhedra developed from pentagonal building blocks.

Experimental Methods

Materials

All reactions were performed under N_2 using standard Schlenk techniques. Solvents were distilled prior to use. Acetonitrile was distilled over 3 Å sieves and toluene was distilled using an MBraun solvent purification system. Triethylamine was provided and distilled by Dr. Hong-cai Zhou's research group at Texas A&M University. Dimethylsulfoxide (DMSO) and dimethylformamide (DMF) were purchased from Sigma Fisher Scientific and Alfa Aesar, respectively, and used without further purification. Glassware was appropriately cleaned and oven-dried before use. $[Fe_5^{II}(bmtz)_5(MeCN)_{10} \supset [SbF_6][SbF_6]_9$ (3^{36d}) and $[Ni^{II}(MeCN)_6][SbF_6]_2$, bmtz and bptz were prepared under dry, air-free conditions according to reported methods.^{36b, 36d, 75a, 75c}

Tetra-2-pyridinylpyrazine (tppz) and terephthalic acid (tpa acid) were purchased from Sigma Aldrich and dried *in vacuo* prior to use. Tetrapyrido[3,2-*a*:2',3'-*c*:3'',2''-*h*:2''',3'''-*j*]phenazine (tpphz) and bis-tetrabutylammonium terephthalate ($[\text{nBu}_4\text{N}]_2[\text{tpa}]$), were synthesized according to established literature procedures.¹²⁸ David Kempe synthesized tetraethylammonium cyanide ([TEA][CN]) and Carolyn Gunthardt synthesized bis(triphenylphosphine)iminium hexacyanoosmate ([PPN]₃[Os(CN)₆]) according to group and literature procedures in collaboration with this project.¹²⁹

Characterization Methods

Samples for IR analysis were prepared as Nujol mulls between KBr plates and were analyzed using a Nicolet 740 FT-IR spectrometer. Electronic absorption spectra were obtained on a UV-1601 PC Shimadzu Recording UV-Visible Spectrophotometer. ¹H NMR spectra were obtained at 20°C using the 300 MHz Mercury spectrometer or the 500 MHz Inova Spectrometer, as specified. 1D NMR spectra were collected upon spinning the probe at 20 Hz, while 2D spectra were obtained without spinning the probe.

Atomic Force Microcopy (AFM) and Scanning Tunneling Microscopy (STM) images were obtained in collaboration with Dr. Batteas by Dr. Brad Ewers and Ms. Alison Pawlicki. Atomically clean highly ordered pyrolytic graphite (HOPG) and gold (Au(111)) on mica surfaces were used to collect images of several of the products. The HOPG surface was prepared by mechanically cleaving the surface according to the Scotch Tape method. This includes placing and peeling off a piece of tape from the HOPG surface to exfoliate surface. The Au(111) on mica surface was prepared by first applying UV radiation for ten minutes, rinsing with purified water and ethanol, drying under N₂ and then applying UV

radiation for five minutes, rinsing with purified water and ethanol, drying under N₂. Once prepared, the sample was soaked in ethanol for ten more minutes to reduce any remaining impurity off of the surface. Samples were then dropcast on the surfaces, such that the sample covered a portion of the center of the surface.

AFM images were obtained on an Agilent 500 in non-contact mode or contact mode under a force load of less than 1nN, as specified. AFM is a microscopic technique that images surfaces by maintaining a constant force between the atomic tip of the instrument's cantilever and the sample surface.¹³⁰ A constant force is maintained between the tip and the sample by adjusting for weak short-range chemical, van der Waals and electrostatic forces, and this force can result in physically contacting the surface (contact mode), tapping along the surface (tapping mode) or not contacting the surface (non-contact mode).¹³⁰ STM images were obtained on a Nanosurf Easyscan2 under an applied current of 20 – 250 amps at 1 – 2 volts, as indicated. STM images were collected by scanning a conducting probe with an atomically sharp tip over the conductive sample.¹³¹ The tip was brought close to the surface, within several angstroms, using a piezoelectric controller, and a constant current was applied to the sample through the tip. The electric current was able to tunnel from the tip, across the vacuum gap, through the sample and to the conducting platform. The image was collected in constant current mode. The applied current is proportional to the local density of states of the sample and the gap distance between the tip and the sample. In order to generate the STM images, the voltage was modified to maintain a constant current between the tip, sample and conducting platform,

and the resulting images describe the combination of the change in the local density of states and the physical topology of the sample.¹³¹

Reflection data for each single crystal were collected at 110 K on either an MWPC detector using a CuK α source ($\lambda = 1.54178 \text{ \AA}$), APEXII CCD detector using a MoK α source ($\lambda = 0.71073 \text{ \AA}$) or a photon CMOS detector using a micro-focus MoK α source ($\lambda = 0.71073 \text{ \AA}$), as specified. The reflection data were integrated using SAINT⁷⁶ in the APEXII software suite.⁷⁷ Absorption corrections were performed using SADABS⁷⁸ and the crystal structures were solved by direct methods using SHELXS⁸⁰ as implemented in the OLEX2 software suite.⁸¹ The final crystal structures were refined by least squares refinement with SHELXL.⁸² All non-hydrogen atoms were refined anisotropically.

Syntheses

[Fe(tppz)₂][SbF₆]₂ (18)

A 20 mL acetonitrile solution of **3** (59.6 mg, 14.0 μmol) was added to an 80 mL acetonitrile and 5 mL DMF solution of tppz (44.8 mg, 115.3 μmol). Over the course of several hours, the reaction underwent a color change to a darker blue, and the mixture was stirred at 45°C for 1 day. Toluene was added as a precipitating solvent and the resulting black solid was collected upon filtration, yield (slightly wet): 85 mg. The solid was recrystallized with toluene, and the product was characterized by single crystal x-ray diffraction (*vide infra*): [Fe(tppz)₂][SbF₆]₂ (**18**).

Representative reaction of tpphz and 3: tpphz+3

A 30 mL acetonitrile solution of **3** (40 mg, 9.5 μmol) was added to a 40 mL acetonitrile suspension of tpphz (14.8 mg, 38.1 μmol). The mixture was stirred at 45°C

for five days. Upon a color change to a deep teal green, a portion of the solution was dried *in vacuo* for NMR characterization. Another portion of this reaction solution was retained, toluene was added as a precipitating solvent and the solid was analyzed with STM and AFM methods, *vide infra*. The remaining solution was stirred 45°C for several more days to monitor the solution, but the reaction solution turned red. The decomposed reaction solution was discarded. Similar reaction conditions were followed and electronic absorption spectra were obtained over the course of the reaction, *vide infra*. Similar reaction conditions were followed for reactions of tpphz and **3** at 25°C, 65°C and at 45°C with the addition of excess C₆₀ as a potential templating agent, *vide infra*.

Representative reaction of tpa acid, triethylamine, DMF and 3: tpa acid+3

In an acetonitrile-liquid nitrogen slush bath, a 140 mL acetonitrile solution of **3** (60.0 mg, 14.2 μmol) was added to a solution of triethylamine (2 mL), DMF (4 mL) and tpa acid (10 mg, 60.2 μmol). The slush bath was slowly warmed to 25°C over the course of 12 hours. From the initial deep blue reaction solution, a dark green solid precipitated and was collected through filtration, rinsed with acetonitrile and dried on the fritted funnel. Yield: 30 mg.

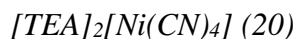
Representative reaction of [nBu₄N]₂[tpa] and 3: [nBu₄N]₂[tpa]+3

A 100 mL acetonitrile suspension of [nBu₄N]₂[tpa] (14.1 mg, 34.4 μmol) was added to a 10 mL acetonitrile solution of **3** (58 mg, 13.8 μmol). The deep blue mixture was stirred at 45°C for seven days. Upon color change to a deep teal green, a portion of the solution was dried *in vacuo* for characterization. Toluene was added as a precipitating solvent and the solid was collected via filtration, rinsed with toluene and dried on the

fritted funnel. The product was analyzed with NMR, STM and AFM methods, *vide infra*.
Yield: 45.6 mg.



A 5 mL acetonitrile suspension of bptz (6.2 mg, 25.4 μmol) was added to an 10 mL acetonitrile solution of $[\text{Ni}(\text{MeCN})_6][\text{SbF}_6]_{10}$ (21.1 mg, 25.9 μmol). The orange solution was stirred under air-free conditions at 25°C for 1 hour. To this reaction solution was added a 3 mL acetonitrile solution of $[\text{PPN}]_3[\text{Os}(\text{CN})_6]$ (5 mg, 2.7 μmol), and the final reaction was stirred under N_2 for one week. The reaction solution deepened in color to a dark amber, and the solution was concentrated under vacuum. The solution was crystallized with toluene, and the product was characterized by single crystal X-ray diffraction: $[\text{Ni}_4^{\text{II}}(\text{bptz})_2(\text{bptz})^{-2}(\text{MeCN})_8\supset\text{MeCN}][\text{SbF}_6]_6$ (**19**). IR (KBr mull), cm^{-1} : 2083 ($\text{C}\equiv\text{N}$, impurity or side product), 1605 ($\text{C}=\text{N}$), 662 ($\text{Sb}-\text{F}$).



A 5 mL acetonitrile suspension of bmtz (7.6 mg, 31.9 μmol) was added to an 5 mL acetonitrile solution of $[\text{Ni}(\text{MeCN})_6][\text{SbF}_6]_{10}$ (24.5 mg, 31.5 μmol). The orange solution was stirred under air-free conditions at 25°C for 1 hour. To this reaction solution was added a 10 mL acetonitrile solution of $[\text{TEA}][\text{CN}]$ (40.2 mg, 257.2 μmol), and the final reaction was stirred under N_2 for one week. The reaction deepened in color to a dark orange. The solid was recrystallized over toluene, and the product was characterized single crystals from both methods of crystallization were characterized by by single crystal X-ray diffraction: $[\text{TEA}]_2[\text{Ni}(\text{CN})_4]$ (**20**).

Computational Methods

From the crystal structure of **3**^{36d} and atomic coordinates of the proposed bridging ligands, simplified (μ -Bridging Ligand)(**3**)₂ models were developed for each of the N-donor (tpphz and tppz) and O-donor, dianionic bridging ligands (tpa, adipate, glutarate and succinate). The structure of (μ -Os(CN)₆)(**6**)₂ was also constructed from the crystal structure of **6**^{36b} and the atomic coordinates of the Os(CN)₆³⁻ anion. The model structures were fully optimized with the semi-empirical Neglect of Differential Diatomic Overlap (NDDO)⁴⁶ method, Parametrization Method 6 (PM6)⁴⁷. The restricted Hartree Fock (RHF)⁸⁴ and unrestricted Hartree Fock (UHF)⁸⁵ keywords were applied to the closed shell (μ -Bridging Ligand)(**3**)₂ and open-shell (μ -Os(CN)₆)(**6**)₂ complexes respectively. The hybridization of the carbon and nitrogen atoms and the total charge was assigned for each structure, and the multiplicity was determined automatically by the software. Each geometry optimization converged at a “medium” self-consistent field (SCF) with a tolerance of 1.0×10^{-5} eV and upon reaching a gradient norm of less than 0.4 kcal/mol/Å. These structures were optimized within the VAMP⁸³ module of Materials Studio 7.0,¹⁴ by Accelrys Software Inc. Proposed polyhedral structural models of tpphz- and tpa-bridged polyhedra were developed by Professor Steven Wheeler using the crystal structure of **3**^{36d} and atomic coordinates of the respective bridging moieties. The structures were imported into Materials Studio 7.0¹⁴ for analysis. Graphical displays of the computational results and predicted structures were generated by the Materials Studio Visualizer.

The energetic cost associated with the binding, bending and bridging of the tpa ligand at each Fe^{II} vertex was evaluated by DFT methods. The tpa²⁻ bridging group was simplified

to the mono-anion benzoate to simplify the following calculations. Three metallo-complexes were partially optimized (PO) by the BP86 functional,⁵³⁻⁵⁴ the Stuttgart/Dresden multi-electron fully-relativistic effective core potentials for Fe^{II},⁵⁵ and the 6-31+g(d) basis set⁵² for the remaining atoms in Gaussian 09.⁸⁶ The complexes included a pentagonal vertex (A) with formula [Fe^{II}(bmtz)₂(MeCN)₂]²⁺, a polyhedral vertex (B) with formula [Fe^{II}(bmtz)₂(benzoate)]⁺ and an intermediate vertex (Int) with formula [Fe^{II}(bmtz)₂(benzoate)]⁺. Vertices A and B were PO by optimizing the atomic coordinates of the hydrogen atoms and restraining the remaining non-hydrogen atoms. Vertex Int was PO by optimizing the atomic coordinates of the hydrogen atoms and benzoate ligand and restraining the bmtz and Fe^{II} moieties. Additionally, the benzoate and acetonitrile moieties were fully optimized (FO) at the BP86/6-31+g(d) level of theory.⁵²⁻⁵⁴ The energies associated with binding (ΔE_{A-Int}), bending (ΔE_{Int-B}) and bridging (ΔE_{A-B}) of the tpa bridging ligand were calculated from the final energies of the appropriate FO and PO components.

Results and Discussion

The Fe^{II} and Ni^{II} pentagonal metallacycles, **3** and **6** respectively, have been pursued as supramolecular building blocks for elaborating larger, polyhedral architectures, Figure 50. Judiciously chosen organic bridging ligands and inorganic bridging complexes were identified to impart the appropriate symmetry for polyhedral formation, and will be discussed in the following sections.

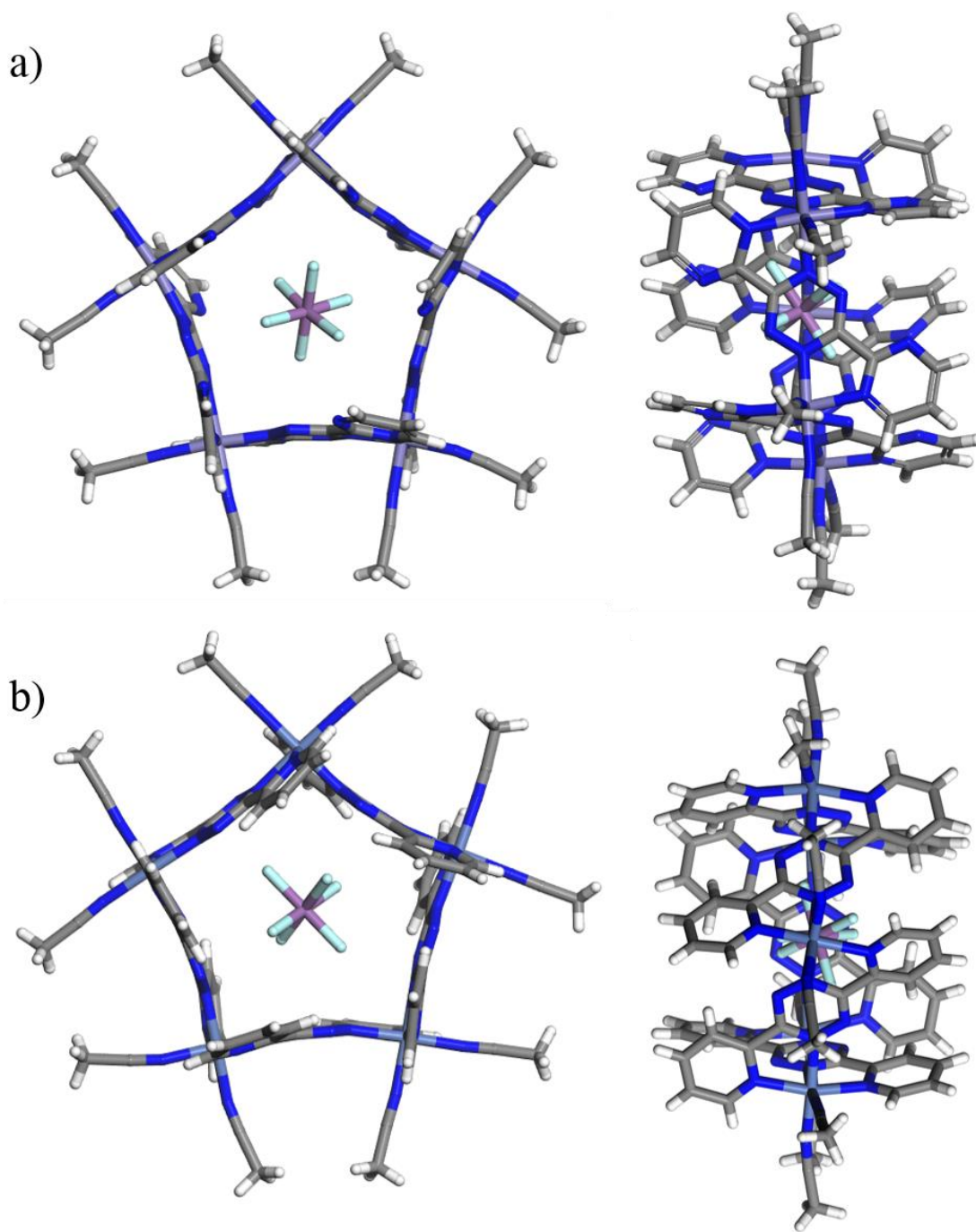


Figure 50. Metallacyclic building blocks: a) **3** with cationic framework shown for $[\text{Fe}_5^{\text{II}}(\text{bmtz})_5(\text{MeCN})_{10} \supset \text{SbF}_6]^{9+}$ ^{36d} and b) **6** with cationic framework shown for $[\text{Ni}_5^{\text{II}}(\text{bptz})_5(\text{MeCN})_{10} \supset \text{SbF}_6]^{9+}$.^{36b} Non-templating anions removed for the sake of clarity. Graphical display generated by the Materials Studio Visualizer.¹⁴

Organic bridging ligands

N-donor bridging ligands were first explored in order to provide a neutral, all-N coordination sphere and include tppz and tpphz, Figure 51. Simplified (μ -Bridging Ligand)(**3**)₂ models were developed for tppz and tpphz and FO at the NDDO/PM6/RHF level of theory^{46-47, 84} to explore the flexibility of these ligands, Figure 51.

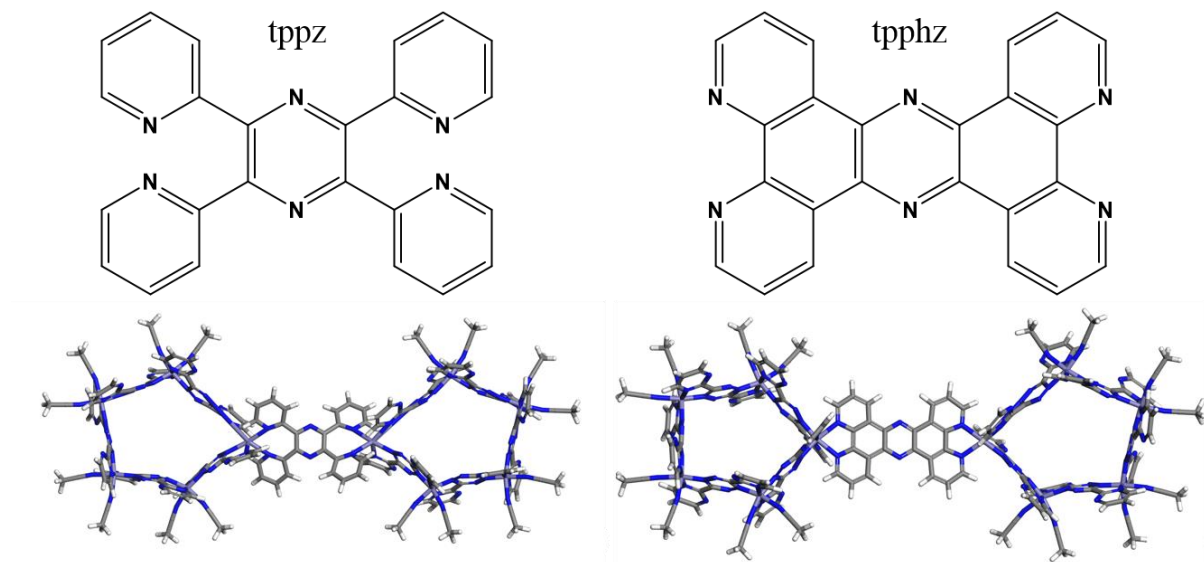


Figure 51. N-Donor ligands tppz and tpphz. Molecular structures and the optimized (μ -Bridging Ligand)(**3**)₂ models for each ligand. Graphical display generated by the Materials Studio Visualizer.¹⁴

The $(\mu\text{-tppz})(\mathbf{3})_2$ complex optimized fully but resulted in a highly strained complex, particularly at the Fe^{II} vertices that are bridged. However, the bridging ligand demonstrated a high degree of flexibility that was desired for the polyhedral bridging groups and was pursued experimentally, Figure 51. The reaction of tppz and **3** at 25°C and at 45°C caused the supramolecular metallacycle **3** to decompose into a mononuclear complex composed of two tppz molecules bound to Fe^{II} as tris-chelates, complex **18** in Table 14 and Figure 52. The resulting complex **18** is isomorphic to the $[\text{Fe}(\text{tppz})_2][\text{PF}_6]$ complex¹³² which has previously been reported. Instead of bridging the pentagonal units, the chelate effect promoted the formation of the tris-chelate complex at the expense of the bis-chelating bmtz in **3**. The $[\text{SbF}_6]^-$ anions interact closely with the pyrazine and pyridinyl groups of neighboring complexes and the anion- π interactions propagate packing of **18** in columns along the *b*-axis, Figure 52b and c. The tppz was not further explored as a bridging moiety.

Table 14. Crystallographic refinement parameters for **18 – 20**.

Compound	18	19	20
Empirical formula	C ₄₈ H ₃₂ F ₁₂ FeN ₁₂ Sb ₂	C _{71.68} H _{67.52} F _{35.77} N _{35.84} Ni ₄ Sb _{5.96}	C ₂₀ H ₄₀ N ₆ Ni
Formula weight	1304.2	3071.15	423.29
Temperature/K	111.15	100	100
Crystal system	monoclinic	triclinic	monoclinic
Space group	<i>P</i> 2 ₁ / <i>n</i>	<i>P</i> $\bar{1}$	<i>P</i> 2 ₁ / <i>n</i>
a/Å	11.4303(5)	13.007(11)	7.8833(5)
b/Å	29.4875(13)	14.953(13)	11.1725(7)
c/Å	14.2835(6)	28.39(3)	14.0195(8)
α/°	90	83.632(17)	90
β/°	99.865(2)	88.121(16)	104.830(2)
γ/°	90	77.768(15)	90
Volume/Å³	4743.1(4)	5363(8)	1193.65(13)
Z	4	2	2
ρ_{calc} g/cm³	1.826	1.902	1.178
μ/mm⁻¹	12.261	2.28	0.828
F(000)	2560	2973	460
Crystal size/mm³	0.08 × 0.07 × 0.03	0.192 × 0.09 × 0.034	0.128 × 0.112 × 0.112
Radiation	CuK α (λ = 1.54178)	MoK α (λ = 0.71073)	MoK α (λ = 0.71073)
2θ range for data collection/°	40.864 to 127.298	4.33 to 55.132	5.42 to 51.486
Index ranges	-6 ≤ <i>h</i> ≤ 11, -30 ≤ <i>k</i> ≤ 2, -15 ≤ <i>l</i> ≤ 12	-14 ≤ <i>h</i> ≤ 16, -19 ≤ <i>k</i> ≤ 13, -35 ≤ <i>l</i> ≤ 36	-9 ≤ <i>h</i> ≤ 9, -13 ≤ <i>k</i> ≤ 13, -16 ≤ <i>l</i> ≤ 17
Reflections collected	5019	26322	17152
Independent reflections	4704 [<i>R</i> _{int} = 0.0338, <i>R</i> _{sigma} = 0.0645]	19857 [<i>R</i> _{int} = 0.0188, <i>R</i> _{sigma} = 0.0556]	2274 [<i>R</i> _{int} = 0.0339, <i>R</i> _{sigma} = 0.0224]
Data/restraints/parameters	4704/0/301	19857/412/1548	2274/0/128
Goodness-of-fit on F²	1.038	1.089	0.833
Final R indexes [<i>I</i> ≥ 2σ (<i>I</i>)]	<i>R</i> ₁ = 0.1093, <i>wR</i> ₂ = 0.2765	<i>R</i> ₁ = 0.0518, <i>wR</i> ₂ = 0.1001	<i>R</i> ₁ = 0.0288, <i>wR</i> ₂ = 0.0930
Final R indexes [all data]	<i>R</i> ₁ = 0.1407, <i>wR</i> ₂ = 0.3207	<i>R</i> ₁ = 0.0760, <i>wR</i> ₂ = 0.1089	<i>R</i> ₁ = 0.0406, <i>wR</i> ₂ = 0.1038
Largest diff. peak/hole / e Å⁻³	3.30/-3.46	2.41/-0.98	0.22/-0.53

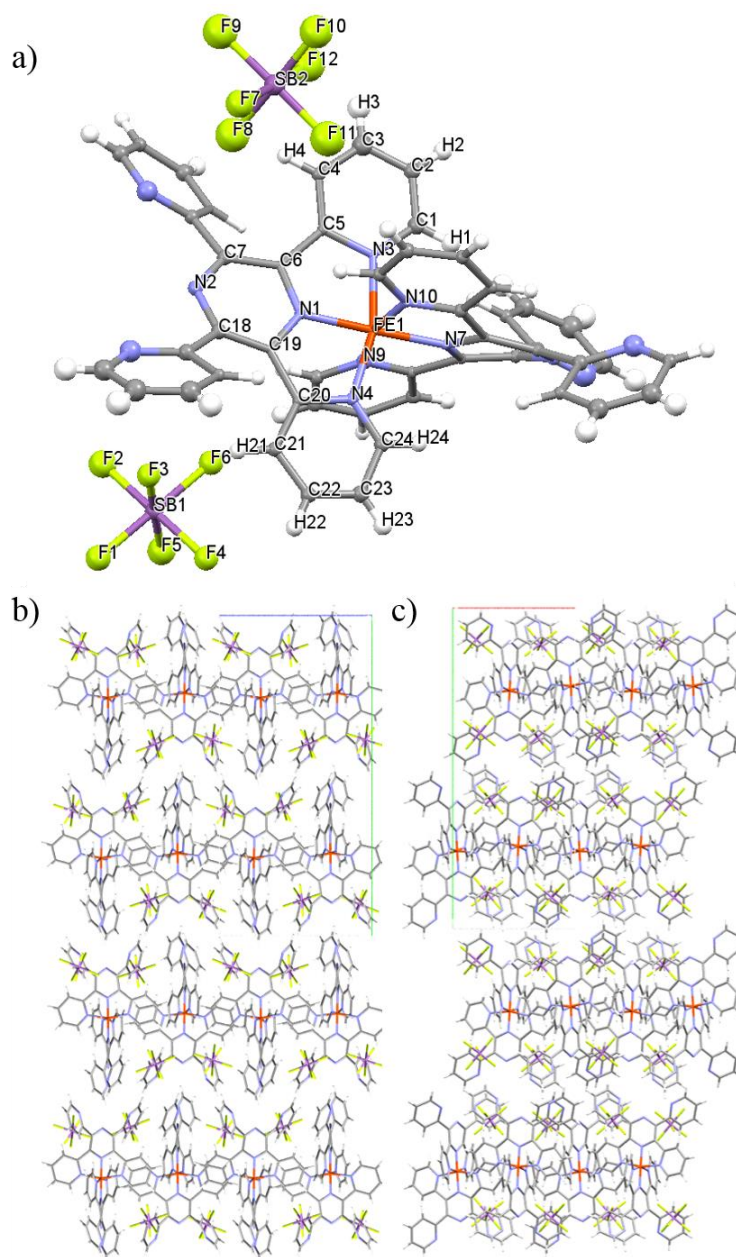


Figure 52. a) Thermal ellipsoid view of **18**. Crystal packing diagrams of **18** b) along the *a*-axis and c) along the *c*-axis. Graphical display generated by the Mercury⁹⁰ and PovRay¹³³ visualizers. Select bond distances (Å): Fe1-N1 1.862(14), Fe1-N3 1.968(13), Fe1-N4 1.947(14), N3-C1 1.36(2), N1-C6 1.37(2), Sb1-F1 1.872(14). Select bond angles (°): N1-Fe1-N3 82.0(6), N3-Fe1-N4 165.5(6), N1-Fe1-N7 178.4(6), N1-Fe1-N9 99.0(6), N3-C5-C6 114.2(14), N1-C6-C5 111.0(14), F1-Sb1-F2 90.3(6), F1-Sb1-F6 178.3(6).

The second N-donor bridged complex, $(\mu\text{-tpphz})(\mathbf{3})_2$ complex, demonstrated suitable bridging of the pentagonal metallacycles upon semi-empirical optimization, with significantly less strain at the bridged vertices, with a similar binding motif as the previously published $(\mu\text{-tpphz})\text{Ru}^{\text{II}}(2,2'\text{-bipyridine})_2$ and $(\mu\text{-tpphz})\text{Os}^{\text{II}}(2,2'\text{-bipyridine})_2$ complexes.^{128a} To further probe the propensity of tpphz to appropriately facilitate polyhedral complexation, a theoretical model of the predicted tpphz-bridged polyhedra was constructed by Dr. Steven Wheeler, Figure 53a. The final structure has a diameter of 5.43 nm.

Reactions between **3** and tpphz was performed with excess tpphz at 25°C and 45°C. The dark green 25°C and 45°C products were isolated, dropcast on separate prepared gold surfaces, and imaged by STM methods in collaboration with Dr. James Batteas by Dr. Brad Ewers, Figure 53. The structures synthesized at 25°C were imaged with a current of 250 pA at 1 V, Figure 53b. The resulting structures have an approximate diameter of 1 nm, which is similar to the size of a single pentagonal metallacycle. The pentagonal structures may be aggregating or partially bridged, but polyhedral formation is not occurring. The 45°C sample was imaged under the application of a current at 20 pA and 2 V. The structures in the image are considerable larger, and the circled structures have an average diameter of 4.6 nm, Figure 53b. While a portion of the relative increase in size may be biased from the increase in applied voltage, the size of the 45°C products appears to be roughly converging to the predicted 5.43 nm diameter of the tpphz-bridged polyhedra. The variety of product sizes that were identified highlight the need for further refinement of the synthetic conditions in order to obtain a discrete product.

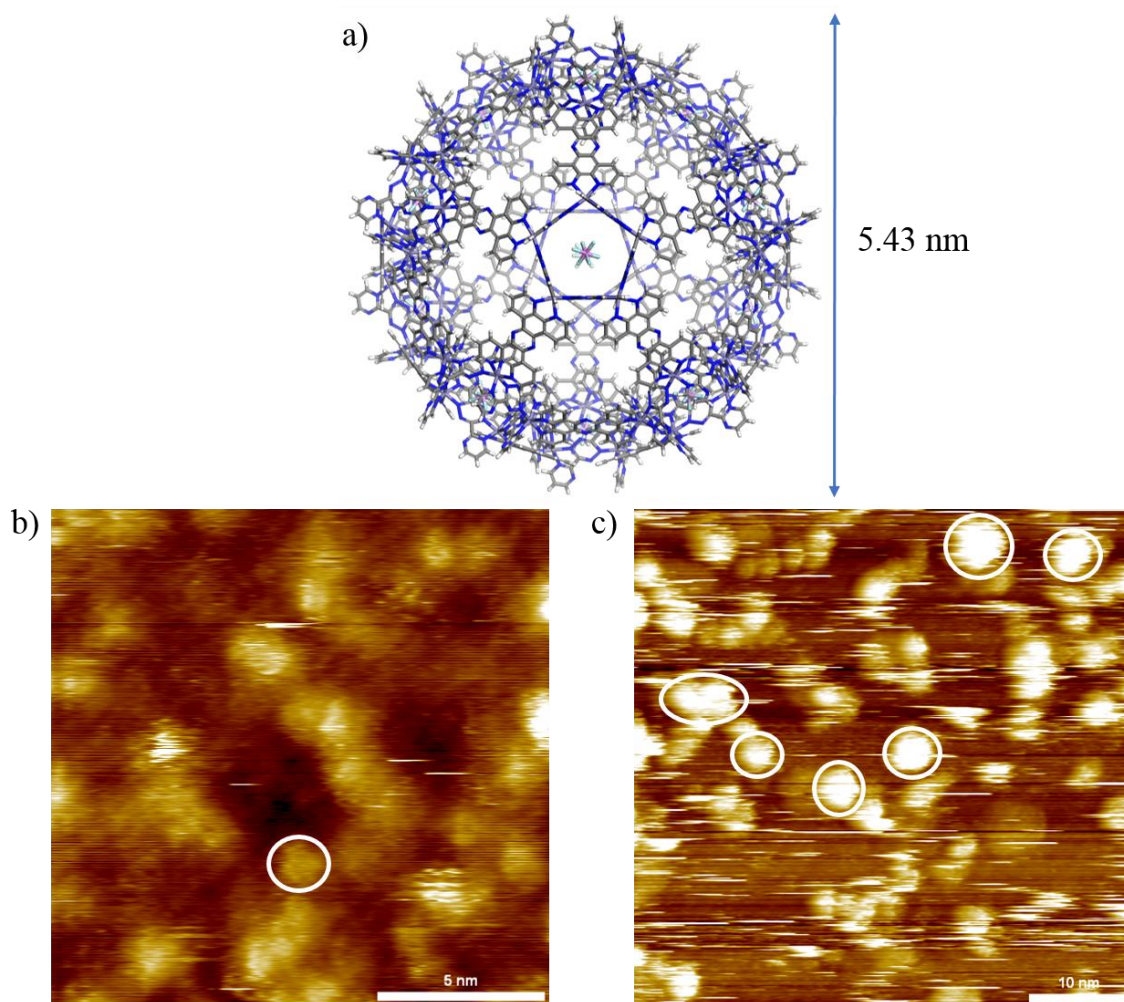


Figure 53. a) Predicted structure of tpphz+**3** with a diameter of 5.43 nm. Graphical display generated by the Materials Studio Visualizer.¹⁴ b) STM image of the 25°C tpphz+**3** product and the small structures have an approximate diameter of 1 nm. Image collected under an applied current of 1V and 250 pA. c) STM image of the 45°C tpphz+**3** product. Image collected under an applied current of 2V and 20 pA. The circled structures have an average diameter of 4.6 nm.

¹H NMR spectra were collected during the course of the 45°C reaction to more readily monitor the convergence of the tpphz+**3** reaction towards a discrete product, Figure 54. Initially, the aromatic region of the ¹H NMR spectrum contained a series of undefined resonances, Figure 54a, indicative of initial aggregation and intermediate formation identified previously by STM in Figure 53a. Upon progression of the tpphz+**3** reaction, the region of resonances converged to a series of distinct resonances which is indicative of a single product, Figure 54b. As the reaction continued at 45°C for several weeks, a red solid precipitated from the dark green reaction solution that was only soluble in DMSO. The breadth of the aromatic region and lack of distinguishable peaks indicated that the dark green complex previously characterized had decomposed into a series of decomposition products, Figure 54c. Following similar reaction conditions, the tpphz+**3** reaction was performed at 65°C and probed by ¹H NMR spectroscopy, Figure 54d. The resonances at 7.67 and 8.88 ppm indicate that much of **3** decomposed into free bmtz at such high temperature, but a small portion of the “final” tpphz+**3** product was observed, with particular clarity in the 7 – 7.5 ppm region.

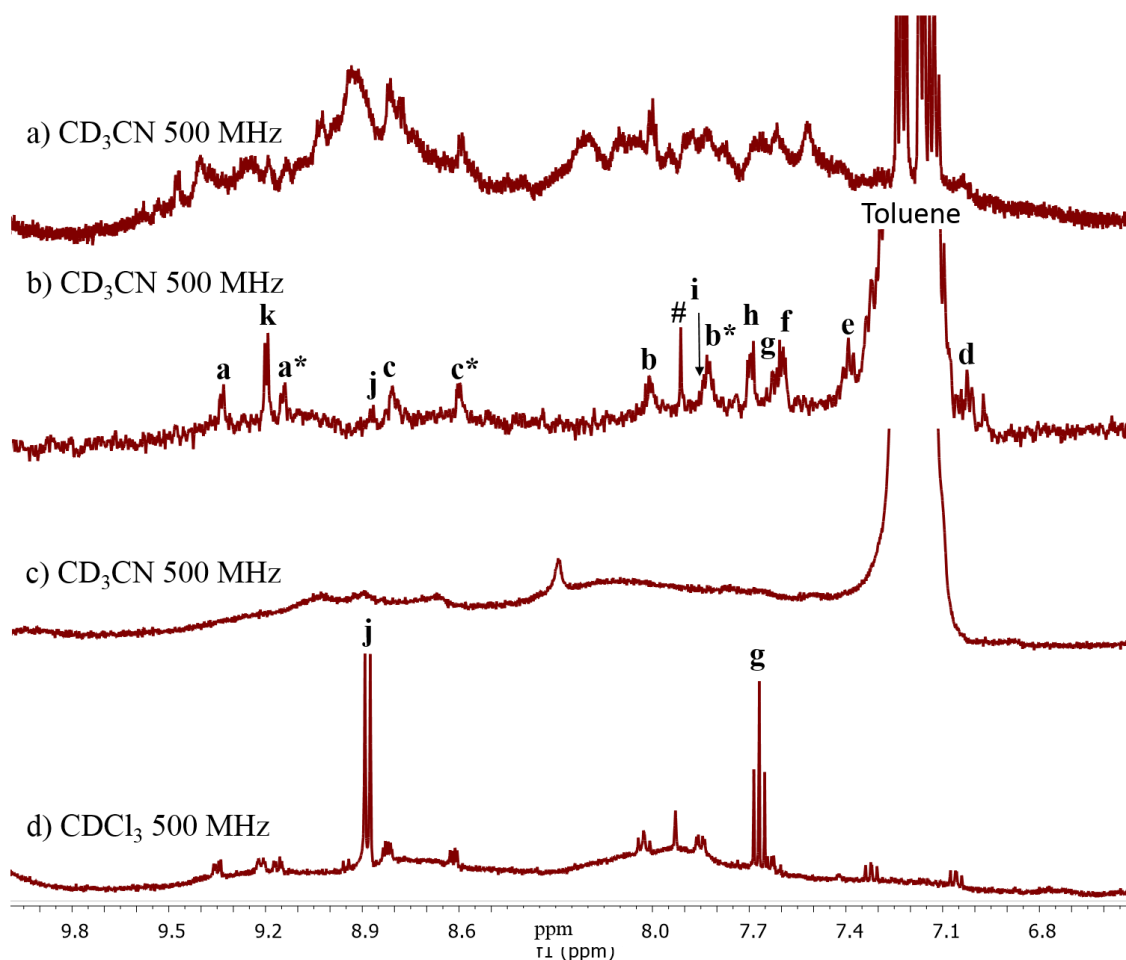


Figure 54. NMR of tpphz+3 reaction at several stages: a) initial, b) final product, c) decomposition product, d) overheated but residual final product.

As labeled in Figure 54b, Resonances **a**, **b** and **c** are attributed to the 4/4', 5/5', and 6/6' bmtz proton resonances of $\mathbf{3}^{36d}$. Resonances **a***, **b*** and **c*** correspond to the 4/4', 5/5', and 6/6' proton resonances of $\mathbf{3}^{36d}$ that are shifted upfield by 0.5 ppm. The resonances, **d** – **f** and **h**, have been attributed to the tpphz ligand but the assignments remain ambiguous. Due to the decomposition of the complex in Figure 54d, the resonances labeled by **g** and **j** have been attributed to free bmtz, despite the upfield shift by 0.2 ppm

of the resonance at 8.9 ppm that corresponds to the 4/6 protons of bmtz. Furthermore, as identified by ^1H COSY-NMR, *vide infra*, resonances **i** and **k** correspond to two coupled groups of protons that are shifted downfield from the expected bmtz resonances by 0.1 – 0.2 ppm. Due to the proportional relationship of these resonances to **a-c**, **a*-c***, **d-f** and **h** in Figure 54b and Figure 54d, these resonances may correspond to a symmetrically bound bmtz ligand. Overall, structural assignments based on this series of NMR spectra remain ambiguous.

From the series of ^1H NMR spectra, resonances for both the bmtz and tp-phz ligands indicate coordination at the Fe^{II} vertices. The presence of the **3** and “shifted **3**” resonances suggests that the pentagonal structure is intact but possibly being shielded on one side by the presence of the tp-phz ligand. This could occur upon binding and bending of the tp-phz such that tp-phz more closely contacts and shields the “interior” bmtz protons upon formation of a polyhedral structure. If a polyhedron was being formed, the symmetry of the tp-phz ligand would be expected to be expressed by three resonances at a 2:1 ratio with each of the bmtz proton resonances, however, six resonances have been attributed to the tp-phz ligand and the integration is not 2:1. Determining the exact integration for the resonances was challenging due to the poor resolution of the NMR spectra in Figure 54b, but the approximate integration of **a – c**, **a***, and **c*** is 1:1. **d – f** and **h** integrate to approximately 1.5 – 2 and **i** is a shoulder for **b***. The NMR spectrum in Figure 54d shows separation between **b*** and **i** and the approximate integration is 1 for both. The resonances could indicate that the tp-phz is non-symmetrically binding at the Fe^{II} vertex and forming an alternative structure, i.e. $[\text{Fe}^{\text{II}}(\text{bmtz})_2(\text{tp-phz})]^{2+}$ or $[(\mu\text{-tp-phz})(\text{Fe}^{\text{II}}(\text{bmtz})_2)_2]^{4+}$.

UV-visible spectrometry was also performed to qualitatively monitor the progression of the tpphz+**3** reaction at 45°C. As can be seen in Figure 55, the absorbance at 575 nm, characteristic of **3**, shifts over the course of the reaction to 652 nm. Additionally, two bands appear at 480 nm and 530 nm. The work by Bolger and coworkers identifies that, for Ru^{II}, two bands in the 400 – 550 nm range are indicative of the [(μ-tpphz)(Ru(bpy)₂)₂]⁴⁺ complex, but for Os^{II}, two bands in the 400 – 550 nm region occur for both the [(μ-tpphz)(Os(bpy)₂)₂]⁴⁺ and [Os(bpy)₂(tpphz)]²⁺ complexes. Absorbance at higher wavelengths of 620 – 640 nm only occurred upon complexation of the tpphz ligand to the transition metals. Additionally, the free ligand was ruled out because it was previously characterized and only exhibits absorption bands at wavelengths less than 380 nm. The absorption spectra of tpphz+**3** support the coordination of bmtz and tpphz at the Fe^{II} centers, but the mode of coordination was unable to be clarified. Furthermore, the broad absorbance of this complex in the visible range prevented dynamic light scattering from providing structural information because the wavelengths of the lasers available for this method were fully absorbed by the complex instead of being scattered.

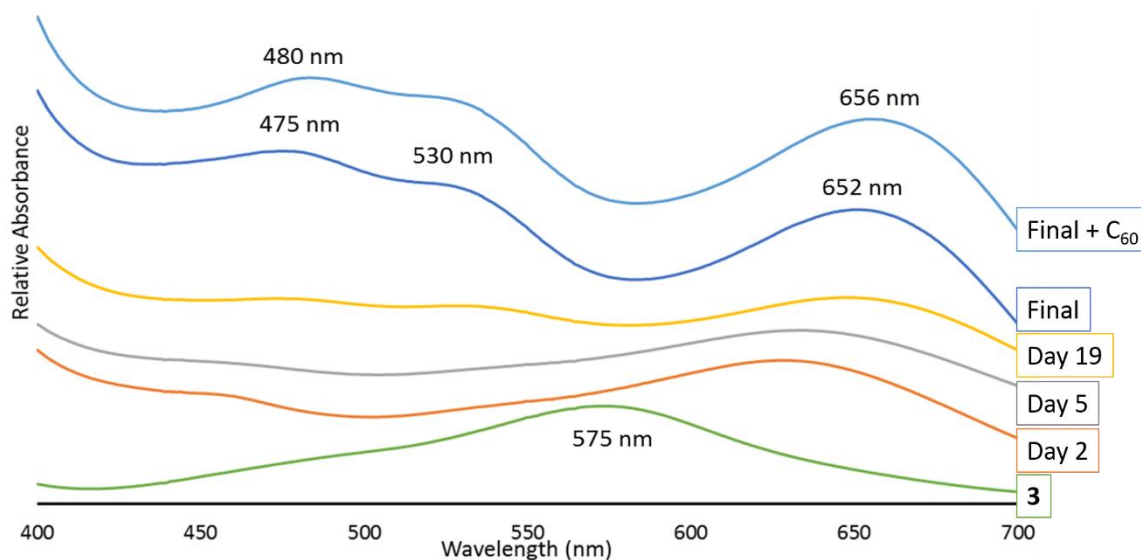


Figure 55. Qualitative UV-visible spectral analysis during the course of the tpphz+**3** reaction at 45°C.

In an attempt to provide a templating agent to stabilize the sensitive tpphz+**3** product, buckminsterfullerene, C₆₀, was included in the reaction of tpphz and **3**. According to the UV-visible spectrum, the product converged to a similar structure, Figure 55, but there was no appreciable stability gained by the template. The C₆₀ molecule has a diameter of approximately one quarter the size of the internal diameter of the predicted polyhedral structure and is likely too small to provide adequate stability. This method of stabilization was not pursued further.

While crystallization methods continue, additional bridging ligands were considered. Anionic, O-donors were considered as bridging ligands because the dicarboxylate ligands have been shown to provide strong coordination and access to varying degrees of flexibility. The scope of O-donor bridging ligands included tpa acid

(and tetrabutylammonium terephthalate, $[\text{Bu}_4\text{N}]_2[\text{tpa}]$), adipic acid, glutaric acid and succinic acid, Figure 56. (μ -Bridging Ligand)($\mathbf{3}$) $_2$ models were optimized for each of the deprotonated, bis-bidentate ligands terephthalate, adipate, glutarate and succinate. The simplified models were FO at the NDDO/PM6/RHF level of theory.^{46-47, 84}

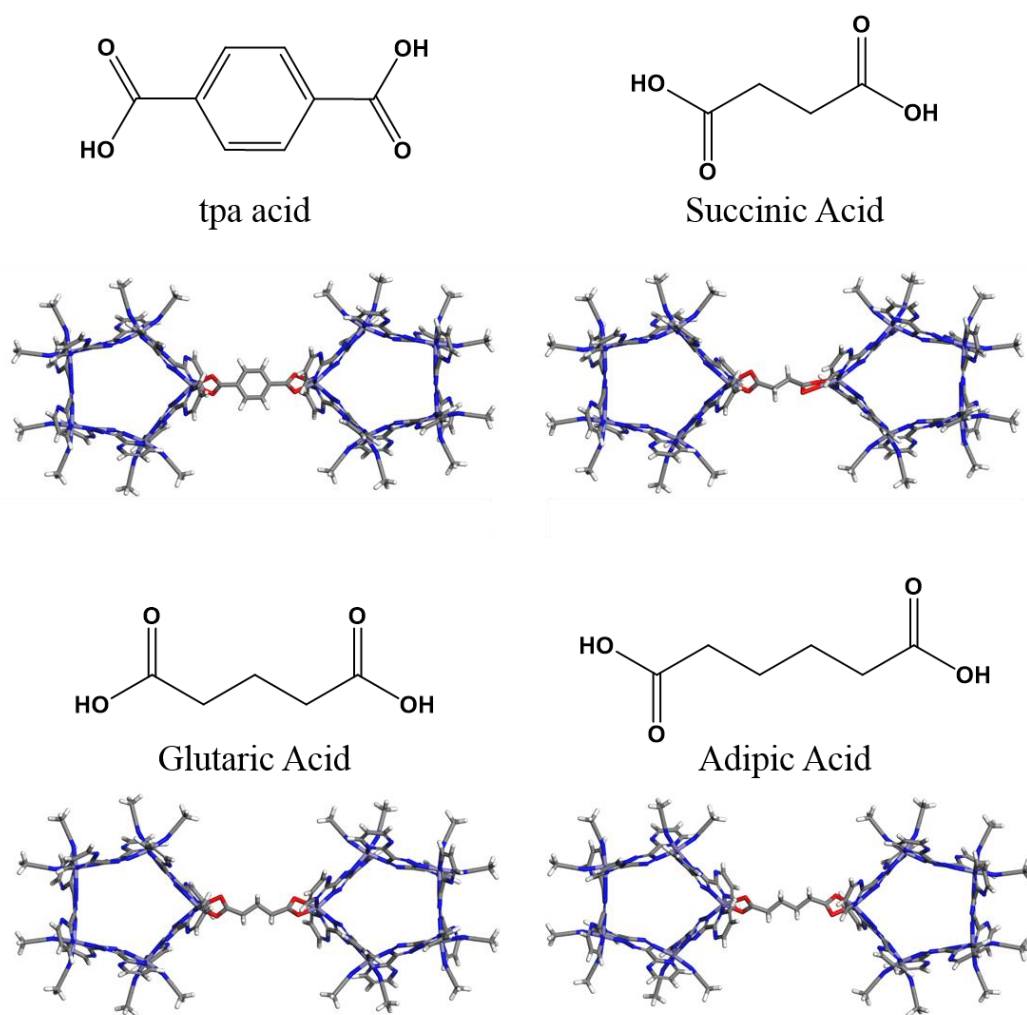


Figure 56. O-Donor ligands tpa acid, succinic acid, glutaric acid and adipic acid. Molecular structures and the optimized (μ -Bridging Ligand)($\mathbf{3}$) $_2$ models for each ligand.

The aliphatic bridging ligands, including adipate, glutarate and succinate, are very flexible and were expected to allow the necessary movement of the metallacycle building blocks upon reaction. Preliminary reactions of the dicarboxylic acids, $[\text{nBu}_4\text{N}]_2[\text{succinate}]$ and $[\text{Na}]_2[\text{succinate}]$ were performed following the typical reaction conditions outlined for tpa acid+**3** and $[\text{nBu}_4\text{N}][\text{tpa}]+\mathbf{3}$. The reaction products were analyzed using AFM methods by Ms. Alison Pawlicki in Dr. Batteas' lab in non-contact mode with less than 1 nN of applied force. The reactions did not promote polyhedral formation, but instead resulted in two major products, a smaller structure (3 nm diameter) and a larger, asymmetric oligomeric type formation (7 – 16 nm in diameter), as exemplified by the image of the adipic acid+**3** reaction product in Figure 57.

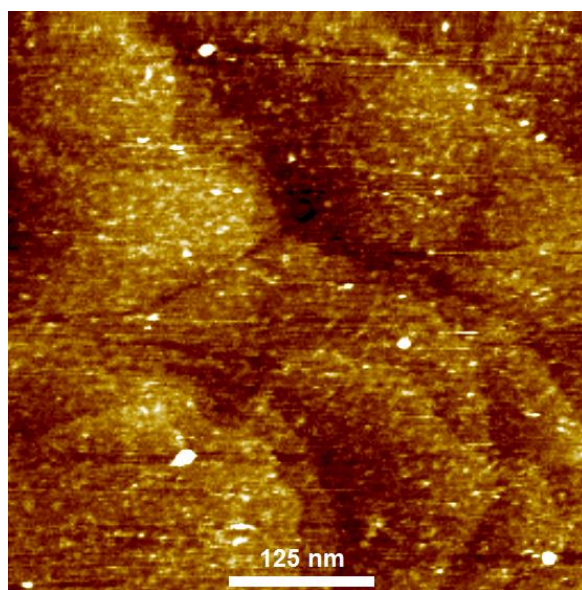


Figure 57. AFM image of adipic acid+**3** product. Image collected in non-contact mode under an applied force load of <1nN.

The O-donor bridged complex $(\mu\text{-tpa})(\mathbf{3})_2$ was optimized to an ideal coordination and bridging geometry, which supported the use of tpa as a bridging moiety due to the appropriate size and flexibility of the ligand. Furthermore, a theoretical model of the predicted tpa-bridged polyhedra was successfully constructed by Dr. Steven Wheeler. The final structure has a diameter of 5.02 nm, Figure 58a.

The initial reaction of tpa acid+ $\mathbf{3}$ was performed with excess ligand to encourage coordination and at 25°C. The reaction immediately aggregated and polymerized into an insoluble product. In order to slow down this reaction and promote the formation of a discrete, stable product, the reaction was performed in an acetonitrile-liquid nitrogen slush bath at -82°C and slowly warmed to room temperature overnight. The resulting dark precipitate was entirely insoluble, but was drop-cast on HOPG and Au(111) on mica surfaces for analysis by AFM and STM methods by Dr. Brad Ewers, Ph.D., of the Batteas group.

The HOPG surface was first imaged by AFM methods in contact mode under less than 1 nN force load, Figure 58b. The structures did not demonstrate significant adherence to the HOPG surface, likely due to the protruding bmtz ligands that preclude the complex from anchoring to the surface. The bright white line is a single structure that is being pushed across the HOPG surface by the tip AFM cantilever arm. The diameter was unable to be accurately measured since the sample was moving, but the height was measured along the blue, red and pink traces. From these traces, the height of the structure was determined to be approximately 4.5 – 5 nm, Figure 58c, and is strikingly similar to the predicted height of 5.02 nm, Figure 58a.

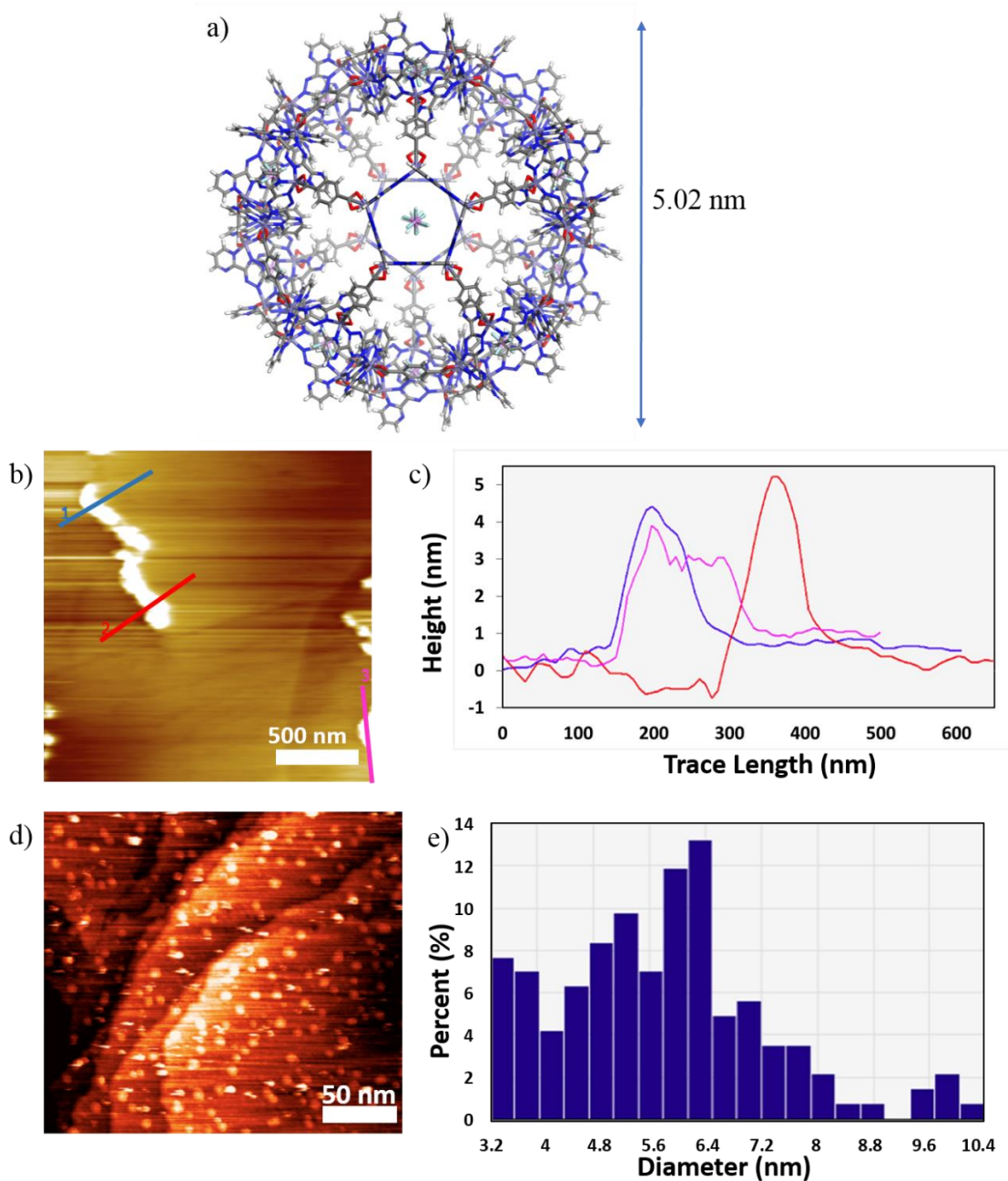


Figure 58. a) Predicted structure of tpa+3 with a diameter of 5.02 nm. Graphical display generated by the Materials Studio Visualizer.¹⁴ b) AFM image of the tpa acid+3 product drop-cast on the HOPG surface. Image collected in contact mode with <1nN force load. c) Analysis of trace height across the product. d) STM image of the tpa acid+3 product drop-cast on gold surface. Image collected under an applied current of 1 nA at 0.5 V. e) Histogram analysis of the diameter of the identified structures.

The sample on the Au(111) on mica surface was imaged by STM methods, with an applied current of 0.5 V and 1 nA, Figure 58d. The width of the bright white spots, denoting the sample, were measured and tabulated in the histogram in Figure 58e. The histogram demonstrates that a series of structures with various sizes are forming, instead of the desired discrete product. Regardless, the majority of the products have a diameter between 4.5 and 6.5 nm, which is similar to the predicted polyhedral diameter.

The data and images for the reaction of tpa acid+**3** suggest that a portion of the polyhedral structures were being formed, Figure 58. In order to mediate the insolubility of the final product and to remove the presence of DMSO from the reaction (to dissolve tpa acid), the tetrabutylammonium terephthalate salt was synthesized and used in the remaining reactions. The reaction of $[\text{Bu}_4\text{N}]_2[\text{tpa}]+\mathbf{3}$ did not go to completion in the liquid N_2 /acetonitrile slush bath, but, instead, required heating at 45°C. The final dark green product was isolated with toluene and characterized by ^1H NMR, Figure 59a. The $[\text{Bu}_4\text{N}]_2[\text{tpa}]+\mathbf{3}$ product exhibits similar resonances to the product of tpphz+**3**, Figure 54. As in the ^1H NMR spectra for tpphz+**3**, many of the resonances can be identified as free bmtz (*), a benzene impurity (#), **3** (**a** – **c**) and **3** that is shifted down-field (**a*** – **c***). The resonances labeled by **d** – **h** in Figure 59a were initially ascribed to the tpa ligand, but there are only four (typically symmetric) protons on the ligand. Therefore, not all of the resonances can describe this ligand and must be characteristic of another species. The integration between each resonance included in **a** – **c**, **a*** – **c***, and **d** – **g** has a ratio of 1:1. **f** has an integration of 0.5 and **h** has a relative integration of 2. The **h** and **g** resonances at 9.21 and 7.83 integrate in a 2:1 ratio with each other and could be indicative of a secondary

bmtz ligand that is shifted downfield by approximately 0.1 ppm. The “shifted bmtz” could also be indicative of non-coordinated pyrimidine rings from the mononuclear complex $[\text{Fe}^{\text{II}}(\text{bmtz})_2(\text{tpa})(\text{MeCN})]$. ^1H -COSY NMR spectroscopy was performed to identify the protons resonances that are correlated to each other with the intention of illuminating the structure, Figure 59b. The resulting off-diagonal peaks show correlation between several of the bmtz and shifted-bmtz resonances and $[\text{tpa}]^{2-}$ resonances, Figure 59 and Table 15. The ^1H -COSY NMR spectra supports that there is coordination of bmtz and tpphz at the Fe^{II} vertices but is inconclusive as to the overall structure formed.

In collaboration with Alison Pawlicki, Ph.D. Candidate and NSF Fellow, in Dr. Batteas’ lab, AFM images were collected of the $[\text{nBu}_4\text{N}]_2[\text{tpa}]+3$ sample. The sample was drop-cast on HOPG, submerged in ethanol in order to more gently probe the size of the particles and imaged in non-contact mode under a force load of less than 1nN. The resulting images of the sample identified stacks of compounds with heights that are a multiple of 0.7 Å and that have a range of diameters from 20 – 40 nm, Figure 60. There was, therefore, no evidence of polyhedral formation, possibly due to decomposition in ethanol or because the polyhedral structures are not in fact being formed.

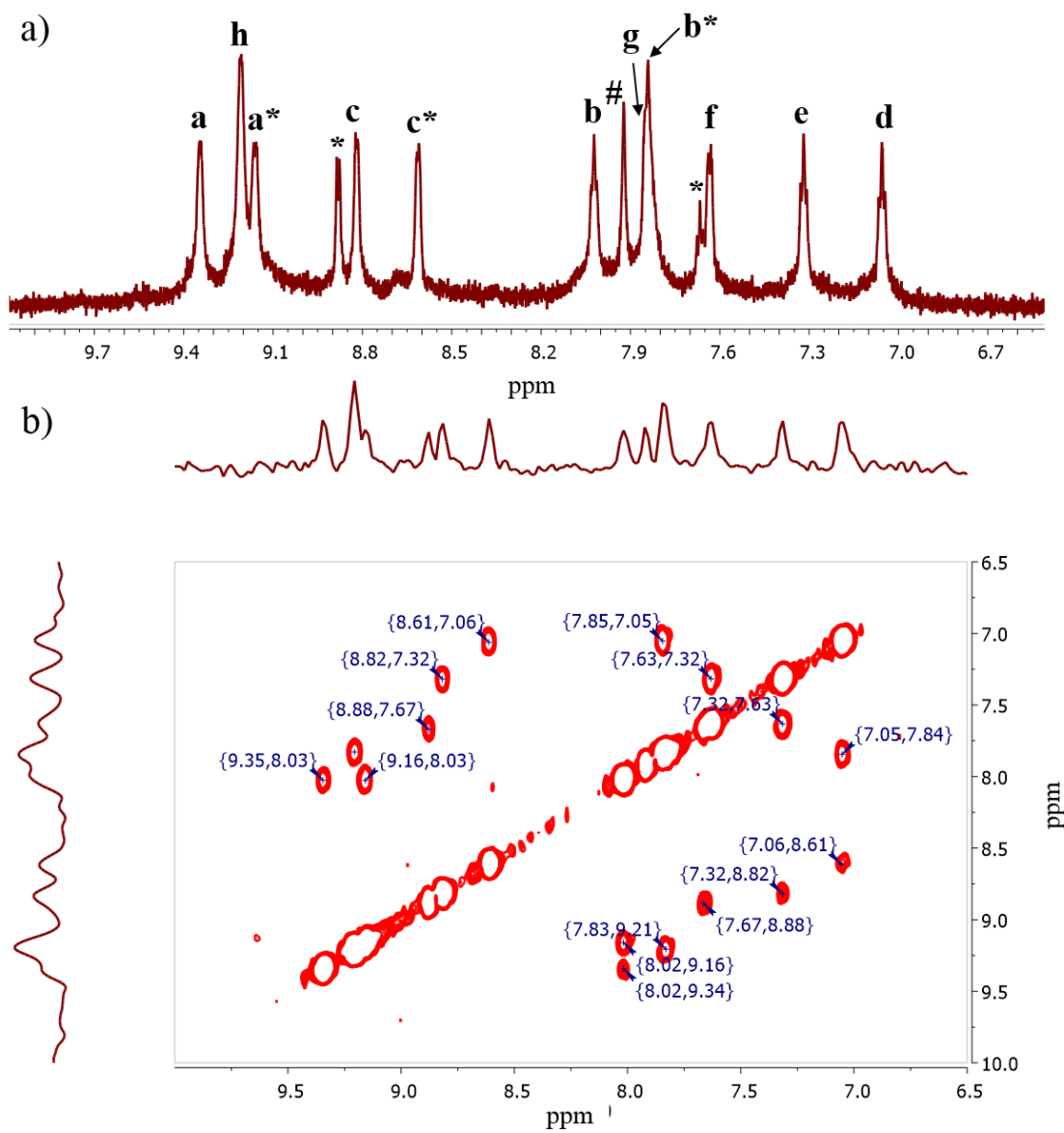
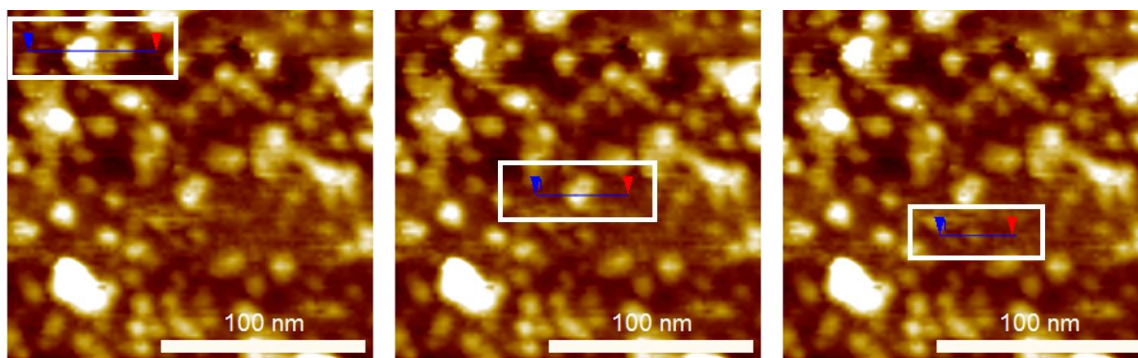


Figure 59. NMR spectra of $[\text{nBu}_4\text{N}]_2[\text{tpa}] + 3$. a) ^1H NMR and b) ^1H -COSY NMR.

Table 15. Assignment of ^1H -COSY Correlations for the $[\text{Bu}_4\text{N}]_2[\text{tpa}]+3$ sample.

Correlation	Label	Assignment
7.63 – 7.32	f – e	tpa – tpa
7.85 – 7.05	g or b* – d	tpa or (5/5')* - tpa
8.61 – 7.06	c* – d	(6/6')* - tpa
8.82 – 7.32	c – e	6/6' – tpa
8.88 – 7.67	“Free” bmtz	4/6 – 5
9.16 – 8.03	a* – b	(4/4')* - 5/5'
9.21 – 7.83	h – g	“shifted bmtz”
9.35 – 8.03	a – b	4/4' – 5/5'



Height: 2.8 nm

Height: 1.4 nm

Height: 0.74 nm

Figure 60. AFM images of $[\text{Bu}_4\text{N}]_2[\text{tpa}]+3$ product. Image collected in non-contact mode under an applied force load of $<1\text{nN}$.

Due to the inconclusive imaging and solution studies, computational efforts were pursued using DFT to probe the energy associated with tpa coordination and bending at a single Fe^{II} vertex. Model structures of the vertices A, B and Int were created from the crystal structure of **3** and the predicted tpa-bridged polyhedral structure and PO as described previously. The tpa ligand was modeled by one benzoate anion, and the benzoate and acetonitrile moieties were FO. The final energies of the PO vertices and FO structures were evaluated to determine the binding energy (ΔE_{A-Int}), bending energy (ΔE_{Int-B}), and overall bridging energy (ΔE_{A-B}) of tpa (modeled by benzoate) at each Fe^{II} vertex, Figure 61. The ΔE_{A-Int} , -147.42 kcal/mol, was more energetically favorable than the ΔE_{A-B} , -35.51 kcal/mol. The difference in energy between Vertex Int and B, ΔE_{Int-B} , was attributed to the bending of the tpa group, 111.91 kcal/mol. The formation of the significantly more thermodynamically Vertex Int at each pentagonal vertex would likely preclude the steric strain required for polyhedral formation. Performing the reaction of [ⁿBu₄N]₂[tpa]+**3** at 45°C may provide enough energy to promote the formation of polyhedral architectures, but the strain associated with bending the bridging ligand to accommodate to the polyhedral vertex B likely contributes to the facile decomposition of the reaction products. The AFM and STM images in combination with the experimental and theoretical efforts remain inconclusive and additional experimental studies are required to identify the final tpphz+**3** and [ⁿBu₄N]₂[tpa]+**3** structures.

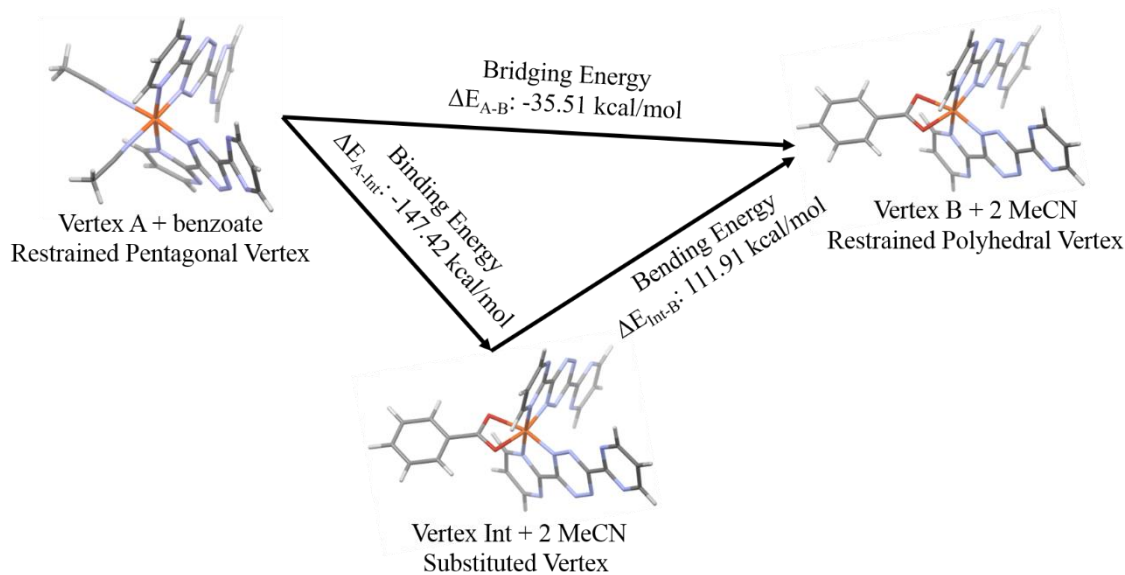


Figure 61. DFT analysis of the energetic favorability of tpa bridging, binding and bending. tpa modeled as benzoate.

Inorganic bridging complexes

Cyano-metallates were also pursued as linear bridging groups to explore the possible architectures and magnetic properties afforded by the complex ions. Magnetic coupling was envisioned between the unpaired electrons of the paramagnetic Ni^{II} and 4d/5d transition metals through the cyanide ligand. Cyanide has been shown to provide strong ferromagnetic or antiferromagnetic coupling, depending on the nature of the orbitals involved in the coupling.¹³⁴ While the remainder of this chapter is focused on the architectural challenge of using cyano-metallates as bridging groups, there are several examples of strong cyanide coupling in the literature, in particular by the Dunbar group.^{134a} As a proof of concept, the $(\mu\text{-Os}(\text{CN})_6)(\mathbf{6})_2$ complex was optimized at the NDDO/PM6/UHF^{46-47, 85} level of theory in Materials Studio 7.0¹⁴, Figure 62.

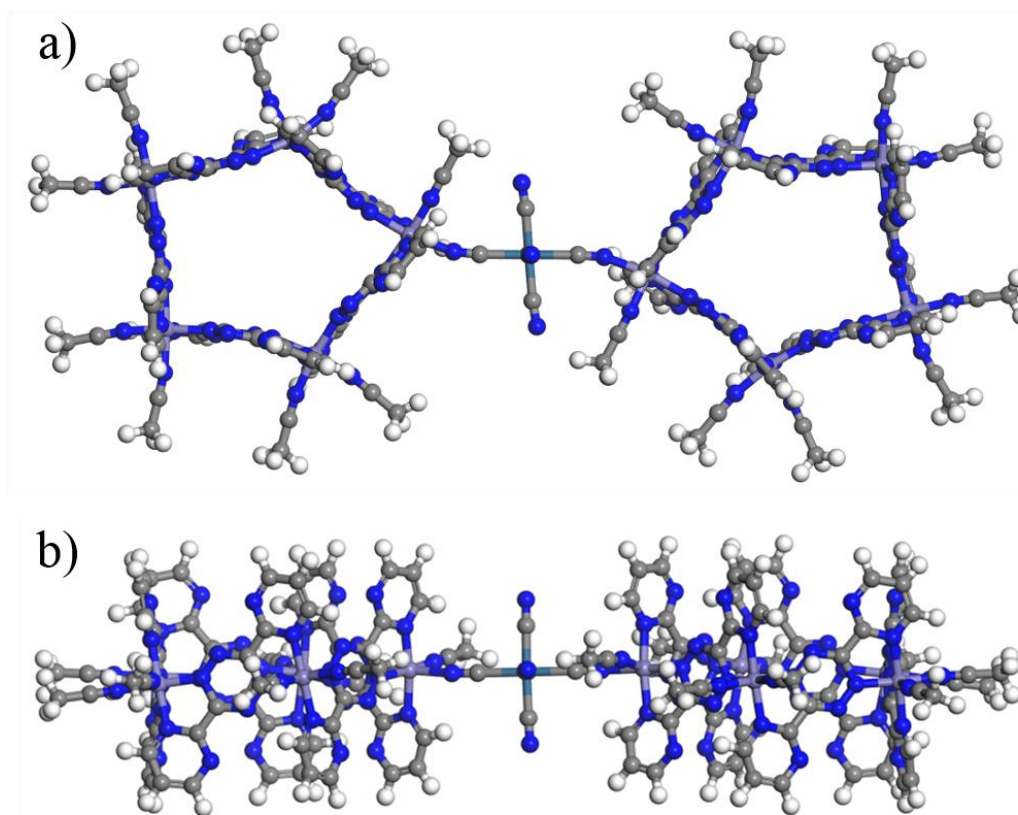


Figure 62. The a) top and b) profile views of the optimized $(\mu\text{-Os}(\text{CN})_6)(\mathbf{6})_2$ complex at the NDDO/PM6/UHF^{46-47, 85} level of theory in Materials Studio 7.0¹⁴. Graphical display generated by the Materials Studio Visualizer.¹⁴

The octahedral cyano-metallate was predicted to bridge the pentagonal architectures with only moderate distortion at the Ni^{II} vertices. While the formation of $\text{Os}(\text{CN})_6$ -bridged polyhedra were the eventual goal, the $(\mu\text{-Os}(\text{CN})_6)(\mathbf{6})_2$ complex was first to probe the ability of the $[\text{Os}(\text{CN})_6]^{3-}$ group to coordinate and bridge **6**. The 1:2 reaction between $[\text{PPN}]_3[\text{Os}(\text{CN})_6]$ and **6** was performed in acetonitrile, and, over the course of a week, the reaction solution darkened to a deep amber color. The product was concentrated,

crystallized with toluene, and analyzed with X-ray diffraction methods in collaboration with Dr. Brian Dolinar, a member of the Dunbar group.

The resulting structure underwent supramolecular rearrangement in solution and resulted in the first supramolecular rectangle with a formula of $[\text{Ni}_4^{\text{II}}(\text{bptz})_2(\text{bptz})^-]_2(\text{MeCN})_8 \supset \text{MeCN}][\text{SbF}_6]_6$, **19**, as further described by Table 14, Table 16, Table 17, Figure 63 and Figure 64. Several of the $[\text{SbF}_6]^-$ anions exhibited positional disorder and were modeled using bond length and thermal parameter restraints. Likewise, the non-templating acetonitrile ligands demonstrated partial occupancy between the three solvent molecules. The disordered solvent molecules were modeled with thermal parameter restraints and an idealized geometry.¹³⁵

The resulting metallacycle framework consists of four Ni^{II} ions, two neutral bptz ligands and two reduced radical bptz^- ligands and the structure is formed around an acetonitrile molecule. From the well-refined structure (Figure 63), the average N-N bond distance for the neutral bptz ligands was 1.31 Å, and the average N-N bond distance for the reduced bptz^- ligands was 1.38 Å (Table 16), similar to that reported for other radical bptz complexes.¹³⁶ The presence of only six $[\text{SbF}_6]^-$ anions further suggests that the metallacyclic framework contains two radical ligands. The reduction of the bptz ligand was not likely facilitated by the trivalent osmium complex, but may have occurred spontaneously or at the expense of a sacrificial moiety in solution, as has been observed for bmtz.^{110, 137} Oxidation of the rectangular metallacycle was expected to be rather facile, supported by the formation of an alternative solvate of **6** upon performing the reaction between $[\text{PPN}]_3[\text{Os}(\text{CN})_6]$ and **6** under less scrupulously dry conditions.

The thermal ellipsoids of the templating acetonitrile molecule appear to be elongated in the direction of the neutral bptz indicating that the solvent molecule is slightly disordered within the cavity along the direction with the most space, Figure 64. Shionoya and coworkers were able to synthesize a square Zn^{II} metallacycle without a templating moiety⁶⁸, but this rectangular metallacycle is the first metallacycle templated around an acetonitrile molecule. The reduced framework retains a positive charge overall but the close-contact of the neutral acetonitrile with the reduced bridging ligands is favored over the $[\text{BF}_4]^-$ anion. This structure will be further evaluated through theoretical and experimental means in the future to continue deconvoluting the roles of size and symmetry in the templation of metallacycles. While osmium-cyanometallate coordination did not occur, the rectangular metallacycle **19** is the first example of a bptz- or bmtz-bridged metallacycle with reduced bridging ligands. This provides future opportunities for exploring the coupling between paramagnetic Ni^{II} centers by the reduced bptz ligand. This study of the ligand radical mediated $\text{Ni}^{\text{II}}\text{-Ni}^{\text{II}}$ coupling will likely result in improved magnetic behavior compared with the neutral bridged compound **4**.^{36a}

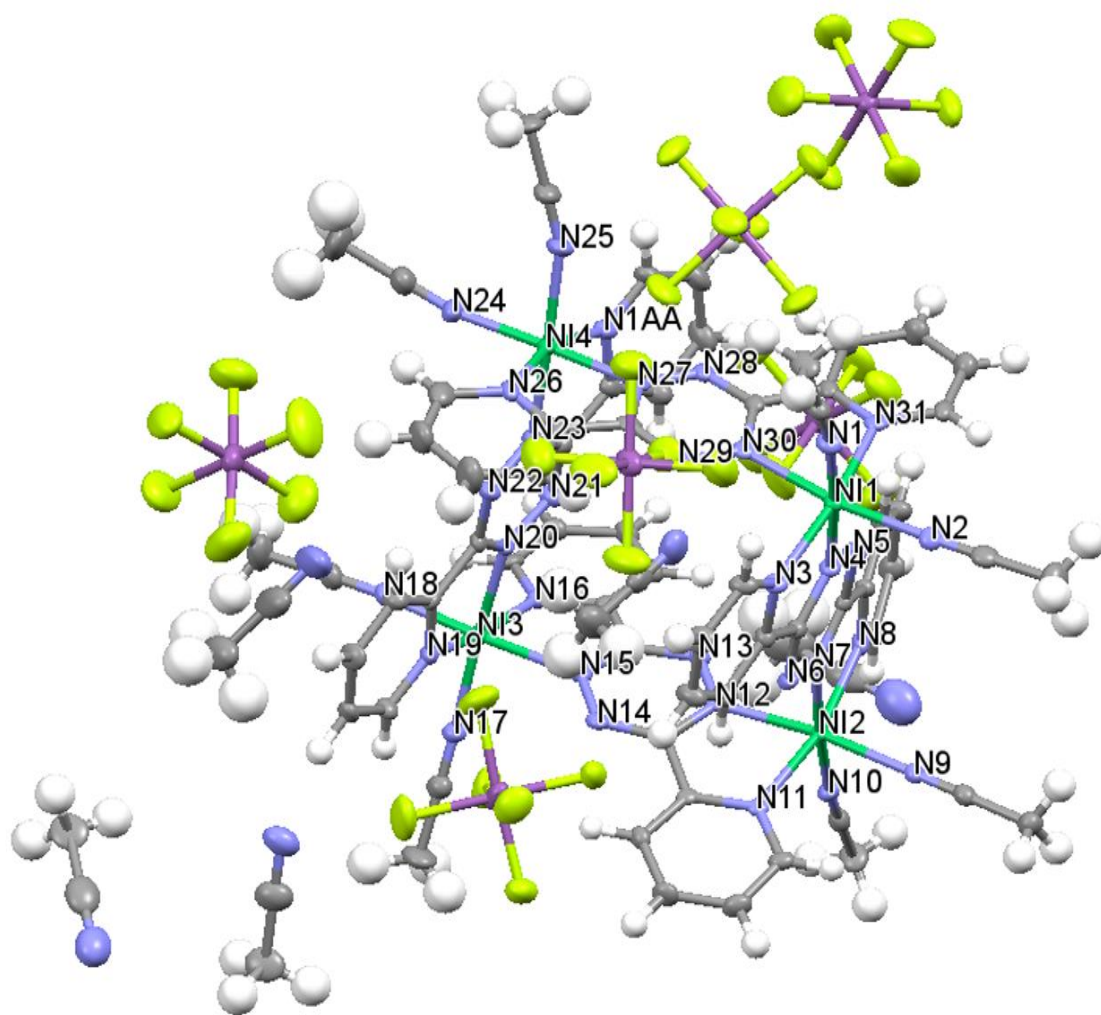


Figure 63. Thermal ellipsoid view of the asymmetric unit of **19**. Graphical display generated by the Mercury⁹⁰ visualizer.

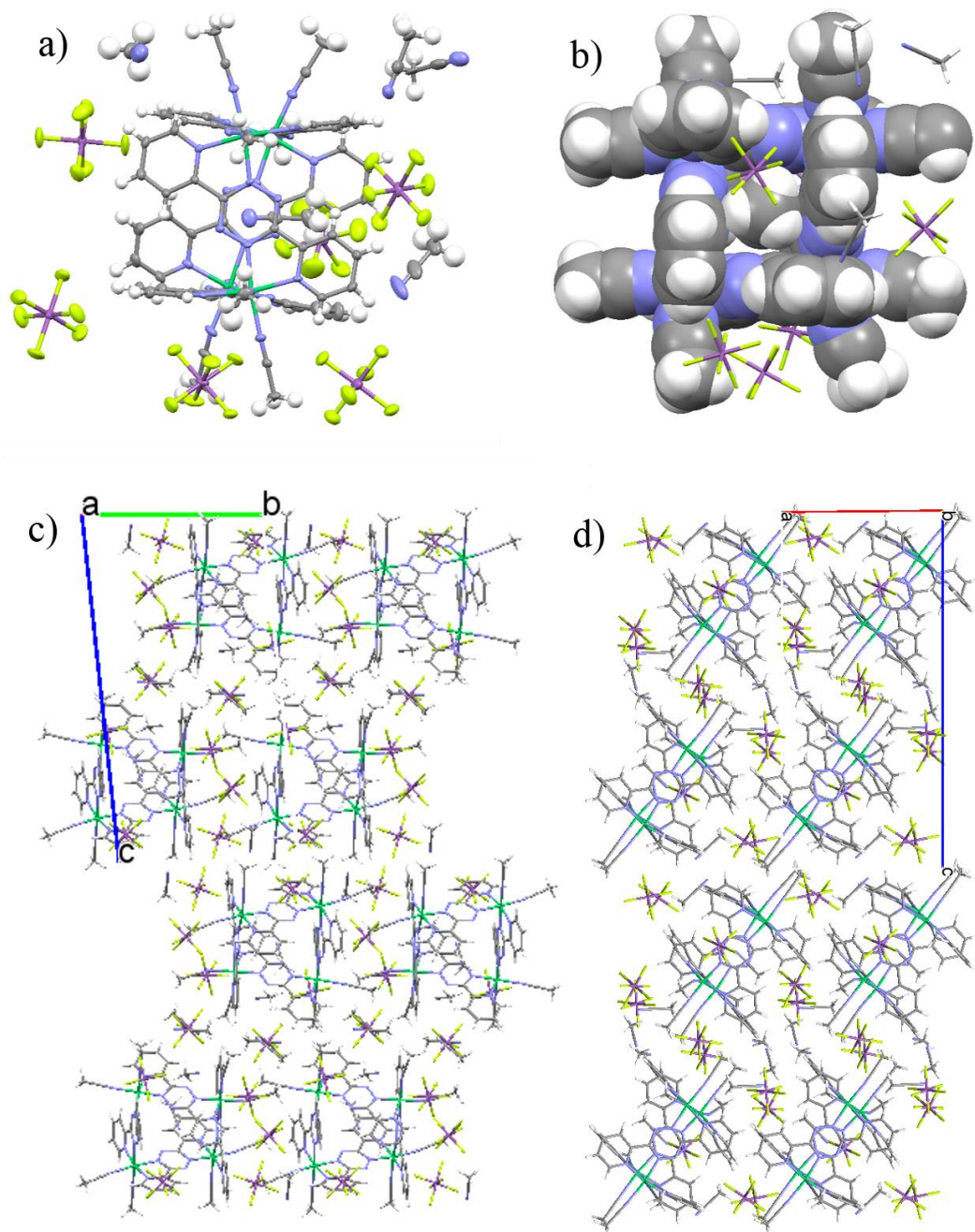


Figure 64. a) Thermal ellipsoid view of the profile view of **19**. b) Space-filling view of the framework of **19**, showing close-assembly around the encapsulated acetonitrile molecule. Crystal packing diagrams of **19** c) along the a-axis and d) along the b-axis. Graphical display generated by the Mercury⁹⁰ visualizer.

Table 16. Select Ni-N and N-N bond lengths (Å) of **19**.

Atom	Atom	Length/Å	Atom	Atom	Length/Å	Atom	Atom	Length/Å
Ni1	N1	2.048(5)	Ni4	N1AA	2.083(6)	N15	C27	1.337(8)
Ni1	N2	2.051(6)	Ni4	N23	2.023(5)	N20	N21	1.384(6)
Ni1	N3	2.074(5)	Ni4	N24	2.038(6)	N20	C42	1.342(7)
Ni1	N4	2.018(5)	Ni4	N25	2.060(5)	N21	C43	1.313(7)
Ni1	N30	2.092(5)	Ni4	N26	2.095(6)	N22	N23	1.373(7)
Ni1	N31	2.115(5)	Ni4	N27	2.079(5)	N22	C42	1.315(7)
Ni2	N7	2.029(5)	N4	N5	1.369(7)	N23	C43	1.313(8)
Ni2	N8	2.069(5)	N4	C10	1.340(7)	N27	N28	1.317(7)
Ni2	N9	2.073(5)	N5	C11	1.317(7)	N27	C57	1.358(8)
Ni2	N10	2.082(5)	N6	N7	1.379(7)	N28	C58	1.325(8)
Ni2	N11	2.093(5)	N6	C10	1.324(7)	Sb1A	F1A	1.870(4)
Ni2	N12	2.108(5)	N7	C11	1.347(7)	Sb1A	F2A	1.881(4)
Ni3	N15	2.128(5)	N12	N13	1.319(7)	Sb1A	F3A	1.863(4)
Ni3	N16	2.065(5)	N12	C26	1.339(7)	Sb1A	F4A	1.863(4)
Ni3	N17	2.059(5)	N13	C27	1.337(8)	Sb1A	F5A	1.874(4)
Ni3	N18	2.076(5)	N14	N15	1.319(7)	Sb1A	F6A	1.878(4)
Ni3	N19	2.062(5)	N14	C26	1.337(7)			
Ni3	N20	2.026(5)						

Table 17. Select N-Ni-N bond angles (°) of **19**.

Atoms	Angle (°)	Atoms	Angle (°)	Atoms	Angle (°)
N1-Ni1-N2	89.5(2)	N8- Ni2-N9	96.5(2)	N20- Ni3-N15	87.31(18)
N1- Ni1-N3	93.7(2)	N8- Ni2-N10	92.75(19)	N20- Ni3-N16	88.97(19)
N1- Ni1-N30	88.8(2)	N8-Ni2-N11	166.33(18)	N20- Ni3-N17	171.7(2)
N1- Ni1-N31	97.42(19)	N8- Ni2-N12	91.16(19)	N20- Ni3-N18	94.51(19)
N2- Ni1-N3	96.8(2)	N9- Ni2-N10	89.94(19)	N20- Ni3-N19	79.57(19)
N2- Ni1-N30	171.3(2)	N9- Ni2-N11	94.6(2)	N1AA- Ni3-N26	161.70(19)
N2- Ni1-N31	94.2(2)	N9- Ni2-N12	172.35(18)	N23- Ni3-N1AA	79.11(19)
N3- Ni1-N30	91.8(2)	N10- Ni2-N11	95.21(19)	N23- Ni3-N24	90.2(2)
N3- Ni1-N31	164.41(19)	N10- Ni2-N12	89.60(18)	N23- Ni3-N25	173.9(2)
N4- Ni1-N1	172.4(2)	N11- Ni2-N12	77.82(19)	N23- Ni3-N26	89.73(19)
N4- Ni1- N2	92.55(19N)	N16- Ni3-N15	77.66(19)	N23- Ni3-N27	91.58(18)
N4- Ni1-N3	78.86(19)	N16- Ni3-N18	94.3(2)	N24- Ni3-N1AA	98.2(2)
N4- Ni1-N30	90.23(18)	N17- Ni3-N15	88.23(19)	N24- Ni3-N25	85.7(2)
N4- Ni1-N31	89.68(19)	N17- Ni3-N16	96.92(19)	N24- Ni3-N26	96.3(2)
N30- Ni1-N31	77.6(2)	N17- Ni3-N18	90.9(2)	N24- Ni3-N27	173.8(2)
N7- Ni2-N8	80.01(19)	N17- Ni3-N19	94.3(2)	N25- Ni3-N1AA	97.0(2)
N7- Ni2-N9	90.73(18)	N18- Ni3-N15	171.7(2)	N25- Ni3-N26	95.2(2)
N7- Ni2-N10	172.8(2)	N19- Ni3-N15	99.8(2)	N25- Ni3-N27	93.0(2)
N7- Ni2-N11	91.92(18)	N19- Ni3-N16	168.39(18)	N27- Ni3-N1AA	88.0(2)
N7- Ni2-N12	90.70(18)	N19- Ni3-N18	88.5(2)	N27- Ni3-N26	77.8(2)

To further explore the possibilities of reactivity and connectivity with cyanide, [TEA][CN] was added in excess to a solution of **6**. The solutions were stirred at 25°C for one week, and both reaction solutions deepened in color. The solution was crystallized with toluene, resulting in single-crystals of [TEA]₂[Ni^{II}(CN)₄], **20**., Figure 65 and Table 14.

The positional disorder of the [TEA]⁺ cations and the water molecule centered at O1 was modeled appropriately but removed from Figure 65 for the sake of visual clarity. Instead of metallacyclic formation, **6** underwent decomposition in solution to form a square planar Ni^{II} homoleptic cyanide complex. This complex has been previously reported and, using the more efficient published synthetic routes, the complex may prove to be an interesting, albeit diamagnetic, building block for future cyanide studies by the Dunbar group.¹³⁸

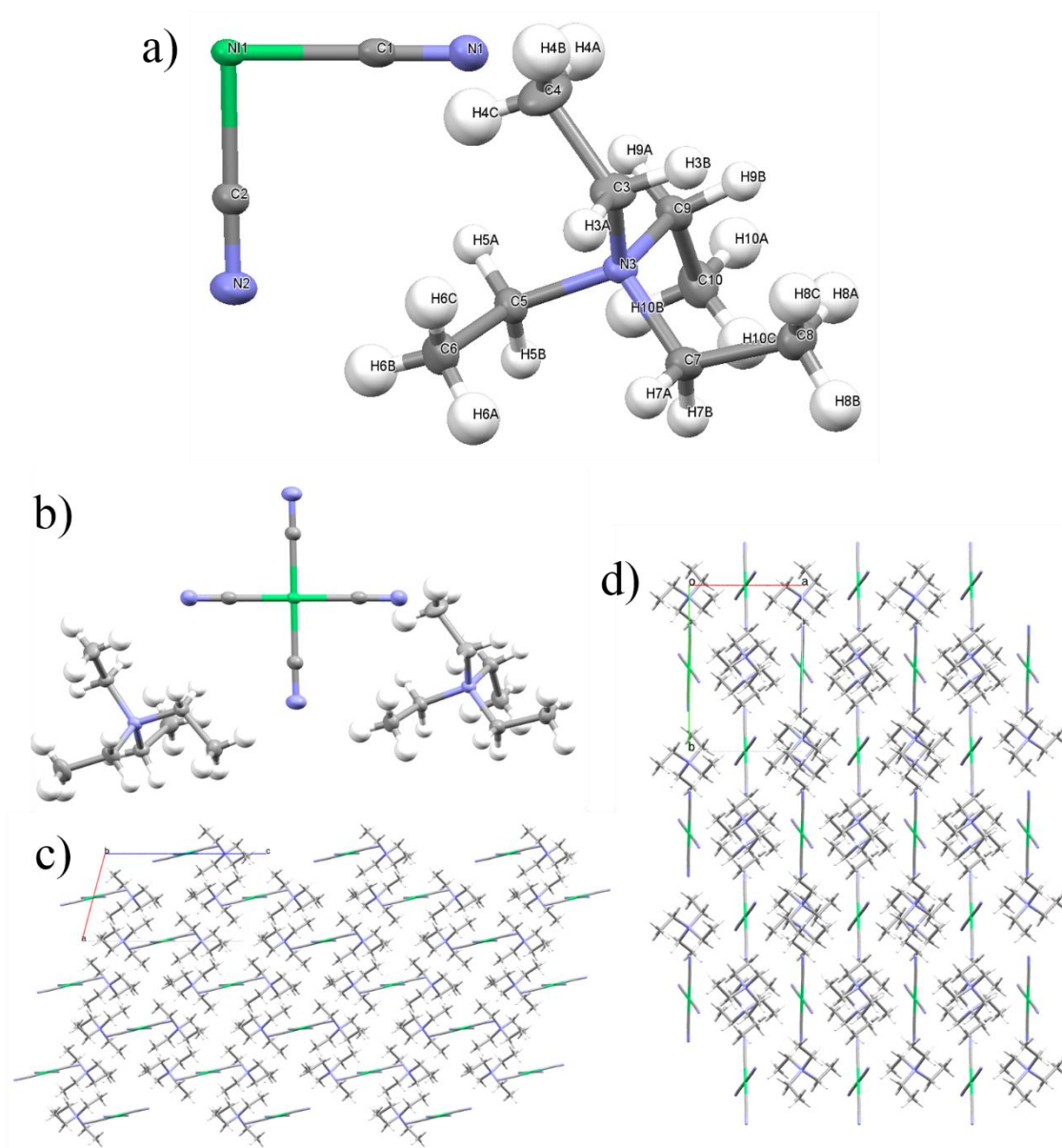


Figure 65. a) Thermal ellipsoid view of the asymmetric unit of **20**. b) Charge neutral portion of **20**. Crystal packing diagrams of **20** c) along the *b*-axis and d) along the *c*-axis. Graphical display generated by the Mercury⁹⁰ and PovRay¹³³ visualizers. Select bond distances (Å): Ni1-C1 1.8717(19), C1-N1 1.150(2), Ni1-C2 1.8725(18), C2-N2 1.154(2), N3-C3 1.515(2), C3-C4 1.513(3). Select bond angles (°): C1-Ni1-C1^{symm. generated} 180.00(4), C1-Ni1-C2 91.16(8), C1-Ni1-C2^{symm. generated} 88.84(8), Ni1-C1-N1 177.78(16), C3-N3-C5 111.88(14), C3-N3-C7 107.34(14), N3-C3-C4 115.62(16).

Conclusions and Future Outlook

Supramolecular truncated icosahedral polyhedra have been envisioned upon bridging the pentagonal metallacycles with linear organic or inorganic bridging moieties. The compilation of AFM, STM, UV-Vis and ^1H NMR data for the $\text{tpphz}+\mathbf{3}$, $\text{tpa acid}+\mathbf{3}$ and $[\text{nBu}_4\text{N}]_2[\text{tpa}]+\mathbf{3}$ complexes indicate that there is some degree of coordination of the bis-bidentate bridging ligands at the Fe^{II} vertices. AFM and STM images of the products suggest that the structures have sizes approximately similar to the predicted tpphz - and tpa -bridged polyhedra, and NMR spectra of the complexes contain a series of distinct resonances that suggest that the tpphz - and tpa -bound structures retain similar symmetry to the pentagonally building blocks. The theoretical analysis of the energy associated with binding, bending and bridging at a singular tpa -bound Fe^{II} vertex support that the coordination and curvature necessary at each vertex for polyhedral formation is energetically favorable, but that overcoming the strain associated with the curvature of the bridging ligand is rather significant, 111.91 kcal/mol. Collectively, the data are inconclusive regarding the exact connectivity and size of the $\text{tpphz}+\mathbf{3}$, $\text{tpa acid}+\mathbf{3}$ and $[\text{nBu}_4\text{N}]_2[\text{tpa}]+\mathbf{3}$ structures. Future efforts to characterize these complexes with DOSY-NMR, in collaboration with Dr. Howard Williams at Texas A&M University, and 2D-MS, in collaboration with Dr. Xiaopeng Li at Texas State University, are expected to provide greater insight into the relative size and coordination of the complexes. More stable pentagonal building blocks, with Ni^{II} or Ru^{II} metal vertices, would also promote a more stable polyhedral complex.

Efforts to bridge the paramagnetic Ni^{II} pentagonal architectures were pursued with [TEA][CN] and [PPN]₃[Os(CN)₆] but did not result in the formation of bridged pentagonal metallacycles. Instead, the reaction of **6** with [TEA][CN] resulted in the square planar homoleptic cyanide Ni^{II} complex [TEA]₂[Ni^{II}(CN)₄]. Alternatively, the reaction of [PPN]₃[Os(CN)₆] with **6** led to the reduction, supramolecular rearrangement and formation of the first rectangular Ni^{II}-metallacycle, **19**. The architecture consists of Ni^{II} ions bridged by two neutral bptz and two reduced bptz ligands that were templated around an acetonitrile ligand. Magnetic communication may be afforded across the radical bptz bridges, resulting in potentially interesting magnetic properties that can be explored in the future.

CHAPTER V

THE ROLE OF ANION- π INTERACTIONS IN THE INHIBITION OF MALATE SYNTHASE BY PHENYL-DIKETO ACID SUBSTRATES: DEVELOPING PREDICTIVE COMPUTATIONAL METHODS TO ADVANCE DRUG DEVELOPMENT ALGORITHMS

Introduction

Tuberculosis (TB) claimed 1.5 million lives in 2014 alone¹³⁹ and has been estimated to persist in either the infectious or latent form in approximately one-third of the world's population.¹⁴⁰ TB cases are often successfully treated with first- and second-line drugs,¹³⁹ nevertheless TB continues to threaten the global population due to ever-increasing drug resistance and indefinite persistence, even under harsh conditions.^{139, 141} To circumvent these issues, drug development has pursued specific biological targets critical to the life cycle of *Mycobacterium tuberculosis* (*Mtb*), the bacterium responsible for TB infection.^{41, 142}

The glyoxylate shunt within the tricarboxylic acid (TCA) cycle of *Mtb* has been recognized as an important target for drug development because it is critical for the persistence and infection of the bacterium¹⁴³ and is absent from the TCA cycle of humans.¹⁴⁴ The glyoxylate shunt bypasses two carbon dioxide generating steps of the TCA cycle and propagates the cycle under carbon limiting conditions,¹⁴⁵ Figure 66.

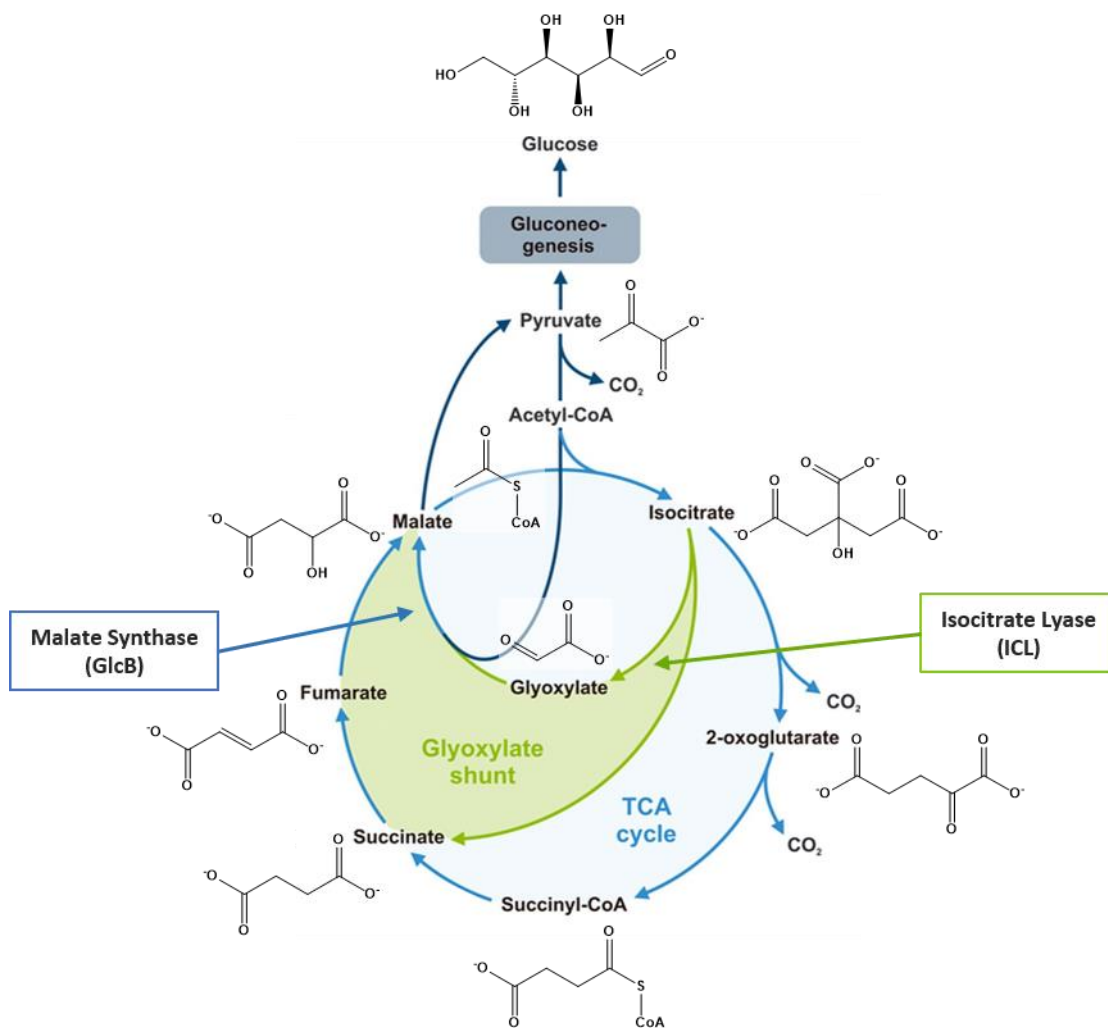


Figure 66. The role of the glyoxylate shunt within the tricarboxylic acid (TCA) cycle of *Mycobacterium tuberculosis*. Adapted and reproduced with permission from Kaufmann, et al.^{145c}

The first enzyme in the glyoxylate shunt, isocitrate lyase, decomposes isocitrate into glyoxylate and succinate.¹⁴⁶ The second enzyme in the shunt, malate synthase (GlcB), promotes the reaction of glyoxylate with one molecule of acetyl coenzyme-A to form malate, which is introduced back into the TCA cycle.^{144a, 144b} While both enzymes have

been identified as necessary for bacterial virulence,^{41, 143b} GlcB has garnered particular interest as a target for anti-TB drug development because of the large, static active site present in the protein.^{143b, 147} Using structure-guided drug development, Sacchetti and coworkers screened a library of glyoxylate-like molecules for inhibition against GlcB⁴¹. Phenyl-diketo acids (PDKAs), Figure 67, demonstrate favorable inhibition, potency and toxicity.⁴¹

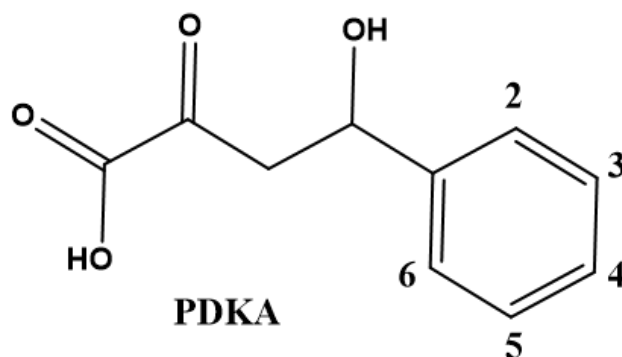


Figure 67. PDKA framework with labeled phenyl positions 2 – 6.

Protein crystallography of PDKA (white molecular framework) bound in the active site of GlcB (green molecular framework) reveals that the binding motif resembles that of glyoxylate-bound GlcB,^{144a} Figure 68. The diketo acid tail of the PDKA molecule binds to the catalytic magnesium ion and participates in H-bonding interactions along the diketo backbone. PDKA substituents at the 2-*ortho* position participate in hydrogen-halogen interactions with Arginine (Arg) 339. Additionally, the aryl moiety of the PDKAs

participate in an anion- π interaction with the anionic carboxylate terminus of Aspartate (Asp) 633.¹⁴⁸ All of these non-covalent interactions, identified by dashed lines in Figure 68, have generated interest in designing PDKAs that maximize intermolecular interactions in order to increase inhibition, in particular, by using the anion- π interaction. In order to maximize the non-covalent interactions between the inhibitor and active site, the molecular design of the drug molecules were considered using computer-aided drug design methods.

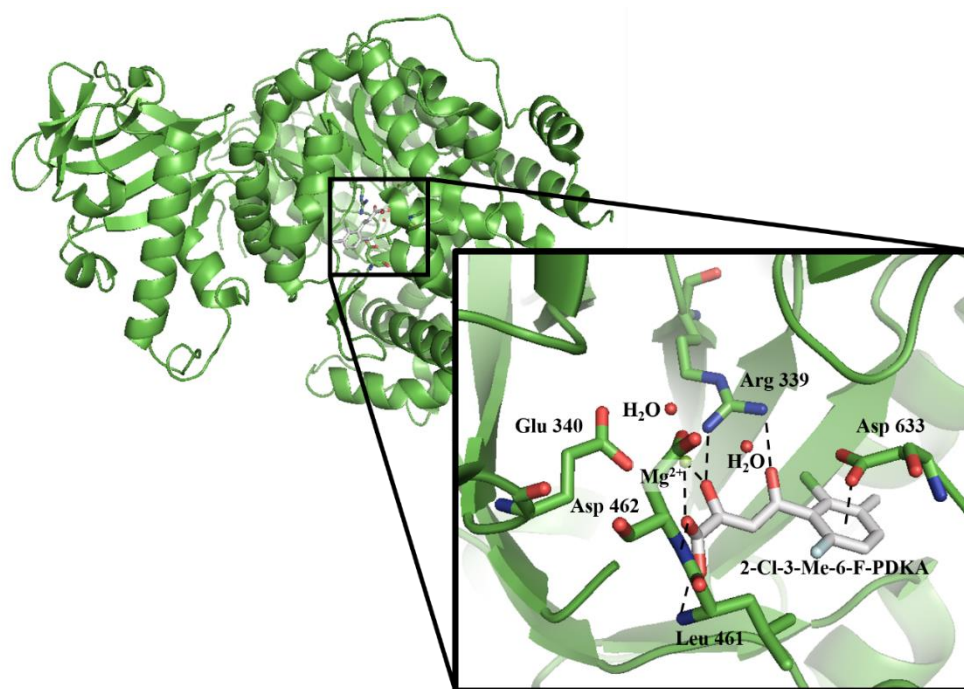


Figure 68. Crystal structure of GlcB upon inhibition by 2-F-3-Me-6-Cl-PDKA. Structure 3SB0,⁴¹ accessed from RSCB Protein Data Bank.⁴² (Inset) GlcB active site and the residues that participate in close-contacts (green framework) with the PDKA (white framework). Non-interacting residues that obstructed the inset visualization were removed for clarity. Supramolecular interactions identified by dashed lines. Graphical display generated by the PyMol visualizer.⁴³

The ever-growing field of computer-aided drug development (CADD) has had a significant impact on the design of target drugs in the pharmaceutical community over the last three decades. CADD has provided insight for developing lead molecule drugs through both ligand-based and structure-based drug development techniques.¹⁴⁹ Ligand-based techniques predict molecules that demonstrate similar structural properties to known active compounds using comparative molecular field analysis and pharmacophore techniques.¹⁵⁰ Significant strides have been made by ligand-based methods especially in situations with limited structural information regarding the biological target. For structurally-characterized systems, structure-based techniques consider the molecular structure of the targeted biological site and identify molecules that are predicted to interact favorably with this target. Structure-based design benefits from a library of methods, including, but not limited to, visualization software, docking studies, molecular dynamics simulations and quantum mechanical calculations.¹⁵⁰⁻¹⁵¹ Algorithms are used to evaluate the complexity of the interactions with the biological target and to predict binding by considering steric, electrostatic, hydrophobic/hydrophilic and H-bonding contributions.^{150a, 152} While the general PDKA framework was identified using structure-based drug design methods, further optimization of the molecules was stunted because current predictive methods overlook weaker non-covalent interactions paramount within many biological systems, such as the anion- π interaction active in the PDKA-GlcB active site.

The anion- π interaction has been broadly defined as an attractive, non-covalent interaction between an anion and the face of an aromatic system.^{23a, 25-27, 33} Applying this

broad definition, anion- π interactions have been increasingly identified within several classes of biological supramolecular systems and processes over the last few years. Matile and coworkers have evaluated the role of anion- π interactions in trans-membrane anion transport,^{40a, 153} and they have developed naphthalenediimides oligomers that transport anions across the membranes of large unilamellar vesicles purely by anion- π interactions.^{40b} The synthesis of artificial anion-channels based on anion- π interactions has been touted as an opportunity to develop chloride channel replacement therapy for treating channelopathies, such as cystic fibrosis.^{40b}

Chakravarty and coworkers have demonstrated that η^6 anion- π interactions are prevalent in protein structures and contribute to macromolecular folding of DNA hairpins and proteins.³⁹ Zlatovic and coworkers demonstrated the role of anion- π interactions in stabilizing porphyrin-containing protein structures.¹⁵⁴ Of the nearly three hundred anion- π interactions identified in the study, approximately 30% of the residues involved in anion- π interactions were located at stabilization centers of the proteins. Anion- π interactions have also been shown to contribute to the interactions of proteins with other biological macromolecules, such as DNA and RNA.^{28b} As discovered by Quiñonero and coworkers, the π -systems of the nucleic acid polymers interact favorably with anionic protein residues.^{28b} In fact, the DNA and RNA adducts demonstrate preferential interactions with different anionic residues due to the different binding along the respective nucleic acid backbones, resulting in varying angles and distances available to the approaching anionic residues.^{28b}

In this vein, several studies of the structures within the Protein Data Bank (PDB)⁴² have continued to highlight the prevalence of anion- π interactions within protein structures.¹⁵⁵ Deyà and coworkers first studied anion- π interactions between proteins and small molecules by examining interactions within the active sites of flavin-dependent enzymes.^{30b, 156} Across the fifty-one enzymes studied in-depth, the role of the anion- π interaction present in the active site varied in nature from inhibition to promotion of the enzymatic activity.^{30b} Additionally, an anion- π interaction has been shown to facilitate the activity of the flavin-dependent enzyme sulfide-quinone oxidoreductase by stabilizing the anionic intermediate that is critical in the mechanism of action.¹⁵⁶ Deyà and coworkers also investigated the inhibition of the urate oxidase enzyme by anions such as cyanide.¹⁵⁷ Urate oxidase promotes the oxidation of uric acid, but cyanide has been shown to inhibit the enzyme by participating in an anion- π interaction that further induces a π - π interaction.

After the identification of the anion- π interaction involved in PDKA-GlcB binding by Sacchettini and coworkers,⁴¹ the substituent effects of the 2-*ortho*-PDKAs and the long-range electrostatic interaction of the catalytic Mg^{2+} ion on GlcB inhibition were explored computationally by Frontera and coworkers.¹⁵⁸ The model active site that they used consisted of the Mg^{2+} ion, the monoanionic PDKA and two formate anions. One formate anion was used to complete the tetrahedral coordination sphere around Mg^{2+} , which varied from the octahedral coordination sphere of the crystal structure. The second formate anion represented the Asp 633 residue and was restrained in an idealized orientation at approximately 3 Å over the center of the substituted phenyl group of the PDKA, Figure 69a. The formate anion above the PDKA was restrained with respect to the

prescribed orientation above the PDKA moiety and the remainder of the model active site was optimized using second order Møller-Plesset perturbation theory (RI-MP2)^{44a-c, 159} with the def2-TZVP^{44d, 44e} basis set in Turbomole6.4.¹⁶⁰ The basis set superposition error (BSSE) and the BSSE-corrected interaction energies were calculated for each complex using the counterpoise-corrected method⁸⁷. The optimization caused the PDKA inhibitor to relax from the twisted position it is required to adopt in the biological active site. Comparing the protein crystal structures and the respective optimized active sites for the unsubstituted-PDKA and the 2-ortho-PDKAs reveals that the torsion of the PDKA backbone is lost upon full optimization, Figure 69b. The resulting displacement of the centroid of the PDKA aryl group ranges from 4.2 to 5.1 Å for the PDKA, Table 18. The aryl displacement is not shown for 2-Cl-PDKA nor per-F-PDKA because the crystal structure is not available for these PDKA-GlcB complexes.

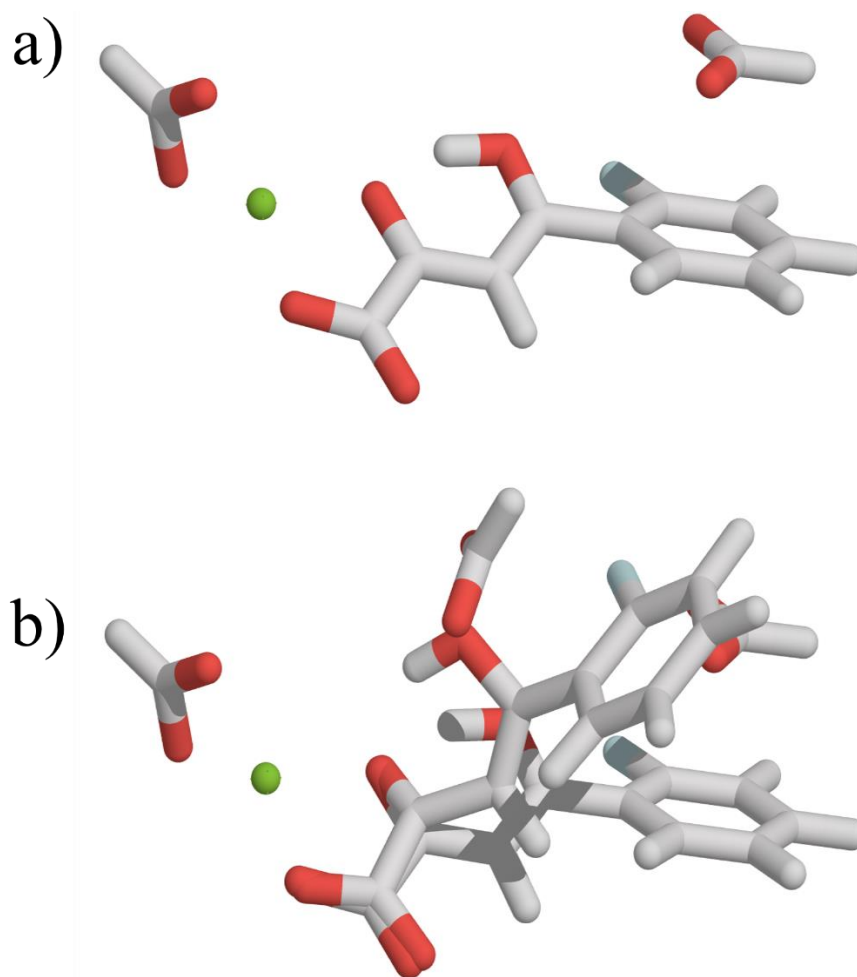


Figure 69. Schematic representations of the a) fully optimized, model active site for 2-GlcB by Frontera et al.¹⁵⁸ and b) an overlay of this model active site with the analogous groups from the protein crystal structure.¹⁶¹ Graphical display generated by the PyMol⁴³ and PovRay¹³³ visualizers.

Table 18. Comparison of the anion- π interaction energies of the partially-optimized, model active sites for the unsubstituted- and 2-*ortho*-PDKAs at the BSSE-corrected RI-MP2/def2-TZVP level of theory¹⁵⁸. Evaluation of the displacement of the PDKA aryl group from each respective crystal structure⁴¹.

PDKA	RI-MP2/ def2-TZVP/BSSE (kcal/mol)	Aryl Displacement (Å)
Unsubstituted	-10.6	4.5
2-F-PDKA	-12.2	5.1
2-Cl-PDKA	-11.9	No Crystal Structure Available
2-Br-PDKA	-11.9	4.4
2-Me-PDKA	-11.4	4.2
Per-F-PDKA	-19.7	No Crystal Structure Available

Using this simplified model active site, the study identified that an increase in the electron-withdrawing nature of the 2-*ortho* substituent corresponds to a decrease in the IC₅₀ value, the concentration at which half of the protein experiences inhibition, and therefore, an increase in the efficacy of the drug. The long-range electrostatic interaction between the anionic Asp 633 analogue and the catalytic Mg²⁺ ion was shown to enhance the anion- π interaction because the aromatic conjugation was polarized in response to the positively charged Mg²⁺, effectively increasing the “ π -acidity” of the aryl group.¹⁵⁸ The natural extension of this study presumes that additional electron-withdrawing substituents lead to increased inhibition, but this proposed hypothesis does not persist experimentally. While the anion- π and long-range electrostatic interactions evaluated in this study do persist in the protein crystal structure, the significant deviation of the partially optimized model active sites from the crystal structures renders the conclusions highly qualitative

and exposes the need for a biologically relevant approach to modeling the PDKA-GlcB system.

Presented in this chapter is the first computational method that appropriately accommodates the anion- π interaction in order to evaluate the PDKA-GlcB protein active site and predict the binding affinity of the PDKA substrate within GlcB. This study has employed the protein crystal structures of an extensive library of twenty-one PDKA-bound protein crystal structures and a catalogue of inhibition data, as characterized experimentally by researchers in the laboratory of Dr. Sacchettini. The Descriptive and Pre-screened Predictive Methods described in this chapter provide a medicinal chemistry guide for the future of structure-based drug design involving anion- π interactions.

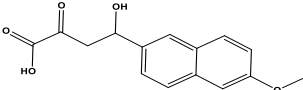
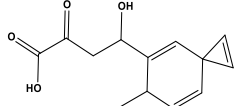
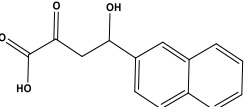
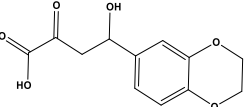
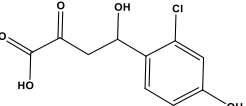
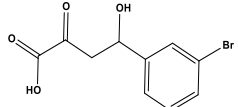
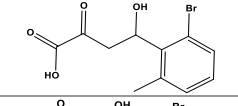
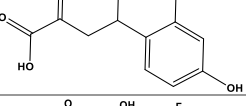
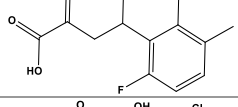
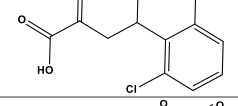
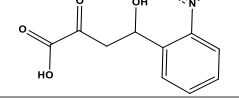
Experimental Methods

Experimental methods were performed by researchers in Dr. Sacchettini's laboratory according to previously described methods.⁴¹ GlcB was cloned upon mutation of the Cysteine (Cys) 619 residue to Alanine residue, followed by purification. PDKAs **21** – **43**, Table 19, were synthesized and combined with GlcB, and the IC₅₀ values were measured for the PDKA-bound GlcB complexes. Upon crystallization of the PDKA-GlcB complexes, structural data were collected at the Argonne National Lab APS synchrotron and solved by Dr. Inna Kreiger in Dr. Sacchettini's lab. The refined structures will be deposited in the RSCB Protein Data Bank⁴² (PDB) at the discretion of the Sacchettini group. Isothermal titration calorimetry (ITC) was performed according to standard methods for **21-24** PDKA-GlcB complexes by Dr. Hsiao-ling Huang in Dr. Sacchettini's lab.

Table 19. PDKA molecules synthesized and characterized in complex with GlcB. Each respective IC₅₀ value is included.

#	Substituent	Structure	IC ₅₀ (μM)
21	Unsubstituted		2.1
22	2-F		0.2
23	2-Cl		0.5
24	2-Br		0.6
25	2-Me		1.1
26	Per-F		>50
27	2-Cl-3-Me-6-F		5.5
28	2,6-F		1.6
29	2-Br-3-OH		0.06
30	3-OH		0.1
31	5-OH		0.5
32	4-Me		6.1

Table 19 Continued.

33	Methoxynaphth		~1.5
34	3-CycloProp-6-Me		Not Provided
35	Naphth		0.5
36	Dioxine		1.1
37	2-Cl-4-OH		0.007
38	3-Br		0.8
39	2-Br-6-Me		17.4
40	2-Br-4-OH		0.005
41	2-F-3-Me-6-F		6.6
42	2,6-Cl		1.0
43	2-Nitro		2.8

Computational Methods

Single point (SP), partially-optimized (PO), or fully-optimized (FO) calculations (depending on the specific model as described in the Results and Discussion section) were performed using the M06-2X functional^{19b, 56, 108} and the 6-31+g(d) basis set⁵² in Gaussian 09.⁸⁶

From the SP, PO or FO calculations (as appropriate), interaction energies were obtained as a difference in energy between the final complex and the sum of the model active site parts. The interaction energy of a single component with the rest of the active site, for example “substrate” B within the “complex” ABC, was obtained as the difference in energy between the final (PO or FO) complex, ABC, and the sum of the SP energies of the substrate, B, and the complex without the substrate, A C.

SP and PO interaction energies were also calculated for the substituted-benzene and Cl⁻-substituted-benzene complexes of **21** – **24** at the MP2/def2-TZVP⁴⁴ level of theory in Gaussian 09.⁸⁶ Electrostatic potential (ESP) maps for several of the neutral PDKAs were plotted for each ligand FO at the M06-2X/6-31+g(d) level of theory.^{19b, 52, 56, 108} Solvent-Accessible surface areas at 1.4 Å were calculated for the FO PDKAs **21** – **24** using the Atoms Volumes & Surfaces tool within the Materials Studio 7.0¹⁴ suite, produced by Accelrys, Inc.

Results and Discussion

Influence of Substituent Effects upon PDKA-GlcB Inhibition

Inhibition of GlcB, a critical enzyme within the life cycle of *Mycobacterium tuberculosis*, by PDKA molecules occurs through a series of non-covalent interactions,

including an important anion- π interaction, Figure 68. The presence of this anion- π interaction between the protein and the inhibitor has prompted a series of investigations into the relationship between the PDKA substituent and the drug's binding affinity.¹⁵⁶ The dipole-driven, substituent-dependence of anion- π interactions has been previously established in the literature.^{19b, 24a} As discussed by Wheeler and coworkers, the electronegativity and inductive field effects of the substituent induce a σ -dipole between the substituent and the carbon atom on the aromatic framework.^{19a} Substituents that cause the carbon atom to be partially positive, referred to as “electron-withdrawing” substituents for the remainder of this chapter, induce attractive σ -dipole interactions between the carbon atom and an anion. Substituents that cause the carbon atom to be partially negative, referred to as “electron-donating” substituents for the remainder of this chapter, induce repulsive σ -dipole interactions between the carbon atom and an anion.

Initially, the IC_{50} values of the PDKAs, Table 19, were considered to be likely indicators of the strength of the anion- π interaction between the PDKA and Asp 633.^{41, 156} The IC_{50} value signifies the concentration at which fifty percent of the protein macromolecules are inhibited, so, as the IC_{50} value decreases, the efficacy of the PDKA drug increases. As electron-withdrawing substituents were added to the PDKA aryl moiety, the IC_{50} value was predicted to decrease,^{41, 156} but this does not occur. As the number of fluoro-substituents increases for PDKAs **22** < **28** < **26**, an increase in the respective IC_{50} values is observed, exactly opposite to the expected efficacy response. This disparity has been attributed to steric, entropic, desolvation or biological factors that are preventing the molecules from accessing the GlcB active site.

In order to determine the approximate propensity of each of PDKA to participate in anion- π interactions, the interaction between substituted benzene molecules, with analogous substituents to **21** – **43**, and a chloride anion was evaluated. First, the substituted benzene rings with were fully optimized, and a chloride ion was placed above the centroid of each of the FO structures. The coordinates of the substituted benzene molecules, with substituents analogous to **21** – **43** were restrained and the Cl^- was optimized along the z-axis, Figure 70. The anion- π interaction energies were calculated for each of the PO Cl^- -substituted-benzene complexes, Table 20.

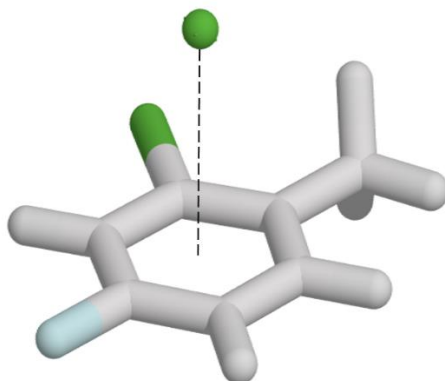


Figure 70. Substituted-benzene analogue of **27** in complex with Cl^- . Model was PO along the Cl^- -centroid axis, denoted by the dashed line. Graphical display generated by the PyMol⁴³ and PovRay¹³³ visualizers.

Table 20. Anion- π interaction energies for each of the complexes of Cl^- and the substituted-benzene analogues of **21** – **43**. Comparable calculations performed at the MP2/def2TZVP level of theory are reported in parentheses.

#	Substituent	Energy (kcal/mol)	#	Substituent	Energy (kcal/mol)
21	Unsubstituted	1.71 (3.88)	32	4-Me	1.03
22	2-F	-0.76 (1.55)	33	Methoxynaphth	0.97
23	2-Cl	-1.26 (1.48)	34	3-CycloProp-6-Me	0.88
24	2-Br	-2.11 (1.41)	35	Naphth	0.70
25	2-Me	1.03	36	Dioxine	0.39
26	Per-F	-11.95	37	2-Cl-4-OH	-1.69
27	2-Cl-3-Me-6-F	-4.17	38	3-Br	-2.11
28	2,6-F	-3.41	39	2-Br-6-Me	-2.43
29	2-Br-3OH	-2.38	40	2-Br-4-OH	-2.55
30	3-OH	1.28	41	2-F-3-Me-6-F	-3.72
31	5-OH	1.28	42	2,6-Cl	-4.31
			43	2-Nitro	-6.69

In general, the data in Table 20 indicate that electron-withdrawing substituents contribute to favorable anion- π interactions between Cl^- and the substituted-benzene molecules and that electron-donating substituents contribute to unfavorable anion- π interactions between Cl^- and the substituted-benzene molecules. Upon increasing the

number of electron-withdrawing substituents (i.e. **22**, **28** and **26**), the strength of the respective anion- π interactions also increases. Interestingly, the anion- π interaction energies increase according to **21** (Unsubstituted) \ll **22** (F) $<$ **23** (Cl) $<$ **24** (Br). SP energies were calculated for these complexes at the MP2/def2-TZVP⁴⁴ level of theory, values in parentheses in Table 20, and were able to validate the trend in interaction energies calculated at the M06-2X/6-31+g(d)^{19b, 52, 56, 108} level of theory. A similar halide-substituent trend in interaction energies were described by Wheeler and coworkers,^{19a} resulting from inductive/field effects.^{19a} The M06-2X function has previously been demonstrated to be able to evaluate non-covalent interactions, and is highly recommended for non-covalent interactions in biological systems.¹⁶² The M06-2X functional has been shown to only moderately undercompensate for dispersion, with respect to the *ab initio* calculations,^{19a} and has been found to model polarizability very well.¹⁶³ Therefore, the M06-2X functional was used to evaluate the remainder of the models within this study.

Considering the PDKA series with respect to the substituted-benzene analogues, each PDKA has the same substitution at the first position, namely the diketo acid backbone that is deprotonated within the active site. Since this backbone is consistent for each PDKA structure, the relative predicted propensity of each of the substituted-benzene molecules to participate in anion- π interactions can be extended to the PDKAs **21** – **43**, i.e. the Cl⁻- π model. Finally, the relationship between the Cl⁻- π model and the IC₅₀ values was probed in Figure 71. As can be seen, there is no correlation between the propensity of the PDKAs to participate in anion- π interactions and the IC₅₀ values.

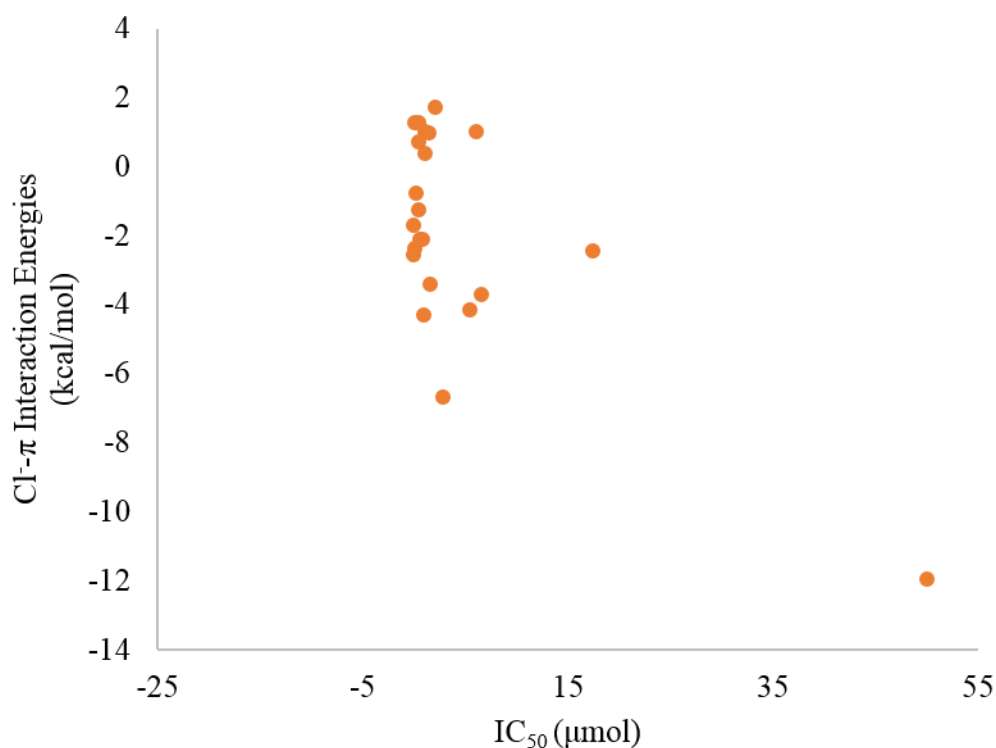


Figure 71. Comparison of the IC₅₀ values derived from each PDKA-GlcB complex and the respective interaction energies of chloride with each substituted-benzene analogue for **21 – 33, 35 – 43**. IC₅₀ value for **34** not provided.

In order to circumvent the biological complications associated with evaluating IC₅₀ values, the thermodynamic components of this system were evaluated using isothermal titration calorimetry, ITC. Isothermal titration calorimetry (ITC) was initially developed as a method to simultaneously calculate the equilibrium rate constant and change in enthalpy for acid-base equilibria¹⁶⁴ and has since developed into a biophysical method that can be used to elucidate the thermodynamic and kinetic contributions of the interactions of proteins with other proteins and substrates.¹⁶⁵ Thermodynamic evaluations of protein-ligand interactions involve measuring the change in heat, or enthalpy, associated with the

interaction, the reaction rate constant (K_{eq}), and the stoichiometry of the interaction. From these components, the Gibbs free energy and the entropy are calculated, according to Equations 11 – 13:¹⁶⁵

$$K_{eq} = \left\{ \frac{[Complex]}{[Receptor]} \times [Ligand] \right\}_{equilibrium} \quad \text{Equation 11}$$

$$\Delta G^\circ = -RT \ln K_{eq} \quad \text{Equation 12}$$

$$\Delta G = \Delta G^\circ + RT \ln \left\{ \frac{[Complex]}{[Receptor]} \times [Ligand] \right\}_{actual} = \Delta H - T\Delta S \quad \text{Equation 13}$$

Using ITC, Dr. Hsiao-ling Huang in Professor Sacchettini's lab, calculated the Gibbs free energy, enthalpy and entropy of inhibition for **21 – 24**, Table 21. There is significant similarity in the Gibbs free energy terms despite the variation in the entropic and enthalpic terms. This compensation of enthalpy and entropy often presents a challenge to drug discovery,¹⁶⁶ and may be mitigated by fine-tuning the molecular design of the substrate to optimize either the enthalpic or entropic term in such a way as to minimize the perturbation of the other term.

Table 21. Thermodynamic components of PDKA-GlcB binding for **21** – **24**, evaluated by ITC and the respective Cl⁻- π interaction energies of the analogously substituted benzene molecules.

PDKA	PDKA	ΔH (kcal/mol)	ΔS (cal/mol/K)	ΔG (kcal/mol)	Cl⁻-π Interaction (kcal/mol)
21	Unsubstituted	-1.53	25.3	-9.07	1.71
22	2-F	-3.46	18.3	-8.91	-0.76
23	2-Cl	-5.94	8.13	-8.36	-1.26
24	2-Br	-5.74	8.37	-8.16	-2.11

Neither the overall free energy nor the entropy factor correlates to the propensity of the PDKA series to participate in anion- π interactions, as relatively approximated by the Cl⁻- π model. The entropy and overall Gibbs free energy terms are contingent upon solvation and degrees of rotational freedom of substituents on the bound and free ligand, among other factors. By varying the 2-*ortho* substituent in structures **21** – **24**, the electrostatic nature and total surface area of the molecules is being affected. It was hypothesized that the entropic factor may be closely connected to the ability of each PDKA to order the solvent molecules that come into contact with the substituents. The solvent accessible surface area was calculated for the FO PDKAs **21** – **24** in Materials Studio 7.0 and compared to the ITC derived Entropy, Figure 72. As can be seen, there is a direct relationship between the solvent-accessible surface area and the entropy for **21** – **24**; as the solvent-accessible surface area increases, the entropy of the PDKA-GlcB system proportionally decreases. The larger surface areas of **23** and **24** provide more area in which

the solvent can order and decreases the entropy of the system. Additional and more elegant modeling of the entropy and free energy is beyond the scope of this chapter.

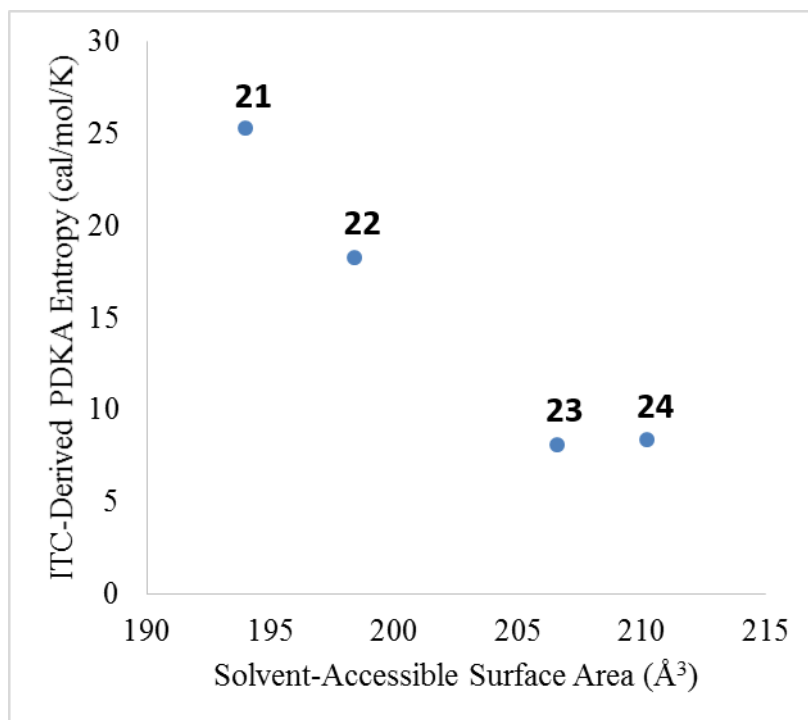


Figure 72. Comparison of ITC-Derived Entropy and the Solvent-Accessible Surface Area for **21 - 24**.

This study focuses on the enthalpic contribution, which is indicative of the binding energy of the substrate within the protein active site. The enthalpic term and the relative Cl⁻- π interaction energy for the *2-ortho*-PDKA series exhibit a proportional relationship, Table 21. As the approximate propensity of the PDKA to participate in anion- π

interactions increases, the binding enthalpy of the PDKA within the active site also increases. Therefore, the presence of the anion- π interaction within the active site provides a strategic opportunity to use these calculations to design a molecular structure to improve inhibition.

Development of the Model Active Site

Exploration of Active Site Contributions

In order to improve on the simplistic Cl⁻- π model in a biologically-relevant manner, active sites including the PDKA and a portion of the GlcB active site were envisioned and explored. As depicted by Active Site A (AS-A) in Figure 73a, the first model active site that was developed included the neutral PDKA inhibitor and an acetate analogue of Asp 633. AS-A was PO by restraining the coordinates of the non-hydrogen atoms and optimizing the hydrogen atom placement for each of the PDKA-GlcB crystal structures available at that time, including **1**, **22**, **25**, **27**, **30**, **32**, **34 – 37**, **42** and **43**. The AS-A interaction energies were calculated from SP energies of the AS-A complex and respective constituents, but no correlation was observed between the anion- π interaction energies in the AS-A complexes and the IC₅₀ values nor with the Cl⁻- π interaction energies, Figure 73a.

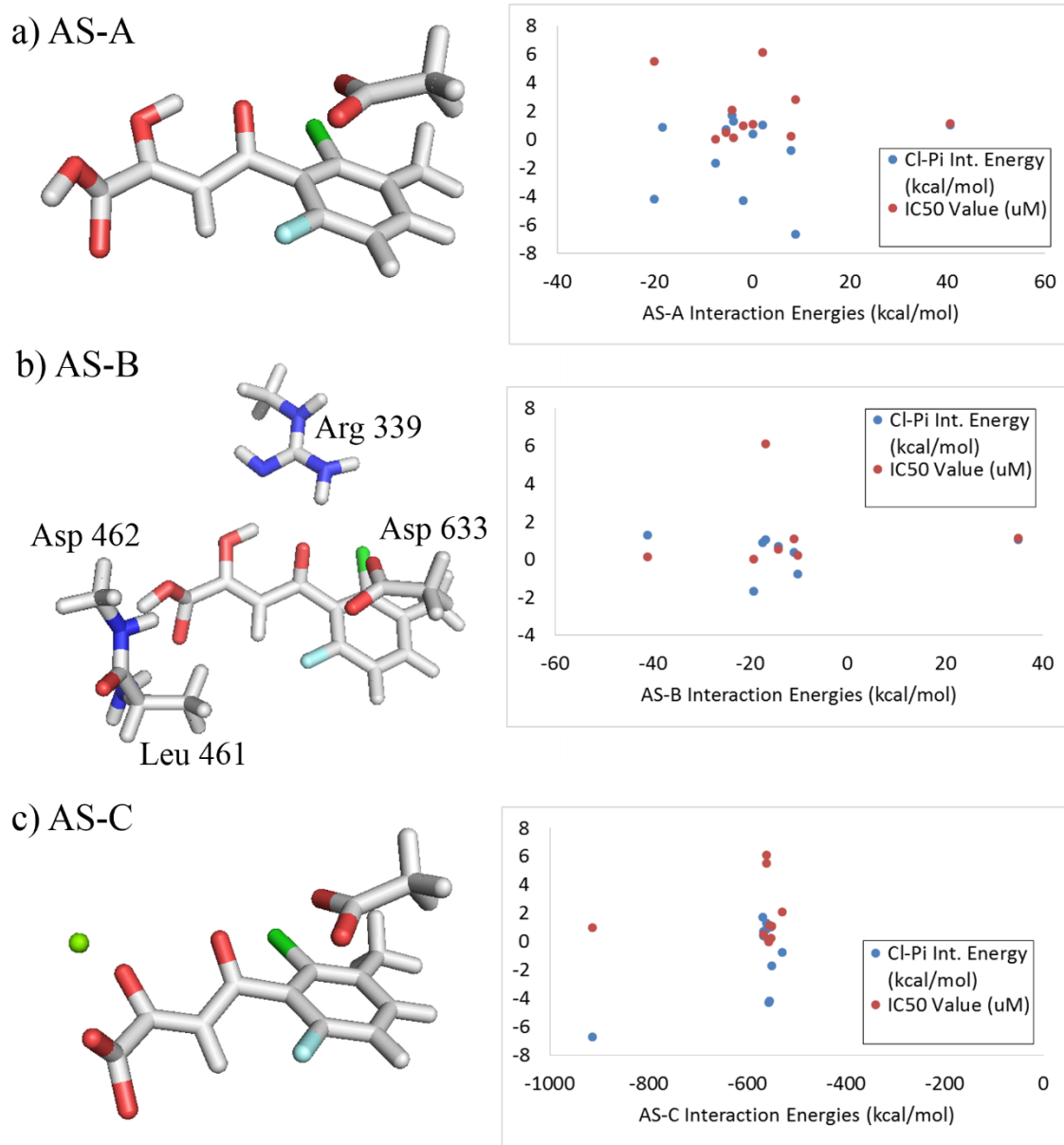


Figure 73. Initial Model Active Sites, including a) AS-A, involving neutral PDKA and an acetate analogue of Asp 633; (b) AS-B, involving neutral PDKA and analogues of Asp 633, Arg 339, Asp 462 and Leu 461; and (c) AS-C, involving the dianionic PDKA, Mg^{2+} ion, and acetate analogue of Asp 633. Graphical displays generated by the Materials Studio Visualizer.¹⁴

It was hypothesized that the model active site was over-simplified and that by including additional residues that participate in non-covalent interactions with the PDKA, the interaction energies might yield a correlation to previous data. To this end, Active Site B (AS-B) includes the neutral PDKA and portions of the Asp 633, Arg 339, Asp 461, and Leu 462 residues, Figure 73b. The AS-B complexes were PO. SP energies of the components were used to calculate the interaction energy of the PDKA with the remainder of the active site. The PDKA interaction energies in the AS-B complexes did not correlate to the IC₅₀ values nor to the Cl⁻- π interaction energies, Figure 73b.

The electrostatic potential (ESP) map of each neutral PDKA ligand was generated to explore the incongruity of the interaction energies in Figure 73a and Figure 73b. ESP maps portray the interaction of a positive point charge with the electron density of a molecule at a certain distance from the nuclei, and the interaction at each point is indicated by color. Blue portions of the ESP map correlate to attractive areas for interaction by negative point charges. As can be seen in Figure 74, the terminal aryl moiety would have a neutral, if not slightly repulsive, interaction with an idealized negative charge. Additionally, the red ESP region on the diketo acid tail at the ketone group adjacent to the phenyl ring would certainly lead to repulsion of a close-contacting anion. This likely contributes to the orientation of the Asp 633 residues closer to the *5-meta* and *6-para* positions in the crystal structures. The energetic range was standardized for the plots in Figure 74, from 50 to -50 kcal/mol, and highlights the differences in the propensity of the neutral molecules to interact with anions, depending on the polarizability of the PDKA

substituents. In order to polarize the electron-density along the diketo acid backbone and induce “ π -acidity” of the aryl group, the GlcB active site was reconsidered.

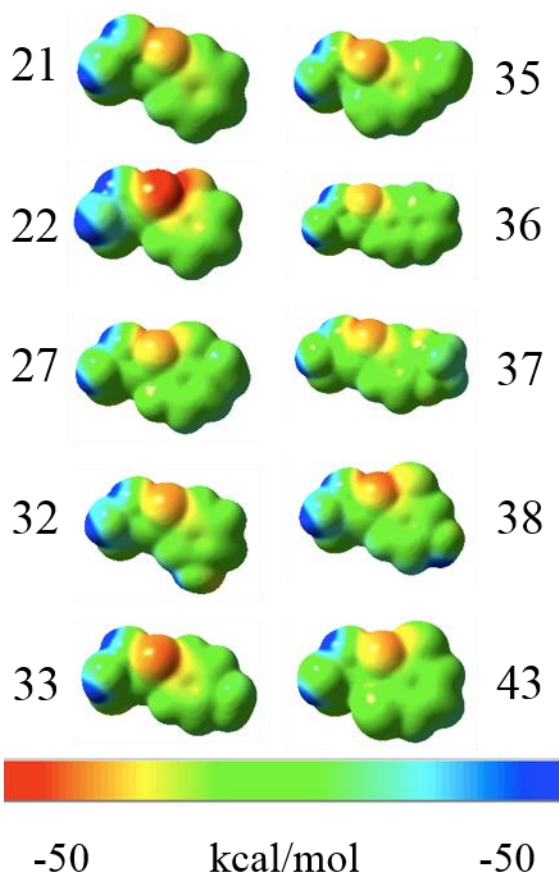


Figure 74. ESP Maps of select neutral PDKAs generated at isodensity values of 0.02 a.u. from the M06-2X/6-31+g(d)^{19b, 56, 108-52} in Gaussian 09.⁸⁶ Graphical display generated by the AMPAC Graphical User Interface Visualizer.¹⁶⁷

In the active site of the protein crystal structure, the catalytic magnesium ion binds to the PDKA and polarizes the electron density down the conjugated diketo acid backbone.

This molecular polarization is functionally important in the mechanism of action when the protein cleaves acetyl-coenzyme A for the production of malate,⁴¹ Figure 1. In fact the PDKAs require 2-ortho-substitution to avoid retro-Claisen decomposition upon polarization of the electron density along the backbone.⁴¹ Therefore, the Mg^{2+} ion was incorporated into the model active site, Active Site C (AS-C), along with the di-anionic PDKA and the acetate analogue of Asp 633, Figure 73c. The AS-C complexes were PO and the anion- π interaction energy of the Asp 633 analogue in the AS-C complexes was calculated from SP energies of the AS-C components, Figure 73c. The favorable interaction energies ranged from -450 to -950 kcal/mol, so the long-range electrostatic interaction of the Mg^{2+} ion was identified. While the interaction energies were far too strong to be representative, the concept of tempering the electrostatic impact of the Mg^{2+} ion with additional ligands was considered.

Consideration of Simplified Model Active Site

It was noted at this time in the progress of this investigation that Frontera and coworkers published a theoretical study on the role of the anion- π interaction and the long-range electrostatic interaction of the catalytic Mg^{2+} ion on PDKA inhibition of GlcB, as outlined in the introduction to this chapter.¹⁵⁸ PO of the simplified model active site allowed the PDKA inhibitor to relax and enforced a geometry between the Asp 633 analogue and the aryl portion of the PDKA not present in the crystal structure. While this approach is inaccurate as a quantitative method for analyzing this system, it posed as a standard by which I could further evaluate the ability of the M06-2X/6-31+g(d) level of theory to handle non-covalent interactions. Upon PO of the simplified model active sites

for **21** – **26** using the M06-2X/6-31+g(d) methods, the resulting interaction energy of the PDKA in the model active site was calculated and was shown to be comparable to the reported interaction energies, Table 22. The ability of the DFT M06-2X/6-31+g(d) methods to successfully reproduce the interaction energies of the ab initio methods further supported the continued use of the DFT methods in this study.

Table 22. Comparison of the anion- π interaction energies of the PO model active sites for **21** – **26** previously published by Frontera and coworkers,¹⁵⁸ as reported at the RI-MP2/def2-TZVP level of theory and upon evaluation at M06-2X/6-31+g(d) level of theory.

PDKA	Substituent	RI-MP2/def2-TZVP/BSSE (kcal/mol)	M06-2X/6-31+g(d) (kcal/mol)
21	Unsubstituted	-10.6	-11.8
22	2-F	-12.2	-13.6
23	2-Cl	-11.9	-13.2
24	2-Br	-11.9	-14.6
25	2-Me	-11.4	-12.6
26	Per-F	-19.7	-22.3

Identification of the Appropriate Model Active Site

A biologically-relevant model active site was developed from a comparative analysis of the entire assembly of crystal structures, residues and non-covalent interactions involved in PDKA-GlcB binding for **21-22**, **24-25**, **27-43**. Single crystals of **23** and **26**

bound in the active site of GlcB have been unable to be grown, despite intense efforts by Dr. Inna Kreiger of the Sacchettini lab.

Within each descriptive model active site, exemplified in Figure 75, the PDKA is deprotonated at the terminal carboxylate group and binds as a ditopic ligand to the catalytic magnesium ion. The full octahedral coordination environment of the catalytic Mg^{2+} includes Glu 340 and Asp 462 (simplified to formate anions) and two water molecules. The full coordination sphere of Mg^{2+} is retained to provide the appropriate polarizing electrostatic interaction between the PDKA and Mg^{2+} . The Arg 339 residue is included in the model to facilitate H-bonding interactions along the diketo acid tail, balance the charge of the active site and provide steric and electrostatic contributions to the orientation of Asp 633. Within the model active site, the Arg 339 residue is protonated at the terminal methanimine and simplified to amino(methylamino)methaniminium. The final component of the active site model is the Asp 633 residue which is deprotonated at the terminal carboxylate. The Asp 633 residue participates in long-range electrostatic interactions with Mg^{2+} and Arg 339 and in an anion- π interaction with the aryl portion of the PDKA.

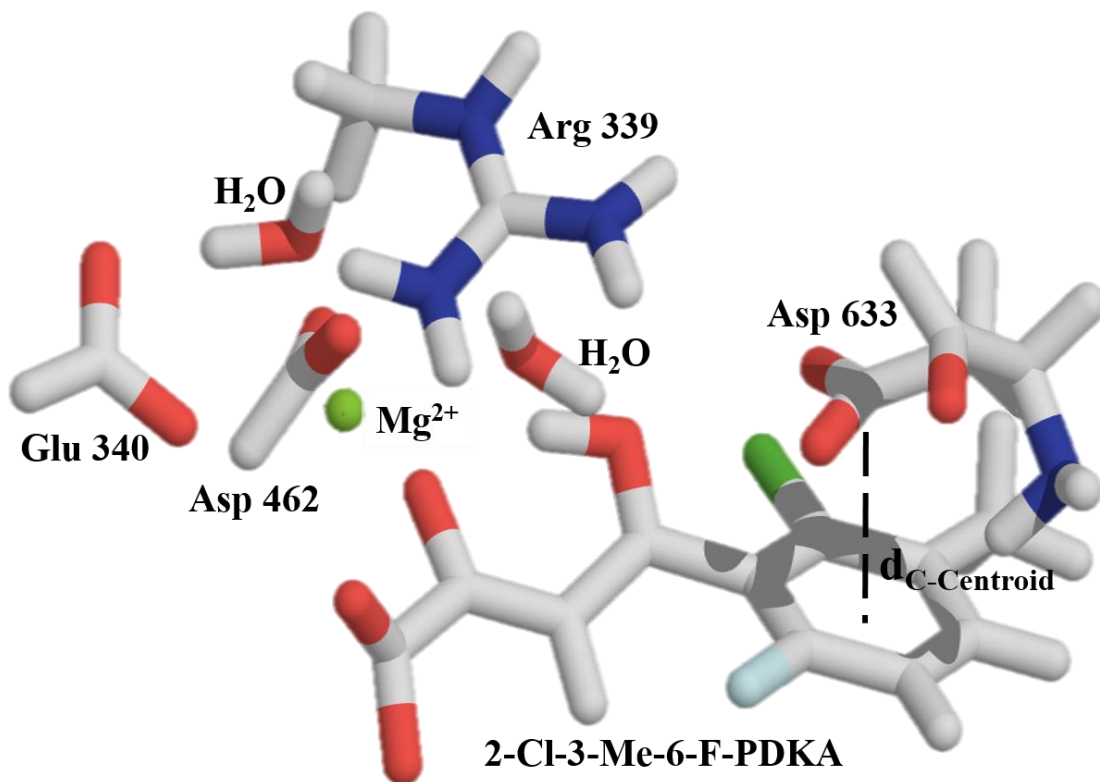


Figure 75. PDKA-GlcB model active site, including four simplified residue analogues of Asp 633, Arg 339, Glu 340 and Asp 462; the catalytic Mg^{2+} ion; two water molecules and the mono-anionic PDKA inhibitor. Graphical display generated by the PyMol⁴³ and PovRay¹³³ visualizers.

Upon overlaying the library of active sites from the PDKA-bound GlcB crystal structures **21-22**, **24-25**, **27-43**, Figure 76a, there is significant correlation of the atomic positioning and angles of interaction for the inhibitor, Mg^{2+} , water molecules, Glu 340, Asp 462, Arg 339, and the heteroatoms on the backbone of the Asp 633 residue. The overlay of crystal structures also highlights the significant range of movement at the anionic terminus of Asp 633, Figure 76b, resulting from the anion- π interaction and the

series of long-range electrostatic interactions acting upon the residue. This flexibility enables the residue to participate in anion- π interactions that, depending on the PDKA, span prototypical η^6 , weakly covalent donor- π acceptor and σ -type Meisenheimer complexes.^{25a, 168}

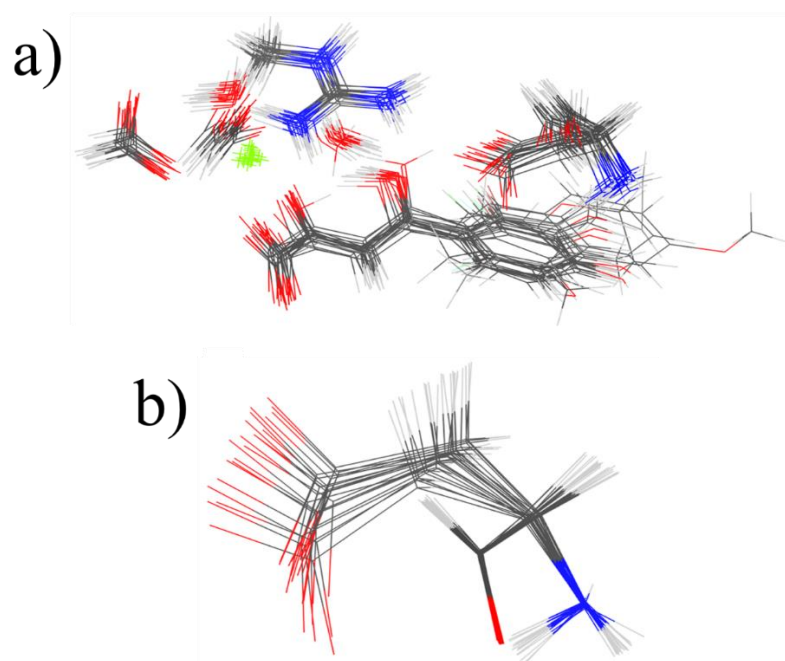


Figure 76. Structural comparison of PDKA-bound active sites from crystal structures with **21-22, 24-25, 27-43**. a) Overlay of the descriptive active site, aligned by the PDKA backbone. b) Overlay of the Asp 633 residue, aligned by the N and O atoms on the residue backbone. Graphical display generated by the Materials Studio Visualizer.¹⁴

In light of Active Sites A-C and the over-simplified active site reported by Frontera and coworkers,¹⁵⁸ the aim of this study was to develop an active site that not only yielded

appropriate interaction energies of the active site but also reproduced the interaction orientation associated with the binding of the PDKA. Due to the electrostatic sensitivity and the broad range of movement of Asp 633 evidenced by Figure 76b, the orientation of the residue with respect to the parent crystal structures was used to gauge the proficiency of each model system described in the following sections, both energetically and sterically.

Development of a reference model, the H-optimized model

For each model active site **21-22**, **24-25** and **27-43**, the coordinates of the non-hydrogen atoms were restrained and the hydrogen atoms were optimized (the grey atoms and purple atoms respectively identified in Figure 77). From single point energies of the constituents of the partially optimized structures, the binding enthalpy of each PDKA in the respective H-optimized model active site was calculated. The resulting series of structures, the H-optimized series, provided a baseline for evaluating the following computational models according to the Asp 633 orientation and the PDKA binding enthalpy.

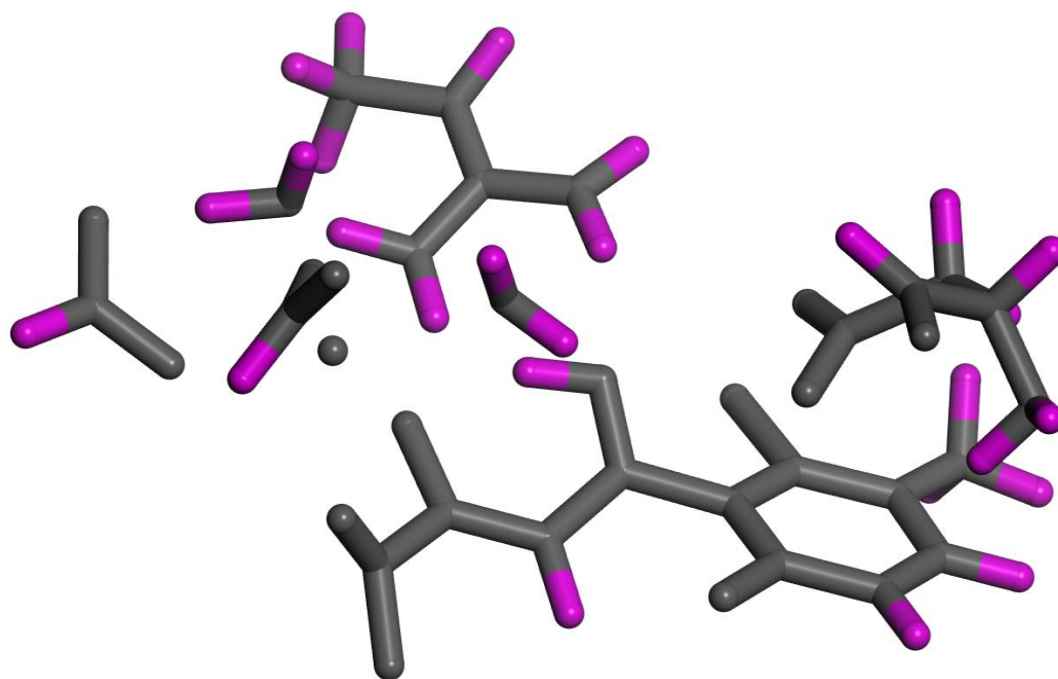


Figure 77. H-optimized Model **27** Structure with the optimized hydrogen atoms identified in purple. Graphical display generated by the Materials Studio Visualizer.¹⁴

Development of the Descriptive Active Site Model

Each respective model active site for the library of PDKA-GlcB structures was partially optimized to obtain the Descriptive Model system. The atomic coordinates of the heteroatoms along the backbone of Asp 633, the non-hydrogen atoms comprising the PDKA inhibitor, Mg^{2+} , water molecules, Asp 462, Glu 340, and Arg 339 were restrained (grey atoms in Figure 78). The remaining atoms of Asp 633 and the hydrogen atoms were optimized (the blue atoms in Figure 78), resulting in the Descriptive Model series.

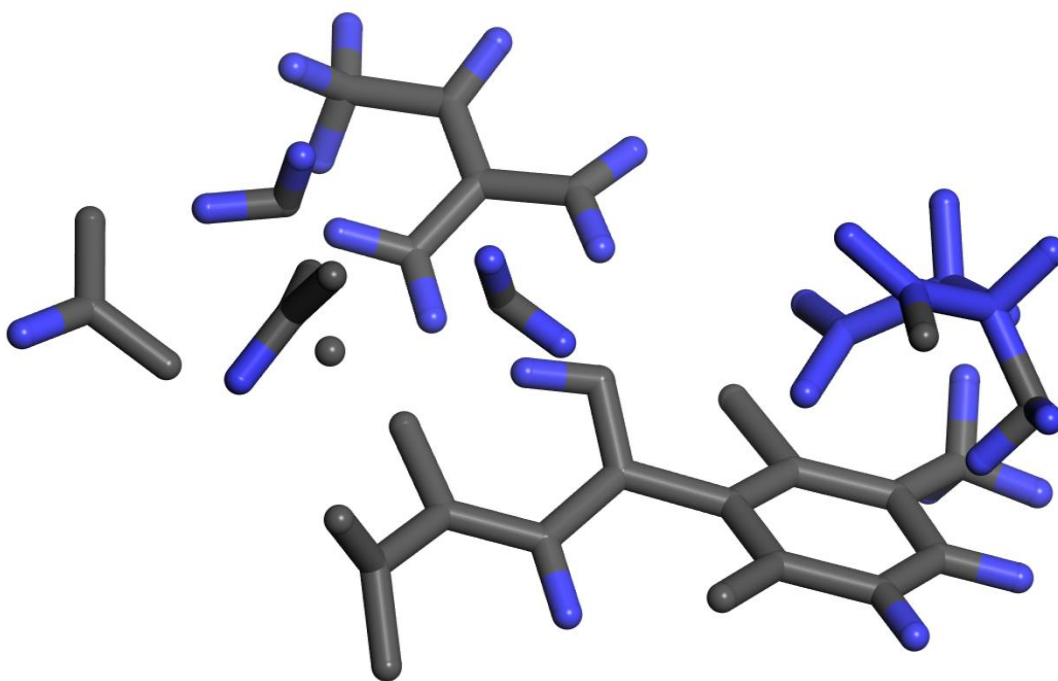


Figure 78. Descriptive Model 27 Structure with the optimized atoms identified in blue. Graphical display generated by the Materials Studio Visualizer.¹⁴

The distance between the carbon atom of the Asp 633 carboxylate group and the centroid of the PDKA aryl moiety ($d_{C\text{-Centroid}}$) was compared for each of the respective H-optimized and Descriptive Model structures. There is significant agreement between the $d_{C\text{-Centroid}}$ distances for each pair of H-optimized and Descriptive Model structures, with an average accuracy of within 0.13 Å that is well within the resolution accuracy of the protein crystal data,⁴¹ Figure 79.

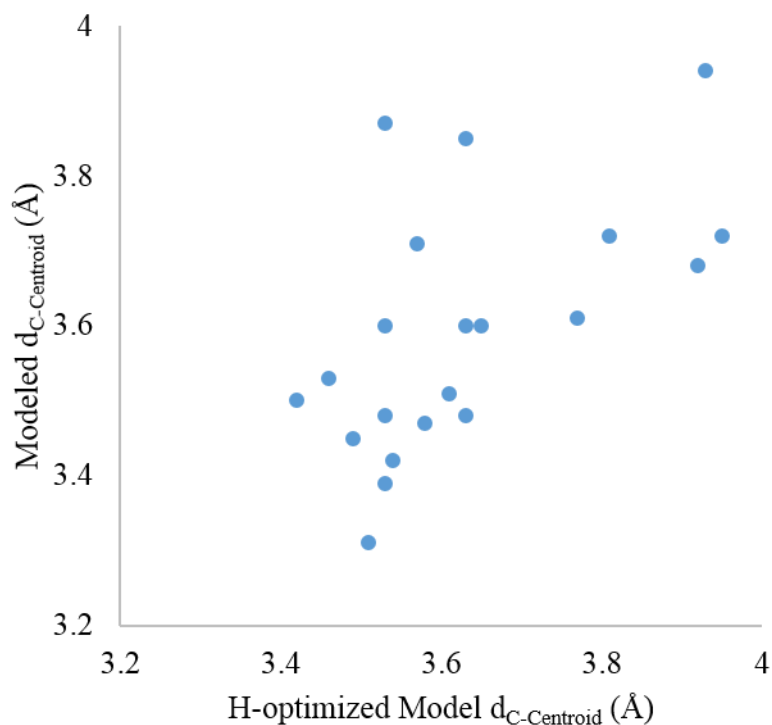


Figure 79. Comparison of the $d_{C-Centroid}$ for the Descriptive and the H-optimized Models, with an average accuracy of 0.13 Å.

The considerable agreement between the Asp 633 orientation for the H-optimized and Descriptive Model systems supports the conclusion that the model active site includes the appropriate steric and electrostatic active site constituents. Overlays of several representative pair of H-optimized and Descriptive Model active sites are visualized in Figure 80. For structures **22**, **24** and **25** (structure **25** not depicted), the arm of the Asp 633 residue rotates in order to access a more energetically favorable orientation within the model active site that is not observed within the protein active site, Figure 80. For a couple of the pairs of H-optimized and Descriptive active sites, there appears to be a large

difference in the $d_{C\text{-Centroid}}$ values, but the Asp 633 residue simply shifts across the face of the PDKA and maintains the same distance from the centroid. For the pair of structures for **33**, the difference of $d_{C\text{-Centroids}}$ is only 0.01 Å. For other pairs of structures, such as those for **21**, the difference in $d_{C\text{-Centroid}}$ does not appear to be significant but is on the higher end of discrepancy at 0.16 Å. With such a precise model, small discrepancies are able to be identified, but overall, the Asp 633 residue is very accurately oriented in the PO Descriptive Model active sites.

The PDKA binding enthalpies for Descriptive Models **21 – 22, 24 – 25, 27 – 43** were calculated using single point energies of the components. The PDKA binding enthalpies for **21, 22** and **24** were compared to the enthalpy measured by the ITC experiments, portrayed relative to H-optimized **21** in Figure 81. The lack of correlation between the experimental and Descriptive Model enthalpies is likely due to the over rotation of the Asp 633 upon optimization, as seen in the overlays for **22** and **24** in Figure 80

Descriptive Model

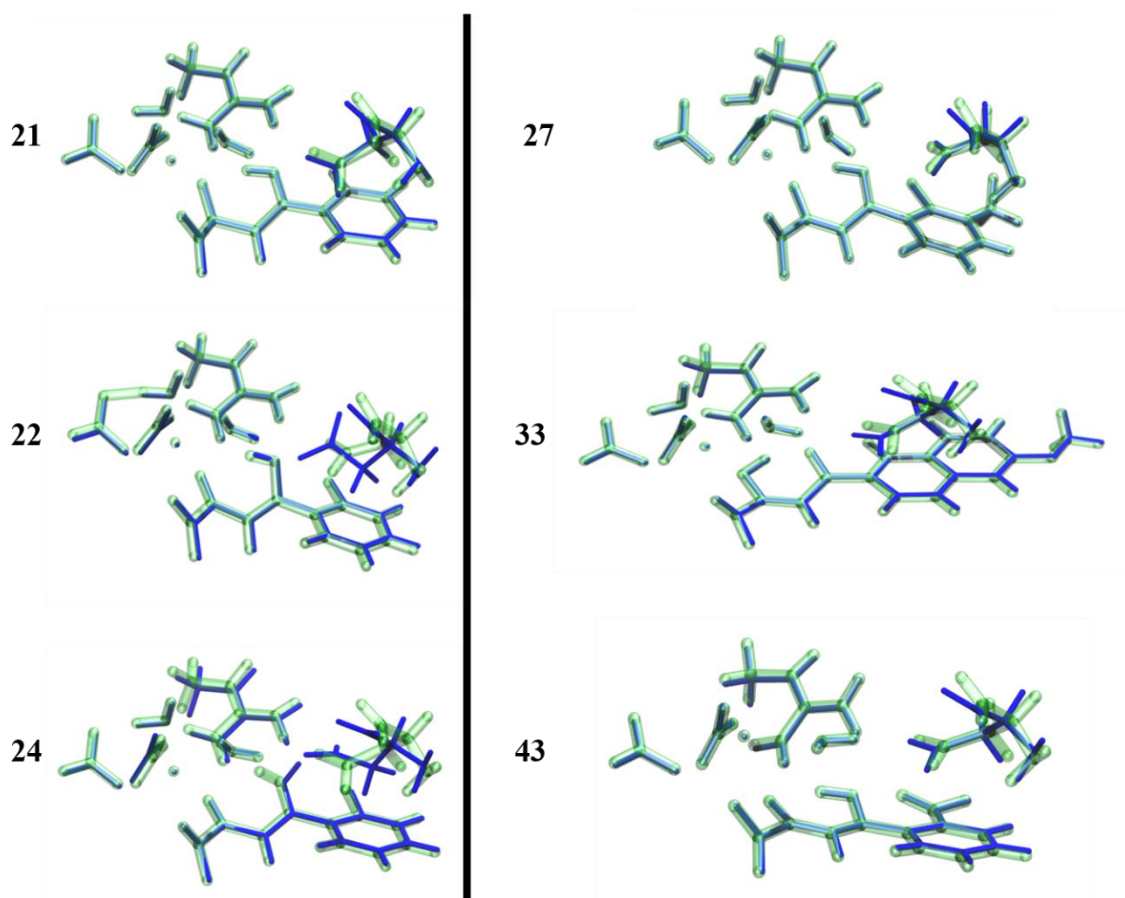


Figure 80. Overlays of the respective H-optimized (blue) and Descriptive (green) Model Active Sites for representative structures **21**, **22**, **24**, **27**, **33** and **43**. Graphical display generated by the VMD¹⁶⁹ and PovRay¹³³ visualizers.

In the H-optimized system, the Asp 633 orientation is not altered from that in the protein crystal structure, but the H-optimized binding enthalpies do not correlate to the ITC-derived PDKA binding enthalpies, Figure 81. This may be a result of the resolution of the protein crystal structure, solved at $\sim 1.8 - 2 \text{ \AA}$ resolution, or the restraints applied

upon solving the crystal structure. While highly resolved for a protein crystal structure, the degree of uncertainty associated with the atomic coordinates may be sufficient enough to contribute to such disparity of the interaction energies for the H-optimized Model series. Further ITC experiments may help to clarify this inconsistency.

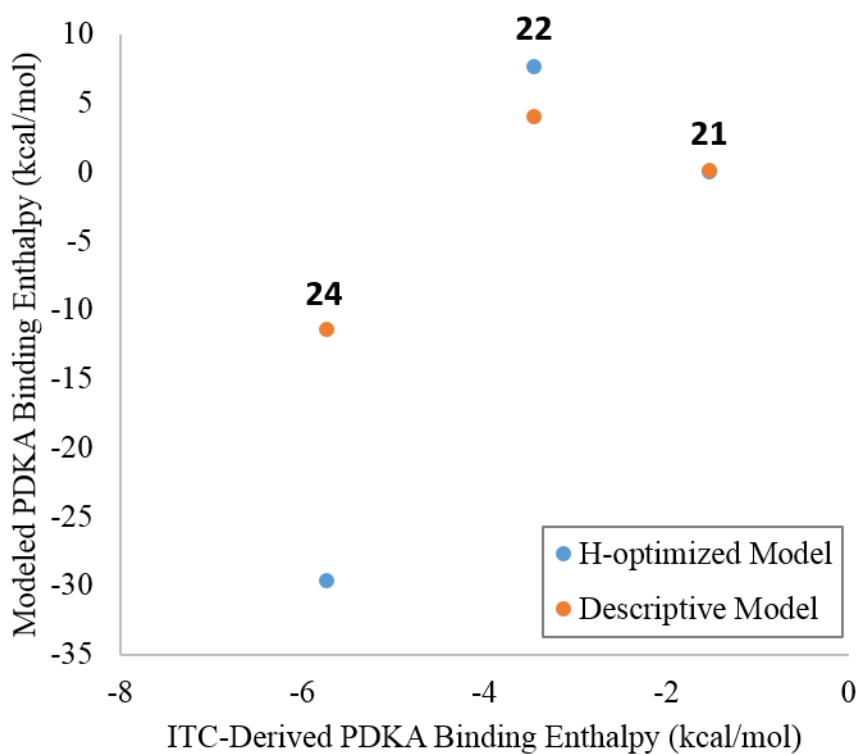


Figure 81. Comparison of the PDKA binding enthalpies of the ITC experiments and the H-optimized (blue) and Descriptive Models (orange) for **21** - **24**, shown relative to H-optimized **21**.

In the absence of ITC data for the remainder of the PDKA-GlcB complexes, the PDKA binding enthalpies for the Descriptive Model series were compared to those of the H-optimized series, portrayed relative to H-optimized Model **21** in Figure 82. There is strong agreement between the PDKA binding enthalpies of the Descriptive Model and H-optimized systems, with an average difference in enthalpy of 5.05 kcal/mol across the series of structures in Figure 82. The two structures that demonstrate a difference in the Descriptive and H-optimized PDKA enthalpies of greater than 20 kcal/mol undergo reorientation of the Asp 633 residue upon partial optimization of the Descriptive Model active site. The arm of the residue twists to find a more energetically stable position that is not allowed within the protein active site due to steric constraints, resulting in a significant difference in PDKA binding energies.

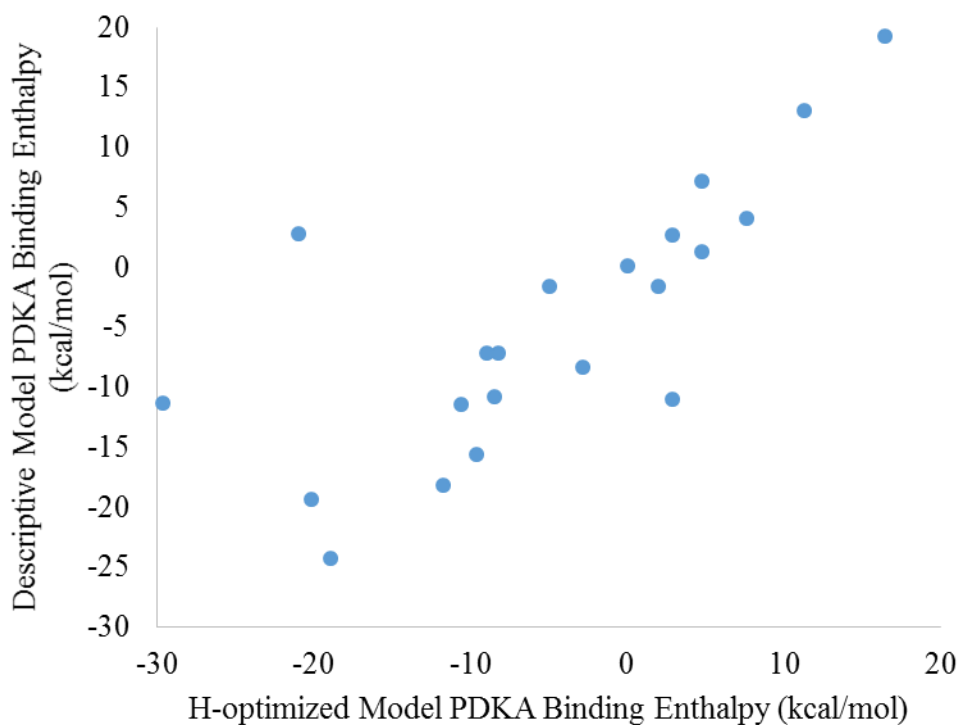


Figure 82. Comparison of the PDKA binding enthalpies calculated for the Descriptive and H-optimized Model structures, shown relative to H-optimized **21**.

Investigations of Alternative Descriptive Model Active Site Methods

Several attempts were made to improve the accuracy of the Descriptive Model. First, the N- and O-atoms restraining the Asp 633 residue were removed and the alpha-C on the residue was used to restrain the moiety, Alternative Active Site A, Alt-A. This was envisioned as a method for mitigating the adoption of an improper torsion at the alpha carbon upon PO of the Descriptive Model Active sites for **22**, **24** and **25**. Therefore, the atomic coordinates of the alpha-carbon (green atom in Figure 83a), the Mg²⁺, water

molecules, Glu 461, Asp 462, Arg 339, and PDKA were restrained (grey atoms in Figure 83a) while the remainder of the Asp 633 residue and hydrogen atoms were optimized (yellow atoms in Figure 83a). For the subset of structures analyzed, the Asp 633 residue did not adopt the ideal orientation of that in the crystal structure and the average $d_{C\text{-Centroid}}$ discrepancy increased significantly.

The impact of the hydrogen-halogen interactions between the Arg 339 and the 2-*ortho*-PDKA substituents were incorporated for **21**, **22** and **24** in Alternative Active Site B, Alt-B. The Alt-B active site was partially optimized by allowing the substituted-phenyl ring, hydrogen atoms and the arm of Asp 633 to optimize while the heteroatoms of Asp 633 and the remaining non-hydrogen atoms were restrained. The optimized atoms are identified in red and the restrained atoms are in grey in Figure 83b. For **22** and **24**, there was rotation of the 2-*ortho*-substituted aryl group resulting in shorter hydrogen-halogen interactions, resulting in shorter X-H contacts by an average of 0.17 Å. Such rotation deviates significantly from the protein crystal structure, likely due to the additional steric constraints of the active site that are not included in the model active site. Expanding the active site to include all of the steric constraints would be too computationally expensive, so the atomic coordinates of the aryl portion of the PDKA were not optimized in further models to mimic the effects of the steric restraints.

While including the entire cavity would be too computationally intensive, an expanded Alternative Model Active Site was evaluated, Alt-C. This expanded model included portions of the Asp 461 and Leu 462 residues that participate in H-bonding interactions along the diketo acid PDKA backbone, Figure 83c. Including more of the

active site was hypothesized to improve the accuracy of the orientation of the Asp 633 residue. However, evaluation of this larger active site resulted in a lower accuracy of the $d_{C\text{-Centroid}}$, 0.14.Å, at higher computational cost and therefore was discarded.

Finally, the protonation of the PDKA was modified to the keto and enol forms of the Descriptive Active Site and a simplified version. The PDKA was additionally protonated to the neutral acid form of the molecule. The resulting series of structures composed the Alternative Active Site D, Alt-D in Figure 83d. The variously protonated versions of PDKA were partially optimized by optimizing the hydrogen atoms and restraining all of the non-hydrogen atoms. The interaction energies of the resulting structures were significantly weaker than the Descriptive Active Site counterparts. While not pursued further, it was interesting to note that, for several of the forced-enol tautomers, the proton spontaneously migrated to the keto-position due to the greater favorability. The keto-protonation form was retained for all of the Descriptive and Predictive Active sites.

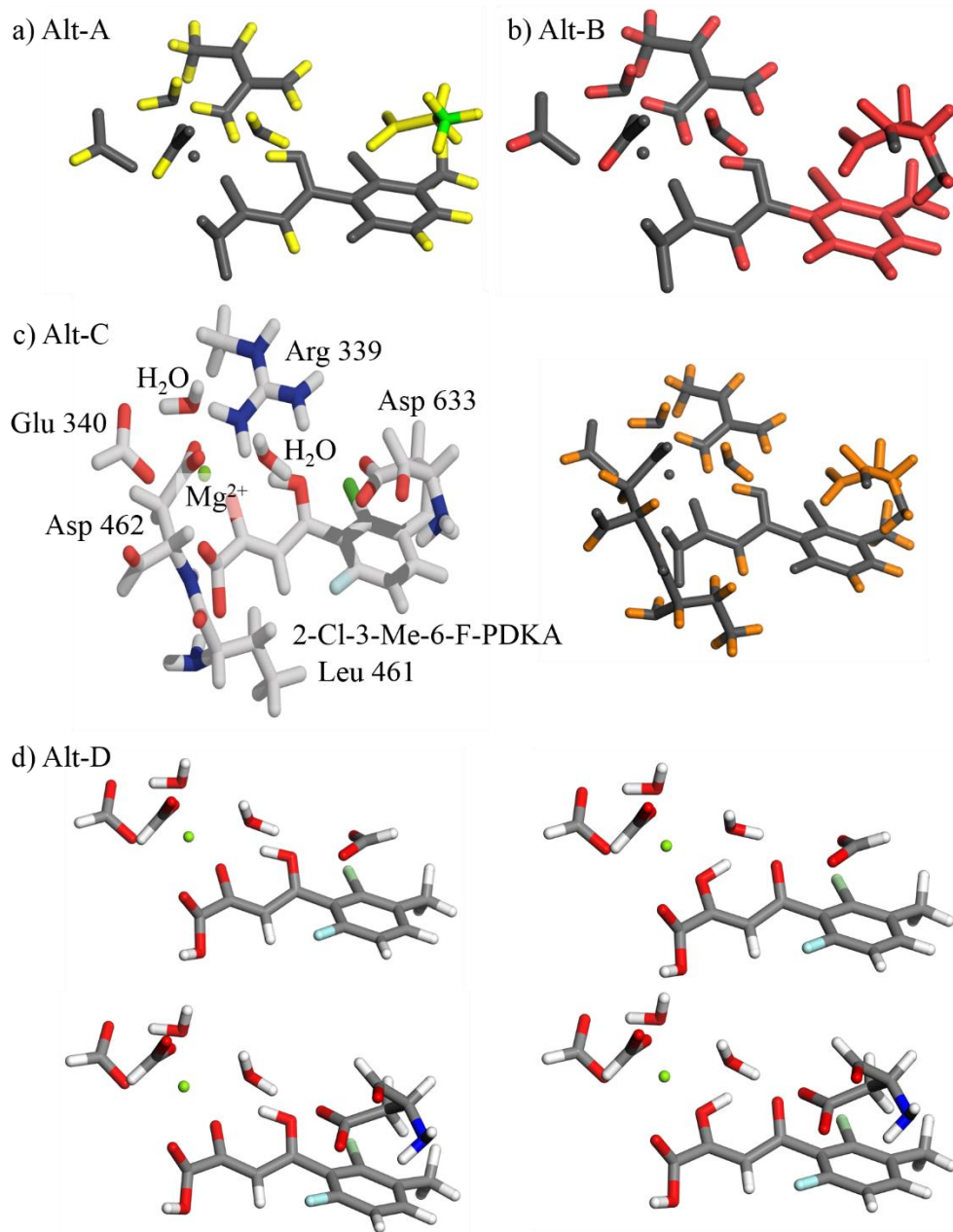


Figure 83. Alternative Model Active Sites, Alt A - D. Graphical display generated by the Materials Studio Visualizer.¹⁴

Conceptualization of a Predictive Active Site Model

The Descriptive Active Site Model is useful for exploring the interactions involved in PDKA binding, but the utility of the model is restricted to those systems that have been previously synthesized and crystallized. In order to develop a tool that complements the library of CADD methodologies, a Predictive Active Site Model was needed that could predict the orientation of the Asp 633 residue upon binding and, most importantly, the PDKA binding enthalpy. To this end, several predictive models were explored.

First, in Predictive Model A, Pre-A, the Asp 633 residue was rotated away from the PDKA. While restraining the hetero-atoms on the Asp 633 backbone and the non-hydrogen atoms in the remainder of the active site, the Asp 633 residue and the hydrogen atoms were optimized. The degree of rotation of the Asp 633 residue was too large for the optimization to overcome, resulting in incorrect final orientations of the aspartate residue for many of the PDKAs, Figure 84. Pre-A highlighted that a more appropriate starting structure was necessary for future methods and was not pursued.

Upon further considering the overlay of active sites in Figure 76, the atomic positions for the Mg^{2+} , water molecules, Glu 340, Asp 642, Arg 339, and the heteroatoms of the Asp 633 are considerably aligned. From this alignment, the average atomic coordinates of the common atoms in the active site, excluding the PDKA substituents, were calculated for Predictive Model B, Pre-B. The asymmetrical PDKA phenyl ring was replaced with a phenyl group with typical bond lengths and angles. For each of the PDKA structures, analogous substituents were added to the phenyl group. The hetero-atoms on the Asp 633 backbone and the non-hydrogen atoms in the remainder of the average active

site were restrained and the Asp 633 residue and the hydrogen atoms were optimized. Averaging the coordinates of diverse systems resulted in extremely strained bond angles and incompatible bond lengths for the majority of the active site, so this method was not pursued further. Predictive Model C, Pre-C, refined this concept by calculating the average atomic coordinates of the Asp 633. Upon substituting the average residue orientation for Asp 633 in each PDKA crystal structure, the hydrogen atoms and the orientation of the residue were optimized with the rest of the active site being restrained. While the $d_{C\text{-Centroid}}$ is reasonable with respect to **27** in Figure 84, the bond lengths and bond angles were not ideal. Pre-B and Pre-C models were unsuitable for optimization for the PDKAs and were not pursued.

In Predictive Model D, Pre-D, Asp 633 was replaced for each of the active site structures by the Asp 633 from the unsubstituted PDKA. The residue was translated such that the heteroatoms along the aspartate backbone were aligned with those in the original crystal structure, providing ample room for rotation of the residue from the PDKA starting from a biologically relevant position. The aspartate, excluding the heteroatoms along the backbone, and the hydrogen atoms were optimized while the remaining atoms of the active site were restrained. Pre-D was analyzed on a subset of structures but produced an average accuracy of the $d_{C\text{-Centroid}}$ to within 0.17 Å.

While the Pre-A through D models often resulted passable $d_{C\text{-Centroid}}$ values, the models were contingent upon using portions of the native crystal structures for each PDKA (Pre-A, C and D) or an active site with non-ideal bond lengths or angles (Pre-B).

Using either of these types of approaches is not feasible for predicting accurate PDKA interactions within PDKA-GlcB complexes without having the crystal structures.

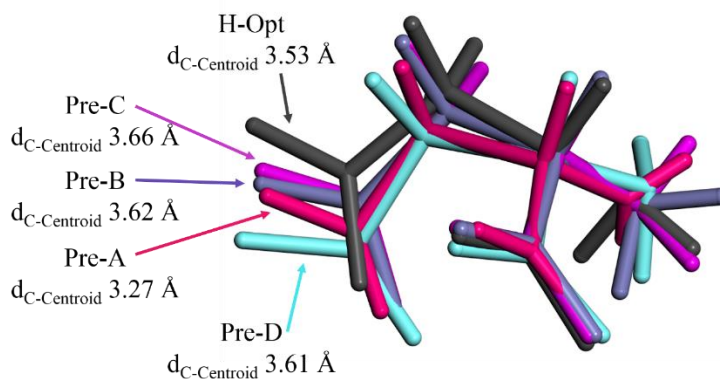


Figure 84. Comparison of the PO Asp 633 residue for each of the Predictive Models A - D with H-Optimized for **27**. Graphical display generated by the Materials Studio Visualizer.¹⁴

Evaluation of the Predictive Active Site Model

The Predictive Active Site Model was therefore developed as a template-based method to predict the binding interactions of PDKAs within GlcB. The PDKA-bound GlcB active site of tri-substituted **27** was selected as the Predictive Model template because **27** has been shown to have high activity with GlcB in the esterified form and the active site for **27** was successfully evaluated by the Descriptive Active Site Model. The orientation of Asp 633 within the active site of **27** is also oriented closer to the PDKA than average and was hypothesized to be a suitable starting point for PDKAs with desirable anion- π interactions with Asp 633. For the Predictive Model active sites, the geometry of

the template structure of **27** was retained while the PDKA substituents were modified for PDKAs **21** - **43**. The atomic coordinates of the heteroatoms along the backbone of Asp 633, non-hydrogen atoms comprising the PDKA inhibitor (except for the substituents), Mg^{2+} , water molecules, Asp 462, Glu 340, and Arg 339 were restrained (grey atoms in Figure 85). The remaining atoms of Asp 633, the hydrogen atoms, and the modified aryl substituents were optimized (green atoms in Figure 85).

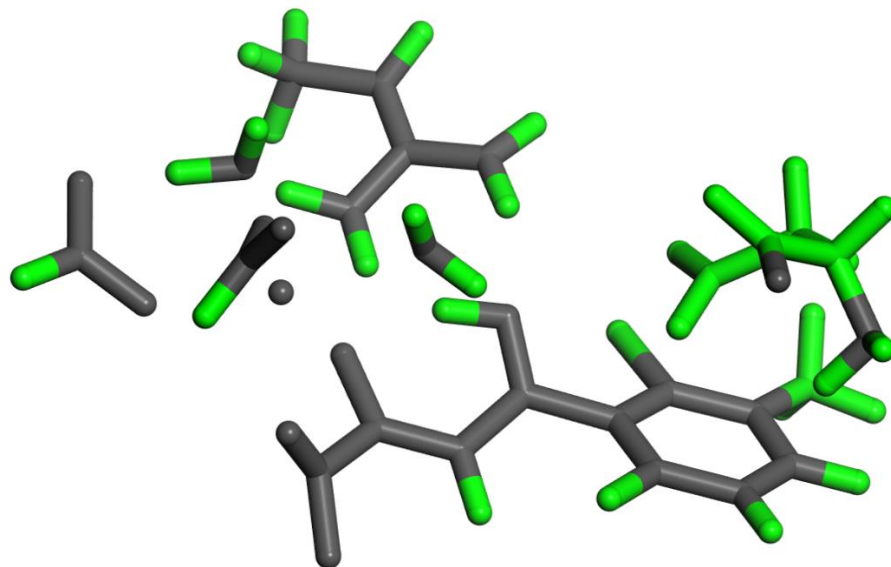


Figure 85. Predictive Model **27** Structure with the optimized atoms identified in green. Graphical display generated by the Materials Studio Visualizer.¹⁴

Alternative templates were explored in a like manner using active sites **21**, **31**, **35**, **36**, **37** and **43**. Templates **21** and **31** were more suited for electron-donating groups, and templates **35** and **36** were applied to PDKAs with extended ring-systems. Templates **27**,

37 and **43** were used to evaluate the PDKAs with electron-withdrawing substituents. By averaging the three $d_{\text{C-Centroid}}$ values produced for each PDKA evaluated by **27**, **37** and **43**, the average accuracy of the $d_{\text{C-Centroid}}$ value was incredibly high, with an average discrepancy of 0.04 Å for a subset of PDKAs with electron-withdrawing substituents. However, the averaged $d_{\text{C-Centroid}}$ value does not correspond to a physically relevant structure and was therefore discarded in favor of using **27** as the sole template in the Predictive Active Site Model.

Upon partial-optimization of the Predictive Model active sites using template **27**, each $d_{\text{C-Centroid}}$ was compared to the respective H-optimized structures. There is correlation between the Predictive and H-optimized structures, especially for structures with strongly electron-withdrawing PDKA substituents, and the average accuracy of the $d_{\text{C-Centroid}}$ for the entire Predictive Model series is 0.16 Å, within the accuracy of the crystal data, Figure 86a. For those structures with electron-donating substituents and $d_{\text{C-Centroid}}$ values of greater than 3.7 Å, the Predictive Model does not model the H-opt $d_{\text{C-Centroid}}$ as well as the Descriptive Model, Figure 86a and b. However, for the PDKA-GlcB structures with electron-withdrawing substituents and $d_{\text{C-Centroid}}$ values of less than 3.7 Å, the Predictive Model more accurately models the structures than does the Descriptive Model, Figure 86a and b. The PDKA binding enthalpy was also calculated for each of the templated structures and suitably reproduced the interaction energies of the H-optimized system, especially those PDKAs with strong binding enthalpies and short $d_{\text{C-Centroid}}$ contacts. The average deviation between the Predictive Model enthalpies and the H-optimized series is 11.1 kcal/mol, Figure 86b. The Descriptive Model does reproduce the H-optimized PDKA

binding enthalpies in a more proportional fashion, Figure 86b, but, as previously discussed, this metric does not necessarily signify error on the part of the Predictive Model due to the possible inaccuracy of the H-optimized model PDKA binding enthalpies, Figure 81. Due to the predisposition of the Asp 633 for close-contact with the PDKA, the Predictive Active Site Model most accurately reproduces the crystal structure orientations and binding enthalpies for those PDKAs with electron-withdrawing substituents and, consequently, strong PDKA binding interactions.

In light of the extensive characterization of the 2-*ortho*-PDKA series, structures **21** - **24** were considered to further appraise the Predictive Model. The crystal structure of **3** has been unable to be grown and characterized, but, for structures **21**, **22** and **24**, the average accuracy of the $d_{C-Centroid}$ for the Predictive Model is 0.12 Å. The predictive models for **22** and **24** demonstrate high accuracy upon comparison to the experimental structures, less than 0.03 Å, and the optimized orientation of the Asp 633 residue is significantly more ideal for the Predictive Models of **22** and **24** than the Descriptive Models, Figure 87. The majority of the $d_{C-Centroid}$ discrepancy of the **21** – **24** subset arises from the final orientation of Predictive Model **21**. The predisposition of the template active site for close Asp 633 contact enables the Asp 633 residue in **21** to access local energetic minima for the anion- π interaction that are closer to the PDKA than achieved in the protein crystal structure, with a difference in the $d_{C-Centroid}$ of 0.32 Å. Regardless, the accuracy of the $d_{C-Centroid}$ for Predictive Model **21** is still quite similar to the resolution of the crystal data for **21**.

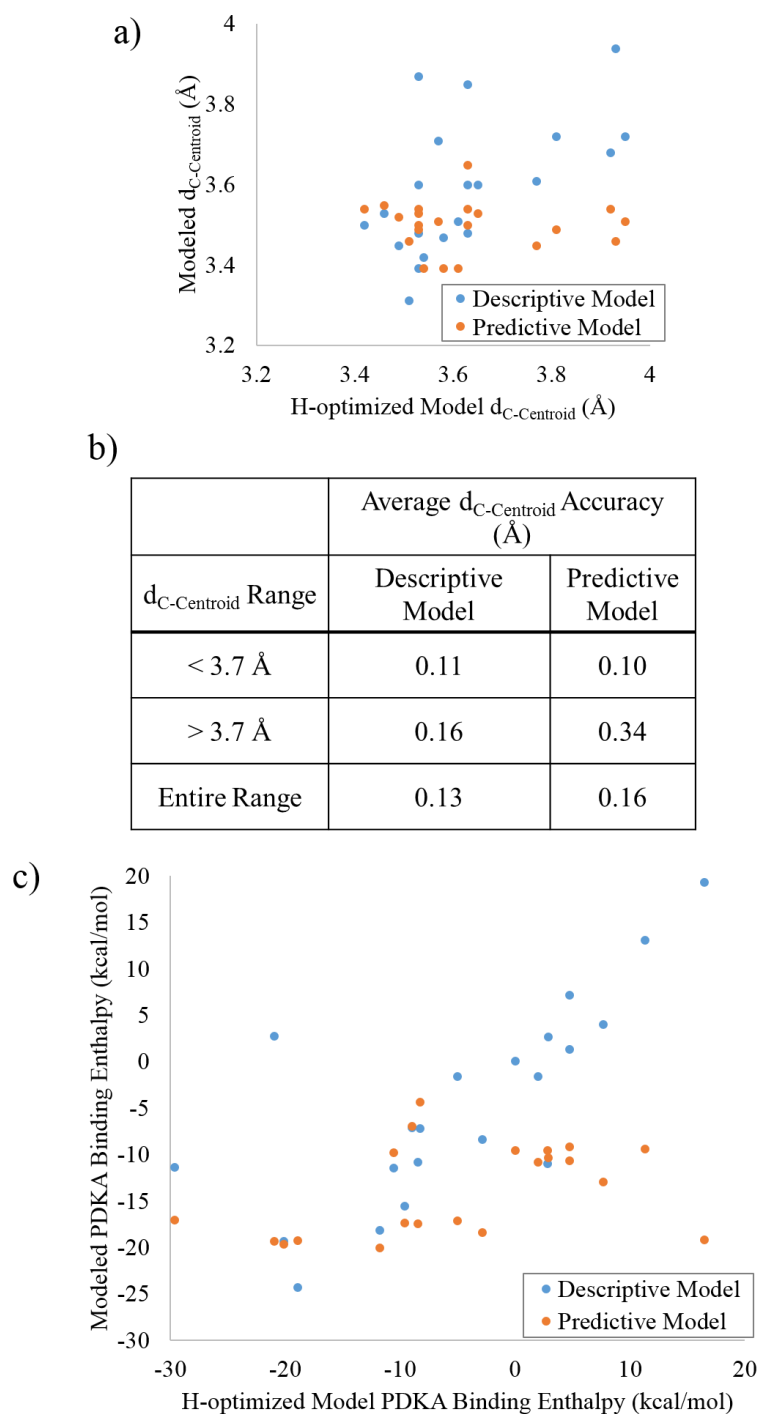


Figure 86. Comparison of the a) $d_{C-Centroid}$ values, plotted for the Descriptive and Predictive Models against the H-optimized model, b) groups of PDKA-GlcB structures and the average $d_{C-Centroid}$ accuracy, and the c) PDKA binding enthalpies between both the Descriptive and Predictive Model Active Sites and the H-optimized Model.

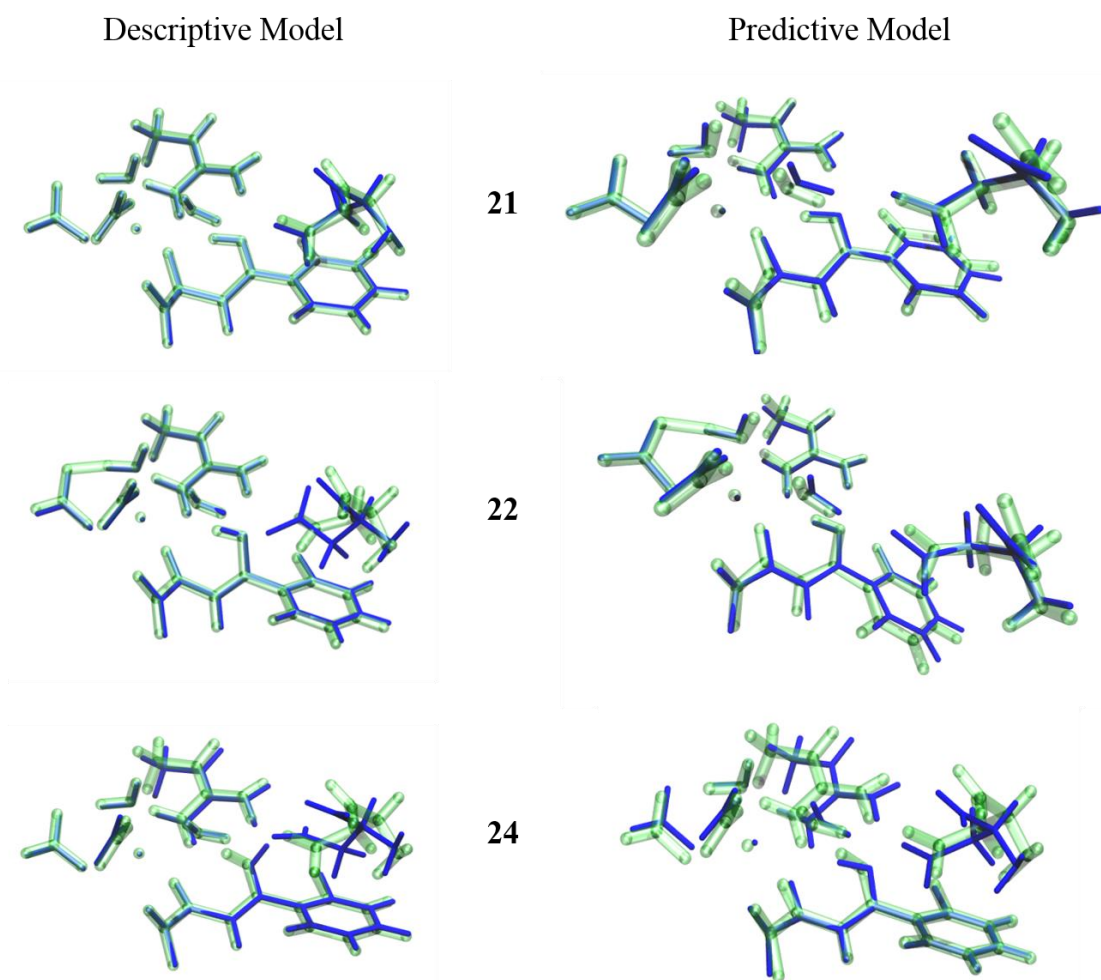


Figure 87. Overlays of the respective H-optimized (blue) and Model Active Sites (green) for the Descriptive and Predictive Models of **21**, **22**, and **24**. Graphical display generated by the VMD¹⁶⁹ and PovRay¹³³ visualizers.

Furthermore, the PDKA binding enthalpies of the Predictive Model system were compared to those derived by ITC and a directly proportional relationship was identified, Figure 88. The deviation of the 2-Cl-PDKA modeled enthalpy from ideal proportionality may result from the difference in PDKA orientation between the template and 2-*ortho*-

PDKA crystal structures but is acceptable in light of the error inherent to micro-ITC measurements, typical error ranging from 3 - 25%.¹⁷⁰ Therefore, the proportional relationship of the predicted and measured binding enthalpies strongly supports the utility of the Predictive Model. This model successfully determines the orientation of Asp 633 as it participates in an anion- π interaction with the PDKA and evaluates the relative PDKA binding enthalpy for the 2-*ortho*-PDKA series.

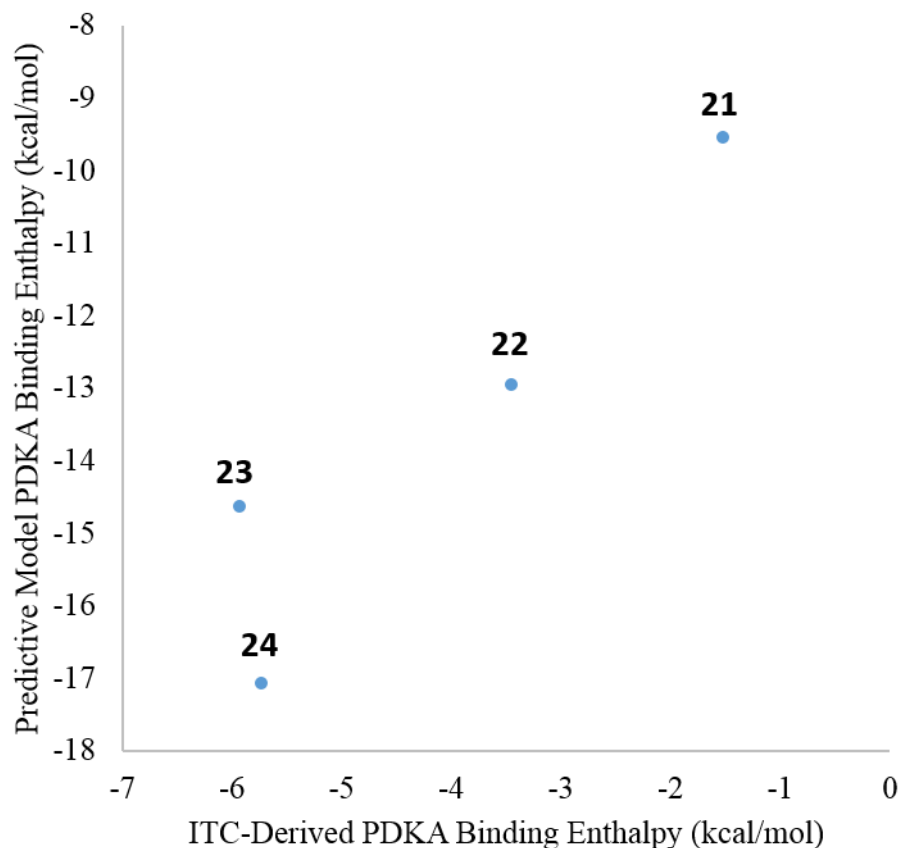


Figure 88. Comparison of the PDKA binding enthalpies of the ITC experiments and the Predictive Model, modeled binding enthalpy shown relative to H-optimized **21**.

Development of a Pre-Screened Predictive Method

While the Predictive Active Site Model meets the initial goals of the study, evaluating one single PDKA has a moderately high computational cost. On average, partially optimizing a Predictive Model structure utilizes 180 hours of processor time. The level of processing resources necessary to screen a library of potential PDKAs would be quite intensive, so a pre-screening method was needed to moderate this issue. Harkening back to the original evaluation of Cl⁻- π interaction energies of the analogous substituted-benzene molecules, the Cl⁻- π interaction model demonstrates significant correlation to the ITC-derived binding enthalpy. As can be seen in Figure 89a, the proportional relationship between the Predictive PDKA binding enthalpy and the ITC enthalpy data is very nearly mirrored by the proportional relationship between the Cl⁻- π interaction energy and the ITC enthalpy data. In fact, comparison of the Predictive Model binding enthalpies and the Cl⁻- π interaction energies follows a relatively linear regression for the remainder of the PDKA structures, Figure 89b. While the orientation of the active site constituents is fixed in the template-based model, the strength of the interactions available for the modified PDKA scales based on the PDKA substituent(s). The Cl⁻- π interaction model only probes the change in the anion- π interaction energy, but this interaction energy is proportional to the overall binding enthalpy as calculated by the Predictive Active Site Model due to the substituent effects and the cooperativity of the non-covalent interactions.

The relationship between the two models is not completely proportional, especially for the very strongly bound anion- π interactions. This is due to the fact that the anchored residues can only interact with the PDKA as strongly and as closely as allowed by the

protein structure framework (and model). The Cl^- - π model does not predict the PDKA binding enthalpy with complete precision, but it can be used to identify PDKAs that will strongly bind in the model active site, in excess of 15 kcal/mol. Also, the Cl^- - π model requires significantly fewer computational resources. Therefore, the Cl^- - π model can be used as a screening method to narrow the field of PDKA candidates to those that will have favorable anion- π and, therefore, binding interactions. Of these narrowed structures, the Predictive Active Site Model can be applied in order to more thoroughly study the binding strength and interactions involved with each PDKA.

Conclusions and Future Outlook

Infection by *Mycobacterium tuberculosis* continues to impact the world's population in epidemic proportions, but new drugs and combination therapies are constantly being developed to address this threat. Structure-based drug development and computer-aided drug development methodologies have met with success but are insufficient for evaluating and optimizing the series of non-covalent interactions involved in the PDKA inhibition of GlcB, in particular the anion- π interaction. Through this study, a DFT method of exploring the non-covalent interactions involved in PDKA-GlcB binding has been developed and applied in order to predict binding affinities of PDKAs for future drug development.

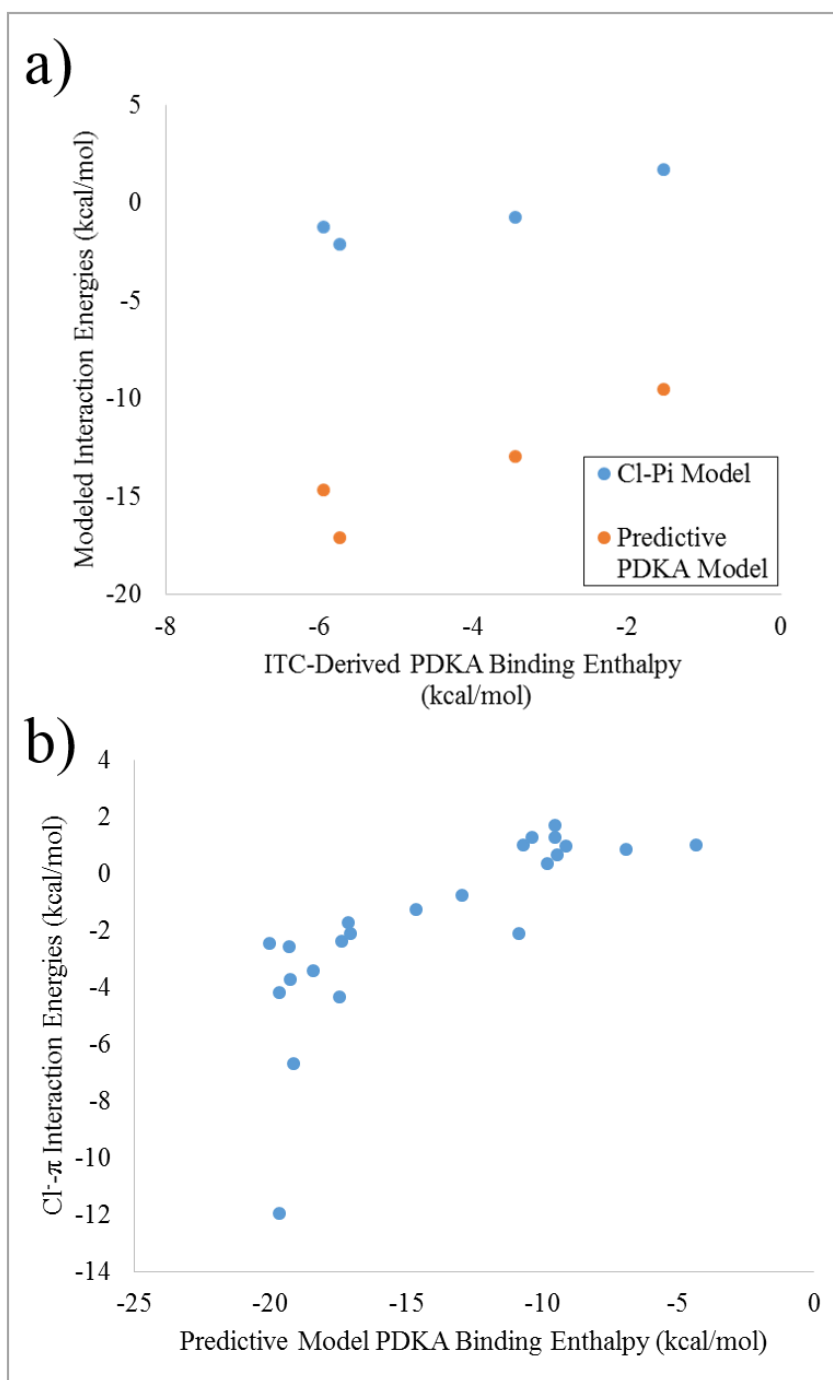


Figure 89. Correlation between the Cl⁻- π Interaction Model and the Predictive Active Site Model is exemplified by (a) Similar proportional relationships between the respective binding energies and the ITC-derived binding enthalpy, and by a (b) Proportional relationship between the Cl⁻- π interaction energies and the Predictive PDKA binding enthalpies (shown relative to H-optimized **21**).

The anion- π interaction that was identified upon inhibition of GlcB was initially hypothesized to direct inhibition, but the corresponding IC₅₀ values and ITC data belie the complexity of the biological and chemical interactions involved in inhibition. Theoretical DFT methods were therefore used to investigate the enthalpic contributions to PDKA-GlcB inhibition, with particular interest in the anion- π interaction involvement. Model active sites were developed for each PDKA by judiciously incorporating portions of the PDKA-GlcB active site from the crystal data that participate in binding the substrate. Upon partial optimization of each active site, the Descriptive Active Site Model accurately replicates the orientation of the Asp 633 orientation, within 0.13 Å, as it participates in an anion- π interaction with the PDKA and other long-range electrostatic interactions. The PDKA binding enthalpy was calculated for each PDKA-GlcB complex in the Descriptive Model series and the Hydrogen-optimized series. The strong agreement of the PDKA binding enthalpy, as compared to the H-optimized model system, highlights the importance of identifying and incorporating critical non-covalent interactions for accessing an electrostatic understanding of the active site.

Using Descriptive Model active site **27** as a template, the Predictive Active Site Model was developed as a method for calculating the relative binding affinities of PDKA molecules with GlcB. The Predictive Model accurately calculates the orientation of Asp 633 as it engages in an anion- π interaction and long-range electrostatic interactions. The Predictive Model also proportionally models the PDKA binding enthalpy. The Predictive Model and ITC-derived PDKA binding enthalpies show a directly proportional relationship for the *2-ortho*-PDKA series. Descriptive Model **27** functions as an accurate

template for **21 – 24**, but several other templates were discussed as being more accurate for specific PDKA types, i.e. PDKAs with electron donating substituents or extended systems. It may be advantageous in the future to consider additional templates as the library of PDKAs grows.

The Predictive Active Site Model is effective for predicting the Asp 633 orientation and binding enthalpy within the PDKA-GlcB active site but is too computationally expensive to screen all of the possible combinations of PDKA substituents. However, the Cl⁻- π Model demonstrates a proportional relationship with the Predictive Active Site binding enthalpies. This correlation identifies the importance of the anion- π interaction within the PDKA-GlcB active site, both for directing the binding of the Asp 633 residue and as a relative approximation of the strength of the non-covalent interactions involved in the active site. Therefore, the Cl⁻- π Model has been identified as a screening method to identify promising PDKA targets for further evaluation by the Predictive Active Site Model.

The results of this study have demonstrated, for the first time, the importance of incorporating anion- π interactions into CADD methodologies, providing a guide for future medicinal chemistry pursuits. Future research will benefit from efforts to identify promising PDKA targets through the Cl⁻- π screening and Predictive Active Site Model. As further ITC experiments characterize PDKA inhibition, empirical optimization of the template methods can also be realized. It would be particularly stimulating to combine the Predictive Active Site Model with an accurate entropic model, accounting for both Gibbs Free Energy terms. Initial efforts to model the entropy factor the solvent-accessible surface

areas have shown a proportional relationship to the entropy factor derived from the ITC data, but this simplistic model requires refinement on a larger sample size. Sophisticated evaluations of the Gibbs Free Energy associated with protein inhibition will benefit from incorporating this accurate evaluation of anion- π and other non-covalent interactions into further CADD algorithms.

CHAPTER VI

CONCLUSIONS

Supramolecular chemistry involving anion- π interactions provides “wide horizons” for exploration.¹ The studies contained in this dissertation describe theoretical and experimental efforts to evaluate, predict and employ the non-covalent anion- π interaction amidst other mitigating structural and energetic factors in supramolecular inorganic and biological systems.

The first study in this dissertation encompasses a predictive, semi-empirical method for identifying combinations of transition metals, templating anions and bridging ligands that lead to stable metallacyclic architectures with ideal anion- π overlap. The fully optimized (FO) square and pentagonal structures, involving 15 transition metals and 2 types of bridging ligands, were compared to a series of 13 FO tetrahedral and 5 FO octahedral anions in order to identify the most likely anion-metallacycle combinations to facilitate suitable anion- π overlap. Empirical and *ab initio* analyses were used to establish the accuracy of the semi-empirical treatment of the metallacycle frameworks, metal-N bonds and anions, and to determine the propensity of each anion to participate in anion- π interactions. The empirical and *ab initio* results were used to filter the semi-empirical predictions such that the remaining the metallacycle and anion pairs are predicted to participate in ideal anion- π overlap, Figure 30 and Figure 31. The ideal structural predictions include square metallacycles for each transition metal templated by several

tetrahedral anions, as well as several pentagonal metallacycles templated by the $[\text{AsF}_6]^-$ and $[\text{SbF}_6]^-$ anions.

Future experimental efforts are planned to target the new supramolecular metallacycles identified by this computational study. Additional theoretical efforts would be useful for refining the set of ideal predicted architectures by evaluating the coordination flexibility about each transition metal. Furthermore, the propensities of larger anions, such as $[\text{BiCl}_6]^{3-}$, $[\text{TeCl}_6]^{2-}$, $[\text{TaF}_7]^{2-}$ and $[\text{NbF}_7]^{2-}$, to participate in anion- π interactions leading to the templation of metallacycles with higher nuclearities should also be explored. In order to facilitate anion-templation and encapsulation, larger bridging ligands will be necessary, such as the ligand in Figure 90. Overall, the multifaceted theoretical approach described in this chapter presents an alternative method for predicting stable supramolecular architectures and may be extended to other supramolecular systems in the future.

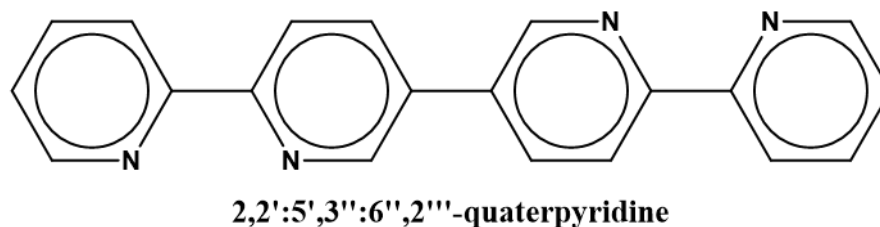


Figure 90. Extended bridging ligand that may foster larger metallacyclic architectures.

The second study in this dissertation is an exploration of a library of supramolecular Ag^I coordination complexes, polymers and extended networks in order to disentangle the hierarchy of factors that direct supramolecular Ag^I assemblies. The first factor that facilitates such a wide variety of architectures is the soft, d¹⁰ Ag^I ion that exhibits significant coordination flexibility. The second factor that influences Ag^I coordination is the combination of energetic and structural contributions of the N-heterocyclic bridging ligands. As the number of N atoms on the N-heterocyclic ligands increases, the variety of structural motifs, flexibility and π -acidity of the ligand series increases, leading to greater involvement of non-covalent interactions in the architectures. The third factor directing the Ag^I assembly is the series of non-covalent interactions in the system, particularly the interactions involving the anions. While the interaction energies of the non-covalent interactions were fractional components of the total interaction energies of the system, the optimization of these non-covalent interactions resulted in varied Ag^I-bptz architectures according to the size and symmetry of the anion. The final factor that determines the supramolecular nature of the Ag^I assemblies is the solvent. The choice in precipitating solvent has been shown to have a significant stabilizing effect on the structure of [Ag₄(μ -bmtz)₃][(BF₄)₄] _{∞} •nC₆H₆, and in light of this structure, additional substituted-benzene solvents (toluene and xylenes) are predicted to stabilize similar architectures.

This survey of the Ag^I architectures supports previous qualitative analyses of the factors contributing the symmetry and packing interactions of Ag^I complexes. The theoretical studies described herein can be elaborated through combined experimental and

computational efforts to explore each of these factors in more depth. The role of the electronic configuration and Lewis acidity of the metal ion will be probed by exploring the bppn, bptz and bmtz coordination of Na⁺, Mg²⁺ and even Cd²⁺. Computational studies will be directed at probing the energetic impact of modifying the identity of the ligand in each type of architecture, as possible with respect to the coordination motif of each complex. Experimental efforts will investigate the architectures formed by 2,5-bis(2'-pyridyl)pyrazine, the alternative *syn*-conformation of the bppz ligand. In order to further explore the non-covalent interaction within the systems, future studies will benefit from evaluating a larger model structure, including more of the non-covalent interactions integral to the architectures. Additional experimental studies involving the bevy of anions identified to foster favorable anion- π interactions in Chapter II will also expand the understanding of the roles of symmetry and size of the anions on the final Ag^I architectures. Finally, future work will benefit from a combined theoretical and experimental approach to further elucidate the role of solvent in these supramolecular architectures.

In Chapter IV, supramolecular polyhedral architectures were predicted to form by bridging the Fe^{II} (**3**) and Ni^{II} (**6**) pentagonal metallacycles with linear organic and inorganic bridging moieties. Imaging and solution studies of tpphz+**3**, tpa acid+**3** and [nBu₄N]₂[tpa]+**3** indicate a degree of symmetrical coordination, but the data remain inconclusive regarding the structural connectivity. Theoretical efforts identify that overall polyhedral coordination is energetically favored, but the intermediate non-bridged,

coordination structure is significantly more energetically favorable and may preclude polyhedral formation.

In order to conclusively determine the structure of the $\text{tpphz}+\mathbf{3}$ and $[\text{Bu}_4\text{N}]_2[\text{tpa}]+\mathbf{3}$ products, future reactions will be characterized by DOSY-NMR, in collaboration with Dr. Howard Williams at Texas A&M University, and by two-dimensional mass spectrometry, in collaboration with Dr. Xiaopeng Li at Texas State University. The instability of the $\text{tpphz}+\mathbf{3}$ and $[\text{Bu}_4\text{N}]_2[\text{tpa}]+\mathbf{3}$ complexes may also be improved by employing more stable metallacyclic building blocks. The predicted bmtz-bridged Ni^{II} and Ru^{II} pentagonal metallacycles would impart stability to the architecture, and the predicted Ru^{II} -based metallacycle would also facilitate NMR solution studies of progressing reactions.

Initial efforts have explored the reaction of the more stable Ni^{II} pentagonal building block with inorganic bridging moieties. Instead of resulting in the intended bridged-metallacyclic architecture, the reaction of **6** with $[\text{PPN}]_3[\text{Os}(\text{CN})_6]$ produced the first rectangular Ni^{II} -metallacycle. The structure is assembled around a neutral acetonitrile molecule and is bridged by two neutral bptz and two reduced bptz ligands. This complex provides an opportunity to explore the magnetic communication between Ni^{II} vertices through the radical bptz ligands, approximately realizing the very initial motivations for pursuing the first reaction between $[\text{Ni}^{\text{II}}(\text{MeCN})_6][\text{BF}_4]_2$ and bptz by former members of the Dunbar group in 1999.

Ultimately, the pursuit of polyhedral architectures will benefit from judicious ligand development. Theoretical studies will be used to identify ligands that provide

appropriate binding motifs, coordination flexibility and bridging energies, and experimental models will be developed between the pentagonal building blocks and the bidentate capping ligand analogues of each ideal bridging ligand. From these foundational efforts, bis-bidentate and tris-bidentate bridging ligands will then be synthesized that incorporate an appropriate angle along the ligand or degree of controlled flexibility that reduces the strain associated with bridging the polyhedra and promotes self-assembly of the predicted polyhedral architectures. The combination of linear, bidentate bridging ligands may also suitably facilitate supramolecular assembly of polyhedra, as exemplified in Figure 91. The combination of two bidentate bridging ligands per vertex could be envisioned to facilitate a similar type of pentagonal bridging as predicted for bis-bidentate or tris-bidentate bridging ligands. The added coordination flexibility of the monodentate ligands would significantly reduce the strain associated with the non-ideal bite angle at the metal centers. As research continues in the direction of developing larger supramolecular architectures based on the anion-templated metallacyclic building blocks, the implications of the anion- π interactions stabilizing these large structures present an interesting opportunity for supramolecular creativity and exploration. Modifying the bridging ligands to promote additional interactions with surfaces or performing anion-dependent interconversion studies between hypothetical polyhedral architectures of coordinated pentagonal structures and extended coordination networks of square metallacycles are just a couple of facets available for exploration through the different layers of supramolecular chemistry in this project.

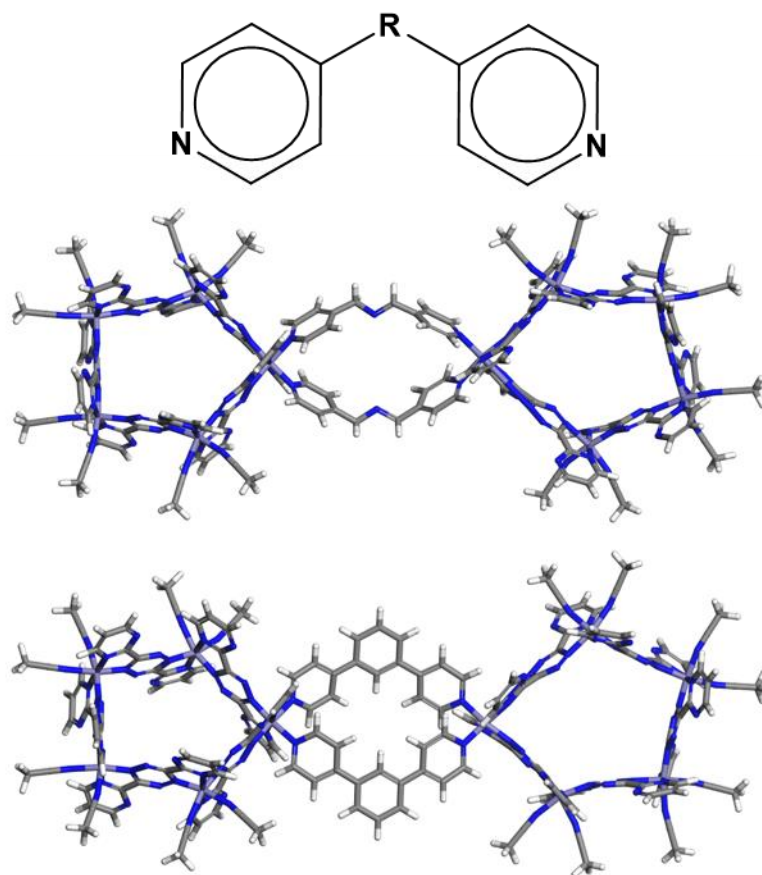


Figure 91. Linear bridging ligands that may impart flexibility and stability to the bridged polygons and polyhedra.

The study in Chapter V presents the first theoretical DFT-method for employing non-covalent interactions, with particular focus on the anion- π interaction, to evaluate and predict the interactions of drug molecules in target active sites. This study was pursued by considering a series of PDKA-bound GlcB protein structures, an important protein target for the treatment of *Mycobacterium tuberculosis*. Model active sites were developed for each PDKA by judiciously incorporating portions of the PDKA-GlcB active site from the

crystal data that participate in binding the substrate. Furthermore, a template-based, Predictive Active Site Model was developed to predict the relative binding orientations and energetic affinities of various PDKA molecules in GlcB. Through the series of non-covalent interactions evaluated within the model, the Predictive Model accurately calculates the orientation of Asp 633 binding with respect to each PDKA and proportionally models the resulting PDKA binding enthalpy. While the current active site template is suitable for the bank of PDKAs currently characterized, it may be advantageous in the future to consider additional active site templates as the library of PDKAs grows and tailor the Predictive Model active site template according to the type of substituents on the PDKA phenyl ring. The Predictive Active Site Model effectively determines the Asp 633 orientation and binding enthalpy within the PDKA-GlcB active site but is too computationally expensive to screen all of the possible combinations of PDKA substituents. Alternatively, the Cl⁻- π Model demonstrates a proportional relationship with the Predictive Active Site binding enthalpies, so the Cl⁻- π Model has been employed as a screening method to identify promising PDKA targets for further evaluation by the Predictive Active Site Model.

This study has, for the first time, demonstrated the importance of incorporating anion- π interactions into CADD methodologies in order to evaluate drug targets through the entire scope of contributing non-covalent interactions. Future efforts will be directed at identifying promising PDKA targets through the Cl⁻- π screening and Predictive Active Site Model, and these theoretical efforts will be bolstered as additional ITC experiments are available to characterize PDKA inhibition. In order to develop a thermodynamically

complete CADD package, it will be critical to combine these enthalpy studies with an accurate entropic model. Sophisticated evaluations of the entropic factors and the overall Gibbs free energy associated with protein inhibition will benefit from incorporating this accurate evaluation of anion- π and other non-covalent interactions into further CADD algorithms.

Positioned at the interface of chemistry, biology and physics, the exciting field of Supramolecular Chemistry has truly provided an interdisciplinary approach to considering chemistry. As described in this dissertation, the combination of theoretical and experimental research is able to help researchers unravel the complexities of supramolecular inorganic and biological systems and provides insight into the streamlining of experimental efforts based on sound hypotheses.

REFERENCES

1. Lehn, J. M., Supramolecular chemistry. *Science* **1993**, *260* (5115), 1762-1763.
2. Lehn, J.-M., *Supramolecular Chemistry*. Wiley-VCH Verlag GmbH & Co. KGaA: 2006.
3. Steed, J., Atwood, J., *Supramolecular chemistry*. Second ed.; John Wiley & Sons, Inc.: 2009.
4. The Nobel Prize in Chemistry in 1987.
http://www.nobelprize.org/nobel_prizes/chemistry/laureates/1987/press.html (Date accessed April 28, 2016).
5. (a) Constable, E. C.; Housecroft, C. E., Coordination chemistry: The scientific legacy of Alfred Werner. *Chemical Society Reviews* **2013**, *42* (4), 1429-1439; (b) The Nobel Prize in Chemistry 1913.
http://www.nobelprize.org/nobel_prizes/chemistry/laureates/1913/ (Date accessed May 12, 2016).
6. Lichtenthaler, F. W., 100 years “Schlüssel-Schloss-Prinzip”: What made Emil Fischer use this analogy? *Angewandte Chemie International Edition in English* **1995**, *33* (23-24), 2364-2374.
7. Pauling, L., The nature of the chemical bond. *Journal of the American Chemical Society* **1931**, *53* (4), 1367-1400.
8. Watson, J. D.; Crick, F. H. C., Molecular structure of nucleic acids: A structure for deoxyribose nucleic acid. *Nature* **1953**, *171* (4356), 737-738.

9. Pedersen, C. J., Cyclic polyethers and their complexes with metal salts. *Journal of the American Chemical Society* **1967**, *89* (26), 7017-&.
10. Lehn, J. M., Cryptates - Chemistry of macropolycyclic pnclosure complexes. *Accounts Chem. Res.* **1978**, *11* (2), 49-57.
11. (a) Cram, D. J.; Kaneda, T.; Helgeson, R. C.; Brown, S. B.; Knobler, C. B.; Maverick, E.; Trueblood, K. N., Host-guest complexation. 35. Spherands, the first completely preorganized ligand systems. *Journal of the American Chemical Society* **1985**, *107* (12), 3645-3657; (b) Cram, D. J., Preorganization - From solvents to spherands. *Angewandte Chemie-International Edition in English* **1986**, *25* (12), 1039-1057.
12. (a) Babaian, E. A.; Barden, L. M.; Hrcncir, D. C.; Hunter, W. E.; Atwood, J. L., Indium-based liquid clathrates. *Journal of inclusion phenomena* **1987**, *5* (5), 605-610; (b) Chichak, K. S.; Cantrill, S. J.; Pease, A. R.; Chiu, S.-H.; Cave, G. W. V.; Atwood, J. L.; Stoddart, J. F., Molecular borromeian rings. *Science* **2004**, *304* (5675), 1308-1312; (c) Bravo, J. A.; Raymo, F. M.; Stoddart, J. F.; White, A. J. P.; Williams, D. J., High yielding template-directed syntheses of [2]rotaxanes. *European Journal of Organic Chemistry* **1998**, *1998* (11), 2565-2571; (d) Vögtle, F.; Müller, W. M.; Wehner, W.; Buhleier, E., Noncyclic cryptates. *Angewandte Chemie International Edition in English* **1977**, *16* (8), 548-549.
13. Simmons, H. E.; Park, C. H., Macrobicyclic amines. *Journal of the American Chemical Society* **1968**, *90* (9), 2428-2429.

14. *Materials Studio Modeling Environment*, Release 7.0; Accelrys Software Inc.: San Diego, 2007.
15. The Nobel Prize in Chemistry 2003.
http://www.nobelprize.org/nobel_prizes/chemistry/laureates/2003/ (Date accessed May 12, 2016).
16. Glasser, L.; Jenkins, H. D. B., Lattice energies and unit cell volumes of complex ionic solids. *Journal of the American Chemical Society* **2000**, *122* (4), 632-638.
17. Muller, P., Glossary of terms used in physical organic chemistry (IUPAC Recommendations 1994). In *Pure and Applied Chemistry*, 1994; Vol. 66, p 1077.
18. Cramer, C. J., *Essentials of Computational Chemistry: Theories and Models*. Second ed.; John Wiley & Sons: West Sussex, England, 2006.
19. (a) Wheeler, S. E.; McNeil, A. J.; Müller, P.; Swager, T. M.; Houk, K. N., Probing substituent effects in aryl–aryl interactions using stereoselective diels–alder cycloadditions. *Journal of the American Chemical Society* **2010**, *132* (10), 3304-3311; (b) Wheeler, S. E., Understanding substituent effects in noncovalent interactions involving aromatic rings. *Accounts Chem. Res.* **2013**, *46* (4), 1029-1038; (c) Raju, R. K.; Bloom, J. W. G.; An, Y.; Wheeler, S. E., Substituent effects on non-covalent interactions with aromatic rings: Insights from computational chemistry. *Chemphyschem* **2011**, *12* (17), 3116-3130; (d) Wheeler, S. E.; Bloom, J. W. G., Toward a more complete understanding of noncovalent interactions involving aromatic rings. *Journal of Physical Chemistry A* **2014**, *118* (32), 6133-6147.

20. Hunter, C. A., Meldola Lecture. The role of aromatic interactions in molecular recognition. *Chemical Society Reviews* **1994**, *23* (2), 101-109.
21. Sinnokrot, M. O.; Sherrill, C. D., Unexpected substituent effects in face-to-face π -stacking interactions. *The Journal of Physical Chemistry A* **2003**, *107* (41), 8377-8379.
22. (a) Mahadevi, A. S.; Sastry, G. N., Cation- π interaction: Its role and relevance in chemistry, biology, and material science. *Chemical Reviews* **2013**, *113* (3), 2100-2138; (b) Dougherty, D. A., The cation- π interaction. *Accounts Chem. Res.* **2013**, *46* (4), 885-893.
23. (a) Schottel, B. L.; Chifotides, H. T.; Dunbar, K. R., Anion- π interactions. *Chemical Society Reviews* **2008**, *37* (1), 68-83; (b) Chifotides, H. T.; Dunbar, K. R., Anion- π interactions in supramolecular architectures. *Accounts Chem. Res.* **2013**, *46* (4), 894-906.
24. (a) Wheeler, S. E.; Houk, K. N., Are anion/ π interactions actually a case of simple charge-dipole interaction? *Journal of Physical Chemistry A* **2010**, *114* (33), 8658-8664; (b) Wheeler, S. E.; Bloom, J. W. G., Anion- π interactions and positive electrostatic potentials of N-heterocycles arise from the positions of the nuclei, not changes in the π -electron distribution. *Chemical Communications* **2014**, *50* (76), 11118-11121.
25. (a) Quiñonero, D.; Garau, C.; Rotger, C.; Frontera, A.; Ballester, P.; Costa, A.; Deyà, P. M., Anion- π interactions: Do they exist? *Angew. Chem.-Int. Edit.* **2002**, *41* (18), 3389-3392; (b) Quiñonero, D.; Garau, C.; Frontera, A.; Ballester, P.; Costa, A.; Deyà, P. M., Counterintuitive interaction of anions with benzene derivatives. *Chemical Physics*

- Letters* **2002**, 359 (5-6), 486-492; (c) Mascial, M.; Armstrong, A.; Bartberger, M. D., Anion-aromatic bonding: A case for anion recognition by π -acidic rings. *Journal of the American Chemical Society* **2002**, 124 (22), 6274-6276.
26. Schneider, H. J.; Werner, F.; Blatter, T., Attractive interactions between negative charges and polarizable arly parts of host-guest systems. *Journal of Physical Organic Chemistry* **1993**, 6 (10), 590-594.
27. Alkorta, I.; Rozas, I.; Elguero, J., Interaction of anions with perfluoro aromatic compounds. *Journal of the American Chemical Society* **2002**, 124 (29), 8593-8598.
28. (a) Frontera, A.; Gamez, P.; Mascial, M.; Mooibroek, T. J.; Reedijk, J., Putting anion- π interactions into perspective. *Angew. Chem.-Int. Edit.* **2011**, 50 (41), 9564-9583; (b) Lucas, X.; Bauzá, A.; Frontera, A.; Quiñonero, D., A thorough anion- π interaction study in biomolecules: On the importance of cooperativity effects. *Chemical Science* **2015**.
29. Garau, C.; Quiñonero, D.; Frontera, A.; Ballester, P.; Costa, A.; Deyà, P. M., Approximate additivity of anion- π interactions: An ab initio study on Anion- π anion- π_2 and anion- π_3 complexes. *Journal of Physical Chemistry A* **2005**, 109 (41), 9341-9345.
30. (a) Mahadevi, A. S.; Sastry, G. N., Cooperativity in noncovalent interactions. *Chemical Reviews* **2016**; (b) Estarellas, C.; Frontera, A.; Quiñonero, D.; Deyà, P. M., Anion- π interactions in flavoproteins. *Chemistry – An Asian Journal* **2011**, 6 (9), 2316-2318.
31. (a) Giles, I. D. Experimental and theoretical investigations of anion- π interactions metallacyclic architectures of first-row transition metals and N-heteroaromatic ligands.

- Texas A&M University, College Station, 2012; (b) Chifotides, H. T.; Giles, I. D.; Dunbar, K. R., Supramolecular architectures with π -acidic 3,6-bis(2-pyridyl)-1,2,4,5-tetrazine cavities: Role of anion- π interactions in the remarkable stability of Fe(II) metallacycles in solution. *Journal of the American Chemical Society* **2013**, *135* (8), 3039-3055.
32. Zhao, Y.; Domoto, Y.; Orentas, E.; Beuchat, C.; Emery, D.; Mareda, J.; Sakai, N.; Matile, S., Catalysis with anion- π interactions. *Angewandte Chemie International Edition* **2013**, *52* (38), 9940-9943.
33. Berryman, O. B.; Johnson, D. W., Experimental evidence for interactions between anions and electron-deficient aromatic rings. *Chemical Communications* **2009**, (22), 3143-3153.
34. (a) Aragay, G.; Frontera, A.; Lloveras, V.; Vidal-Gancedo, J.; Ballester, P., Different nature of the interactions between anions and HAT(CN)₆: From reversible anion- π complexes to irreversible electron-transfer processes (HAT(CN)₆ = 1,4,5,8,9,12-Hexaazatriphenylene). *Journal of the American Chemical Society* **2013**, *135* (7), 2620-2627; (b) Chifotides, H. T.; Schottel, B. L.; Dunbar, K. R., The π -accepting arene HAT(CN)₆ as a halide receptor through charge transfer: Multisite anion interactions and self-assembly in solution and the solid state. *Angew. Chem.-Int. Edit.* **2010**, *49* (40), 7202-7207.
35. (a) Demeshko, S.; Dechert, S.; Meyer, F., Anion- π interactions in a carousel copper(II)-triazine complex. *Journal of the American Chemical Society* **2004**, *126* (14), 4508-4509; (b) de Hoog, P.; Gamez, P.; Mutikainen, H.; Turpeinen, U.; Reedijk, J., An

aromatic anion receptor: Anion- π interactions do exist. *Angew. Chem.-Int. Edit.* **2004**, *43* (43), 5815-5817; (c) Gamez, P.; Mooibroek, T. J.; Teat, S. J.; Reedijk, J., Anion binding involving π -acidic heteroaromatic rings. *Accounts Chem. Res.* **2007**, *40* (6), 435-444.

36. (a) Campos-Fernandez, C. S.; Clerac, R.; Dunbar, K. R., A one-pot, high-yield synthesis of a paramagnetic nickel square from divergent precursors by anion template assembly. *Angew. Chem.-Int. Edit.* **1999**, *38* (23), 3477-3479; (b) Campos-Fernandez, C. S.; Clerac, R.; Koomen, J. M.; Russell, D. H.; Dunbar, K. R., Fine-tuning the ring-size of metallacyclophanes: A rational approach to molecular pentagons. *Journal of the American Chemical Society* **2001**, *123* (4), 773-774; (c) Campos-Fernandez, C. S.; Schottel, B. L.; Chifotides, H. T.; Bera, J. K.; Bacsa, J.; Koomen, J. M.; Russell, D. H.; Dunbar, K. R., Anion template effect on the self-assembly and interconversion of metallacyclophanes. *Journal of the American Chemical Society* **2005**, *127* (37), 12909-12923; (d) Giles, I. D.; Chifotides, H. T.; Shatruk, M.; Dunbar, K. R., Anion-templated self-assembly of highly stable Fe^{II} pentagonal metallacycles with short anion- π contacts. *Chemical Communications* **2011**, *47* (47), 12604-12606.

37. (a) Schottel, B. L.; Bacsa, J.; Dunbar, K. R., Anion dependence of Ag(I) reactions with 3,6-bis(2-pyridyl)-1,2,4,5-tetrazine (bptz): isolation of the molecular propeller compound [Ag₂(bptz)₃][AsF₆]₂. *Chemical Communications* **2005**, (1), 46-47; (b) Schottel, B. L.; Chifotides, H. T.; Shatruk, M.; Chouai, A.; Perez, L. M.; Bacsa, J.; Dunbar, K. R., Anion- π interactions as controlling elements in self-assembly reactions of Ag(I) complexes with π -acidic aromatic rings. *Journal of the American Chemical Society* **2006**, *128* (17), 5895-5912.

38. Meyer, E. A.; Castellano, R. K.; Diederich, F., Interactions with aromatic rings in chemical and biological recognition. *Angew. Chem.-Int. Edit.* **2003**, *42* (11), 1210-1250.
39. Chakravarty, S.; Sheng, Z.-Z.; Iverson, B.; Moore, B., “ η^6 ”-Type anion- π in biomolecular recognition. *FEBS Letters* **2012**, *586* (23), 4180-4185.
40. (a) Mareda, J.; Matile, S., Anion- π slides for transmembrane transport. *Chemistry – A European Journal* **2009**, *15* (1), 28-37; (b) Dawson, R. E.; Hennig, A.; Weimann, D. P.; Emery, D.; Ravikumar, V.; Montenegro, J.; Takeuchi, T.; Gabutti, S.; Mayor, M.; Mareda, J.; Schalley, C. A.; Matile, S., Experimental evidence for the functional relevance of anion- π interactions. *Nat Chem* **2010**, *2* (7), 533-538.
41. Krieger, I. V.; Freundlich, J. S.; Gawandi, V. B.; Roberts, J. P.; Gawandi, V. B.; Sun, Q.; Owen, J. L.; Fraile, M. T.; Huss, S. I.; Lavandera, J. L.; Ioerger, T. R.; Sacchettini, J. C., Structure-guided discovery of phenyl-diketo acids as potent inhibitors of *M. tuberculosis* Malate Synthase. *Chemistry & Biology* **2012**, *19* (12), 1556-1567.
42. Berman, H. M.; Westbrook, J.; Feng, Z.; Gilliland, G.; Bhat, T. N.; Weissig, H.; Shindyalov, I. N.; Bourne, P. E., The Protein Data Bank. *Nucleic Acids Research* **2000**, *28* (1), 235-242.
43. Schrodinger, LLC, The AxPyMOL Molecular Graphics Plugin for Microsoft PowerPoint, Version 1.8. 2015.
44. (a) Head-Gordon, M.; Pople, J. A.; Frisch, M. J., MP2 energy evaluation by direct methods. *Chemical Physics Letters* **1988**, *153* (6), 503-506; (b) Sæbø, S.; Almlöf, J., Avoiding the integral storage bottleneck in LCAO calculations of electron correlation. *Chemical Physics Letters* **1989**, *154* (1), 83-89; (c) Frisch, M. J.; Head-Gordon, M.;

- Pople, J. A., A direct MP2 gradient method. *Chemical Physics Letters* **1990**, *166* (3), 275-280; (d) Weigend, F.; Ahlrichs, R., Balanced basis sets of split valence, triple zeta valence and quadruple zeta valence quality for H to Rn: Design and assessment of accuracy. *Physical Chemistry Chemical Physics* **2005**, *7* (18), 3297-3305; (e) Weigend, F., Accurate Coulomb-fitting basis sets for H to Rn. *Physical Chemistry Chemical Physics* **2006**, *8* (9), 1057-1065.
45. Houk, K. H., Electronic structure theory. In *Navigating Chemical Compound Space for Materials and Bio Design: Tutorials*, Department of Chemistry and Biochemistry, UCLA, 2011.
46. (a) Pople, J. A.; Santry, D. P.; Segal, G. A., Approximate self-consistent molecular orbital theory. I. Invariant procedures. *The Journal of Chemical Physics* **1965**, *43* (10), S129-S135; (b) Pople, J. A.; Segal, G. A., Approximate self-consistent molecular orbital theory. II. Calculations with complete neglect of differential overlap. *The Journal of Chemical Physics* **1965**, *43* (10), S136-S151; (c) Pople, J. A.; Segal, G. A., Approximate self-consistent molecular orbital theory. III. CNDO results for AB₂ and AB₃ systems. *The Journal of Chemical Physics* **1966**, *44* (9), 3289-3296.
47. Stewart, J. J. P., Optimization of parameters for semiempirical methods V: Modification of NDDO approximations and application to 70 elements. *Journal of Molecular Modeling* **2007**, *13* (12), 1173-1213.
48. Hohenberg, P.; Kohn, W., Inhomogeneous electron gas. *Physical Review* **1964**, *136* (3B), B864-B871.

49. Kohn, W.; Sham, L. J., Self-consistent equations including exchange and correlation effects. *Physical Review* **1965**, *140* (4A), A1133-A1138.
50. Chai, J.-D.; Head-Gordon, M., Long-range corrected hybrid density functionals with damped atom-atom dispersion corrections. *Physical Chemistry Chemical Physics* **2008**, *10* (44), 6615-6620.
51. (a) Stoll, H.; Metz, B.; Dolg, M., Relativistic energy-consistent pseudopotentials—Recent developments. *Journal of Computational Chemistry* **2002**, *23* (8), 767-778; (b) Jansen, G.; Hess, B. A., Revision of the Douglas-Kroll transformation. *Physical Review A* **1989**, *39* (11), 6016-6017.
52. (a) Clark, T.; Chandrasekhar, J.; Spitznagel, G. W.; Schleyer, P. V. R., Efficient diffuse function-augmented basis sets for anion calculations. III. The 3-21+G basis set for first-row elements, Li–F. *Journal of Computational Chemistry* **1983**, *4* (3), 294-301; (b) Ditchfield, R.; Hehre, W. J.; Pople, J. A., Self-consistent molecular-orbital methods. IX. An extended Gaussian-type basis for molecular-orbital studies of organic molecules. *The Journal of Chemical Physics* **1971**, *54* (2), 724-728; (c) Hehre, W. J.; Ditchfield, R.; Pople, J. A., Self-consistent molecular orbital methods. XII. Further extensions of Gaussian-type basis sets for use in molecular orbital studies of organic molecules. *The Journal of Chemical Physics* **1972**, *56* (5), 2257-2261; (d) Francl, M. M.; Pietro, W. J.; Hehre, W. J.; Binkley, J. S.; Gordon, M. S.; DeFrees, D. J.; Pople, J. A., Self-consistent molecular orbital methods. XXIII. A polarization-type basis set for second-row elements. *The Journal of Chemical Physics* **1982**, *77* (7), 3654-3665; (e) Hariharan, P.

- C.; Pople, J. A., Accuracy of ΔH in equilibrium geometries by single determinant molecular orbital theory. *Molecular Physics* **1974**, *27* (1), 209-214.
53. Becke, A. D., Density-functional exchange-energy approximation with correct asymptotic behavior. *Physical Review A* **1988**, *38* (6), 3098-3100.
54. Perdew, J. P., Density-functional approximation for the correlation energy of the inhomogeneous electron gas. *Physical Review B* **1986**, *33* (12), 8822-8824.
55. Dolg, M.; Wedig, U.; Stoll, H.; Preuss, H., Energy-adjusted ab initio pseudopotentials for the first row transition elements. *The Journal of Chemical Physics* **1987**, *86* (2), 866-872.
56. Zhao, Y.; Truhlar, D. G., The M06 suite of density functionals for main group thermochemistry, thermochemical kinetics, noncovalent interactions, excited states, and transition elements: two new functionals and systematic testing of four M06-class functionals and 12 other functionals. *Theor Chem Account* **2007**, *120* (1), 215-241.
57. (a) Lehn, J. M., Toward self-organization and complex matter. *Science* **2002**, *295* (5564), 2400-2403; (b) Lehn, J. M., Toward complex matter: Supramolecular chemistry and self-organization. *Proceedings of the National Academy of Sciences of the United States of America* **2002**, *99* (8), 4763-4768.
58. Palma, C.-A.; Cecchini, M.; Samori, P., Predicting self-assembly: from empirism to determinism. *Chemical Society Reviews* **2012**, *41* (10), 3713-3730.
59. (a) Chakrabarty, R.; Mukherjee, P. S.; Stang, P. J., Supramolecular coordination: Self-assembly of finite two- and three-dimensional ensembles. *Chemical Reviews* **2011**, *111* (11), 6810-6918; (b) Cook, T. R.; Vajpayee, V.; Lee, M. H.; Stang, P. J.; Chi, K.-

W., Biomedical and biochemical applications of self-assembled metallacycles and metallacages. *Accounts Chem. Res.* **2013**, *46* (11), 2464-2474; (c) Cook, T. R.; Zheng, Y.-R.; Stang, P. J., Metal-organic frameworks and self-assembled supramolecular coordination complexes: Comparing and contrasting the design, synthesis, and functionality of metal-organic materials. *Chemical Reviews* **2013**, *113* (1), 734-777; (d) Northrop, B. H.; Zheng, Y.-R.; Chi, K.-W.; Stang, P. J., Self-organization in coordination-driven self-assembly. *Accounts Chem. Res.* **2009**, *42* (10), 1554-1563; (e) Cook, T. R.; Stang, P. J., Recent developments in the preparation and chemistry of metallacycles and metallacages via coordination. *Chemical Reviews* **2015**, *115* (15), 7001-7045.

60. Fujita, M.; Yazaki, J.; Ogura, K., Preparation of a macrocyclic polynuclear complex, [(en)Pd(4,4'-bpy)]₄(NO₃)₈ (en = ethylenediamine, bpy = bipyridine), which recognizes an organic molecule in aqueous media. *Journal of the American Chemical Society* **1990**, *112* (14), 5645-5647.

61. Stang, P. J.; Cao, D. H., Transition-metal based cationic molecular boxes - Self-assembly of macrocyclic platinum(II) and palladium(II) tetranuclear complexes *Journal of the American Chemical Society* **1994**, *116* (11), 4981-4982.

62. Zhao, L.; Ghosh, K.; Zheng, Y.; Lyndon, M. M.; Williams, T. I.; Stang, P. J., Construction of coordination-driven self-assembled [5 + 5] pentagons using metal-carbonyl dipyrindine ligands. *Inorg. Chem.* **2009**, *48* (13), 5590-5592.

63. Lehn, J.-M., Perspectives in supramolecular chemistry—From molecular recognition towards molecular information processing and self-organization. *Angewandte Chemie International Edition in English* **1990**, *29* (11), 1304-1319.
64. (a) Furlan, R. L. E.; Otto, S.; Sanders, J. K. M., Supramolecular templating in thermodynamically controlled synthesis. *Proceedings of the National Academy of Sciences* **2002**, *99* (8), 4801-4804; (b) Vilar, R., Anion-templated synthesis. *Angewandte Chemie International Edition* **2003**, *42* (13), 1460-1477.
65. Hasenknopf, B.; Lehn, J.-M.; Boumediene, N.; Dupont-Gervais, A.; Van Dorsselaer, A.; Kneisel, B.; Fenske, D., Self-assembly of tetra- and hexanuclear circular helicates. *Journal of the American Chemical Society* **1997**, *119* (45), 10956-10962.
66. Riddell, I. A.; Hristova, Y. R.; Clegg, J. K.; Wood, C. S.; Breiner, B.; Nitschke, J. R., Five discrete multinuclear metal-organic assemblies from one ligand: Deciphering the effects of different templates. *Journal of the American Chemical Society* **2013**, *135* (7), 2723-2733.
67. Lehn, J.-M., From supramolecular chemistry towards constitutional dynamic chemistry and adaptive chemistry. *Chemical Society Reviews* **2007**, *36* (2), 151-160.
68. Bu, X.-H.; Morishita, H.; Tanaka, K.; Biradha, K.; Furusho, S.; Shionoya, M., A spontaneously resolved chiral molecular box: a cyclic tetranuclear Zn complex with DPTZ (DPTZ = 3,6-di-2-pyridyl-1,2,4,5-tetrazine). *Chemical Communications* **2000**, (11), 971-972.
69. Chifotides, H. T.; Dunbar, K. R., Anion- π Interactions in Supramolecular Architectures. *Accounts Chem. Res.* **2013**, *46* (4), 894-906.

70. Funck, E. S. Investigation of anion- π interactions in inorganic, organic and biological systems. Texas A&M University, College Station, 2011.
71. Chakraborty, S.; Mondal, S.; Bhowmick, S.; Ma, J.; Tan, H.; Neogi, S.; Das, N., Triptycene based organometallic complexes: a new class of acceptor synthons for supramolecular ensembles. *Dalton Transactions* **2014**, 43 (35), 13270-13277.
72. (a) Stewart, J. J. P., Application of the PM6 method to modeling the solid state. *Journal of Molecular Modeling* **2008**, 14 (6), 499-535; (b) Cusati, R. C.; Pereira, U. A.; Barbosa, L. C. A.; Maltha, C. R. A.; Carneiro, J. W. M.; Corrêa, R. S.; Doriguetto, A. C., Structural characterization of unusually stable polycyclic ozonides. *Journal of Molecular Structure* **2015**, 1082, 151-161.
73. Stewart, J. J. P., Optimization of parameters for semiempirical methods VI: more modifications to the NDDO approximations and re-optimization of parameters. *Journal of Molecular Modeling* **2013**, 19 (1), 1-32.
74. (a) Buschmann, W. E.; Miller, J. S.; Bowman-James, K.; Miller, C. N., Useful reagents and ligands. Synthesis of $[M^{II}(\text{NCMe})_6]^{2+}$ (M = V, Cr, Mn, Fe, Co, Ni) salts of tetra[3,5-bis(trifluoromethyl)phenyl]borate. *Inorg. Synth.* **2002**, 33, 83-91; (b) Bartley, S. L.; Bernstein, S. N.; Dunbar, K. R., Acetonitrile and cyanide compounds containing metal-metal bonds: syntheses, structures and applications to solid-state chemistry. *Inorg. Chim. Acta* **1993**, 213 (1-2), 213-31.
75. (a) Geldard, J. F.; Lions, F., The organic chemistry of a new weak field tridentate chelating agent. 3,5-di(2-pyridyl)-1,2,4-triazole. *The Journal of Organic Chemistry* **1965**, 30 (1), 318-319; (b) Dallacker, F., Zur darstellung von 1,2,4,5-tetrazinen des

- pyridins und des methylenedioxy-benzols. *Monatshefte für Chemie und verwandte Teile anderer Wissenschaften* **91** (2), 294-304; (c) Kaim, W.; Fees, J., The new tetrafunctional π -acceptor ligand 3,6-bis(2'-pyrimidyl)-1,2,4,5-tetrazine (bmtz) - Diruthenium complexes of bmtz and of its 1,3-dihydro form. *Z. Naturforsch. (B)* **1995**, *50* (1), 123-127.
76. *SAINT, Program for area detector adsorption correction*, Siemens Analytical X-Ray Instruments Inc. : Madison, WI 53719, USA.
77. *APEX2 v2011.6-1*, Bruker AXS: Madison, WI, 2011.
78. Sheldrick, G. M. *SADABS, Program for Siemens area detector absorption correction*, University of Gottingen: Gottingen, Germany.
79. Sheldrick, G. M. *TWINABS*, 2012/1; Georg-August-Universität Göttingen, Göttingen, Germany, 2012.
80. Sheldrick, G. M. *XS*, 2013/1; Georg-August-Universität Göttingen, Göttingen, Germany, 2013.
81. Dolomanov, O. V.; Bourhis, L. J.; Gildea, R. J.; Howard, J. A. K.; Puschmann, H., OLEX2: a complete structure solution, refinement and analysis program. *Journal of Applied Crystallography* **2009**, *42* (2), 339-341.
82. Sheldrick, G., Crystal structure refinement with SHELXL. *Acta Crystallographica Section C* **2015**, *71* (1), 3-8.
83. T. Clark, A. A., B. Beck, F. Burkhardt, J. Chandrasekhar, P. Gedeck, A. Horn, M. Hutter, B. Martin, P. O. Dral, G. Rauhut, W. Sauer, T. Schindler, T. Steinke *VAMP 11.0*, University of Erlangen: Germany, 2011.

84. Roothaan, C. C. J., New developments in molecular orbital theory. *Reviews of Modern Physics* **1951**, 23 (2), 69-89.
85. Pople, J. A.; Nesbet, R. K., Self-consistent orbitals for radicals. *The Journal of Chemical Physics* **1954**, 22 (3), 571-572.
86. Frisch, M. J.; Trucks, G. W.; Schlegel, H. B.; Scuseria, G. E.; Robb, M. A.; Cheeseman, J. R.; Scalmani, G.; Barone, V.; Mennucci, B.; Petersson, G. A.; Nakatsuji, H.; Caricato, M.; Li, X.; Hratchian, H. P.; Izmaylov, A. F.; Bloino, J.; Zheng, G.; Sonnenberg, J. L.; Hada, M.; Ehara, M.; Toyota, K.; Fukuda, R.; Hasegawa, J.; Ishida, M.; Nakajima, T.; Honda, Y.; Kitao, O.; Nakai, H.; Vreven, T.; Montgomery Jr., J. A.; Peralta, J. E.; Ogliaro, F.; Bearpark, M. J.; Heyd, J.; Brothers, E. N.; Kudin, K. N.; Staroverov, V. N.; Kobayashi, R.; Normand, J.; Raghavachari, K.; Rendell, A. P.; Burant, J. C.; Iyengar, S. S.; Tomasi, J.; Cossi, M.; Rega, N.; Millam, N. J.; Klene, M.; Knox, J. E.; Cross, J. B.; Bakken, V.; Adamo, C.; Jaramillo, J.; Gomperts, R.; Stratmann, R. E.; Yazyev, O.; Austin, A. J.; Cammi, R.; Pomelli, C.; Ochterski, J. W.; Martin, R. L.; Morokuma, K.; Zakrzewski, V. G.; Voth, G. A.; Salvador, P.; Dannenberg, J. J.; Dapprich, S.; Daniels, A. D.; Farkas, Ö.; Foresman, J. B.; Ortiz, J. V.; Cioslowski, J.; Fox, D. J. *Gaussian 09*, Gaussian, Inc.: Wallingford, CT, USA, 2009.
87. Boys, S. F.; Bernardi, F., The calculation of small molecular interactions by the differences of separate total energies. Some procedures with reduced errors. *Molecular Physics* **1970**, 19 (4), 553-566.
88. High Performance Research Computing at Texas A&M University
<http://hprc.tamu.edu/> (Accessed date March 1, 2016).

89. Fulton, J. R., Vanadium, niobium and tantalum. *Annual Reports Section "A" (Inorganic Chemistry)* **2013**, 109 (0), 108-118.
90. Macrae, C. F.; Edgington, P. R.; McCabe, P.; Pidcock, E.; Shields, G. P.; Taylor, R.; Towler, M.; van de Streek, J., Mercury: visualization and analysis of crystal structures. *Journal of Applied Crystallography* **2006**, 39 (3), 453-457.
91. (a) Allen, F., The Cambridge Structural Database: a quarter of a million crystal structures and rising. *Acta Crystallographica Section B* **2002**, 58 (3 Part 1), 380-388; (b) Groom, C. R.; Bruno, I. J.; Lightfoot, M. P.; Ward, S. C., The Cambridge Structural Database. *Acta Crystallographica Section B* **2016**, 72 (2), 171-179.
92. Bondi, A., van der Waals volumes and radii. *The Journal of Physical Chemistry* **1964**, 68 (3), 441-451.
93. Cordero, B.; Gomez, V.; Platero-Prats, A. E.; Reves, M.; Echeverria, J.; Cremades, E.; Barragan, F.; Alvarez, S., Covalent radii revisited. *Dalton Transactions* **2008**, (21), 2832-2838.
94. (a) Burns, R. G., *Ionic radii of transition metals and related cations: Mineralogical applications of crystal field theory*. Cambridge University Press: 1993; (b) Shannon, R., Revised effective ionic radii and systematic studies of interatomic distances in halides and chalcogenides. *Acta Crystallographica Section A* **1976**, 32 (5), 751-767.
95. Schottel, B. L. The influence of anion- π interactions between multi-atomic anions and π -acidic ring systems on the self-assembly of coordination compounds Texas A&M University, College Station, TX, 2007.

96. Diaz-Torres, R.; Alvarez, S., Coordinating ability of anions and solvents towards transition metals and lanthanides. *Dalton Transactions* **2011**, 40 (40), 10742-10750.
97. (a) Kelly, A. W.; Nicholas, A.; Ahern, J. C.; Chan, B.; Patterson, H. H.; Pike, R. D., Alkali metal bismuth(III) chloride double salts. *Journal of Alloys and Compounds* **2016**, 670, 337-345; (b) Dutton, J. L.; Tabeshi, R.; Jennings, M. C.; Lough, A. J.; Ragogna, P. J., Redox reactions between phosphines (R_3P ; $R = {}^n\text{Bu}, \text{Ph}$) or carbene (${}^i\text{Pr}_2\text{IM}$) and chalcogen tetrahalides ChX_4 (${}^i\text{Pr}_2\text{IM} = 2,5\text{-diisopropylimidazole-2-ylidene}$; $\text{Ch} = \text{Se}, \text{Te}$; $\text{X} = \text{Cl}, \text{Br}$). *Inorg. Chem.* **2007**, 46 (21), 8594-8602; (c) dos Santos, S. S.; Schulz Lang, E.; Manzoni de Oliveira, G., New versatile organytellurium(IV) halides: Synthesis and X-ray structural features of the telluronium tellurolate salts $[\text{PhTe}(\text{CH}_3)_2]_2[\text{TeX}_6]$ ($\text{X} = \text{Cl}, \text{Br}$) and $[\text{Ph}_3\text{Te}][\text{PhTeX}_4]$ ($\text{X} = \text{Cl}, \text{Br}, \text{I}$). *Journal of Organometallic Chemistry* **2007**, 692 (14), 3081-3088.
98. (a) Manzano, B. R.; Jalon, F. A.; Soriano, M. L.; Carrion, M. C.; Carranza, M. P.; Mereiter, K.; Rodriguez, A. M.; de la Hoz, A.; Sanchez-Migallon, A., Anion-dependent self-assembly of silver(I) and diaminotriazines to coordination polymers: Non-covalent bonds and role interchange between silver and hydrogen bonds. *Inorg. Chem.* **2008**, 47 (19), 8957-8971; (b) Steel, P. J.; Fitchett, C. M., Metallosupramolecular silver(I) assemblies based on pyrazine and related ligands. *Coordination Chemistry Reviews* **2008**, 252 (8-9), 990-1006; (c) Khlobystov, A. N.; Blake, A. J.; Champness, N. R.; Lemenovskii, D. A.; Majouga, A. G.; Zyk, N. V.; Schroder, M., Supramolecular design of one-dimensional coordination polymers based on silver(I) complexes of aromatic nitrogen-donor ligands. *Coordination Chemistry Reviews* **2001**, 222, 155-192.

99. (a) Khlobystov, A. N.; Blake, A. J.; Champness, N. R.; Lemenovskii, D. A.; Majouga, A. G.; Zyk, N. V.; Schröder, M., Supramolecular design of one-dimensional coordination polymers based on silver(I) complexes of aromatic nitrogen-donor ligands. *Coordination Chemistry Reviews* **2001**, 222 (1), 155-192; (b) Chainok, K.; Neville, S. M.; Forsyth, C. M.; Gee, W. J.; Murray, K. S.; Batten, S. R., Supramolecular architecture of silver(I) coordination polymers containing polydentate N-donor ligands. *Crystengcomm* **2012**, 14 (10), 3717-3726; (c) Robin, A. Y.; Fromm, K. M., Coordination polymer networks with O- and N-donors: What they are, why and how they are made. *Coordination Chemistry Reviews* **2006**, 250 (15–16), 2127-2157.
100. Venkataraman, D.; Du, Y.; Wilson, S. R.; Hirsch, K. A.; Zhang, P.; Moore, J. S., A coordination geometry table of the d-block elements and their ions. *Journal of Chemical Education* **1997**, 74 (8), 915.
101. Baxter, P. N. W.; Lehn, J. M.; Fischer, J.; Youinou, M. T., Self-assembly and structure of a 3X3 inorganic grid from 9 silver ions and 6 ligand components. *Angewandte Chemie-International Edition in English* **1994**, 33 (22), 2284-2287.
102. Baxter, P. N. W.; Lehn, J. M.; Baum, G.; Fenske, D., Self-assembly and structure of interconverting multinuclear inorganic arrays: A [4 x]5 -Ag¹²⁰ grid and an Ag¹¹⁰ quadruple helicate. *Chem.-Eur. J.* **2000**, 6 (24), 4510-4517.
103. Butte, W. A.; Case, F. H., The synthesis of some pyridyl-pyridazines and -pyrimidines. *The Journal of Organic Chemistry* **1961**, 26 (11), 4690-4692.

104. Constable, E. C.; Housecroft, C. E.; Kariuki, B. M.; Kelly, N.; Smith, C. B., A near planar disilver complex of 3,6-bis(2-pyridyl)-1,2,4,5-tetrazine. *Inorganic Chemistry Communications* **2002**, *5* (3), 199-202.
105. Constable, E. C.; Housecroft, C. E.; Kariuki, B. M.; Kelly, N.; Smith, C. B., How well do we understand self-assembly algorithms? From prototype grid to polymers. *Comptes Rendus Chimie* **2002**, *5* (5), 425-430.
106. Safin, D. A.; Pialat, A.; Leitch, A. A.; Tumanov, N. A.; Korobkov, I.; Filinchuk, Y.; Brusso, J. L.; Murugesu, M., Anion-induced Ag^I self-assemblies with electron deficient aromatic ligands: anion- π -system interactions as a driving force for templated coordination networks. *Chemical Communications* **2015**, *51* (46), 9547-9550.
107. Lee, C.; Yang, W.; Parr, R. G., Development of the Colle-Salvetti correlation-energy formula into a functional of the electron density. *Physical Review B* **1988**, *37* (2), 785-789.
108. (a) Walker, M.; Harvey, A. J. A.; Sen, A.; Dessent, C. E. H., Performance of M06, M06-2X, and M06-HF density functionals for conformationally flexible anionic clusters: M06 functionals perform better than B3LYP for a model system with dispersion and ionic hydrogen-bonding interactions. *The Journal of Physical Chemistry A* **2013**, *117* (47), 12590-12600; (b) Zhao, Y.; Truhlar, D., The M06 suite of density functionals for main group thermochemistry, thermochemical kinetics, noncovalent interactions, excited states, and transition elements: two new functionals and systematic testing of four M06-class functionals and 12 other functionals. *Theor Chem Account* **2008**, *120* (1-3), 215-241.

109. Rappe, A. K.; Casewit, C. J.; Colwell, K. S.; Goddard, W. A.; Skiff, W. M., UFF, a full periodic table force field for molecular mechanics and molecular dynamics simulations. *Journal of the American Chemical Society* **1992**, *114* (25), 10024-10035.
110. Glöckle, M.; Hübler, K.; Kümmerer, H.-J.; Denninger, G.; Kaim, W., Dicopper(I) complexes with reduced states of 3,6-bis(2'-pyrimidyl)-1,2,4,5-tetrazine: Crystal structures and spectroscopic properties of the free ligand, a radical species, and a complex of the 1,4-dihydro form. *Inorg. Chem.* **2001**, *40* (10), 2263-2269.
111. Davis, A. V.; Yeh, R. M.; Raymond, K. N., Supramolecular assembly dynamics. *Proceedings of the National Academy of Sciences* **2002**, *99* (8), 4793-4796.
112. Lehn, J. M., *Supramolecular chemistry*. Wiley-VCH Verlag GmbH & Co. KGaA: New York, 2006.
113. Kitagawa, S.; Kitaura, R.; Noro, S., Functional porous coordination polymers. *Angew. Chem.-Int. Edit.* **2004**, *43* (18), 2334-2375.
114. (a) Eddaoudi, M.; Moler, D. B.; Li, H. L.; Chen, B. L.; Reineke, T. M.; O'Keeffe, M.; Yaghi, O. M., Modular chemistry: Secondary building units as a basis for the design of highly porous and robust metal-organic carboxylate frameworks. *Accounts Chem. Res.* **2001**, *34* (4), 319-330; (b) Yaghi, O. M.; O'Keeffe, M.; Ockwig, N. W.; Chae, H. K.; Eddaoudi, M.; Kim, J., Reticular synthesis and the design of new materials. *Nature* **2003**, *423* (6941), 705-714; (c) Perry Iv, J. J.; Perman, J. A.; Zaworotko, M. J., Design and synthesis of metal-organic frameworks using metal-organic polyhedra as supermolecular building blocks. *Chemical Society Reviews* **2009**, *38* (5), 1400-1417.

115. Dalgarno, S. J.; Power, N. P.; Atwood, J. L., Metallo-supramolecular capsules. *Coordination Chemistry Reviews* **2008**, *252* (8–9), 825-841.
116. Moulton, B.; Zaworotko, M. J., From molecules to crystal engineering: Supramolecular isomerism and polymorphism in network solids. *Chemical Reviews* **2001**, *101* (6), 1629-1658.
117. Pedersen, C. J., Cyclic polyethers and their complexes with metal salts. *Journal of the American Chemical Society* **1967**, *89* (10), 2495-&.
118. Saalfrank, R. W.; Stark, A.; Peters, K.; Vonschnering, H. G., Adamantoid chelate complexes. *Angewandte Chemie-International Edition in English* **1988**, *27* (6), 851-853.
119. (a) Stang, P. J., Molecular architecture: Coordination as the motif in the rational design and assembly of discrete supramolecular species—Self-assembly of metallacyclic polygons and polyhedra. *Chemistry – A European Journal* **1998**, *4* (1), 19-27; (b) Stang, P. J., From solvolysis to self-assembly. *The Journal of Organic Chemistry* **2009**, *74* (1), 2-20; (c) Leininger, S.; Olenyuk, B.; Stang, P. J., Self-assembly of discrete cyclic nanostructures mediated by transition metals. *Chemical Reviews* **2000**, *100* (3), 853-908; (d) Swiegers, G. F.; Malefetse, T. J., New self-assembled structural motifs in coordination chemistry. *Chemical Reviews* **2000**, *100* (9), 3483-3538.
120. (a) Fujita, M.; Tominaga, M.; Hori, A.; Therrien, B., Coordination assemblies from a Pd(II)-cornered square complex. *Accounts Chem. Res.* **2005**, *38* (4), 369-378; (b) Fujita, M.; Umemoto, K.; Yoshizawa, M.; Fujita, N.; Kusukawa, T.; Biradha, K., Molecular paneling coordination. *Chemical Communications* **2001**, (6), 509-518; (c)

- Fujita, M., Metal-directed self-assembly of two- and three-dimensional synthetic receptors. *Chemical Society Reviews* **1998**, 27 (6), 417-425.
121. (a) Caulder, D. L.; Raymond, K. N., The rational design of high symmetry coordination cluster. *Journal of the Chemical Society, Dalton Transactions* **1999**, (8), 1185-1200; (b) Caulder, D. L.; Raymond, K. N., Supermolecules by design. *Accounts Chem. Res.* **1999**, 32 (11), 975-982.
122. Olenyuk, B.; Levin, M. D.; Whiteford, J. A.; Shield, J. E.; Stang, P. J., Self-assembly of nanoscopic dodecahedra from 50 predesigned components. *Journal of the American Chemical Society* **1999**, 121 (44), 10434-10435.
123. Harris, K.; Fujita, D.; Fujita, M., Giant hollow M_nL_{2n} spherical complexes: structure, functionalisation and applications. *Chemical Communications* **2013**, 49 (60), 6703-6712.
124. Park, J.; Sun, L.-B.; Chen, Y.-P.; Perry, Z.; Zhou, H.-C., Azobenzene-functionalized metal-organic polyhedra for the optically responsive capture and release of guest molecules. *Angewandte Chemie International Edition* **2014**, 53 (23), 5842-5846.
125. Riddell, I. A.; Smulders, M. M. J.; Clegg, J. K.; Nitschke, J. R., Encapsulation, storage and controlled release of sulfur hexafluoride from a metal-organic capsule. *Chemical Communications* **2011**, 47 (1), 457-459.
126. (a) Takezawa, H.; Murase, T.; Fujita, M., Temporary and permanent trapping of the metastable twisted conformer of an overcrowded chromic alkene via encapsulation. *Journal of the American Chemical Society* **2012**, 134 (42), 17420-17423; (b) Fang, Y.;

Murase, T.; Sato, S.; Fujita, M., Noncovalent tailoring of the binding pocket of self-assembled cages by remote bulky ancillary groups. *Journal of the American Chemical Society* **2013**, *135* (2), 613-615; (c) Murase, T.; Nishijima, Y.; Fujita, M., Unusual photoreaction of triquinacene within self-assembled hosts. *Chemistry – An Asian Journal* **2012**, *7* (4), 826-829.

127. (a) Therrien, B.; Süß-Fink, G.; Govindaswamy, P.; Renfrew, A. K.; Dyson, P. J., The “Complex-in-a-Complex” cations $[(\text{acac})_2\text{M}\subset\text{Ru}_6(\text{p}^i\text{PrC}_6\text{H}_4\text{Me})_6(\text{tpt})_2(\text{dwbq})_3]^{6+}$: A Trojan horse for cancer cells. *Angewandte Chemie International Edition* **2008**, *47* (20), 3773-3776; (b) Paul, L. E. H.; Therrien, B.; Furrer, J., Investigation of the reactivity between a ruthenium hexacationic prism and biological ligands. *Inorg. Chem.* **2012**, *51* (2), 1057-1067.

128. (a) Bolger, J.; Gourdon, A.; Ishow, E.; Launay, J.-P., Mononuclear and binuclear tetrapyrrodo[3,2-a:2',3'-c:3'',2''-h:2''',3''''-j]phenazine (tpphz) ruthenium and osmium complexes. *Inorg. Chem.* **1996**, *35* (10), 2937-2944; (b) Angaridis, P.; Cotton, F. A.; Petrukhina, M. A., Bis(diphenylphosphino)methanedicopper(I) units bridged by dicarboxylates. *Inorganica Chimica Acta* **2001**, *324* (1-2), 318-323.

129. (a) Pinkowicz, D.; Southerland, H. I.; Avendaño, C.; Prosvirin, A.; Sanders, C.; Wernsdorfer, W.; Pedersen, K. S.; Dreiser, J.; Clérac, R.; Nehr Korn, J.; Simeoni, G. G.; Schnegg, A.; Holldack, K.; Dunbar, K. R., Cyanide single-molecule magnets exhibiting solvent dependent reversible “On” and “Off” exchange bias behavior. *Journal of the American Chemical Society* **2015**, *137* (45), 14406-14422; (b) Kobler, H.; Munz, R.;

- Gasser, G. A.; Simchen, G., Eine einfache synthese von tetraalkylammoniumsalzen mit funktionellen anionen. *Justus Liebigs Annalen der Chemie* **1978**, 1978 (12), 1937-1945.
130. Yongho, S.; Wonho, J., Atomic force microscopy and spectroscopy. *Reports on Progress in Physics* **2008**, 71 (1), 016101.
131. Moore, A. M.; Weiss, P. S., Functional and spectroscopic measurements with scanning tunneling microscopy. *Annual Review of Analytical Chemistry* **2008**, 1 (1), 857-882.
132. Behnamfar, M. T.; Hadadzadeh, H.; Simpson, J.; Darabi, F.; Shahpiri, A.; Khayamian, T.; Ebrahimi, M.; Amiri Rudbari, H.; Salimi, M., Experimental and molecular modeling studies of the interaction of the polypyridyl Fe(II) and Fe(III) complexes with DNA and BSA. *Spectrochimica Acta Part A: Molecular and Biomolecular Spectroscopy* **2015**, 134, 502-516.
133. *Persistence of Vision Raytracer* Version 3.6; Persistence of Vision Pty. Ltd.: 2004.
134. (a) Pinkowicz, D.; Southerland, H.; Wang, X.-Y.; Dunbar, K. R., Record antiferromagnetic coupling for a 3d/4d cyanide-bridged compound. *Journal of the American Chemical Society* **2014**, 136 (28), 9922-9924; (b) Ruiz, E.; Rodríguez-Forteza, A.; Alvarez, S.; Verdaguer, M., Is it possible to get high TC magnets with prussian blue analogues? A theoretical prospect. *Chemistry – A European Journal* **2005**, 11 (7), 2135-2144.

135. Guzei, I., An idealized molecular geometry library for refinement of poorly behaved molecular fragments with constraints. *Journal of Applied Crystallography* **2014**, *47* (2), 806-809.
136. Schwach, M.; Hausen, H.-D.; Kaim, W., The first crystal structure of a metal-stabilized tetrazine anion radical: Formation of a dicopper complex through self-assembly in a comproportionation reaction. *Inorg. Chem.* **1999**, *38* (10), 2242-2243.
137. Woods, T. J.; Ballesteros-Rivas, M. F.; Ostrovsky, S. M.; Palii, A. V.; Reu, O. S.; Klokishner, S. I.; Dunbar, K. R., Strong direct magnetic coupling in a dinuclear Co^{II} tetrazine radical single-molecule magnet. *Chemistry – A European Journal* **2015**, *21* (29), 10302-10305.
138. Mason, W. R.; Gray, H. B., Electronic structures of square-planar complexes. *Journal of the American Chemical Society* **1968**, *90* (21), 5721-5729.
139. *Global Tuberculosis Report 2015*; 978 92 4 156505 9; World Health Organization: Geneva, 2014.
140. Dolin, P. J.; Raviglione, M. C.; Kochi, A., Global Tuberculosis incidence and mortality during 1990-2000. *Bull. World Health Organ.* **1994**, *72* (2), 213-220.
141. (a) Sacchettini, J. C.; Rubin, E. J.; Freundlich, J. S., Drugs versus bugs: in pursuit of the persistent predator *Mycobacterium tuberculosis*. *Nat. Rev. Microbiol.* **2008**, *6* (1), 41-52; (b) Smith, C. V.; Sharma, V.; Sacchettini, J. C., TB drug discovery: addressing issues of persistence and resistance. *Tuberculosis* **2004**, *84* (1-2), 45-55.
142. (a) Kana, B. D.; Karakousis, P. C.; Parish, T.; Dick, T., Future target-based drug discovery for tuberculosis? *Tuberculosis* **2014**, *94* (6), 551-556; (b) Payne, D. J.;

Gwynn, M. N.; Holmes, D. J.; Pompliano, D. L., Drugs for bad bugs: confronting the challenges of antibacterial discovery. *Nature Reviews Drug Discovery* **2007**, *6* (1), 29-40; (c) Ioerger, T. R.; O'Malley, T.; Liao, R.; Guinn, K. M.; Hickey, M. J.; Mohaideen, N.; Murphy, K. C.; Boshoff, H. I. M.; Mizrahi, V.; Rubin, E. J.; Sasseti, C. M.; Barry, C. E.; Sherman, D. R.; Parish, T.; Sacchettini, J. C., Identification of New Drug Targets and Resistance Mechanisms in Mycobacterium tuberculosis. *Plos One* **2013**, *8* (9).

143. (a) McKinney, J. D.; zu Bentrup, K. H.; Munoz-Elias, E. J.; Miczak, A.; Chen, B.; Chan, W. T.; Swenson, D.; Sacchettini, J. C.; Jacobs, W. R.; Russell, D. G., Persistence of Mycobacterium tuberculosis in macrophages and mice requires the glyoxylate shunt enzyme isocitrate lyase. *Nature* **2000**, *406* (6797), 735-738; (b) Munoz-Elias, E. J.; McKinney, J. D., Mycobacterium tuberculosis isocitrate lyases 1 and 2 are jointly required for in vivo growth and virulence. *Nature Medicine* **2005**, *11* (6), 638-644.

144. (a) Smith, C. V.; Huang, C. C.; Miczak, A.; Russell, D. G.; Sacchettini, J. C.; Bentrup, K. H. Z., Biochemical and structural studies of malate synthase from Mycobacterium tuberculosis. *Journal of Biological Chemistry* **2003**, *278* (3), 1735-1743; (b) Howard, B. R.; Endrizzi, J. A.; Remington, S. J., Crystal structure of escherichia coli Malate Synthase G complexed with magnesium and glyoxylate at 2.0 Å resolution: Mechanistic implications. *Biochemistry* **2000**, *39* (11), 3156-3168; (c) Holmes, R. P., The absence of glyoxylate cycle enzymes in rodent and embryonic chick liver. *Biochimica et Biophysica Acta (BBA) - General Subjects* **1993**, *1158* (1), 47-51.

145. (a) Cioni, M.; Pinzauti, G.; Vanni, P., Comparative biochemistry of the glyoxylate cycle. *Comparative Biochemistry and Physiology Part B: Comparative Biochemistry* **1981**, *70* (1), 1-26; (b) Kornberg, H. L.; Krebs, H. A., Synthesis of cell constituents from C2-units by a modified tricarboxylic acid cycle. *Nature* **1957**, *179* (4568), 988-991; (c) Gengenbacher, M.; Kaufmann, S. H. E., Mycobacterium tuberculosis: success through dormancy. *FEMS Microbiology Reviews* **2012**, *36* (3), 514-532.
146. Sharma, V.; Sharma, S.; Bentrup, K. H. Z.; McKinney, J. D.; Russell, D. G.; Jacobs, W. R.; Sacchettini, J. C., Structure of isocitrate lyase, a persistence factor of Mycobacterium tuberculosis. *Nature Structural Biology* **2000**, *7* (8), 663-668.
147. Anstrom, D. M.; Remington, S. J., The product complex of M-tuberculosis malate synthase revisited. *Protein Science* **2006**, *15* (8), 2002-2007.
148. Clark, J. D.; Okeefe, S. J.; Knowles, J. R., Malate Synthase - Proof of a stepwise Claisen condensation using the double-isotope fractionation test. *Biochemistry* **1988**, *27* (16), 5961-5971.
149. Macalino, S.; Gosu, V.; Hong, S.; Choi, S., Role of computer-aided drug design in modern drug discovery. *Arch. Pharm. Res.* **2015**, *38* (9), 1686-1701.
150. (a) Lounnas, V.; Ritschel, T.; Kelder, J.; McGuire, R.; Bywater, R. P.; Foloppe, N., Current progress in structure-based rational drug design marks a new mindset in drug discovery. *Computational and Structural Biotechnology Journal* **2013**, *5* (6), 1-14; (b) Law, R.; Barker, O.; Barker, J.; Hestekamp, T.; Godemann, R.; Andersen, O.; Fryatt, T.; Courtney, S.; Hallett, D.; Whittaker, M., The multiple roles of computational

- chemistry in fragment-based drug design. *J Comput Aided Mol Des* **2009**, *23* (8), 459-473.
151. Zheng, X.; Gan, L.; Wang, E.; Wang, J., Pocket-based drug design: Exploring pocket space. *The AAPS Journal* **2013**, *15* (1), 228-241.
152. (a) Sliwoski, G.; Kothiwale, S.; Meiler, J.; Lowe, E. W., Computational methods in drug discovery. *Pharmacological Reviews* **2014**, *66* (1), 334-395; (b) Huang, H.-J.; Yu, H. W.; Chen, C.-Y.; Hsu, C.-H.; Chen, H.-Y.; Lee, K.-J.; Tsai, F.-J.; Chen, C. Y.-C., Current developments of computer-aided drug design. *Journal of the Taiwan Institute of Chemical Engineers* **2010**, *41* (6), 623-635.
153. Gorteau, V.; Bollot, G.; Mareda, J.; Matile, S., Rigid-rod anion- π slides for multiion hopping across lipid bilayers. *Organic & Biomolecular Chemistry* **2007**, *5* (18), 3000-3012.
154. Zlatovic, M. V.; Borozan, S. Z.; Nikolic, M. R.; Stojanovic, S. D., Anion- π interactions in protein-porphyrin complexes. *RSC Advances* **2015**, *5* (48), 38361-38372.
155. (a) Robertazzi, A.; Krull, F.; Knapp, E.-W.; Gamez, P., Recent advances in anion- π interactions. *CrystEngComm* **2011**, *13* (10), 3293-3300; (b) Philip, V.; Harris, J.; Adams, R.; Nguyen, D.; Spiers, J.; Baudry, J.; Howell, E. E.; Hinde, R. J., A survey of aspartate-phenylalanine and glutamate-phenylalanine interactions in the Protein Data Bank: Searching for anion- π pairs. *Biochemistry* **2011**, *50* (14), 2939-2950; (c) Jenkins, D. D.; Harris, J. B.; Howell, E. E.; Hinde, R. J.; Baudry, J., STAAR: Statistical analysis of aromatic rings. *Journal of Computational Chemistry* **2013**, *34* (6), 518-522.

156. Bauzá, A.; Quiñonero, D.; Deyà, P. M.; Frontera, A., On the importance of anion- π interactions in the mechanism of sulfide:quinone oxidoreductase. *Chemistry – An Asian Journal* **2013**, 8 (11), 2708-2713.
157. Estarellas, C.; Frontera, A.; Quiñonero, D.; Deyà, P. M., Relevant anion- π interactions in biological systems: The case of urate oxidase. *Angewandte Chemie International Edition* **2011**, 50 (2), 415-418.
158. Bauzá, A.; Quiñonero, D.; Deyà, P. M.; Frontera, A., Long-range effects in anion- π interactions: Their crucial role in the inhibition mechanism of Mycobacterium tuberculosis malate synthase. *Chem.-Eur. J.* **2014**, 20 (23), 6985-6990.
159. Jurecka, P.; Nachtigall, P.; Hobza, P., RI-MP2 calculations with extended basis sets-a promising tool for study of H-bonded and stacked DNA base pairs. *Physical Chemistry Chemical Physics* **2001**, 3 (20), 4578-4582.
160. Ahlrichs, R.; Bär, M.; Häser, M.; Horn, H.; Kölmel, C., Electronic structure calculations on workstation computers: The program system turbomole. *Chemical Physics Letters* **1989**, 162 (3), 165-169.
161. Krieger, Inna V.; Freundlich, Joel S.; Gawandi, Vijay B.; Roberts, Justin P.; Gawandi, Vidyadhar B.; Sun, Q.; Owen, Joshua L.; Fraile, Maria T.; Huss, Sofia I.; Lavandera, J.-L.; Ioerger, Thomas R.; Sacchettini, James C., Structure-guided discovery of phenyl-diketo acids as potent inhibitors of M. tuberculosis Malate Synthase. *Chemistry & Biology* **2012**, 19 (12), 1556-1567.

162. Jones, G. J.; Robertazzi, A.; Platts, J. A., Efficient and accurate theoretical methods to investigate anion- π interactions in protein model structures. *The Journal of Physical Chemistry B* **2013**, *117* (12), 3315-3322.
163. Wu, T.; Kalugina, Y. N.; Thakkar, A. J., Choosing a density functional for static molecular polarizabilities. *Chemical Physics Letters* **2015**, *635*, 257-261.
164. (a) Christensen, J. J.; Izatt, R. M.; Hansen, L. D.; Partridge, J. A., Entropy titration. A calorimetric method for the determination of ΔG , ΔH , and ΔS from a single thermometric titration lab. *The Journal of Physical Chemistry* **1966**, *70* (6), 2003-2010; (b) Hansen, L. D.; Christensen, J. J.; Izatt, R. M., Entropy titration. A calorimetric method for the determination of ΔG° (K), ΔH° and ΔS° . *Chemical Communications (London)* **1965**, (3), 36-38.
165. Freyer, M. W.; Lewis, E. A., Isothermal titration calorimetry: Experimental design, data analysis, and probing macromolecule/ligand binding and kinetic interactions. In *Methods in Cell Biology*, Academic Press: 2008; Vol. Volume 84, pp 79-113.
166. (a) Ford, D. M., Enthalpy-entropy compensation is not a general feature of weak association. *Journal of the American Chemical Society* **2005**, *127* (46), 16167-16170; (b) Bronowska, A. K., Thermodynamics of ligand-protein interactions: implications for molecular design, thermodynamics - interaction studies - solids, liquids and gases. Pirajan, J. C. M., Ed. InTech: 2011. <http://www.intechopen.com/books/thermodynamics-interaction-studies-solids-liquids-and-gases/thermodynamics-of-ligand-protein-interactions-implications-for-molecular-design> (accessed March 18, 2016).

167. Dewar, M. J. S. *AMPAC Graphical User Interface*, Semichem, Inc.: 1997.
168. (a) Berryman, O. B.; Bryantsev, V. S.; Stay, D. P.; Johnson, D. W.; Hay, B. P., Structural criteria for the design of anion receptors: The interaction of halides with electron-deficient arenes. *Journal of the American Chemical Society* **2007**, *129* (1), 48-58; (b) Hay, B. P.; Bryantsev, V. S., Anion-arene adducts: C-H hydrogen bonding, anion- π interaction, and carbon bonding motifs. *Chemical Communications* **2008**, (21), 2417-2428.
169. Humphrey, W.; Dalke, A.; Schulten, K., VMD: Visual molecular dynamics. *Journal of Molecular Graphics* **1996**, *14* (1), 33-38.
170. Baranauskienė, L.; Petrikaitė, V.; Matulienė, J.; Matulis, D., Titration calorimetry standards and the precision of isothermal titration calorimetry data. *International Journal of Molecular Sciences* **2009**, *10* (6), 2752-2762.